Spring 1992

Control of Low-Speed Turbulent Separated Flow Over a Backward-Facing Ramp

John C. Lin
Old Dominion University

CONTROL OF LOW-SPEED TURBULENT SEPARATED FLOW OVER A BACKWARD-FACING RAMP

by

John C. Lin

B.S. May 1980, Old Dominion University
M.E. May 1985, Old Dominion University

A Dissertation submitted to the Faculty of
Old Dominion University in Partial Fulfillment
of the Requirements for the Degree of

DOCTOR OF PHILOSOPHY
MECHANICAL ENGINEERING

OLD DOMINION UNIVERSITY
May 1992

Approved by:

Gregory V. Selby (Director)	Dennis M. Bushnell
Robert L. Ash	Stephen K. Robinson
Arthur C. Taylor	Oktay Baysal

ABSTRACT

CONTROL OF LOW-SPEED TURBULENT SEPARATED FLOW OVER A BACKWARD-FACING RAMP

John C. Lin

Old Dominion University, 1991

Director: Dr. Gregory V. Selby

The relative performance and flow phenomena associated with several devices for controlling turbulent separated flow were investigated at low speeds. Relative performance of the devices was examined for flow over a curved, backward-facing ramp in a wind tunnel, and the flow phenomena were examined in a water tunnel using dye-flow visualization. Surface static pressure measurements and oil-flow visualization results from the wind tunnel tests indicated that transverse grooves, longitudinal grooves, submerged vortex generators, vortex generator jets (VGJ's), Viets' fluidic flappers, elongated arches at $+\alpha$ (positive angle of attack), and large-eddy breakup devices (LEBU's) at $+\alpha$ placed near the baseline separation location reduce flow separation and increase pressure recovery. Spanwise cylinders reduce flow separation but decrease pressure recovery downstream. Riblets, passive porous surfaces, swept grooves, Helmholtz resonators, and arches and LEBU's with $\alpha \leq 0^{\circ}$ had no significant effect in reducing the extent of the separation region. Wall-cooling computations indicated that separation delay on a partially-cooled ramp is nearly the same as on a fully-cooled ramp, while minimizing the frictional drag increase associated with the wall cooling process. Dye-flow visualization tests in the water tunnel indicated that

wishbone vortex generators in the forward orientation shed horseshoe vortices; wishbone vortex generators oriented in the reverse direction and doublet vortex generators shed streamwise counterrotating vortices; a spanwise cylinder located near the wall and LEBU's at $\alpha = -10°$ produced eddies or transverse vortices which rotated with the same sign as the mean vorticity in a turbulent boundary layer; and the most effective VGJ's produced streamwise co-rotating vortices. Comparative wind-tunnel test results indicated that transferring momentum from the outer region of a turbulent boundary layer through the action of embedded streamwise vortices is more effective than by transverse vortices for the separation control application studied herein.

ACKNOWLEDGEMENTS

I would like to take a moment to gratefully acknowledge the individuals who helped me accomplish this work. First, I wish to thank Mr. Dennis M. Bushnell, who suggested the topic of this dissertation, and Dr. Gregory V. Selby for his guidance and direction during the course of this investigation. I am thankful to Drs. Robert L. Ash, Oktay Baysal, and Arthur C. Taylor for serving as members of my dissertation committee. Special thanks are extended to Dr. Stephen K. Robinson for his helpful suggestions and continued support, and to Mr. Floyd G. Howard for his contributions during model development.

Thanks are also extended to Dr. Leonard M. Weinstein for the development of the force balance used in performing device drag measurements, to Mr. Barry S. Lazos for the development of the dye-injection splitter plate, and to Mr. Dan H. Neuhart for his technical support of tests conducted in the NASA Langley 16- by 24-Inch Water Tunnel. In addition, I would like to give special thanks to Mr. John B. (Ben) Anders, Mr. Michael J. Walsh, Dr. Mehdi Khorrami, Dr. Chungsheng Yao, Mr. Rudolph A. King, Miss Cathy B. McGinley, and Mr. Jerry N. Hefner for their helpful comments and discussions. Furthermore, I thank Mrs. Lise P. Crowe and Miss Luisa Nazzaro for their contributions in typing and graphically illustrating of this dissertation, respectively.

Finally, special thanks to my parents, Mr. Rong-An and Mrs. Woan-Chin Lin, for their support and encouragement while pursuing this goal.

TABLE OF CONTENTS

LIST OF TABLES

LIST OF FIGURES

NOMENCLATURE

a	groove depth
b	groove width
c	speed of sound
C_f	skin-friction coefficient, $2\tau_w/\rho U_\infty^2$
C_p	pressure coefficient, $2(P-P_\infty)/\rho U_\infty^2$
d	device diameter
D	skin-friction drag
D_c	cavity diameter
D_o	orifice diameter
e_1,e_2	fluctuating hot-wire signals
e_{n1},e_{n2}	electronic noise within hot-wire systems
e_t	freestream turbulence signal
$\overline{E}$	mean voltage
E_{s1},E_{s2}	amplitudes of the scattered beams
f_D	Doppler frequency, $\frac{2\sin\phi}{\Lambda}u$
f_{s1},f_{s2}	scattered beam frequencies
f_o	Helmholtz frequency, $\frac{c}{2\pi}[S/(l'V+H^2S/3)]^{1/2}$
g	gap between the wall and the nearest body surface
h	device height (distance from wall)
H	cavity length
I	photocurrent, $E_{s1}^2+E_{s2}^2-2E_{s1}E_{s2}\cos[2\pi(f_{s2}-f_{s1})t_i]$
k	local slope of the hot-wire calibration curve, $\frac{\Delta\overline{E}}{\Delta U_\infty}$
ℓ	device chord (streamwise) length
l'	effective length of oscillating mass, $t+\frac{4D_o}{3\pi}\left[2-1.25\frac{D_o}{D_c}\right]$
LEBU	large-eddy breakup device
M	Mach number
P	pressure

P_∞	freestream static pressure
Q	total volumetric flow rate
R_θ	Reynolds number based on momentum thickness, $\frac{U_\infty \theta}{\nu}$
Re_ℓ	Reynolds number based on chord length, $\frac{U_\infty \ell}{\nu}$
Re_x	Reynolds number based on the distance between the stagnation and the device location, $\frac{U_\infty x}{\nu}$
s	device spanwise width
S	orifice area
t	wall thickness
t_i	time
T	temperature
u	local mean velocity in the x-direction
u_τ	friction velocity, $U_\infty \sqrt{\frac{C_f}{2}}$
U_∞	freestream velocity
v	local mean velocity in the y-direction
V	resonator volume
VG	vortex generator
VGJ	vortex generator jet
VR	velocity ratio or ratio of jet velocity to freestream velocity
W	width of the test section
x	coordinate along the freestream direction with origin at the beginning of turbulent boundary layer (tripping point)
X	$x - x_{s,\text{ref}}$
y	coordinate normal to the wall with origin at the surface
z	coordinate parallel to the wall and along the spanwise direction
Greek Symbols	
α	device inclination angle (angle between the device axis and the wall)
β	device azimuthal angle (angle between the device axis and the freestream direction in a x-z plane)
δ	boundary-layer thickness $\left(\text{based on } \frac{u}{U_\infty} = 0.995\right)$
δ_f	fringe spacing, $\frac{\Lambda}{2 \sin \phi}$
δ^*	displacement thickness, $\int_o^\delta \left(1 - \frac{u}{U_\infty}\right) dy$

Δ	differential value
θ	momentum thickness, $\int_o^\delta \frac{u}{U_\infty}\left(1-\frac{u}{U_\infty}\right)dy$
λ	spanwise or lateral distance between each geometric cycle
Λ	wavelength
ρ	density
μ	viscosity
ν	kinematic viscosity, μ/ρ
τ_w	wall shear stress
ϕ	half-angle of the two beams defining the probe volume
ω_z	spanwise (lateral) component of mean vorticity, $\frac{\partial v}{\partial x}-\frac{\partial u}{\partial y}$
Subscripts	
dev	device location
FP	flat plate reference value
m	mean value
max	maximum value
max,ref	maximum reference (or baseline) value
r	reattachment point
r,ref	reference reattachment point
s	separation point
s,ref	reference separation point
t	total value
t,∞	total freestream value
w	wall value
∞	freestream value
Superscripts	
$'$	rms fluctuating value
$+$	value in law-of-the-wall variables, multiplying by $\frac{u_\tau}{\nu}$ for length scale or dividing by u_τ for velocity scale

CHAPTER 1

INTRODUCTION

1.1 General Background

The classical concept of flow separation from a continuous surface is governed by two factors, *adverse pressure gradient* and *fluid viscosity*. In order to remain attached to the surface, the fluid in a boundary layer must have enough momentum to overcome the kinetic energy loss associated with the adverse pressure gradient and the viscous dissipation along its flow path. This loss has a more pronounced effect near the wall where the momentum is much less than in the outer part of the shear layer. If the flow retardation is such that further advancement of the fluid is no longer possible, then the surface streamline nearest to the wall leaves the bounding surface at this point and the boundary layer is said to separate (Maskell [1]*). At separation, the rotational flow region next to the wall abruptly thickens, the normal velocity component increases, and the boundary-layer approximations are no longer valid.

Due to the large energy losses associated with boundary-layer separation, the performance of many practical devices is often controlled by the separation location. Hence, separation flow control is of extreme importance for many technological applications of fluid mechanics. Controlling flow separation can result in an increase in system performance with consequent energy conservation as well as weight and space savings. Typical applications include: (1) efficient inlets and diffusers, (2) improved high-lift airfoils, (3) aircraft stall/spin control, (4) reduced fuselage/body drag, and (5) effective low Reynolds number airfoils.

*The numbers in brackets indicate references.

One specific goal of current interest is to develop a standby turbulent flow separation control scheme for fuselages or high Reynolds number bodies with Stratford closure [2]. The Stratford-closure concept consists of flow with continuously near-zero skin friction throughout the region of pressure rise such that the flow achieves the pressure rise in the shortest possible distance and with the least possible dissipation of energy. Due to its near-zero wall shear, the Stratford closure has a very low frictional drag, but as a result, it is also subject to flow separation caused by flow-field disturbances or off-design operating conditions. The optimum standby separation control scheme for this application should utilize the best combination of the following criteria: (1) minimum system penalty when not deployed (e.g., minimum volume and weight addition, low pressure drag, etc.), (2) effectiveness in controlling turbulent flow separation, (3) passive operation, and (4) rapid deployability.

In a two-dimensional boundary layer, the criterion for time-averaged separation corresponds to zero mean velocity gradient at the wall $\left(\text{i.e., } \frac{\partial u}{\partial y}\Big|_w = 0\right)$, or zero wall friction. If the momentum near the wall can be replenished, then separation is either delayed or eliminated (i.e., separation control). Common separation control techniques typically involve one or more of the following approaches [3,4]: (a) mitigation of applied pressure gradients; (b) removal of low-momentum, near-wall flow; (c) addition of streamwise momentum to the near-wall flow, either from an external source or through local redirection of higher momentum outer flow into the wall region; or (d) imposition of a *slip* layer at the wall. The choice of a particular control technique is usually dictated by system considerations, such as parasitic or device drag, system complications (due to weight, volume, complexity, and/or structural considerations), cost, reliability, performance sensitivity, and (for automobiles) styling. Typically, research on separation control devices involves limited parametric studies of a particular device/approach as applied to a particular flow situation. The present investigation is focused on a comparison of a wide range of separation control

techniques applied to a separated turbulent flow, which are introduced and discussed in the following sections.

1.2 Review of Previous Work and Possible Extensions for Separation Control

1.2.1 Transverse and Swept Grooves

The concept of using transverse surface grooves for delaying separation in diffusers evidently was originated in the Soviet Union by Migay [5–8]. Chang [9] and Stull [10,11] also indicated that grooves aligned transverse to the direction of the flow are effective in controlling separation. Up to a 50% bluff-body drag reduction was reported by Howard et al. [12,13] via small, transverse shoulder grooves. Migay [7,8] suggested that the grooves function similar to *roller bearings*. In other words, the mechanism for transverse-groove separation control appears to be one of simply substituting several small regions of separation (which effectively provide a wall slip boundary condition) for a larger separated-flow region. Transverse grooving is one of the few techniques that can establish a slip layer at the wall without actually translating the wall itself. This approach has been studied, thus far, mainly in low Reynolds number flows and has been presently extended toward the more relevant, higher Reynolds number region. In the investigations cited, the Reynolds number based upon the distance between stagnation point and transverse grooves, Re_x, was less than 8×10^5, while Re_x for the present study was approximately 5.1×10^6. Improving the *roller bearing* effect by making the flow more three-dimensional through swept grooves was also a subject for the present investigation.

1.2.2 Riblets

Research is also necessary to determine whether the *effective slip layer* produced by small longitudinal grooves similar to the NASA riblets [14,15] has a beneficial effect

on flow separation. The use of riblets constitutes one of the more successful turbulent skin-friction reduction techniques developed in the early 80's. The riblet surface consists of flow-aligned grooves which have heights and spacings on the order of the turbulent wall streak and burst dimensions [14–16]. Symmetric V-groove riblets with heights and spacings of 12 to 15 wall units were shown to yield drag reductions on the order of 8% for flat plates with zero pressure gradient [14,15].

If riblets are to be applied to aircraft wings as well as to the fuselage, the effect of riblets on turbulent flow separation must be examined. Riblets modify the skin friction and momentum of the fluid near the wall. Whether or not the reduced near-wall momentum due to the riblets will enhance or delay separation needs to be determined. Truong et al. [17] showed that riblets reduce both the displacement thickness, δ^*, and momentum thickness, θ, in diffusers, which suggests riblets might delay separation if the resulting value of the shape factor (δ^*/θ) is reduced. Schlichting [18] indicated that when values of the shape factor increase from 1.3 for a zero pressure gradient turbulent boundary layer to that of between 2 and 4.9 for an adverse pressure gradient, the flow is said to have separated. A recent study by King et al. [19] showed delayed flow separation in a diffuser with riblets having nondimensional heights, $h^+ > 25$. In zero-pressure gradient flows, these are heights for which the riblets would increase rather than decrease the skin friction, as reported by Walsh [14]. The present study examined the effect of both skin-friction increasing and decreasing riblets on flow separation.

1.2.3 Passive Porous Surfaces

It is well known that active boundary-layer suction can remove the low-momentum near-wall flow and control flow separation [4,9]. It has also been shown that passive bleed via porous surfaces can prevent shock-wave/boundary-layer separation on the surface of transonic airfoils [20–24]. Passive shock/boundary-layer control provides drag reduction through placement of an empty subsurface plenum covered by a porous top surface and

located at the airfoil chordwise position where a shock wave impinged upon the boundary layer. The higher pressure behind the shock wave circulates flow through the cavity to the lower pressure region ahead of the shock, resulting in a more gradual viscous-inviscid interaction, a series of weaker shock waves, and reduced pressure gradients. The effects of this recirculation reduce both boundary-layer separation and wave drag. Raghunathan et al. [25] conducted experiments on a two-dimensional low speed diffuser with passive control. The passive control consisted of porous surfaces made of holes and slots connected by a breather passage. Passive control postponed the stall and reduced buffet levels in the diffuser. Their test confirmed that passive controls for flow separation are not restricted to transonic speeds. Examining the effectiveness of the passive porous surfaces for flow separation control via recirculating self-bleed at low speeds was also a subject for the present investigation.

1.2.4 Longitudinal Grooves

One method of redirecting outer flow momentum is the three dimensionalization of a two-dimensional mean flow through longitudinal grooves [13,26–28]. Howard et al. [13,26] indicated that large longitudinal V-grooves in the shoulder of a bluff body can produce up to 33% net drag reduction. Their experiments suggested that the streamwise vorticity generated by the pumping action of the *attached* groove flow decreased the size of the flow separation region. This is also an example of locally mitigating the imposed adverse pressure gradient through the technique of partial *boattailing* for separation control. Selby and Miandoab [28] reported that the base pressure of a blunt trailing-edge airfoil with surface grooves increased with increasing groove depth and angle. They speculated that *minimally* attached flow in the grooves is the mechanism by which fluid of higher momentum is redirected to the base flow region to affect an increase in the pressure. In the present investigation, studies were conducted to compare the

effectiveness of this longitudinal groove technique for (two-dimensional) flow separation control.

1.2.5 Submerged Vortex Generators

Conventional passive vortex generators with device height, h, on the order of the boundary-layer thickness, δ, have long been known to increase the mixing (through direct wallward momentum transfer) between external streams and boundary layers. First introduced by Taylor [29–31], these vortex generators consist of a row of small plates or airfoils that project normal to the surface and are set at an angle of incidence to the local flow to produce an array of streamwise trailing vortices. Taylor-type vortex generators are commonly used to delay boundary-layer separation [32], to enhance aircraft wing lift [33–35], to reduce afterbody drag of aircraft fuselages [36,37], and to avoid or delay separation in subsonic diffusers [38–40]. However, Taylor-type vortex generators produce significant parasitic drag, which causes a reduction in vehicle efficiency (unless the devices are retracted when not needed).

By taking advantage of the fullness of the mean velocity profile in a high Reynolds number turbulent boundary layer, a recent optimization approach [41–45] reduced the generator height, h, to only a fraction of δ to form *submerged vortex generators*. Kuethe [41] examined several wave-type submerged vortex generators with h/δ of 0.27 and 0.42 that were successful in reducing the intensity of separation-induced acoustic disturbances in the wake region by suppressing the formation of the Karman vortex street and reducing the area of the velocity deficit in the wake. Kuethe's vortex generators use the *Taylor-Goertler instability* to generate streamwise vortices within the boundary layer when the fluid is caused to flow over a concave surface. Holmes et al. [42] demonstrated a significant reduction in interior noise on a Gulfstream III corporate aircraft at cruise conditions through application of very low profile ($h/\delta \approx 0.1$) submerged vortex generators. These vortex generators delayed shock-induced boundary-layer separation

as well as attenuated the vortices shed from the canopy shock wave, minimizing two major sources of noise. A recent study by Rao and Kariya [43] suggested that a concave slat-type submerged vortex generator with $h/\delta \sim 0.625$ may retain its effectiveness at a much smaller h/δ. The authors recommended further study to identify optimum geometric parameters of submerged vortex generators and to examine the parasitic drag.

Wheeler's doublets [46] and wishbones [47] are relatively new types of wedge-shaped vortex generators. The submerged vortex generators initially investigated in the present study were these Wheeler devices, since the wedge geometry of Wheeler generators was more robust and easier to apply than vane-type generators. The Wheeler doublet vortex generators were based on cutouts of the NACA flush inlet [48] and consisted of a double row of triangular, ramp-shaped devices resembling overlapping (downstream-pointing) arrowheads. The purpose of the second row was to reinforce the vortices produced by the first row. The wishbone vortex generators, on the other hand, consisted of a single row of V-shaped ramps (two jointed legs with an included angle of approximately 60°) with their apexes pointing downstream. Kehro et al. [44] reported that wishbone devices provided up to 38% drag reduction for a low Reynolds number airfoil by controlling its laminar separation bubble. McCormick [45] demonstrated that doublet devices significantly suppressed shock-induced separation and improved boundary-layer characteristics downstream of the shock.

1.2.6 Large-Eddy Breakup Devices at Angle of Attack

A possible alternative to direct momentum pumping by vortex generators is the large-eddy breakup device (LEBU) at a small angle of attack. A LEBU is a thin spanwise ribbon or airfoil with chord $\sim O(\delta)$ placed in the outer part of a boundary layer (parallel to the wall) in order to alter the turbulence structure. It has been suggested that such devices break up the large-eddy structure in the turbulent boundary layer and/or add new structures via the device wake [49,50]. Presumably, these new/altered structures can

augment or diminish the transport of momentum into the near-wall region and therefore attenuate or accentuate the effects of boundary-layer separation. Furthermore, a LEBU set at an angle of attack can generate large transverse dynamic vortical motions [49] and possibly result in augmentation of the cross-section momentum transport via the turbulent Reynolds stress field. One goal of the present investigation was to determine the effect of LEBU devices on boundary-layer separation.

1.2.7 Spanwise Cylinders

Another method of increasing near-wall mixing is through turbulence augmentation via spanwise cylinders. Moser [51] and Sajben et al. [52] successfully used cylinder wakes (dominated by Karman vortex streets) to augment the turbulence in the downstream boundary layer for prevention or delay of flow separation. Marumo et al. [53] reported that the cylinder wake altered the usual boundary-layer structures in the outer region and continued to do so for at least 30δ downstream. It was also shown that variations in the diameter of the cylinder or location above the wall can alter the wall production processes [54]. As the cylinder approached the wall for small gaps, where the gap to diameter ratio approached 0.2 to 0.3, the vortex shed from the cylinder surface nearest the wall (which had the opposite sense to the mean boundary-layer vorticity) was severely damped. As a result, the *control vortices* produced by the cylinder were predominately of a sense which should augment the existing boundary-layer vorticity and enhance turbulent momentum transport from the outer region toward the wall [55]. These flow phenomena and the relative effect of the height, diameter, and streamwise location of the spanwise cylinder on separation control were examined in the present study.

1.2.8 Arches

A dominant feature of the flow over a three-dimensional bluff body (e.g., a vertical cylinder or prism) attached to a plane wall is the periodic shedding of three-dimensional

horseshoe-shaped vortices [56,57]. Of course, such a configuration has a large device drag penalty. One possible means of generating the horseshoe-shaped vortices while keeping the device drag to a minimum is to use arches embedded in the boundary layer. Due to the viscous effect near the arch surfaces, the flow through an arch tends to be slower than the flow around it, possibly resulting in the continuous generation of horseshoe-shaped vortices that could redirect longitudinal momentum to the near-wall flow. To the author's knowledge, no previous study has been performed on the effect of surface arches (and accompanying vortices) on separated flow.

1.2.9 Helmholtz Resonators

The Helmholtz resonators consist of a cavity vented by a small orifice. The cavity and orifice are designed to respond to imposed pressure oscillations caused by the unsteady flow in the shear layer flowing across the orifices. Resonance occurs when the frequency of these oscillations matches the natural frequency of the resonator. Panton and Miller [58] tested a series of resonators at three different resonant frequencies. They showed that strong excitation occurred when the Strouhal number based on the wall shear velocity and orifice diameter was in the range of 30 to 45. A later study [59] showed strong effects of orifice geometry upon excitation; i.e., the exact shape of the orifice sidewall had a drastic effect on resonator response. De Metz and Farabee [60] found that the rms cavity pressure fluctuations were as great as 1.3 times the freestream dynamic pressure. Flynn et al. [61] reported that the Helmholtz resonators caused near-wall momentum oscillation by sucking in high-momentum fluid and expelling low- or zero-momentum fluid into the flow. In their experiment, this disturbance introduced a velocity defect into the streamwise velocity profile which was associated with increased levels of turbulent fluctuations—300% for v' and 30% for u'—and an increased Reynolds shear stress of up to 550%. Tests were performed herein to determine whether this increase in near-wall momentum oscillations via Helmholtz resonators could benefit flow separation control.

1.2.10 Viets' Fluidic Flappers

It has been shown that forced unsteady flow through an asymmetrical rotating cam embedded in the wall can produce large eddies in turbulent boundary layers with zero- and adverse-pressure gradients [62]. By using such a device in a wide-angle diffuser, Viets et al. [63] postponed the flow separation and significantly improved the diffuser's performance. An extension of this concept, from an active to a passive system, was first suggested by Viets et al. [64] in the form of a fluidic flapper device. This device consisted of a small scoop placed at the downstream entrance of a spanwise annular duct that directs flow through the duct and out the upstream exit. This exiting flow should cause the boundary layer on the test surface to separate and disrupt the flow through the duct entrance. Once the flow reattaches, the process repeats itself, creating intermittent large-scale vortical motions without the use of moving parts. In theory, this dynamic process should enhance cross-stream momentum transport in the boundary layer, thus preventing a large separated region downstream. To the author's knowledge, no previous investigation has been made of this flapper concept for flow separation control.

1.2.11 Vortex Generator Jets

The vortex generator jet (VGJ) technique, first proposed and studied by Wallis [65], is an active method for generating longitudinal (streamwise) vortices with jets blown through holes in a solid surface. The holes in the surface are inclined at an angle to the surface, skewed with respect to the freestream direction, and arrayed along the surface much like classical vortex generators. The precise mechanism of the vortex generation process when the jets are skewed is not yet fully understood. It appears that the relatively weak pair of counterrotating vortices that forms within a jet in crossflow is replaced by a system in which, after a short distance, a single stronger streamwise vortex trails downstream close to the surface (keeping some of the original jet fluid with it). Compton and Johnston [66] verified that a pitched and skewed jet in a crossflow

generates a longitudinal vortex downstream. Pearcey and Stuart [67] and Zhang and Li [68] examined the flow physics associated with VGJ's, including the relative strengths of the members of the vortex pair comprising a skewed jet. When placed upstream of a separated-flow region, the jet-induced streamwise vortices have proven effective in reducing the extent of turbulent boundary-layer separation resulting from adverse pressure gradients [65,69,70]. VGJ's have been used to delay turbulent separation on an airfoil [65], in a subsonic diffuser [69], and on a flat-plate model in an adverse pressure gradient [70].

The VGJ flow separation control technique has evidently not been employed operationally—probably because the feasibility of the technique has not been firmly established. If feasible, the approach should have several advantages over conventional vortex generators for active flow control on aircraft surfaces and in jet engines; i.e., (1) jets are generally easy to actuate and have the potential of displaying short response times in situations where rapid deployment is required for controlling separation and/or stall and (2) compared to solid vortex generators, the drag penalty of VGJ's is negligible when the jets are off. This represents an important consideration when cruise speed and operational range of aircraft are considered. From the operational efficiency and economic viewpoint, the VGJ's are probably best used in conjunction with an active suction system, such as that used for laminar flow control (LFC). For example, the air used in a LFC suction system near the leading-edge of a wing (operated for leading-edge region separation control during takeoff/landing) can be bled through the jet holes (appropriately located with respect to the region of flow separation) to produce streamwise vortices that interact with and control the separated flow.

The present study examined various parameters associated with VGJ's for separation control. Parameters that were varied include orifice diameter, jet orientation, jet speed, and streamwise jet location.

1.2.12 Wall Cooling

Fuselage drag reduction using thermal means becomes attractive for future aircraft because cryogenic fuels, such as methane and hydrogen, can be used as thermal reservoirs. Previous studies have concentrated on delaying transition by stabilizing laminar boundary layers with wall cooling [71–74]. The stabilization of a laminar boundary layer can help to reduce viscous drag since it has a lower viscous level than that of a turbulent boundary layer. However, the boundary-layer flow over the fuselage of a commercial transport aircraft is mostly turbulent due to its high Reynolds number range ($Re_\ell \approx 100$ to 300×10^6) and transition to turbulent flow is often accelerated by disturbances present in the nose region (i.e., bugs, windshield wipers, etc.). Since it may not be feasible to maintain laminar flow over realistic bodies, drag reduction via wall temperature control for turbulent flow past fuselage-like bodies was investigated by Lin and Ash [75]. They examined the use of temperature control to reduce the axisymmetric body drag under turbulent boundary-layer conditions. The computational study indicated that partial wall cooling of the afterbody can delay the separation almost as much as the 100% surface coverage case, but, with only about one-fifth to one-sixth the skin-friction drag increase associated with wall cooling. Partial afterbody wall cooling has a potential in achieving net drag reduction for bluff bodies by reducing the pressure drag associated with flow separation.

This partial wall cooling approach, studied for axisymmetric bodies, was extended herein to the two-dimensional case.

1.3 Research Objective

The principal objectives of the current research were: (1) to investigate the relative performance of several passive and active devices for controlling a two-dimensional, turbulent, separated flow on a common test bed (backward-facing curved ramp) at low speeds and (2) to investigate the flow physics downstream of selected flow-control devices

of interest through dye-flow visualization in a water tunnel. The relative performance of all flow-control devices, except for wall cooling, was investigated experimentally through surface pressure measurements and oil-flow visualization. The wall cooling method was investigated numerically via computing separation locations.

The outline of this investigation is as follows: the wind-tunnel and water-tunnel apparatus and tests are described in the second and third chapters, respectively; the relative separation-control performances of all devices, based on results obtained from the wind-tunnel experiments and wall-heat-transfer computations, are discussed in the fourth chapter; and the flow physics associated with selected flow control devices, based on results obtained from the water-tunnel experiments, are discussed in the fifth chapter.

CHAPTER 2

WIND-TUNNEL APPARATUS AND TESTS

2.1 Model Description

Sketches of all flow control devices tested in the present study are illustrated in Figure 2.1. The passive flow control devices examined were transverse and swept grooves, riblets, passive porous surfaces, large longitudinal grooves, submerged vortex generators, large-eddy breakup devices at a small angle of attack, spanwise cylinders, arches, Helmholtz resonators, and Viets' fluidic flappers. The active devices examined were vortex generator jets and wall cooling. All flow control devices except for the wall cooling were investigated experimentally. The wall cooling method was investigated numerically using potential flow and boundary-layer codes. Detailed descriptions of each device and the computer codes are presented in Chapter 4.

2.2 Test Facility

Separation control experiments were conducted in the NASA Langley 20- by 28-Inch Shear-Flow Control Tunnel (see Figure 2.2a for sketch of the wind tunnel). This facility is a low-turbulence ($u'/U_\infty < 0.005$), subsonic, open-circuit wind tunnel with a test section speed range of 7.5 to 150 ft/s. In the current study, all experiments were conducted at a freestream velocity of 132 ft/s. (The uncertainty in freestream velocity was $\pm 0.4\%$.) The freestream reference speed was measured using a pitot-static probe extended from the tunnel ceiling at the front of the test section.

Flow separation was established on a backward-facing curved ramp located approximately 6.5 feet from the test section entrance (see Figure 2.2b for the test configuration in the wind tunnel). A suction slot at the test section entrance was used to remove the converging section boundary layer to eliminate any influence of upstream history on the test boundary layer. The new laminar boundary layer that developed downstream of the suction device was artificially tripped with a 2-in.-wide strip of sandpaper (36 grit). The ceiling height of the test section was adjusted to obtain zero pressure gradient along the test surface upstream of the ramp. The boundary layer on the centerline just ahead of the separation ramp (x = 76 in. or 3280 trip heights) was found to be fully turbulent when measured velocity profiles were compared with Coles' laws of wall and wake (see Appendix A). The boundary-layer thickness, δ, was approximately 1.28 in. in thickness and the uncertainty in δ was $\pm$1.7%. At the same location, the momentum thickness, θ, was 0.135 in., and its spanwise variation across the middle 77% of the test plate was within $\pm$2.5%. The Reynolds number based on momentum thickness, R_θ, was approximately 9100 at the upstream edge of the ramp. See Appendix A for detailed documentation of the above boundary-layer parameters as well as the freestream turbulence intensity measurements that were conducted as part of the initial tunnel survey and validation process.

The baseline (or reference) separation model was a two-dimensional 25° ramp with an 8 in. shoulder radius as shown in Figure 2.3a. The width of the model was 28 in., which spanned the test section. This model produced reasonably two-dimensional separated flow at approximately the midpoint of the ramp and 2δ downstream of the point of horizontal tangency (Figure 2.3b).

The passive porous surfaces and longitudinal, transverse, and swept grooves were located on the ramp itself. All remaining devices were placed at varying distances upstream or downstream of the baseline separation line, based on the distance between the trailing edge of the device and this line. For the discussion herein, this distance X is

always nondimensionalized by the value of δ at the leading edge of the separation ramp (i.e., δ = 1.28 in.). A positive X/δ denotes distance in the downstream direction, and $X/\delta = 0$ is where baseline separation occurred.

2.3 Pressure Distribution

Static pressure orifices were located on the centerline of the separation ramp and floor downstream of the ramp. The pressure orifices on the floor covered approximately two chord lengths of the ramp. The pressure tubes (inner diameter = 0.040 in.) for the orifices were connected to a motor driven scanivalve which connected each orifice sequentially to a single differential (10 torr Barocel) pressure gauge. All surface static pressure measurements were referenced to the freestream static pressure which was measured 24 in. from the entrance of the test section. Because of physical constraints, some models such as transverse grooves, swept grooves, passive porous surfaces, and closely-packed longitudinal grooves did not have pressure orifices on the separation ramp. However, pressure measurements were made for all models on the floor downstream of the separation ramp to study reattachment and pressure recovery. Since the flowfield downstream of many of the separation control devices was three-dimensional in nature, spanwise pressure distribution measurements over (at least) a device wavelength were obtained by moving the flow control devices laterally to several spanwise stations.

The measured baseline (no device) pressure distribution is shown in Figure 2.4. In conjunction with oil-flow visualizations, baseline separation occurred just before the sharply increasing portion of the C_p distribution began to level off and reattachment occurred near the region of maximum C_p. The extent of separation, therefore, was defined as the distance between the observed separation line and the streamwise location where maximum C_p occurred. Similarly, the reattachment distance was defined as the distance between the trailing edge of the model ramp and the streamwise location where maximum C_p occurred. Then, a reduction in the extent of the separated-flow region

typically corresponded to the upstream movement of the location at which maximum C_p occurred. Also shown in Figure 2.4 is the computed (ideal) potential flow pressure distribution. When examining the baseline pressure distribution, it should be pointed out that the flow around a corner (or a shoulder) accelerates and decelerates symmetrically from the potential flow perspective, which is the reason for the pressure drop along the upstream portion of the shoulder. This effect has also been reported by Gersten et al. [84] for flow over a similar-shaped backward-facing curved ramp, as illustrated in Figure 2.5.

2.4 Flow Visualization

The method of *oil dot* flow visualization using a mixture of titanium dioxide and 10 centistoke silicone oil was utilized to determine the surface flow patterns. Figure 2.3b indicates that this method worked quite well in identifying the separation line for the reference model. Oil dots were placed approximately 1-in. apart both spanwise and in the flow direction to obtain an overall flow pattern. Again, because of geometrical constraints, oil-flow visualization was not used on the separation ramps with the passive porous surfaces or with the transverse and swept grooves. In these cases, surface tufts were placed on the separation ramp in an attempt to identify the separation line. In the flow separation region, 0.5-in.-long surface tufts were arranged in a diagonal pattern in such a way that each sequential tuft represented a travel distance of 0.25 in. in the flow direction.

2.5 Drag Measurements

A small force balance was used to measure the device drag of the submerged vortex generators, spanwise cylinders, and arches examined in the current study. The drag balance was attached to a 4-in. × 6-in. test surface with narrow gaps along all four sides and flush mounted on the tunnel floor upstream of the separation ramp. The balance test surface was supported by two vertical supports that were flexible in the flow direction

but rigid in all other directions. A piezoresistive deflection sensor was used to convert the test surface displacement into a signal proportional to the drag force. The range of the drag balance was 0 to 0.44 lb (force) with a resolution of 1.1×10^{-4} lb. The device drag measurements were conducted at a streamwise location of 12.5 in. ($\sim 10\delta$) upstream of the baseline separation line. All results from drag measurements were normalized for equal spanwise coverage and are tabulated in Tables 2.1 to 2.5.

Table 2.1 Device Drag for Vane-Type Vortex Generators

h (in.)	$\frac{h}{\delta}$	λ (in.)	$\frac{\lambda}{h}$	Drag per Device, (lb) $\times 10^{-4}$	Drag per Unit Width, (lb/in.) $\times 10^{-4}$
0.15	0.12	0.6	4	13.2	22.0
0.25	0.2	1.0	4	41.9	41.9
0.50	0.4	2.0	4	220.0	110.0
1.00*	0.8	4.0	4	1014.1	253.5

*Conventional δ-scale vortex generators.

Table 2.2 Device Drag for Doublet Vortex Generators

h (in.)	$\frac{h}{\delta}$	λ (in.)	$\frac{\lambda}{h}$	Drag per Device, (lb) $\times 10^{-4}$	Drag per Unit Width, (lb/in.) $\times 10^{-4}$
0.11	0.09	0.5	4	8.8	17.6
0.125	0.1	1.0	8	18.7	18.7
0.15	0.12	0.75	5	15.8	21.2
0.50	0.4	2.0	4	310.8	155.4

Table 2.3 Device Drag for Wishbone Vortex Generators

h (in.)	$\frac{h}{\delta}$	λ (in.)	$\frac{\lambda}{h}$	Drag per Device, (lb) $\times 10^{-4}$		Drag per Unit Width, (lb/in.) $\times 10^{-4}$	
				Forward Direction	Reverse Direction	Forward Direction	Reverse Direction
0.063	0.05	0.25	4	1.2	1.9	4.8	7.6
0.095	0.07	0.38	4	2.65	4.4	7.0	11.6
0.11	0.09	0.50	4	7.3	8.6	14.6	17.2
0.25	0.2	1.0	4	45.2	56.4	45.2	56.4
0.50	0.4	2.0	4	390.2	390.2	195.1	195.1

Table 2.4 Device Drag for Spanwise Cylinders

d (in.)	$\frac{d}{\delta}$	Drag per Unit Width, (lb/in.) $\times 10^{-4}$
0.13	0.1	149.5
0.25	0.2	311.6
0.50	0.4	611.4

Table 2.5 Device Drag for Arches

Model No.	h (in.)	$\frac{h}{\delta}$	α (deg.)	λ (in.)	$\frac{\lambda}{\delta}$	Drag per Device, (lb) $\times 10^{-4}$	Drag per Unit Width, (lb/in.) $\times 10^{-4}$
1	0.25	0.2	0	2.0	8	13.6	6.8
2	0.50	0.4	0	2.0	4	21.3	10.7
3	0.50	0.4	0	2.0	4	27.2	13.6
4	1.00	0.8	0	4.0	4	71.0	17.8
5	1.00	0.8	0	6.0	6	132.3	22.0
6	1.00	0.8	10	6.0	6	639.3	106.6
7	0.50	0.4	0	3.0	6	60.0	10.0
8	0.50	0.4	10	3.0	6	296.0	49.0

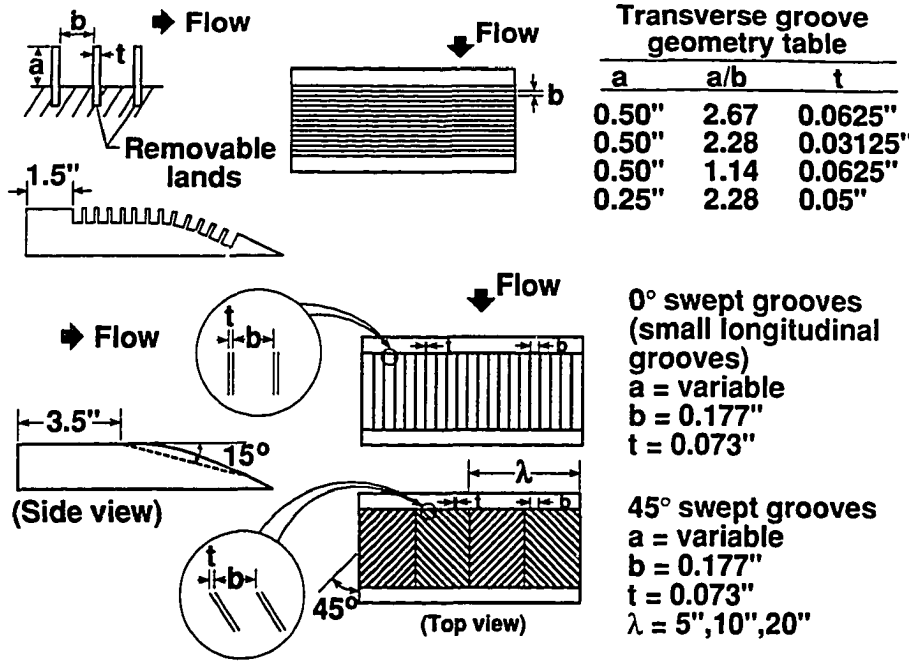

(a) Transverse and swept grooves.

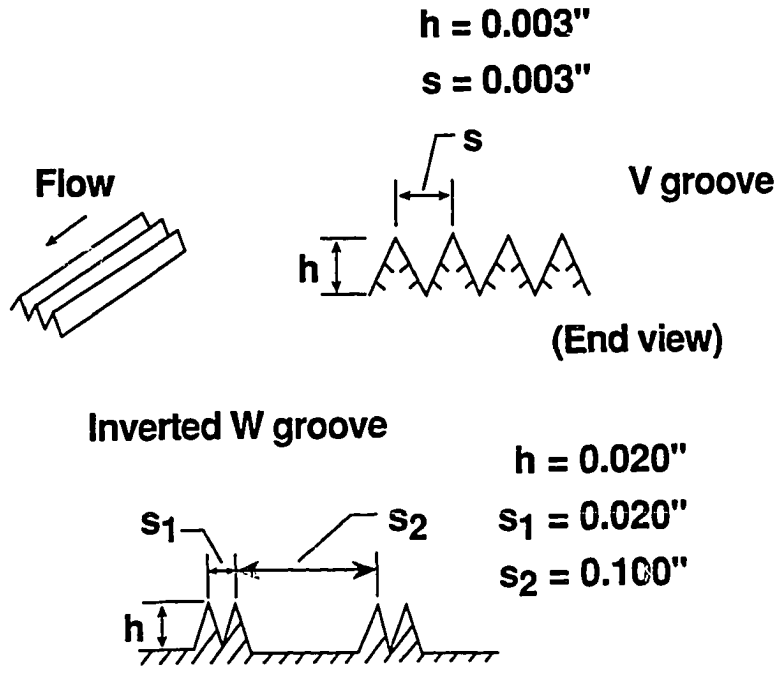

(b) Riblets.

Figure 2.1 Geometry of separation control devices.

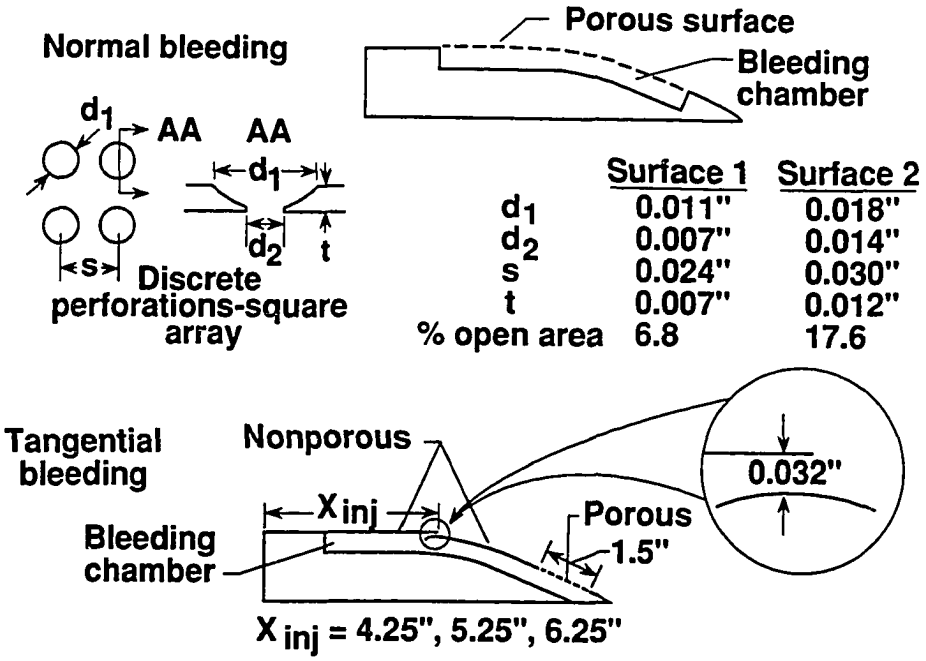

(c) Passive porous surfaces.

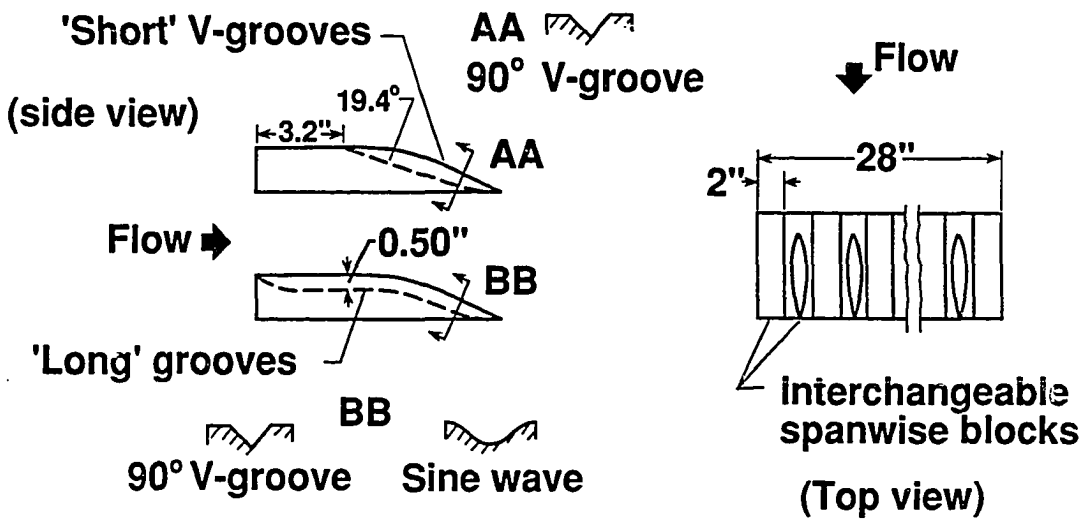

(d) Longitudinal grooves.

Figure 2.1 Continued.

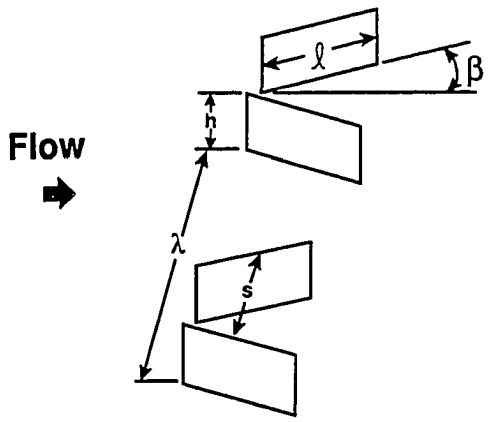

Vane-Type

h	ℓ	s	λ	β
0.15"	0.30"	0.15"	0.6"	15°
0.25"	0.50"	0.25"	1.0"	15°
0.50"	1.00"	0.50"	2.0"	15°
1.00"	2.00"	1.00"	4.0"	15°

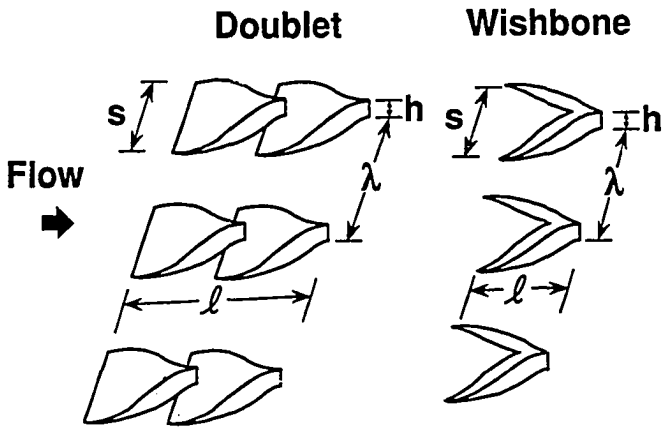

Doublet

h	ℓ	s	λ
0.11"	1.25"	0.42"	0.50"
0.125"	1.60"	0.80"	1.00"
0.15"	1.65"	0.56"	0.75"
0.50"	3.35"	1.62"	2.00"

Wishbone

h	ℓ	s	λ
0.063"	0.20"	0.12"	0.25"
0.095"	0.30"	0.18"	0.38"
0.110"	0.35"	0.25"	0.50"
0.25"	0.84"	0.70"	1.00"
0.50"	1.88"	1.60"	2.00"

(e) Submerged vortex generators.

Figure 2.1 Continued.

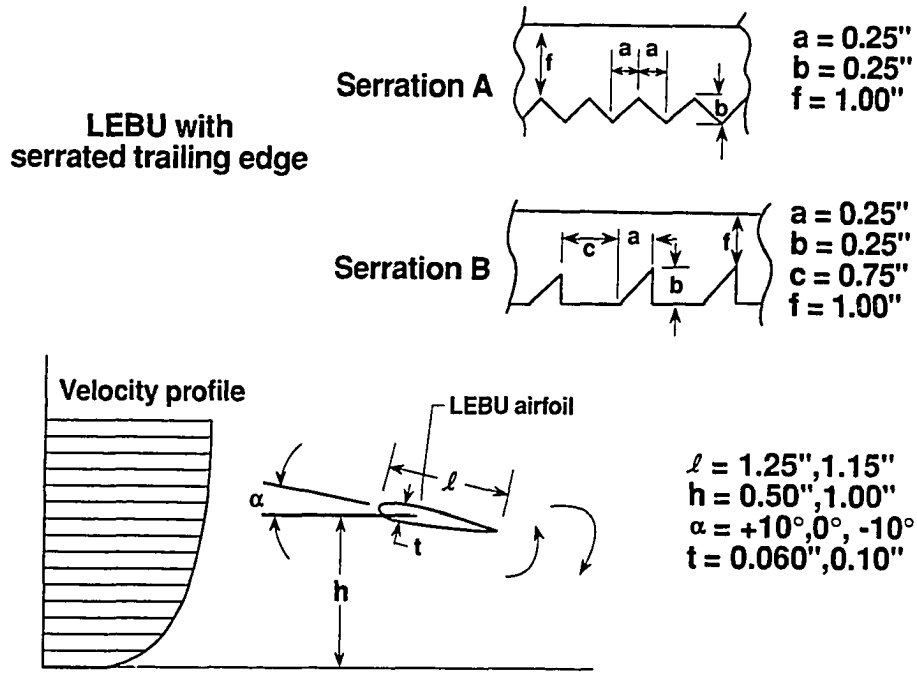

(f) LEBU's at angle of attack.

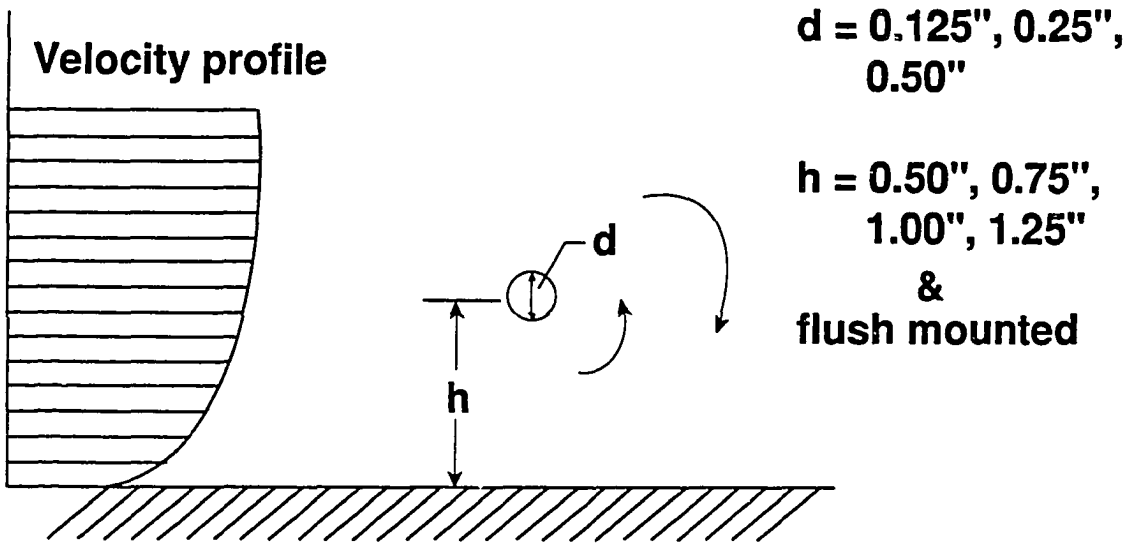

(g) Spanwise cylinders.

Figure 2.1 Continued.

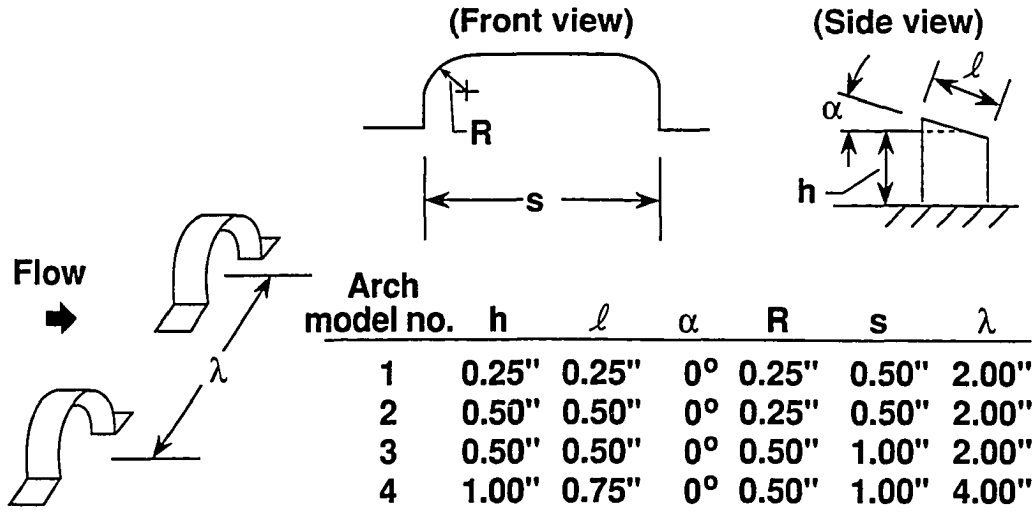

Arch model no.	h	ℓ	α	R	s	λ
1	0.25"	0.25"	0°	0.25"	0.50"	2.00"
2	0.50"	0.50"	0°	0.25"	0.50"	2.00"
3	0.50"	0.50"	0°	0.50"	1.00"	2.00"
4	1.00"	0.75"	0°	0.50"	1.00"	4.00"
5	1.00"	1.00"	0°	0.50"	4.00"	6.00"
6	1.00"	1.00"	10°	0.50"	4.00"	6.00"
7	0.50"	0.50"	0°	0.25"	2.00"	3.00"
8	0.50"	0.50"	10°	0.25"	2.00"	3.00"

(h) Arches.

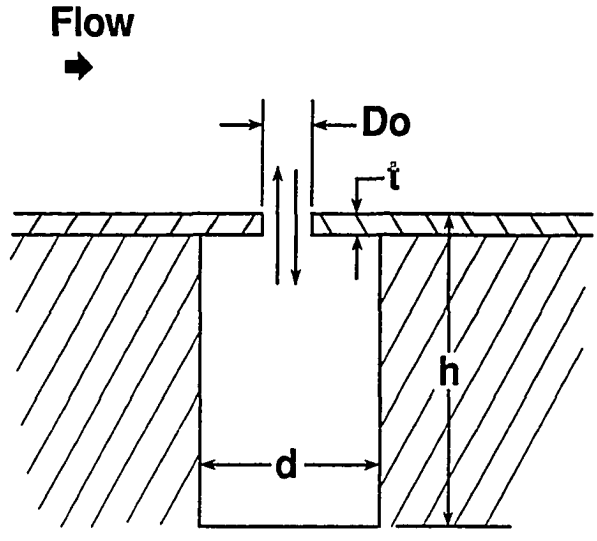

h = 3.00 "
Do = 0.50"
d = 1.00"
t = 0.06"
λ = 1.20"
(Spanwise distance between orifices)

(i) Helmholtz Resonators.

Figure 2.1 Continued.

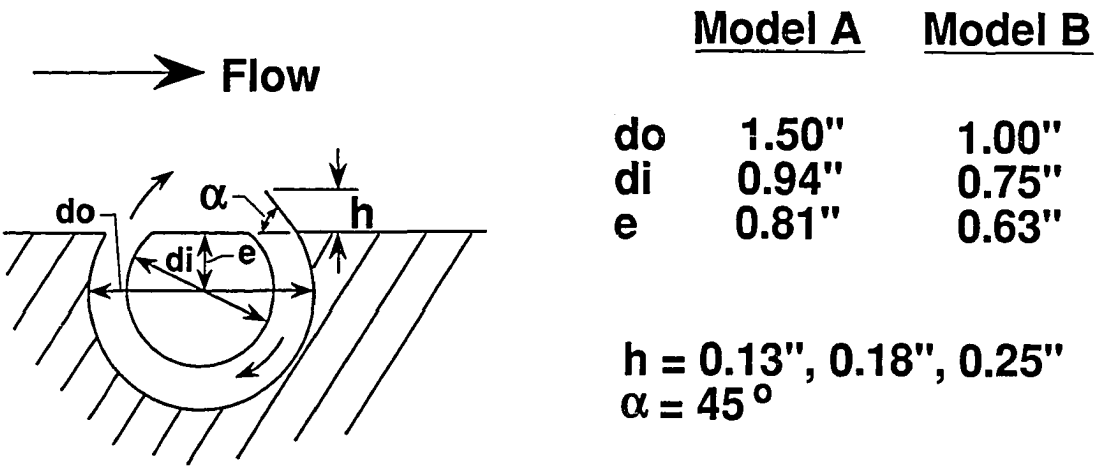

(j) Viets' Fluidic Flappers.

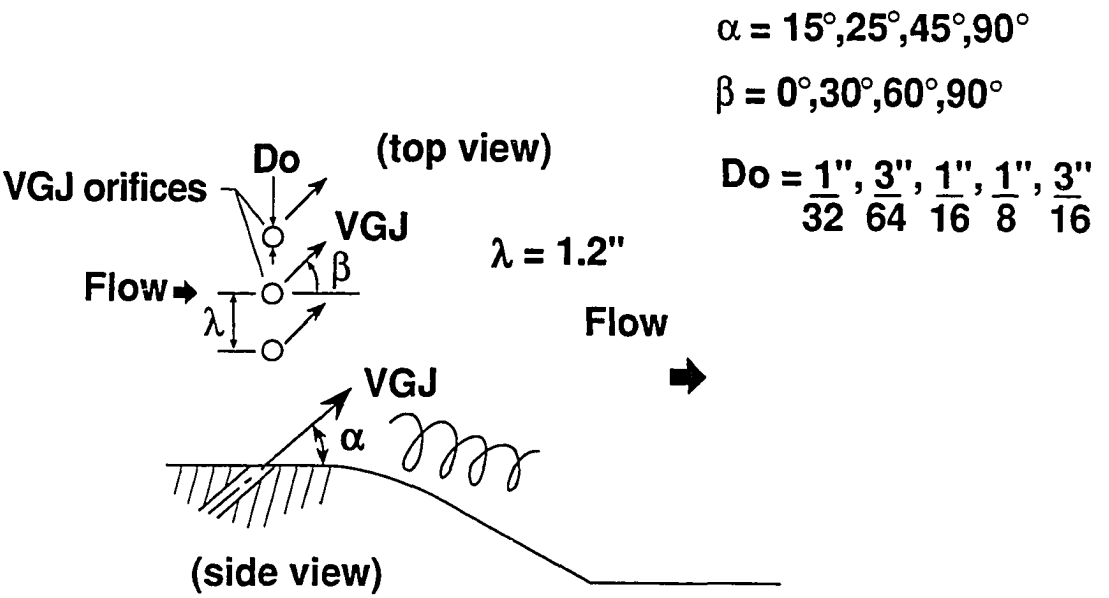

(k) Vortex Generator Jets.

Figure 2.1 Concluded.

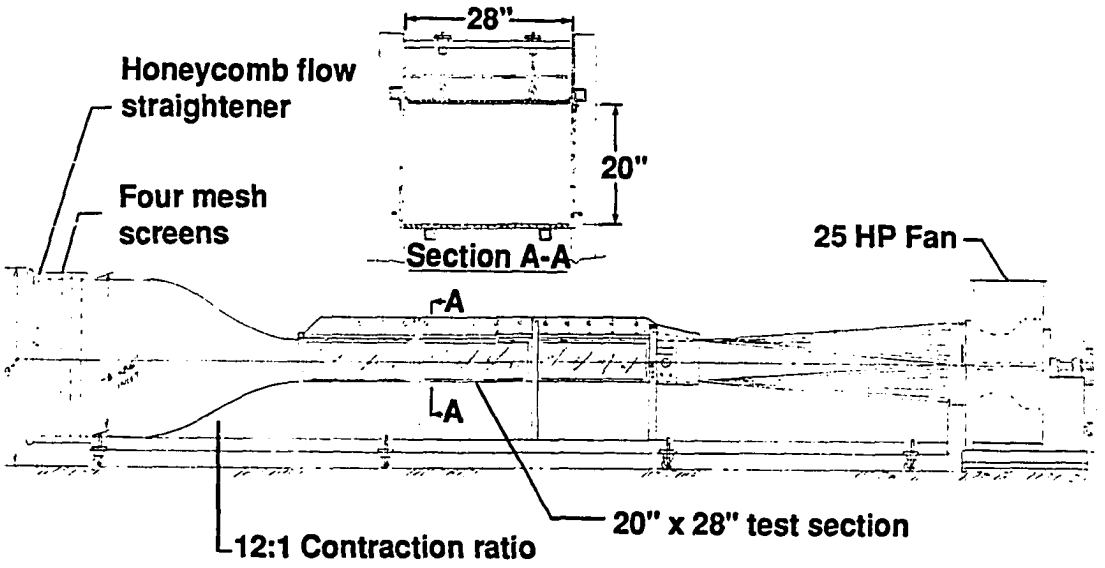

(a) Sketch of wind tunnel.

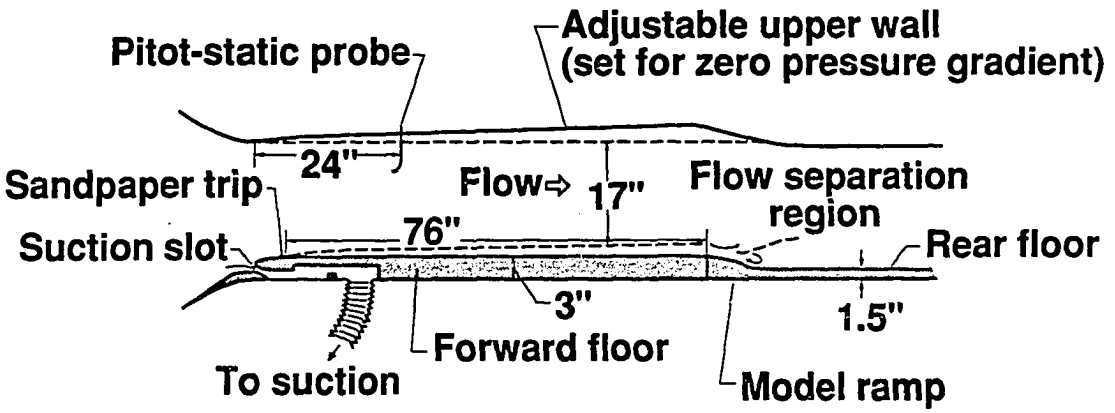

(b) Test configuration in wind tunnel.

Figure 2.2 Langley 20- by 28-Inch Shear-Flow Control Tunnel.

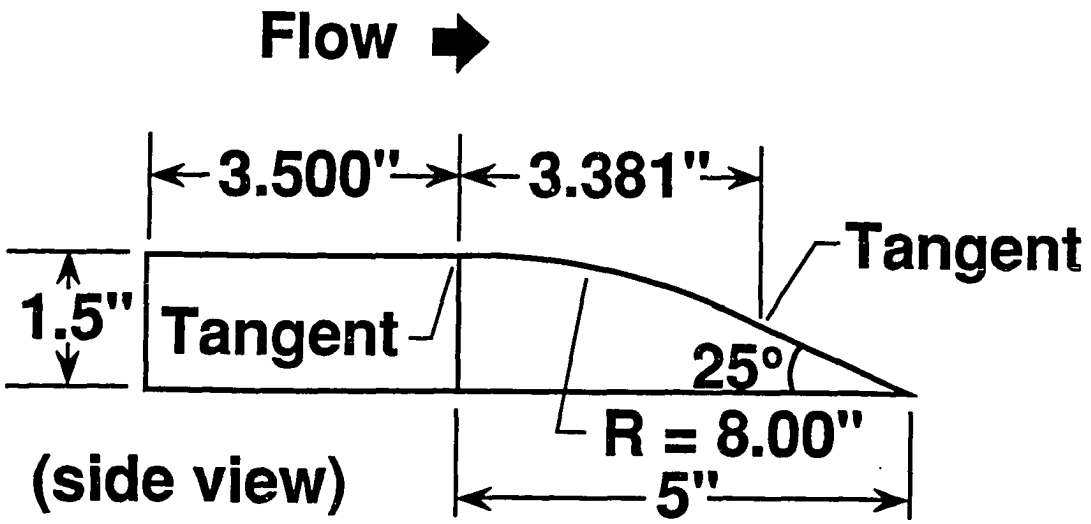

(a) Geometry of model ramp.

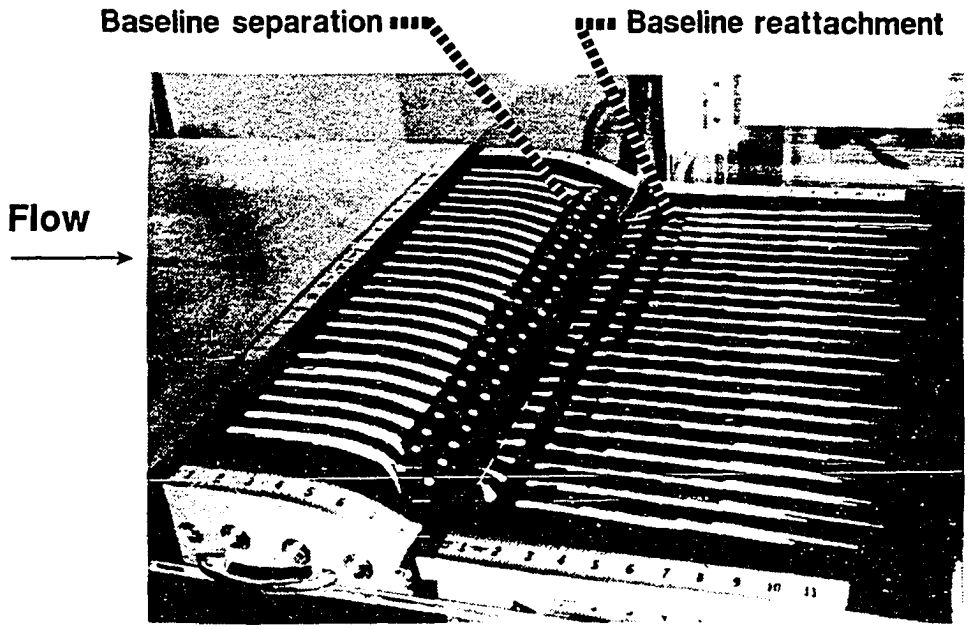

(b) Oil-flow visualization of baseline separation.

Figure 2.3 Reference model ramp.

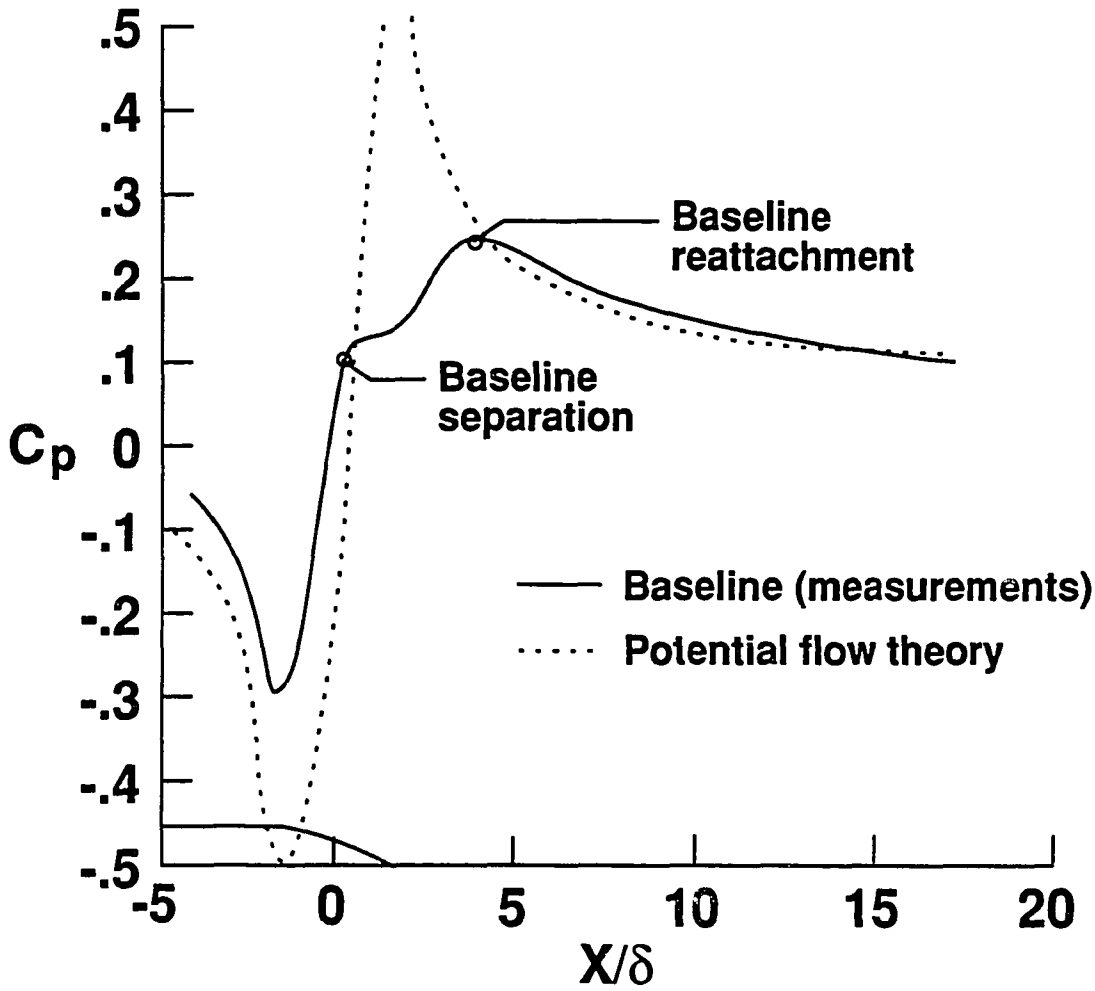

Figure 2.4 Baseline streamwise pressure distribution.

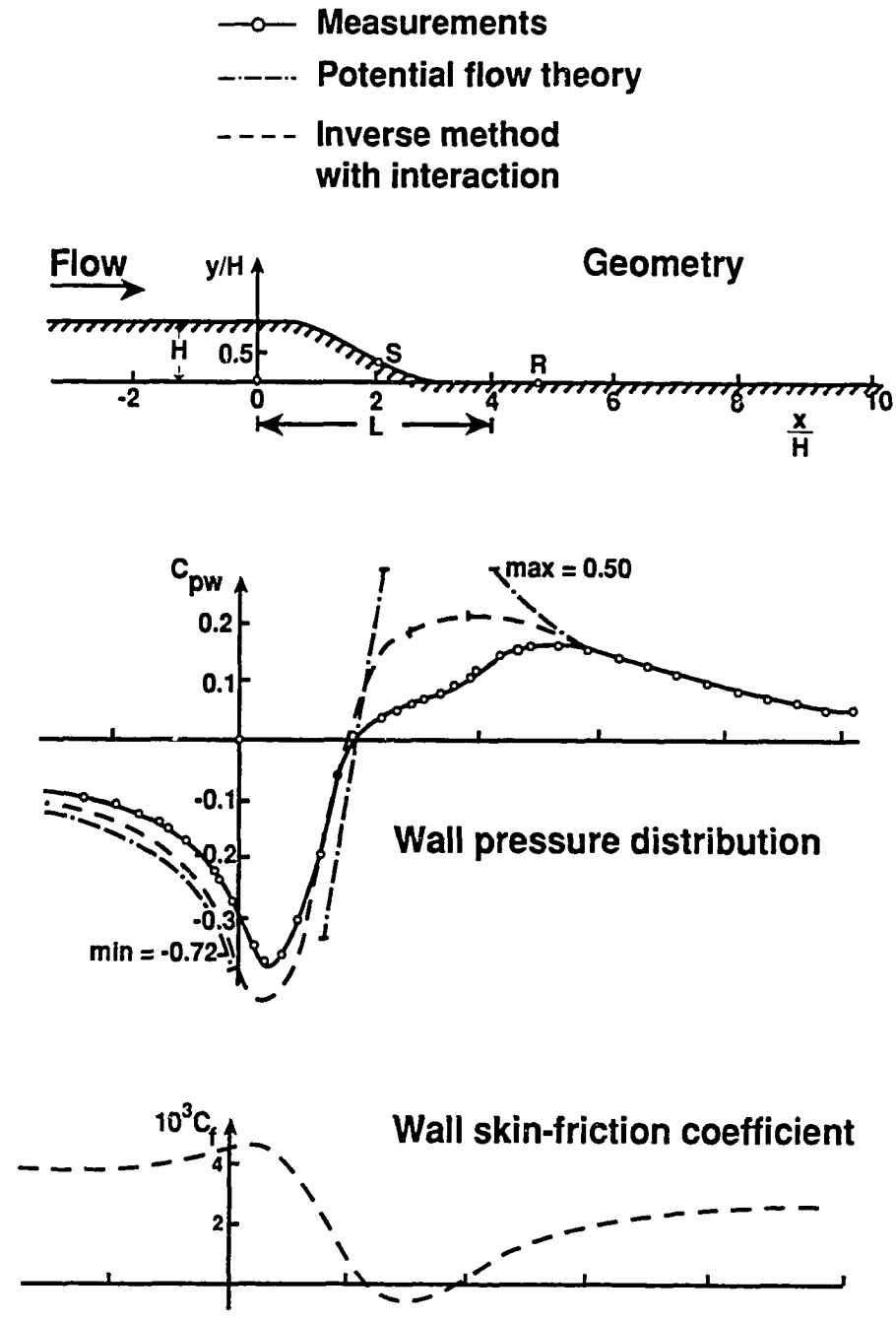

Figure 2.5 C_p and C_f distributions over a backward-facing curved ramp (Gersten et al. [84]).

CHAPTER 3

WATER-TUNNEL APPARATUS AND TESTS

3.1 Test Facility

Dye-flow visualization studies were conducted in the NASA Langley 16- by 24-Inch Water Tunnel (see Figure 3.1a for sketch of the water tunnel). The tunnel has a vertical test section with an available streamwise length of approximately 4.5 ft. A 1-in.-thick splitter plate was mounted in the mid-plane of the test section, as shown in Figure 3.1b. The velocity in the test section was varied between 1 and 8.3 in/s. Flow visualization was performed over the surface of the splitter plate for both a laminar (U_∞ = 1 in/s) and a turbulent boundary layer (U_∞ = 8.3 in/s). A 0.2-in.-diameter two-dimensional boundary-layer trip installed on the splitter-plate surface 2 in. downstream from the leading edge ensured a turbulent boundary layer at the higher freestream speeds. The flow-control devices were located approximately 34 in. (170 trip diameters) downstream of the boundary-layer trip. At the device location, δ was measured to be approximately 1.2 in. for laminar flow and 1.8 in. for turbulent flow. The value of R_θ was measured to be approximately 110 and 1000 for laminar and turbulent flow, respectively. See Appendix B for a detailed description of the water-tunnel boundary-layer surveys using a single-component fiber-optically-linked laser-Doppler velocimeter system.

3.2 Flow Visualization

A 6-in.-wide spanwise dye-injection slot was located approximately 2 in. upstream of the flow-control devices. Both food coloring (red) and fluorescent (fluorescein) dyes were

used. The colored-dye visualization tests produced a global picture of the flow structure while fluorescent dye illuminated by a laser light sheet provided a cross-sectional view of the flow structure. A 200 mW argon laser with a cylindrical lens produced the light sheet used to illuminate both the x-y plane (side view) and the y-z plane (end view). A mirror inclined 45° to the x-y plane was placed downstream of the splitter plate in order to obtain the end view. In addition to dye injection from the floor, LEBU and spanwise cylinder models had dye orifices installed at mid-span to enhance the side view of the downstream vortical structures. Dye was introduced directly through the jet orifices for the tests with the VGJ's. Flow visualization in the turbulent boundary layer was conducted for all devices examined. Because there is little documented information on the Wheeler-type submerged vortex generators and VGJ's, laminar flow visualization results are only included herein for these devices. As an example, for wishbone vortex generators in a laminar boundary layer, Figure 3.2 shows both a typical top (global) view of colored dye visualization and a typical end (plane) view of laser-induced fluorescent dye visualization. All flow visualization tests were documented using a video camera and recorder.

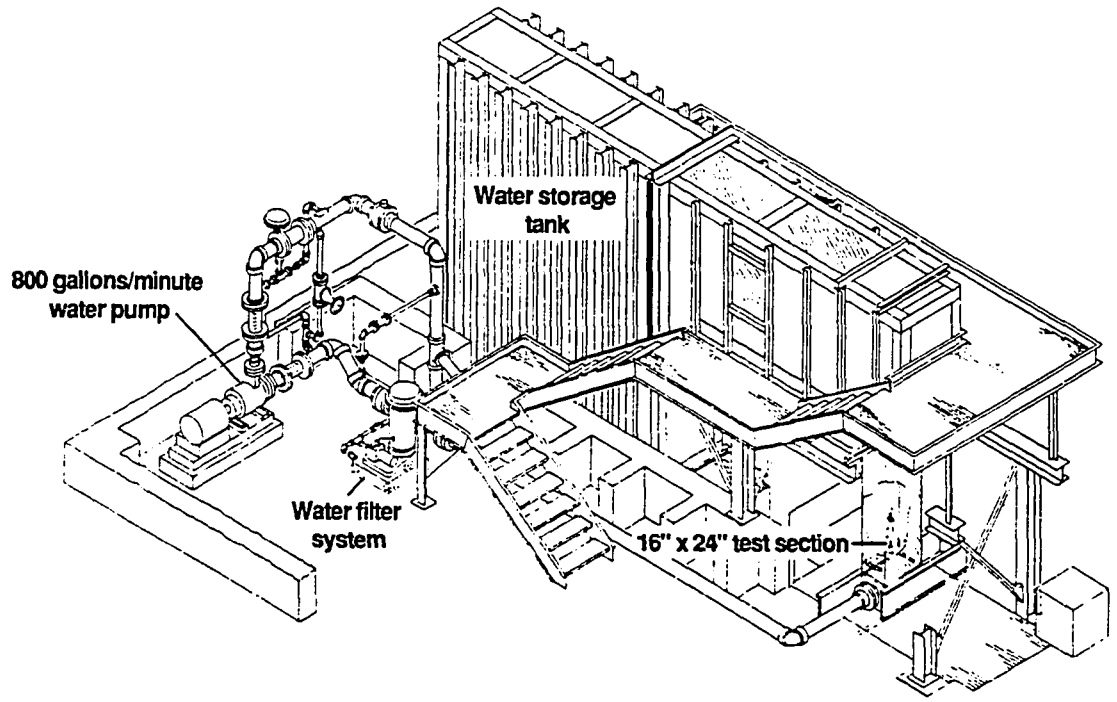

(a) Sketch of water tunnel.

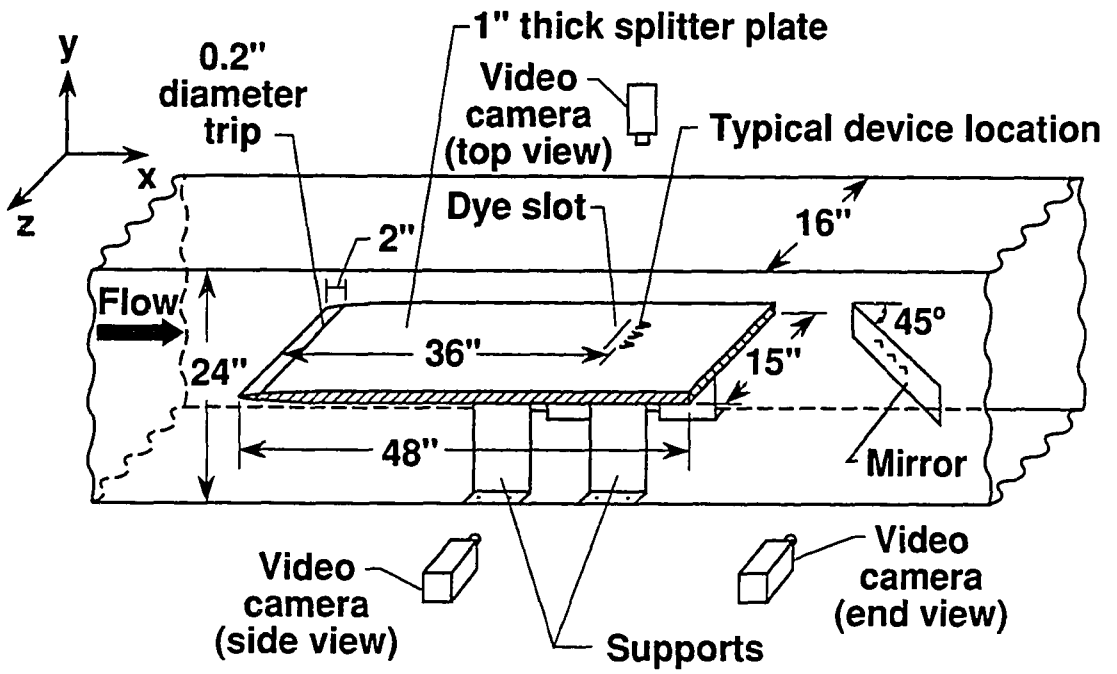

(b) Test configuration in water tunnel.

Figure 3.1 Langley 16- by 24-Inch Water Tunnel.

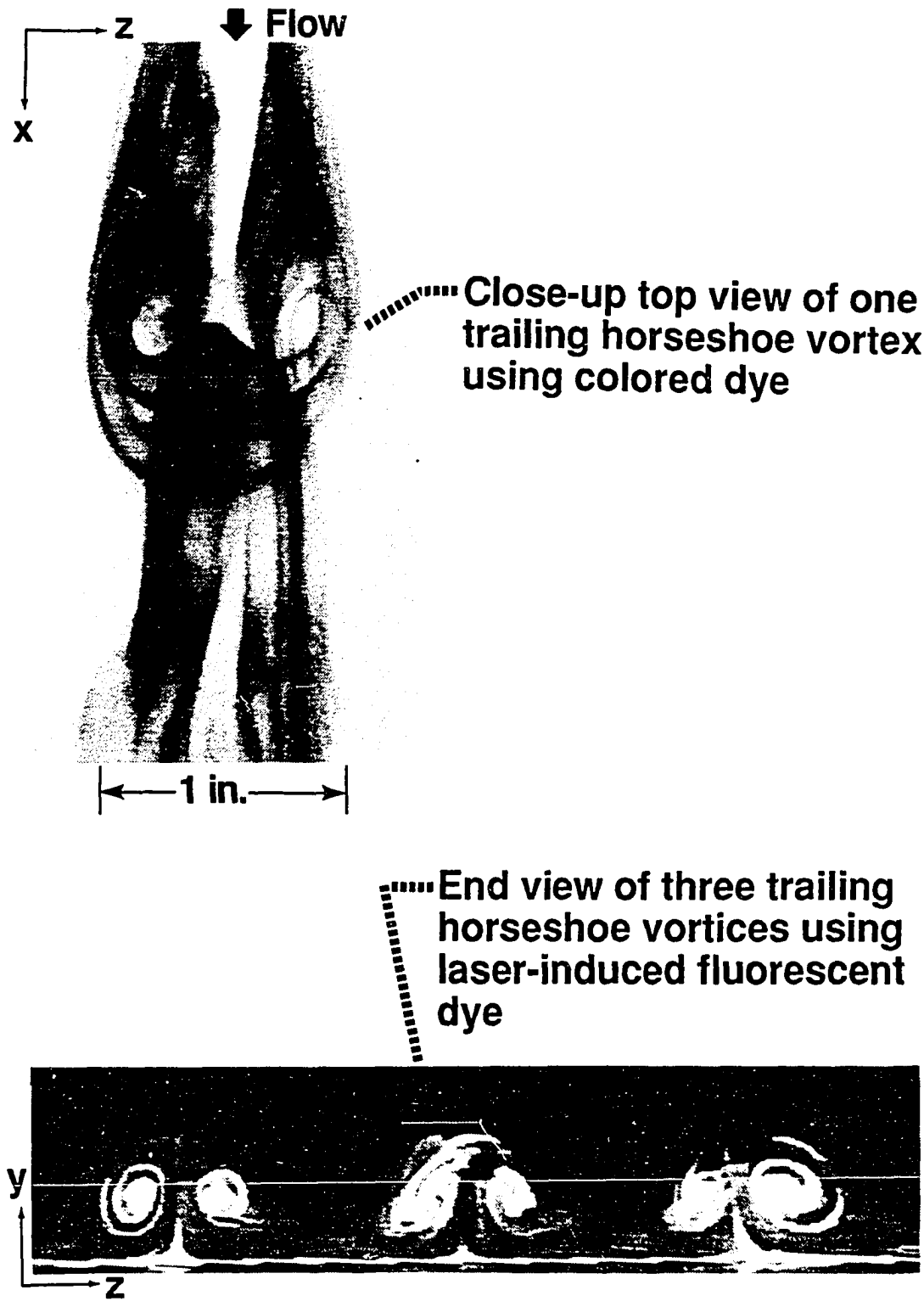

Figure 3.2 Example of dye-flow visualization for forward-facing wishbone vortex generators at $U_\infty = 1$ in/s.

CHAPTER 4

WIND-TUNNEL RESULTS

4.1 Transverse and Swept Grooves

The transverse groove geometry investigated is shown in Figure 2.1a. The grooved area had a spanwise width of 20 in. and was centered along the centerline of the ramp. In the preliminary investigation of this configuration, the optimum transverse groove location was determined by systematically varying the beginning and end of the grooved section in the streamwise direction. Oil-flow visualization of the flow downstream of the ramp with transverse grooves indicated that the optimum location for the beginning of the grooves was about one boundary-layer thickness, δ, upstream of the base-model separation line (or baseline separation) with the grooved region extending one δ downstream of this separation line. The observed separation line (via tuffs) was delayed by approximately 0.25 in. (0.2δ) with respect to the baseline separation. This optimum transverse groove configuration reduced the distance from the separation line to reattachment (i.e., extent of separation) by almost 25%.

The upstream movement of the reattachment points was also verified by the pressure distribution measurements on the floor behind the separation ramp as shown in Figure 4.1. The figure also shows that the optimum transverse groove location is in the *maximum adverse pressure gradient region.* Of the configurations tested, the most effective groove configuration had a groove depth-to-width ratio (a/b) of 2.67. Increasing the groove width by a factor of 2.3 with constant groove depth moved reattachment back to the baseline case while the pressure recovery dropped below that of the baseline level (Figure 4.1).

One possible explanation for this adverse effect is that as a/b is reduced to 1.14, the critical aspect ratio for transition from an open (deep) to a closed (shallow) cavity is approached. Associated with a closed cavity ($a/b < 1$) is an additional separated-flow region within the cavity and increased drag. Cavity flows are said to be *open* if the shear layer reattaches at or downstream of the back wall. *Closed* cavity flows, on the other hand, involve reattachment to the cavity floor and a second separation upstream of the back wall, resulting in high drag and losses [85,86]. Although the optimum transverse groove location remained about the same after reducing both the groove depth and groove width by 50%, the effectiveness of the smaller transverse groove configuration in reducing the extent of separation was also cut in half (down from approximately 25% to 13%). Varying the land (or rib) thickness from 1/16 to 1/32 in. did not change the effectiveness of the transverse grooves.

Flow visualization using surface tufts indicated high amplitude velocity fluctuations near the surface of the transverse grooves. This result is in agreement with the findings of Stull [11] who reported pulsating free-shear layers and the formation of rollers over the grooved section which gave rise to large velocity fluctuations in the near-wall region. The present experiment also indicated that the transverse grooves generated three-dimensional flow, as shown in Figure 4.2. The three-dimensional effects appeared when the transverse-grooved section extended downstream of the base model separation line. The presence of transverse grooves may enhance or introduce a spanwise component in the near-wall flow within the turbulent separation (reverse flow) region. This three-dimensional flow suggests that properly designed swept grooves might enhance the performance of grooves for separation control through introduction of both spanwise and streamwise velocity components within the grooves.

The initial swept grooves investigated consisted of alternating $+45°$ and $-45°$ sweep angle (with respect to the flow direction) shoulder grooves with various widths (see Figure 2.1a). The swept grooves consisted of constant slope (15°) grooves that covered

approximately the same streamwise adverse pressure gradient region as the optimized transverse grooves. Notice that the depth, a, for swept and longitudinal grooves is not constant. It varies from zero at the leading edge of a groove to a maximum of 0.25 in. near the midpoint of a groove. The results indicated that all alternating 45° swept grooves, regardless of spanwise width, increased the reattachment distance and reduced the pressure recovery when compared to the baseline case. Typical three-dimensional flow in the reattachment region is captured in the oil-flow visualization downstream of the 45° alternating (λ = 5 in.) swept groove geometry (see Figure 4.3). The pressure distributions downstream of all 45° alternating swept groove configurations at various geometric widths, λ, are shown in Figures 4.4a and 4.4b. Figure 4.5 shows the downstream floor pressure distribution comparison between the 45° constant (nonalternating) swept grooves, the 0° swept grooves (or small longitudinal grooves), and the 90° swept grooves (or small transverse grooves) of equivalent groove size. The results indicate that both 0° and 90° swept grooves showed a slight improvement over the baseline case as indicated by increased pressure recovery and reduced reattachment distance, while the 45° constant swept grooves performed very similar to the 45° alternating swept grooves, increasing the reattachment distance and reducing the pressure recovery. The adverse effects produced by the 45° swept grooves could be the same as that of the transverse grooves with a/b = 1.14, since the majority of grooves in the longitudinal plane have a/b less than one (corresponding to a closed cavity). Figures 4.6a and 4.6b show the oil flow visualization of longitudinal and 45° constant swept grooves, respectively. It appears that the longitudinal grooves produce straighter surface streamlines downstream of the ramp than either the 45° swept grooves or the transverse grooves. Unlike the *roller bearing* mechanism associated with the transverse grooves, the separation control mechanism for the longitudinal grooves may be the local mitigation of the imposed adverse pressure gradient through the technique of partial *boattailing*.

4.2 Riblets

The riblets investigated in the present study consisted of a 0.003-in.-high ($h^+ \approx 7$) symmetric grooved V-shaped riblet and an inverted 'W' riblet having a height of 0.020 in. ($h^+ \approx 50$) and spacing of 0.10 in. ($s^+ \approx 250$) between the inverted 'W's' (see Figure 2.1b). The h^+ and s^+ values were determined using the following expressions:

$$h^+ = \frac{hu_\tau}{\nu}$$

$$s^+ = \frac{su_\tau}{\nu}$$

where the friction velocity is defined as $u_\tau = U_\infty \sqrt{\frac{C_f}{2}}$. The skin friction values were determined at the ramp location from an empirical relationship (Coles [76]) that relates skin-friction coefficient, C_f, and Reynolds number based on momentum thickness, R_θ (see Figure A.4). Both riblet models were thin films with 0.003-in.-thick adhesive backing. Figure 4.7 shows the drag reduction performance curves (skin friction reduction versus nondimensional riblet height) for the two riblet geometries. These data were from unpublished results of a previous riblet test conducted by Mr. Michael J. Walsh. It was estimated that the 0.003-in. riblet would decrease the skin friction by approximately 6% and the 0.020-in. riblet would increase the skin friction by 15% for their h^+ values of 7 and 50, respectively (Figure 4.7). The riblet films extended from the separation line of the baseline ramp model to an upstream distance of 6 feet ($\sim 56\delta$). The film had a spanwise width of 1 foot and was centered along the centerline of the test section.

Figure 4.8 shows the surface pressure distribution for the baseline ramp, the 0.003-in. riblet (C_f-reducing V-grooves), the 0.020-in. riblet (C_f-increasing inverted W-grooves) and two smooth reference films. A different smooth reference film was used for each riblet so that the smooth reference film and the respective riblet film would have the same nominal thickness (riblet height plus the thickness of the adhesive backing). Figure 4.7 shows that the 0.003-in. riblet and the respective smooth reference produce virtually *no change* in the pressure distributions compared to the baseline case. The deviations

from the baseline are all within the uncertainty range of the C_p measurement (± 0.005). As seen in Figure 4.8, the 0.020-in. riblet enhanced flow separation as indicated by a 40% increase in the extent of separation and a 20% reduction in the maximum pressure recovery. Figure 4.9 compares the oil-flow visualization photographs of the two riblets. Figures 4.9a and 4.9b clearly show the effect of momentum loss over the C_f-increasing riblets as compared to the C_f-reducing riblets. The drag increase associated with the 0.020-in. riblet adversely retarded the near-wall streamwise momentum, resulting in separation enhancement. Furthermore, part of this separation enhancement was caused by the larger protrusion height of the 0.020-in. riblet that created a small but noticeable backward-facing step at the riblet film's trailing edge. This step caused an inflection in the velocity profile downstream. The influence of the backward-facing step is seen in the C_p distributions for the 0.020-in. riblet smooth reference. The C_p distribution for the smooth reference showed a separation enhancement. The separation enhancement was not as large as that for the 0.020-in. riblet which increased the skin friction. This difference is caused by the skin-friction-increasing mechanism associated with the larger riblet. It was also determined that the adverse effect caused by the C_f–increasing riblets could be eliminated by moving the trailing edge of the riblet film further upstream of the baseline separation. Figure 4.10 indicates that the separated region could be decreased by almost 50% if the trailing edge of the riblet film was moved 2δ upstream of the baseline separation. When the trailing edge of the riblet film was placed 15δ upstream of the baseline separation, there was essentially no effect associated with the C_f–increasing riblets.

4.3 Passive Porous Surfaces

The two passive porous surfaces used in the present investigation (see Figure 2.1c) are the same as those used for a wall permeability study by Wilkinson [87]. The self-bleeding chamber (or plenum) underneath the surface had a depth of 0.5 in. and a

spanwise width of 20 in., and was centered along the centerline of the ramp. Flow visualization and pressure measurement results for the present passive porous surfaces indicated that varying surface porosity from Surfaces 1 to 2 (6.8% to 17.6% open area) had little or no effect on the resulting pressure distribution. However, the location of the nonporous area separating the upstream and downstream porous sections had an appreciable effect on reattachment distance.

The downstream floor pressure distributions for various porous/nonporous coverage configurations are shown in Figure 4.11 for Surface 2. The figure shows that the porous surface with a nonporous section near the maximum $+dP/dx$ (Case A, 10.6% open area) provided a 33% reduction in extent of separation when compared to a completely porous surface (Case D, 17.6% open area); however, porous surface coverage of Case A still provided a 20% increase in the extent of separation when compared to the baseline (nonporous) case. The nonporous area at low speeds serves as a *dividing region* between the upstream low pressure (outflow from porous surface) and the downstream high pressure (inflow) regions. An attempt was made to move the normal (passive) injection upstream by increasing the coverage of this *dividing region* further upstream of the maximum $+dP/dx$ region (Case C, 8.2% open area). However, this resulted in an increase in reattachment distance and a decrease in pressure recovery back to the level of Case D. The reason for this poorer performance may be because the decrease in streamwise pressure difference combined with the increase in losses inside the longer, self-bleeding chamber produced inadequate bleed flow. If the coverage of the *dividing region* was extended further upstream such that the percentage of the open area was severely reduced (to about 2% via Surface 1) for the upstream outflow, the results only resembled the baseline case. Outflow further upstream of baseline separation was considered but never tried because of the limited chordwise dimension of the ramp and the reduction in streamwise pressure difference further upstream. In order to drive the self-bleeding flow, a large streamwise pressure difference was preferred. Thus far, all

passive porous surfaces tested were found to adversely affect both the reattachment distance and the pressure recovery when compared to the baseline model. Figure 4.12 shows the adverse effect (an increase in reattachment distance) via oil-flow visualization downstream of a typical passive porous surface (Surface 2, Case A). It is clear from the baseline pressure distributions of Figure 4.11 that normal injection (or outflow) near the beginning of the maximum adverse pressure gradient region enhances flow separation, i.e., normal injection reduces the near-wall streamwise momentum in a region where maximum near-wall momentum is needed. Improvements in separation control might be realized by employing tangential (passive) injection in the low-pressure shoulder region.

Passive tangential slot injection was attempted by replacing the upstream porous surface with a 0.010-in.-thick impervious plate that forms a spanwise 0.032-in. tangential gap pointing downstream over the self-bleeding chamber (Figure 2.1c). Three streamwise locations for the tangential injection were investigated: 2δ, 1δ, and 0δ upstream of baseline separation (corresponding to locations A, B, and C, respectively, in Figure 4.13). Figure 4.13 indicates that while passive slot injection just ahead of baseline separation (location C) has a pressure recovery equivalent to that of the baseline level, the pressure recovery deteriorated significantly as the injection location moved upstream. This is probably due to insufficient mass flow (i.e., pressure driven self-bleeding) through the narrow injection gap in a region where sufficient near-wall momentum is crucial for separation control. Although passive bleeding techniques tested thus far were unsuccessful in reducing flow separation, these techniques may still have application for more severely separated cases, as in the study by Raghunathan et al. [25], where larger adverse pressure gradients exist.

4.4 Longitudinal Grooves

The longitudinal grooves discussed in this section are much larger than the 90° swept grooves and the riblets mentioned earlier (Sections 4.1 and 4.2, respectively). The purpose of the large longitudinal grooves was to provide the pumping (ejector) action of

attached groove flow on the separated flow region. The longitudinal grooves investigated in the present study consisted of 'short' V-groove, 'long' V-groove, and sine-wave groove configurations. The geometry of these longitudinal grooves is summarized in Figure 2.1d. All grooves were located on the shoulder of the ramp model itself. The 'short' V-groove configuration consisted of a constant slope (19.4°) groove from just upstream of the horizontal tangent point to the base of the ramp. The 'long' V-groove and sine-wave groove configurations, on the other hand, consisted of a 0.5-in.-deep groove parallel to the ramp surface from 2.5δ upstream of the horizontal tangent point to the base of the ramp. Each longitudinal groove was cut in a 2-in.-wide spanwise section of the ramp model. The spanwise groove spacing (λ) could be changed by adding or removing one of these spanwise sections. The volume removed for a single groove is 0.75 cubic inches for the 'short' V-groove, 1.5 cubic inches for the 'long' V-groove, and 2.6 cubic inches for the sine-wave groove.

Figures 4.14a and 4.14b show the flow visualization comparison between the 'short' longitudinal V-grooves with a groove spacing of 1.5δ (2 in. apart, 11 grooves total) and the same groove with a groove spacing of 3δ (4 in. apart, 6 grooves total), respectively. The results indicate that the V-grooves spaced 1.5δ apart significantly reduced the distance to reattachment, while the V-grooves spaced 3δ apart provided only a partial improvement in the same region (compare with Figure 2.3b). Figure 4.14 also shows a separation delay of 0.5δ on the smooth surfaces of the ramp (between the grooves) with the 1.5δ groove spacing while the 3δ groove spacing shows no significant delay of separation in this same region with respect to the baseline model. Similar results were obtained for sine-wave grooves and 'long' V-grooves. The downstream floor pressure distributions for all three longitudinal groove cases with the same 1.5δ groove spacing are shown in Figure 4.15a. The closely packed 'short' V-grooves provided the maximum pressure recovery on the downstream floor and Figure 4.15a shows that this configuration reduced the extent of separation by up to 55%. The pressure distributions for all three longitudinal groove

cases with the same 3δ groove spacing are shown in Figure 4.15b. The resulting pressure distributions are all very similar and just slightly above the baseline case. Notice that the 'short' V-grooves are slightly better for separation control than the 'long' V-grooves or the sine-wave grooves while requiring only a fraction of the volume penalty (or loss) of these longer grooves. The volume penalty for the 'short' V-grooves is 50% of that for the 'long' V-grooves and 29% of that for the sine-wave grooves.

4.5 Submerged Vortex Generators

The conventional (δ-scale) vane-type vortex generators investigated consisted of a row of rectangular plates that projected normal to the wall with adjacent generators set at alternating angles of incidence ($\pm 15°$) to the flow to produce an array of streamwise counterrotating vortices. The vortex generators had a height, h, of 1 in. (0.8δ), an aspect (height-to-chord) ratio of 0.5, and a spanwise distance of 4 in. ($\lambda/h = 4$) between each pair of devices (see Figure 2.1e).

Flow-visualization results for the conventional vane-type vortex generator indicate that each pair of the 0.8δ (1 inch) high counterrotating vortex generators provided mostly attached flow directly downstream of the ramp trailing edge (Figure 4.16). However, this attached flow was highly three-dimensional and pockets of recirculating flow could be seen on the separation ramp between adjacent attached flow regions. Figures 4.16a and 4.16b show that when the vortex generators were moved from 5δ to 15δ upstream of the baseline separation, the generators still maintained most of their effectiveness. Pressure distributions at three spanwise locations downstream of the counterrotating vortex generators are presented in Figure 4.17. The three spanwise locations are at a distance of 0, $\lambda/4$, and $\lambda/2$ away from the device centerline. The figure shows significant differences between the C_p distributions for various spanwise locations, which is another indication of the highly three-dimensional flow. Figure 4.17 also indicates that the vane-type counterrotating vortex generator can provide an improved pressure recovery;

however, this vortex generator also reduced the pressure on the shoulder region of the ramp. This effect is desirable if one wants to increase *lift*, but results in a *pressure drag* penalty. The pressure reduction is due to an increase in local velocity resulting from the redirection of high momentum flow from the outer part of the boundary layer. This pressure reduction is probably also an indication that the vortices produced by the counterrotating vortex generators were stronger than necessary. Weaker vortices (smaller vortex generators) would reduce the pressure reduction on the shoulder.

The submerged (sub-δ-scale) vortex generators investigated initially were the Wheeler doublet and wishbone types. The geometry of these vortex generators is shown in Figure 2.1e. The doublet vortex generators consisted of a double row of ramp-shaped devices resembling overlapping (downstream-pointing) arrowheads. The wishbone vortex generators, on the other hand, consisted of a single row of V-shaped ramps with the apex pointing downstream. Each ramp consisted of two joined legs with an included apex angle of approximately 60°. The Wheeler doublet vortex generators investigated varied in height from 0.11 to 0.50 in. (0.09 to 0.40δ), while the wishbones varied from 0.063 to 0.5 in. (0.05 to 0.40δ). Both types were effective in flow separation control.

Flow-visualization results for the Wheeler doublet vortex generators indicate that the optimum streamwise location for these generators was 5 to 10 device heights upstream of the baseline separation line. Figures 4.18a and 4.18b indicate that both the 0.4δ (0.5 in.) and 0.1δ (0.125 in.) high doublet vortex generators were quite effective in reducing the reattachment distance over the baseline case when installed 2δ upstream of the baseline separation line. Although the 0.4δ high doublet vortex generators provided some regions of partially attached flow, there were several well-organized pockets of recirculation at the base of the ramp. In addition, for this geometry separation was delayed by approximately 0.5δ with respect to the baseline case. The 0.1δ high doublet vortex generators also provided partially attached flow at the base of the ramp; however, the recirculation region was not as well organized and less three-dimensional than the

0.4δ high case. The effectiveness of both the 0.4δ and 0.1δ high doublet vortex generators was reduced when the generators were moved further upstream of the baseline separation. Figure 4.19 presents pressure distributions downstream of the doublet vortex generators with the generators mounted 2δ upstream of baseline separation. Figure 4.19a indicates that the 0.4δ high doublet vortex generators produced a small spanwise C_p variation (reflecting the three-dimensional processes shown in the oil flow studies), which is much less than that associated with the 0.8δ high counterrotating vane-type vortex generators. The 0.1δ high doublet vortex generators produced negligible spanwise C_p variations (Figure 4.19b). In addition to the improved pressure recovery downstream of the ramp, the doublet vortex generators, unlike the vane-type counterrotating vortex generators, also minimized the pressure reduction at the shoulder region of the ramp. This effect is especially prevalent with the 0.1δ high generators and is beneficial to pressure-drag reduction.

Similar to the results obtained for the doublet vortex generators, the optimum placement for wishbone vortex generators was 5 to 10 device heights upstream of the baseline separation line. However, Figure 4.20a shows that the 0.09δ (0.11 in.) high wishbone vortex generators with apex pointing downstream (forward or design configuration) still produced a positive (i.e., less separation) effect on C_p even when placed as far as 25 device heights or 2δ upstream of the baseline separation line. At the same device height of 0.09δ, similar results were obtained with the doublet vortex generators and the wishbone vortex generators rotated 180° with apex pointing upstream (reverse configuration). The former case (Figure 4.20c) was slightly more effective than the wishbone generators in the forward configuration (Figure 4.20a), while the latter case (Figure 4.20b) was slightly less effective.

For the same streamwise location of 2δ upstream of the baseline separation, Figure 4.21 shows that the wishbone vortex generators at (or below) 0.063 in. in height (0.05δ or $y^+ \approx 150$) demonstrated an adverse effect on pressure recovery and separation.

It appears that these ultra-small generators do not produce persistent vortices, but function as surface roughness elements promoting separation. At or above heights of 0.095 in. (0.08δ or $y^+ \approx 230$) the wishbone vortex generators were effective. At this ramp location, velocity survey data indicated that a value of y^+ greater than 300 was approximately where the inner (log) region ends and the outer (wake) region begins. Figures 4.22a and 4.22b show that for a device height of 0.25 in. (0.20δ), the wishbone vortex generators with apex pointing upstream provided a steeper pressure recovery than with the apex pointing downstream. This behavior is opposite that observed earlier for a device height of 0.11 in. (0.09δ). Furthermore, the 0.2δ high wishbone vortex generators with apex pointing upstream were more effective in reducing the reattachment distance than the doublet vortex generators of twice the device height (Figure 4.19a). Oil-dot flow visualization photographs are presented in Figure 4.23 for the 0.2δ high wishbone generators for both forward and reverse configurations. The figure shows the reverse configuration provided a less three-dimensional ramp flow than the forward configuration. At this stage of the research program, the exact nature of the effectiveness of the 0.2δ high wishbone vortex generators in the reversed configuration was unclear, and therefore motivated further investigation in the water tunnel.

Based on these initial results for the Wheeler submerged vortex generators, one question often raised was whether separation control effectiveness could be maintained by lowering the device height of the conventional, δ-scale, vane-type vortex generators. Vane-type vortex generators with $h \sim 0.4\delta$, 0.2δ, and 0.1δ were subsequently examined (see Figure 2.1e). The results show that those sub-δ-scale vane-type vortex generators were just as effective in flow separation control as the Wheeler vortex generators. Figure 4.24 shows the effect of device location (nondimensionalized by device height) on both separation and reattachment locations for all vortex generators investigated. These data were averaged over at least one spanwise cycle. This figure confirmed that the optimum streamwise device locations for separation control were between 5 to 10 device

heights upstream of the baseline separation. However, the effectiveness in reducing the separation region, although at a much reduced capacity, still persisted when the vortex generators were placed as far as 100 device heights upstream of the baseline separation. These effects appear true for all vortex generators examined, regardless of the geometry. Furthermore, separation alleviation was adversely affected by placing the generators less than two device heights upstream of the baseline separation. This is probably because this distance ($2h$) was within the minimum traveling distance that the trailing vortices needed to redirect the momentum from the outer region.

It should be noted that the vane-type vortex generators with $h \sim 0.2\delta$ reduced the extent of separation by almost 90% at their most effective location, and were just as effective as the larger $h \sim 0.4\delta$ and $h \sim 0.8\delta$ vane-type generators. The conventional $h \sim 0.8\delta$ vane-type generators actually adversely affected separation control effectiveness by generating excessively strong vortices that caused pockets of recirculating flow via the strong up-sweep motion of vortices, as shown in Figure 4.16. Oil-flow visualization of the $h \sim 0.1\delta$ and $h \sim 0.2\delta$ vane-type vortex generators placed at 2δ upstream of the baseline separation are shown in Figures 4.25a and 4.25b, respectively. Pressure distributions presented in Figure 4.26 confirmed the effectiveness of the $h \sim 0.2\delta$ generators in alleviating separation. This effectiveness, however, was reduced by lowering the device height from 0.2δ to 0.1δ. The maximum pressure recovery difference, using the baseline case as the reference $\left(C_{p_{\max}} - C_{p_{\max,\mathrm{ref}}}\right)$, is shown in Figure 4.27 as a function of nondimensional device location for all vortex generators examined. The figure shows that the maximum pressure recovery is a direct function of the device height. This is probably because the taller devices generated stronger trailing vortices that resulted in higher pressure at reattachment when these vortices impinged upon the test surface. The optimum streamwise device locations for maximum pressure recovery appear to be between 5 to 25 device height upstream of the baseline separation.

Increasing the device height of the vortex generators, however, does adversely increase the device drag significantly, as shown in the drag measurement results of Tables 2.1 to 2.3. The results indicate that as the device height increases, the device drag also increases in almost an exponential manner, creating a severe penalty. The device drag of vane-type vortex generators compares favorably with those of the doublets and wishbones. At $h = 0.4\delta$ in particular, the vane-type vortex generators have 29% less drag than the doublets and 44% less drag than the wishbones. For $h \leq 0.2\delta$, the device drag of vane-type vortex generators approaches the same levels as those of the doublets and wishbones with equivalent heights.

In general, doublet and wishbone generators have similar device drag levels. For example, doublets have 20% less drag for $h = 0.4\delta$ and 20% more drag for $h = 0.09\delta$ when compared to wishbones in the forward direction. Despite their effectiveness in separation control, the 0.2δ high wishbone generators in the reverse direction have 25% more device drag than in the forward direction.

The results for the smaller submerged vortex generators (doublet, wishbone, and vane types) become even more significant when it is noted that, in addition to the minimization of pressure reduction on the shoulder region of the ramp, these generators, being small and in a relatively reduced dynamic pressure region, also incurred the least device-drag penalty. At a height of only about 10% to 20% of the boundary-layer thickness and when placed within $5h$ to $10h$ upstream of the baseline separation, they perform almost as well as a conventional vane-type generator with a device height (and device drag) an order-of-magnitude higher. Simplistically, the effectiveness of the smaller submerged vortex generators is at least partially due to the full velocity-profile characteristic of a turbulent boundary layer. Figure 4.28 shows the location of generator heights relative to the boundary-layer velocity profile in the current study ($Re_\theta = 9100$). Even at a height of 0.1δ and 0.2δ, the local velocity is already 70% and 77% of the freestream value, respectively. Any further increase in height provides only a moderate increase in

local velocity but dramatically increases generator drag. Low-profile, sub-δ-scale, vortex generators with h/δ on the order of 0.1 to 0.2 should be more closely examined for turbulent separation control, especially for applications where device drag is important.

4.6 Large-Eddy Breakup Devices at Angle of Attack

The LEBU configurations investigated consisted of miniature airfoils with a chord length of 1.25 in. (1δ) and a maximum chord thickness of 0.06 in., as shown in Figure 2.1f. The LEBU airfoils were mounted spanwise across the entire test section at heights of 1 in. (0.8δ) and 0.5 in. (0.4δ), angles of attack of $\alpha = +10°$, $0°$, and $-10°$, and streamwise locations ranging from the separation line to 20δ upstream of baseline separation. Both symmetrical and nonsymmetrical serrations were also installed on the trailing edges (see Figure 2.1f) to explore enhancement, if any, of device effectiveness via three-dimensionalization of the downstream wake.

At a height of 0.8δ, LEBU's at the positive angle of attack ($\alpha = 10°$) were always more effective in flow separation control than LEBU's at zero and negative angles of attack, as shown in Figure 4.29 for a typical streamwise location of 2δ upstream of baseline separation. The optimum placement for the LEBU's at the positive angle of attack was directly above the separation location (Figure 4.30) where they acted, at least partly, as *turning vanes*. At this location, the LEBU's were actually located at 1δ downstream of the baseline separation, based on the device trailing edge. The LEBU's reduced the extent of separation by up to 30% when deployed in this configuration. Placing the device further upstream reduced its effectiveness in controlling flow separation. Similar results were obtained for LEBU's mounted at a height of 0.4δ (Figure 4.31); however, they were not as effective as the 0.8δ high devices. The LEBU's with serrated trailing edges did not produce any noticeable changes to the separated flow, as compared to LEBU's without serrations (Figure 4.32). One possible explanation for this result is that the angle of attack of the LEBU's was relatively small (10°) and the

serration chord length was only 0.25 in.; therefore, the resulting projected height of the serrated part of the LEBU was only 0.04 in. (0.03δ) normal to the flow direction. This was perhaps too small to generate vortices that were strong enough to affect the flowfield downstream. Furthermore, at heights of 0.4δ and 0.8δ, any trailing vortices produced by the serrations may be too far away from the horizontal surface to redirect the momentum to the near-wall region.

4.7 Spanwise Cylinders

The spanwise cylinder (or flow control rail) investigated consisted of a cylinder with diameters of 0.13δ, 0.2δ, and 0.4δ (0.125 in., 0.25 in., and 0.50 in., respectively), as shown in Figure 2.1g. The spanwise cylinders were mounted horizontally across the entire test section with heights ranging from flush with the wall to 1.0δ and streamwise locations ranging from the separation line to 20δ upstream of baseline separation.

For flow separation control via cylinder wakes, the most effective diameter was 0.25 in. (0.2δ); the most effective height was 1 in. (0.8δ); and the most effective streamwise location was 5δ upstream of the baseline separation, as shown in Figures 4.33, 4.34, and 4.35, respectively. It should be noted that the cylinder was also effective in reducing the extent of separation when positioned at the separation line and a distance of 0.4δ above the wall. This effect was most likely due to the local mitigation of applied pressure gradients via a solid body instead of device wakes, as in the case of placing the cylinder further (e.g., 5δ) upstream. The shedding frequency of the 0.2δ diameter cylinder at h = 0.8δ was estimated to be approximately 1200 Hz. One important observation is that although the surface oil-flow visualization (Figure 4.36) shows an almost fully attached flow (i.e., extent of separation was reduced by 65%) for the 0.2δ diameter case of Figure 4.33, the pressure distribution shows an adverse effect on pressure recovery. In fact, all the cylinders tested far from the wall produced shifts in the maximum pressure downstream of the ramp to levels that were below the

baseline case, indicating a significant device drag penalty. Apparently the strong wake produced by these cylinders hampered the pressure recovery process by imposing a lower streamwise pressure for surface pressure recovery.

The 0.2δ diameter cylinder was also mounted flush with the wall at various streamwise locations. In order to achieve any positive effect on pressure recovery, the cylinder had to be placed at least 10δ (or $50d$) upstream of baseline separation. If placed any closer, the near-wall momentum deficit produced by the cylinder did not have an adequate distance downstream to be recovered, resulting in adverse pressure recovery. Placing the device at 10 to 20δ upstream of separation allowed the flow to recover a significant portion of the near-wall momentum by the time the separation boundary was reached and resulted in a slight positive effect on downstream pressure recovery (Figure 4.37). Positioning the cylinder away from the wall and closer to the separation line, however, seemed to be more effective in reducing the extent of the separation region than positioning it next to the wall.

Table 2.4 indicates that for the most effective spanwise cylinder with $d \sim 0.2\delta$, the device drag is at least 5 to 7 times larger than for vortex generators of equivalent height (i.e., $h \sim 0.2\delta$).

4.8 Arches

The arch configuration examined consisted of thin plates of metal bent into an *arch-shaped* geometry of varying dimensions, as shown in Figure 2.1h. Three to five arches were mounted in a spanwise row across the test section with height and chord varying from 0.2δ (0.25 in.) to 0.8δ (1 in.) and streamwise location ranging from the separation line to 40δ upstream.

Flow visualization results and surface pressure measurements indicate that none of the arch configurations with $\alpha \leq 0°$ produced any positive effect on flow separation (i.e., reducing the extent of separation, increasing pressure recovery, etc.). The surface

pressure distributions behind a typical arch (model No. 2) at 5δ upstream of baseline separation are displayed in Figure 4.38. The effect produced by the arches, however, appeared to persist a long distance downstream of the devices. Figure 4.39 shows that some aspect of the vortical structures could still be detected by the surface oil flow on the separation ramp upon moving the arches (model No. 4) from 2δ to 40δ upstream of baseline separation. These vortical structures could be the result of normal vortices and/or streamwise vortices generated by the vertical legs and/or the top corners of the arch, respectively.

Arch performance was improved by elongating the top surface of the arch and setting it at a small positive α. Figure 4.40 shows that at the same streamwise location of Figure 4.38 (i.e., 5δ upstream of baseline separation), a much improved pressure recovery over regular arches (models No. 1 to No. 4) was achieved for an elongated arch (model No. 6) with a top surface at an α of 10° and a height of 0.8δ. Surface oil-flow visualization indicated flow attachment directly downstream of the elongated arches. However, the flow attachment was three-dimensional, and pockets of recirculating flow could still be seen on the separation ramp between adjacent attached flow regions (Figure 4.41a). Reducing the height and size of this elongated arch (model No. 6) by one-half (model No. 8) also decreased its effectiveness in separation control. As in the case of LEBU's at an angle of attack, changing α from $-10°$ to $+10°$ enhanced flow separation control, and the most effective streamwise location was at 1δ downstream of the baseline separation (see Figure 4.41b). At this location, elongated arch model No. 6 reduced the extent of separation by up to 50%.

Table 2.5 indicates that for the most effective arch geometry (model No. 6), there is a large device drag penalty associated with a positive angle of attack of 10°. This drag penalty is less than 70% of the value for the spanwise cylinders, but more than twice the penalty incurred by submerged vortex generators with $h \leq 0.25$ in. (0.2δ).

4.9 Helmholtz Resonators

The Helmholtz resonators examined in the current study consisted of a cylindrical subsurface cavity with a diameter of 1 in. and a depth of 2.94 in., as shown in Figure 2.1i. The resonator is covered by a 0.06-in.-thick top plate containing a 0.5-in.-diameter orifice. The Helmholtz frequency, f_o, of a cylindrical resonator is given by the following formula [88]

$$2\pi f_o = c\left[S/(l'V + H^2 S/3)\right]^{1/2}$$

Here, c is the speed of sound, S the orifice area, l' the effective length of oscillating mass, V the resonator volume, and H the cavity length. From this equation one can see that the resonator geometry, together with the speed of sound, determines the Helmholtz frequency. The value of f_o was calculated for the current experiment to be 813 Hz for a test temperature of 70°F. In the present case the orifice diameter, D_o, is comparable in size to the turbulent eddies of the boundary layer. Panton and Miller [58] found, based on tests at a single speed with resonators of various frequencies, that the tuning correlated with the relation

$$30 < 2\pi f_o D_o / u_\tau < 45$$

For the present case, the value of the Strouhal number based on the wall shear velocity and orifice diameter, $2\pi f_o D_o/u_\tau$, was calculated to be 44. Within this Strouhal number range, the tuning between the resonator and the turbulent boundary layer leads to *strong excitation* with very high amplitude oscillation. The resonator becomes an oscillating source-sink of mass at the wall under the boundary layer. Flynn et al. [61] reported that the amplitude of the cavity pressure oscillations was 143 dB or 80% of the freestream dynamic pressure for a similar resonator geometry.

Ten Helmholtz resonators were placed 1.2 in. apart in the spanwise direction and longitudinally at 3.5δ upstream of baseline separation. These resonators produced an audible acoustic disturbance, but their effect on separation control was minimal (see

Figure 4.42). It is believed that these resonators were placed too far upstream of the baseline separation line to be effective in separation control. Flynn et al. [61] reported that the Helmholtz-resonator-induced momentum oscillation was largely attenuated by 3δ downstream of the resonator. Because of geometrical and physical constraints on the location of resonator cavities in the present investigation, 2.8δ upstream of the baseline separation was the closest possible placement of the resonators. The resonators were subsequently placed at 2.8δ, 10δ, and 40δ upstream of baseline separation; however, no evidence of any separation control was found. It is therefore concluded that separation alteration via resonator-induced momentum oscillation is not a promising concept.

4.10 Viets' Fluidic Flappers

The Viets' fluidic flappers investigated consisted of a small scoop, with heights ranging from 0.13 in. (0.1δ) to 0.25 in. (0.2δ). Placed at the downstream entrance of a flush-mounted spanwise annular duct, it directed flow through the duct and out the upstream exit, as shown in Figure 2.1j. Two annular duct (or cavity) geometries, configurations A and B, were examined. Configuration A had a diameter of 1.5 in. for the outer wall and 0.94 in. for the inner wall, while configuration B had a diameter of 1.0 in. for the outer wall and 0.75 in. for the inner wall. The flappers had a spanwise width of 20 in. and were centered along the test-section centerline.

Viets' fluidic flappers were investigated at 3δ upstream of baseline separation. At this streamwise location, all flapper geometries examined enhanced flow separation. Figure 4.43 shows that increasing the scoop height from 0.1δ to 0.2δ further enhanced flow separation and decreased pressure recovery downstream. With the scoop height constant, cavity configurations A and B produced very similar result, with the larger cavity (configuration A) producing slightly better pressure recovery downstream than the smaller cavity (configuration B). Attempts were made to reduce the scoop-induced adverse effect (i.e., device drag associated with local separation downstream of the scoop) by tapering

the scoop wall in the downstream direction. These efforts only made the downstream pressure recovery approach the baseline case, but did not improve upon it. However, for the 0.2δ scoop height cases, a significant improvement occurred when the flapper device was moved further upstream. Figure 4.44 shows a positive effect in separation control, compared to the baseline case, when the flapper device (configuration A) was placed at 10δ upstream of the baseline separation line. At this location, the Viets' flapper device reduced the extent of separation by up to 35%. Furthermore, there was still a slight positive effect in pressure recovery for the device located as far as 40δ upstream of the baseline separation line. Similar results were obtained with cavity configuration B and, to a slightly lesser extent, with no cavity at all (scoop only configuration). A possible explanation for the improvement of pressure recovery when the device was moved from 3δ to 10δ upstream of baseline separation is that the scoop-induced local separated flow did not have enough downstream distance to fully reattach/recover in the former case, whereas in the latter case, it did have a chance to reattach and re-energize the boundary layer. It should be noted that this effect is very similar to that of the 0.2δ diameter flush-mounted spanwise cylinder, as reported in Section 4.7 (Figure 4.37).

4.11 Vortex Generator Jets

Ten vortex-generators-jet (VGJ) orifices (lateral spacing of 1.2 in. or $\sim 0.9\delta$) were nominally located 1.75 in. upstream of the point of horizontal tangency or 3.5δ upstream of baseline separation. The orifice diameters tested were 1/32, 3/64, 1/16, 1/8, and 3/16 in. Orientation of the jets was varied through changes to the jet inclination angle, α (angle between the jet axis and the horizontal plane; $15° \leq \alpha \leq 90°$), and the jet azimuthal angle, β (angle between the jet axis and the freestream direction in a horizontal plane; $0° \leq \beta \leq 90°$). These angles are defined in Figure 2.1k.

Longitudinal pressure distributions (jet orifices located symmetrically with respect to pressure orifices) are presented in Figure 4.45 for a jet orifice diameter, D_o, of 1/16 in.

(α = 45° and β = 90°) as a function of the total volumetric flow rate through the jet orifices. Results indicate an increase in pressure recovery and a reduction in the extent of the separation region with increasing velocity ratio when D_o was held constant. Figure 4.46 shows pressure distributions as a function of jet diameters (D_o = 1/32, 3/64, and 1/16 in.) for values of the jet-to-freestream velocity ratio, VR, of 6.8, 3.0, and 1.7, respectively. For a given volumetric flow rate, Q, of 2.9 ft^3/min., the smallest jet orifice (corresponding to the highest velocity ratio) was the most effective. The best performance in terms of pressure recovery and reduction in the extent of the separation region was obtained with D_o = 1/32 in. (VR = 6.8).

The effect of variations in inclination angle on the pressure recovery (D_o = 1/32 in., β = 90°, and VR = 6.8) is shown in Figure 4.47. The maximum pressure recovery was obtained with 15° $\leq \alpha \leq$ 25°. A positive effect was also obtained with α = 45°; however, a somewhat unexpected result is the negligible effect of α = 90° (i.e., jets blowing vertically) compared with the baseline case. Oil-flow visualizations for α = 15° and 45° (Figures 4.48a and 4.48b, respectively), and the other conditions denoted in Figure 4.47, show that the flow reattaches upstream of the baseline reattachment line for the two inclination angles. In both cases, however, surface streamlines downstream of reattachment are skewed toward the (initial) direction of the jets. The skewness is greater at the lower inclination angle. For both inclination angles, the separation line is three-dimensional, with pockets of separated flow adjacent to pockets of attached flow. The separated flow appears to have a spanwise component which is strongest for α = 15°. The extent of separation was reduced by up to 90% for the α = 15° case.

The effect of varying azimuthal angle on the pressure recovery for VGJ's with D_o = 1/32 in. and α = 15° and 45° are shown in Figures 4.49a and 4.49b, respectively. Maximum pressure recovery was achieved with β = 60° at α = 15° and with β = 90° at α = 45°. These figures show positive effect also for β = 0°, 30°, and 90° at α = 15° and for β = 30° and 60° at α = 45°. Though there was a positive effect at β = 0° with

$\alpha = 15°$, the pressure recovery with $\alpha = 45°$ was identical to the baseline case. Pearcey and Stuart [67] indicated that as the jet azimuthal angle, β, is increased, one member of the pair of counterrotating vortices comprising the jet becomes dominant and is situated close to the surface. The other weaker member of the vortex pair lies above the dominant member. Based on the present results, it appears that this *dominant* vortex was strongest at $60° \leq \beta \leq 90°$. These flow phenomena were examined further in the water tunnel.

Measurements made to determine the spanwise variation in the pressure distribution with D_o = 1/32 in., $\alpha = 15°$, and $\beta = 90°$ are presented in Figure 4.50. Plane "A" passes through the centerline orifice with planes "B", "C", and "D" being $\lambda/4$, $\lambda/2$, and $3\lambda/4$ from the centerline in the spanwise direction. These results indicate minimal spanwise variation in the streamwise pressure distributions.

The effect of the streamwise location of the jet orifices on the pressure recovery is shown in Figure 4.51 (D_o = 1/32 in., VR = 6.8, $\alpha = 15°$, and $\beta = 90°$). For the three cases shown, maximum pressure recovery was obtained with the jet orifices located 3δ to 10δ upstream of the baseline separation line. Even with the jet orifices located 40δ upstream of the baseline separation line, significant pressure recovery was achieved, though reattachment was delayed in comparison with the reattachment location obtained with jet orifices located at 3δ and 10δ.

Several configurations were examined for which adjacent jets were oriented in a manner that has been shown by Johnston and Nishi [70] to produce counterrotating vortices ($\beta = \pm 90°$) rather than co-rotating vortices, as in the case when β was constant for all jets. One such configuration is depicted in Figure 4.52 (D_o = 1/32 in. and $\alpha = 45°$), which shows that the pressure recovery was lower in the three planes examined compared with the results for β = constant. There was also greater spanwise variability in the streamwise pressure distributions for the configuration with counterrotating vortices than with co-rotating vortices. The results for the co-rotating case are similar to those shown

in Figure 4.50. Figure 4.53, the flow-visualization photograph for the counterrotating case, shows pockets of three-dimensional separated flow on the ramp which caused the spanwise variation in the pressure distribution. Also shown are regions of surface flow in which there was early reattachment, as well as delayed separation, compared to the baseline case (Figure 2.3b).

Air injection through a 0.008 by 0.95 in. rectangular slot, oriented as shown in Figure 4.54 (β = 0°, VR = 6.8, and Q = 2.9 ft^3/min.), produced the level of pressure recovery indicated. The slot was designed with a total flow area corresponding to 10 jet orifices with D_o = 1/32 in. The pressure recovery produced by slot injection was less than that produced by VGJ's with α = 15 and 45° (β = 90°). In addition, Figure 4.55 shows that the flow was attached in a small region near the centerline of the model where the slot was located. Consequently, to achieve flow control with slot injection comparable to that obtained with the VGJ's (with the same extent of spanwise treatment, i.e., longer slot) would probably require an order-of-magnitude increase in the air volumetric flow rate through the slot.

4.12 Wall Cooling

The main focus of the current study was to determine trends (for comparison purpose) rather than exact solutions. Therefore, boundary-layer theory was used for the calculation of separation locations. The current boundary-layer method closely parallels that of Cebeci-Smith [89] which predicts turbulent separation over axisymmetric bodies and two-dimensional airfoils very accurately without any change in the turbulence model near separation. Consequently, the present solution approach should also be a reasonable prediction of the separation location for the two-dimensional backward-facing curved ramp used in the wind-tunnel experiments. In the boundary-layer computations, the inviscid pressure distribution was obtained using the GE *stream-tube* potential-flow code [90]. The inviscid pressure distribution, along with various wall temperature conditions,

were then input to the Harris-Blanchard boundary-layer code [91] to calculate the wall shear stress, τ_w, distribution upstream of the ramp and on the ramp leading up to flow separation under turbulent boundary-layer conditions. The computations were made at the following freestream conditions: $U_\infty = 132$ ft/s ($M_\infty = 0.118$), $P_{t,\infty} = 14.5$ psia, and $T_{t,\infty} = 525°$ R. The wall temperature ratio, $T_w/T_{t,\infty}$, was varied between 0.08 and 2. Notice that values of $T_w/T_{t,\infty}$, equal to 0.08 and 0.38 correspond to the saturation temperatures of liquid hydrogen and liquid methane, respectively. The computed value of separation location for the case of adiabatic reference (no wall heat transfer) almost exactly matched the measured value from the wind-tunnel experiments.

The computed τ_w distributions with full and partial surface coverage are shown in Figure 4.56. The resulting τ_w distributions over the backward-facing ramp clearly show that wall cooling delays flow separation while wall heating causes early separation. Figure 4.56a also shows that there was a tremendous increase in wall shear stress associated with the 100% (full) surface coverage wall-cooling case. The opposite was true for wall heating. Figure 4.56b shows that the increase in skin-friction drag (integrated wall shear stress) was reduced by an order of magnitude when partial wall cooling was applied from 2δ upstream of the adiabatic reference ($T_w/T_{t,\infty} = 1$) separation. The effectiveness in separation delay for this partial surface coverage was successfully maintained at 65% of the full surface coverage for $T_w/T_{t,\infty} = 0.08$ and 78% for $T_w/T_{t,\infty} = 0.38$. Figure 4.56c shows that the increase in frictional drag was reduced even further, by another order of magnitude, when partial wall cooling was applied from only 0.2δ upstream of the reference separation. The effectiveness in separation delay for this minimum surface coverage case was still satisfactorily maintained at 50% of the full surface coverage for $T_w/T_{t,\infty} = 0.08$ and 66% for $T_w/T_{t,\infty} = 0.38$. The minimum surface coverage case is important if afterbody wall cooling is used to delay separation on a bluff body. The skin-friction drag increase due to wall cooling must be minimized to obtain the maximum benefit from the pressure drag reduction (due to the delay in

separation on the afterbody). Finally, the partial wall cooling principle can also apply to a heated wall case. Figure 4.56d shows an example of applying partial wall cooling from 2δ upstream of the adiabatic reference separation on a surface that was totally heated ($T_w/T_{t,\infty} = 2$) upstream of the 2δ location. The figure shows that applying partial wall cooling on a heated surface can delay the separation almost as well as on those of the adiabatic reference case (Figure 4.56b).

The physical principle behind separation control via wall cooling in a (compressible gas) turbulent boundary layer can be described in terms of density and viscosity effects. If the surface of a body in a compressible gas, such as air, is cooled, the near-wall fluid will have larger density and smaller viscosity than that in the case with no heat transfer. The smaller viscosity results in a fuller velocity profile and higher speeds near the wall. Combined with the larger density, this yields a higher momentum for the near-wall fluid particles and, hence, the boundary layer becomes more resistant to flow separation.

The wall shear stress increase associated with wall cooling can be explained in terms of the wall-temperature-induced density effect on the near-wall velocity gradient. From the conservation of mass taken across a control volume bounded between the wall and a near-wall streamline, it can be shown that the velocity gradient at the wall, $\left.\frac{du}{dy}\right|_w$, is inversely proportional to wall temperature $\left(\text{i.e., } \left.\frac{du}{dy}\right|_w \sim T_w^{-1}\right)$. The viscosity, μ, is approximately proportional to the square root of temperature (i.e., $\mu \sim T^{\frac{1}{2}}$), according to the Sutherland law of viscosity [83]. Therefore, it follows that the wall shear stress, τ_w, is inversely related to the square root of temperature $\left(\text{i.e., } \tau_w = \mu\left.\frac{du}{dy}\right|_w \sim T_w^{-\frac{1}{2}}\right)$. As a result, a decrease in wall temperature (i.e., wall cooling) would result in an increase in wall shear stress, and the opposite is true for wall heating.

4.13 Performance Summary

The most effective separation-control performance from each device category is summarized in Figures 4.57 and 4.58, as a function of the reduction in the extent of separation and the device aerodynamic drag, respectively. The device separation control performance shown in Figure 4.57 is represented in terms of nthe the the the ondimensionalized separation delay and reduction in reattachment distance. The device separation control effectiveness in Figure 4.58 is represented in terms of nondimensionalized separation delay distance (i.e., $(x_s - x_{s,\mathrm{ref}})/\delta$). The device aerodynamic drag in this figure represented only the drag acting upon the device by the flow. This drag, however, does not include the system drag associated with volume penalty (such as surface grooves, subsurface plumbings for wall heat transfer and VGJ's, and cavities for resonators, flappers, and passive porous surfaces) and power usage of an active system (such as wall heat transfer and VGJ's).

Figures 4.57 and 4.58 indicate that the most effective group of flow separation control devices were those believed to generate streamwise vortices, such as those produced by vortex generators, VGJ's, and large longitudinal grooves. The sub-δ-scale vortex generators with $h \sim 0.2\delta$ were just as effective in delaying separation as the δ-scale vortex generators with $h \sim 0.8\delta$. However, the δ-scale vortex generators had a device drag that was 4 to 6 times larger than the sub-δ-scale vortex generators. The second most effective group of flow separation control devices were those believed to generate transverse vortices, such as those produced by spanwise cylinders, LEBU and elongated arches at $\alpha = +10°$, Viets' flapper, and transverse grooves. The $d \sim 0.2\delta$ spanwise cylinders were the most effective of this group; however, the cylinders also generated the most drag. The elongated arches at $\alpha = +10°$ were 40% less effective in delaying separation than the spanwise cylinder, but with a 66% reduction in the device drag. The minimum coverage wall cooling was about 50% as effective as the maximum coverage wall cooling, but with a skin-friction drag increase of only 0.5% that of the

maximum coverage case. The maximum coverage wall heating enhanced separation but also reduced skin-friction drag significantly. The drag reducing ($h^+ \sim 7$) riblets and Helmholtz resonators had virtually no effect on separation, while the passive porous surfaces and swept grooves examined enhanced separation. All flush mounted flow-control devices such as surface grooves, passive porous surfaces, Helmholtz resonators, and VGJ's were assumed to have a negligible device (skin-friction) drag.

Spanwise cylinders, LEBU's at angle of attack, wishbone and doublet vortex generators, and VGJ's were selected to be further examined in a water tunnel via dye-flow visualization. Of these five devices, the former two were examined for their downstream transverse vortex generation and the latter three were examined for their downstream streamwise vortex generation. The flow-visualization results and associated flow physics are presented in Chapter 5.

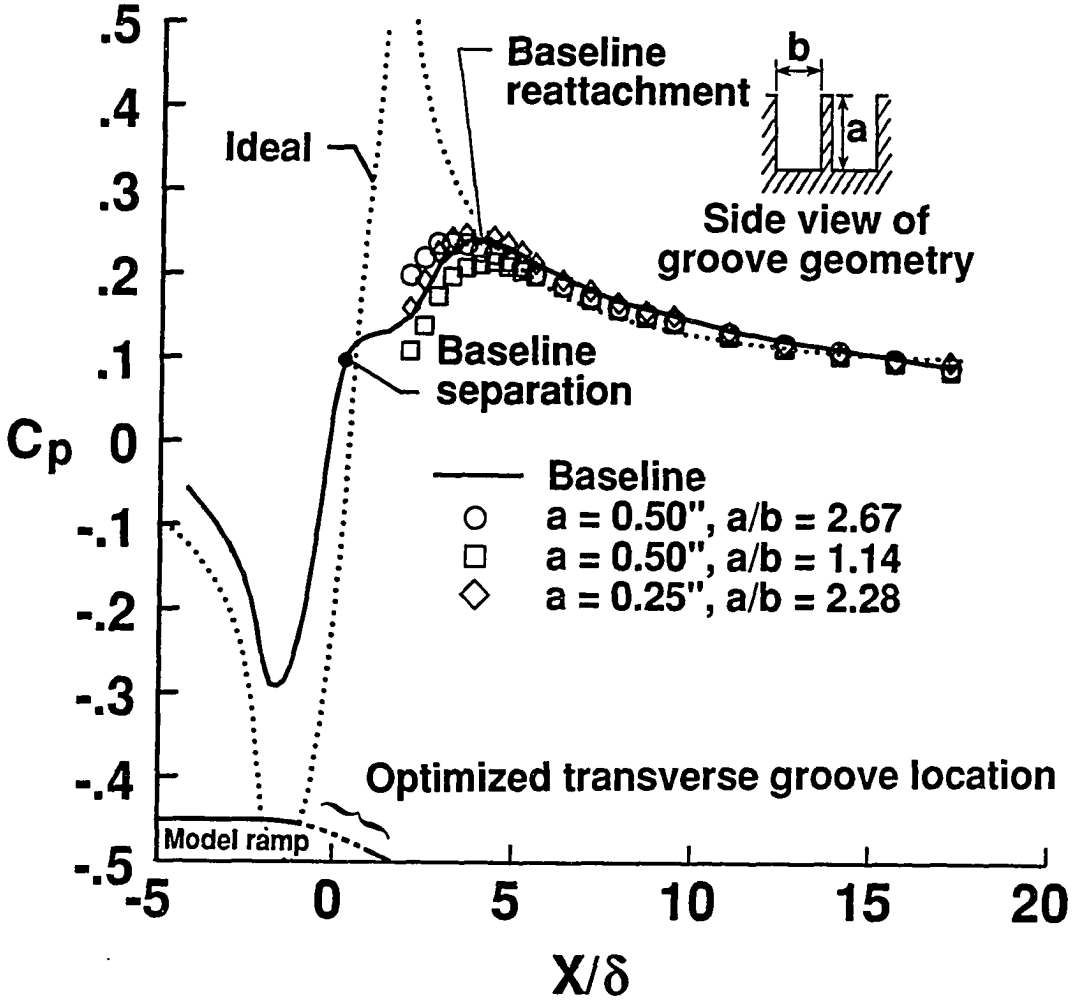

Figure 4.1 Effect of groove geometry on streamwise pressure distribution for transverse grooves.

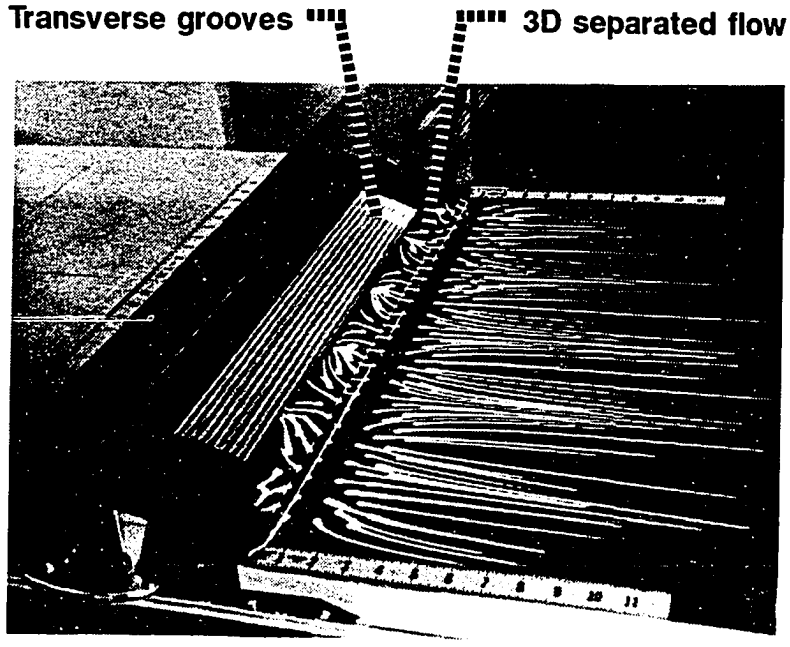

Figure 4.2 Example of three-dimensional flow caused by the transverse grooves.

Figure 4.3 Oil-flow visualization for 45° alternating swept grooves with $\lambda = 5$ in.

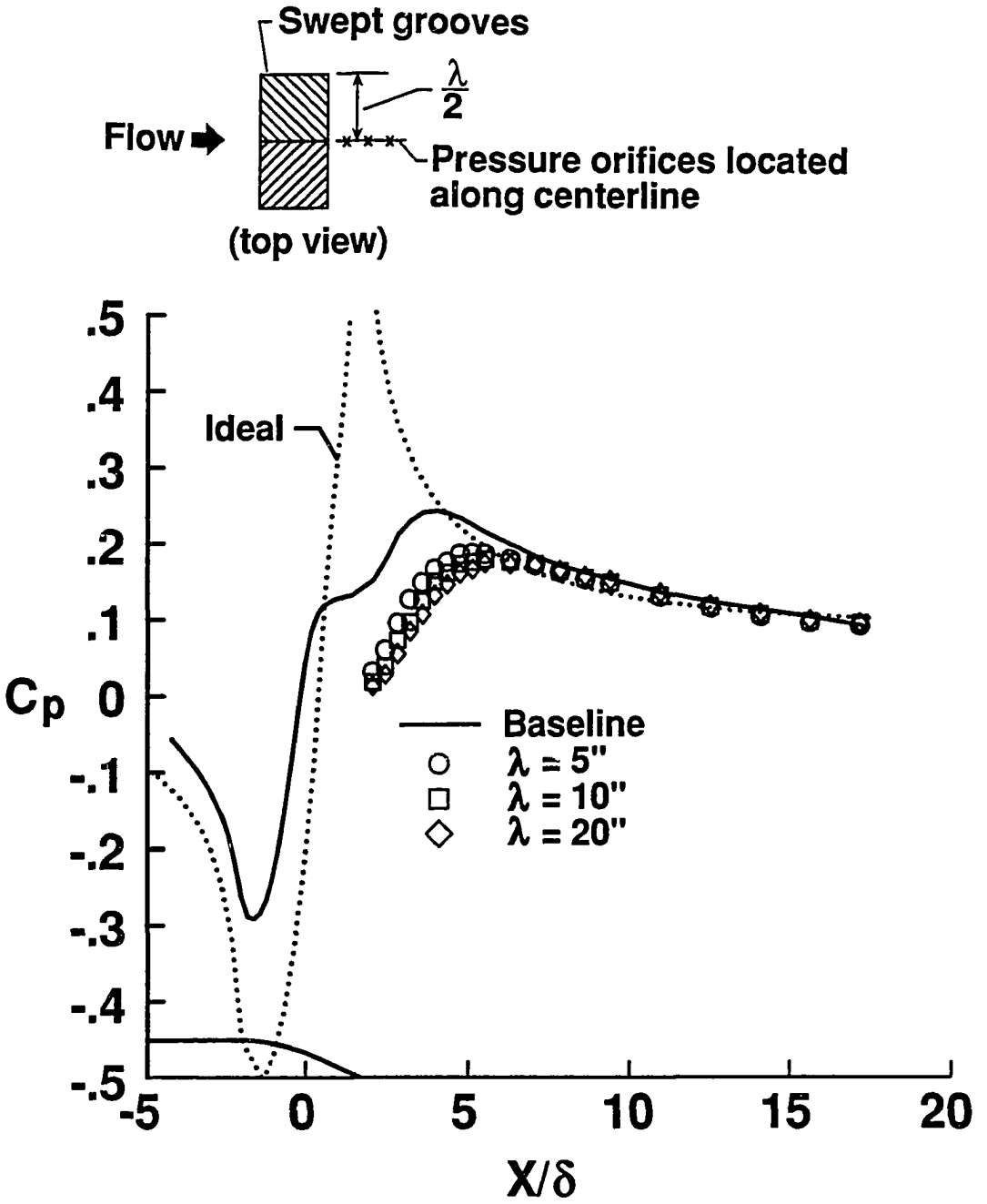

(a) Groove apexes pointing downstream along the centerline.

Figure 4.4 Effect of spanwise geometric cycle and groove orientation on streamwise pressure distribution for alternating 45° swept grooves.

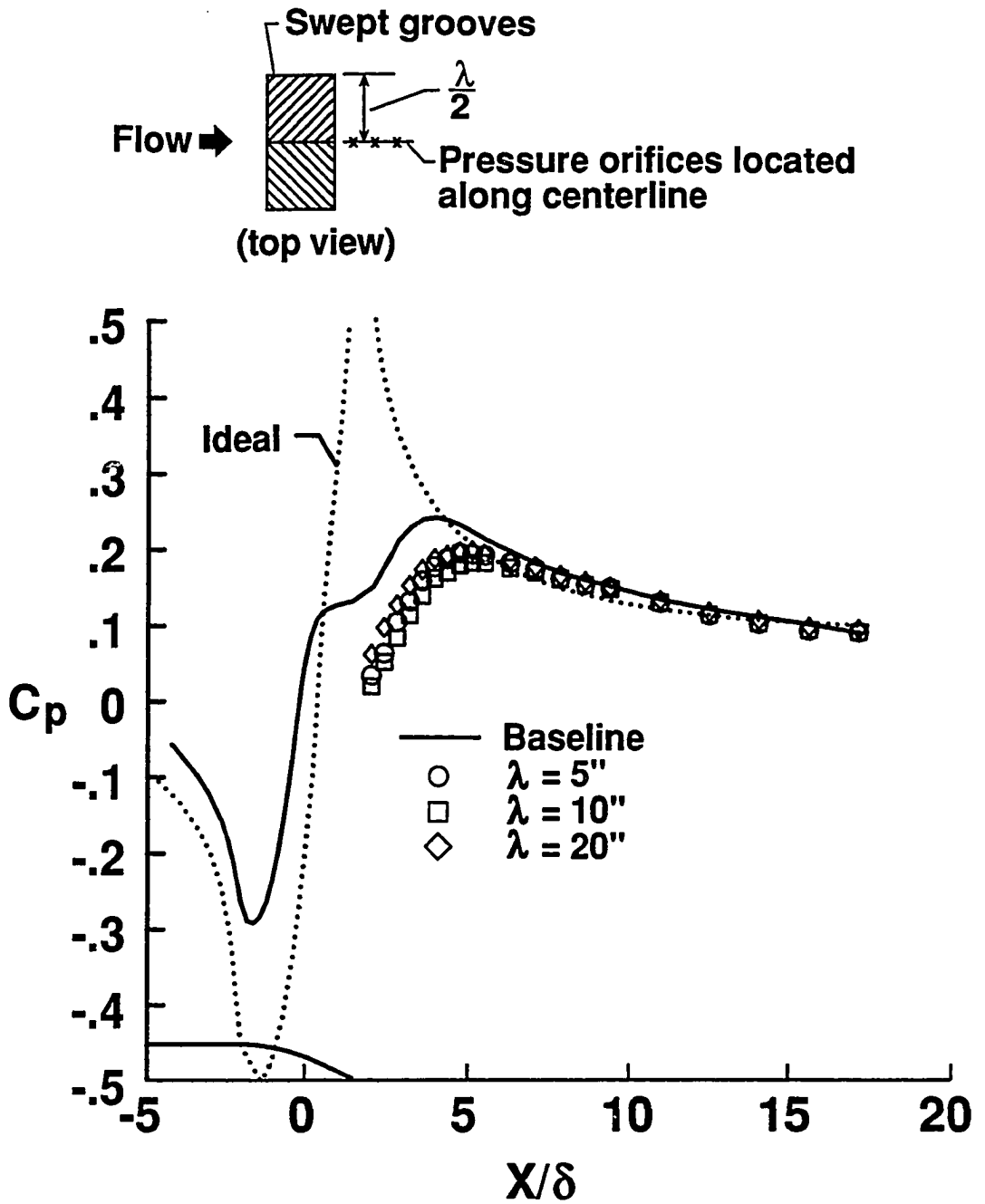

(b) Groove apexes pointing upstream along the centerline.

Figure 4.4 Concluded.

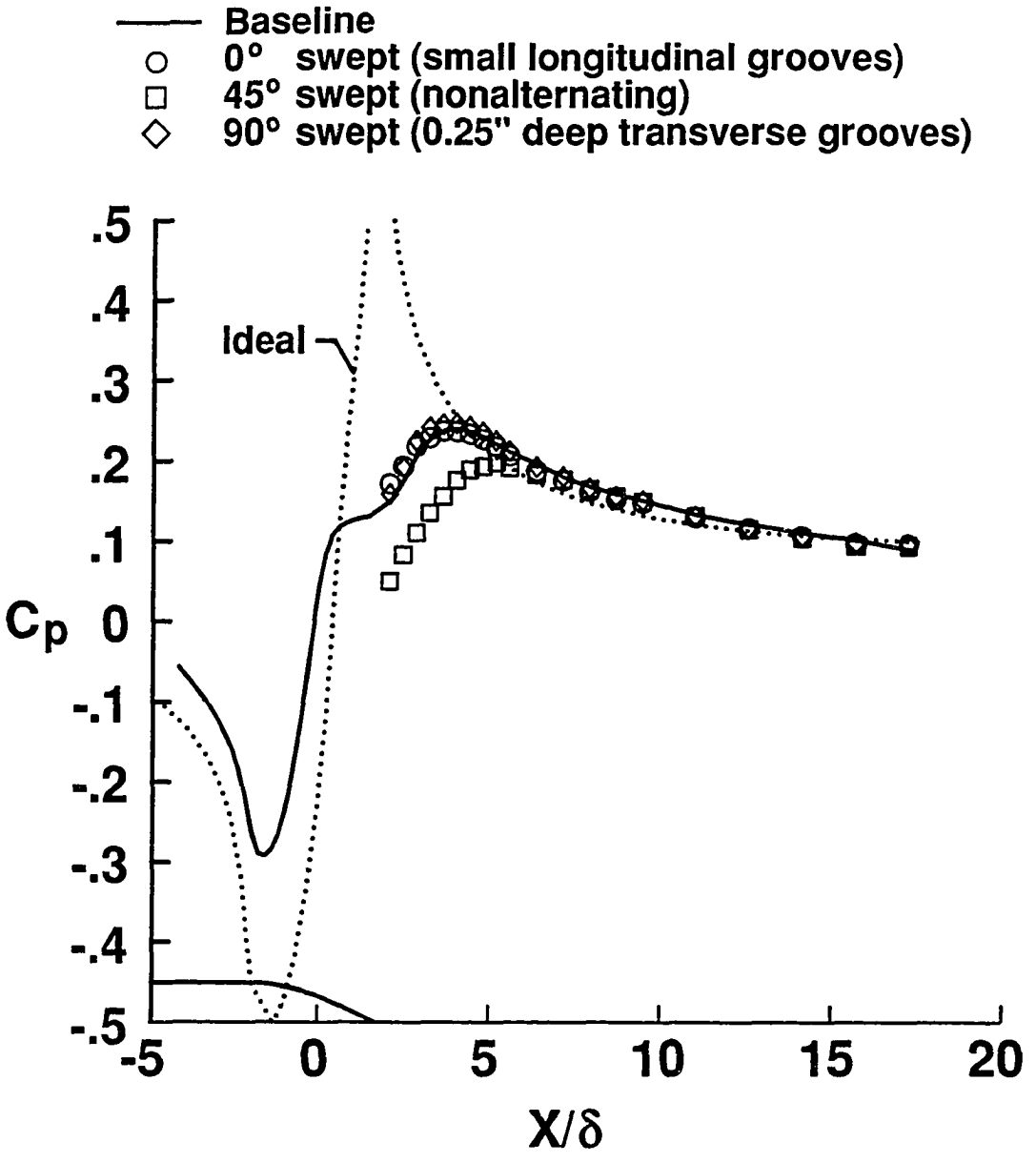

Figure 4.5 Effect of sweep angle on streamwise pressure distribution for swept grooves.

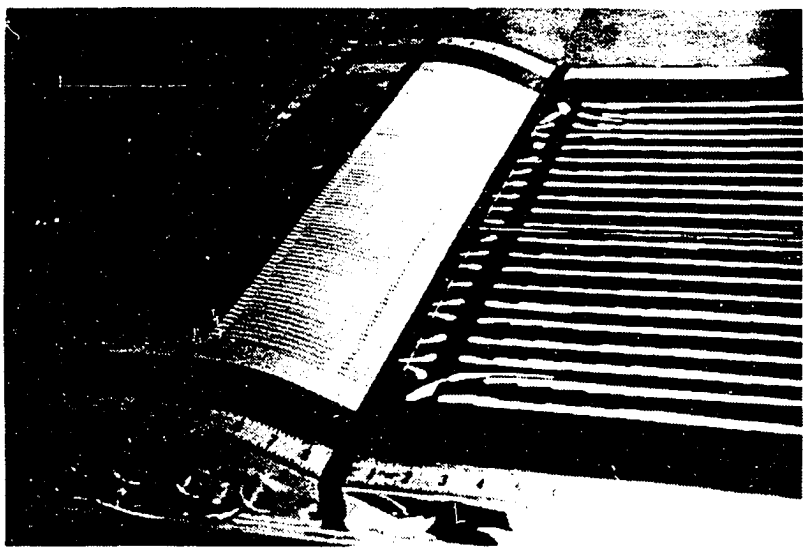

(a) 0° swept (longitudinal) grooves.

(b) 45° (constant) swept grooves.

Figure 4.6 Oil-flow visualizations for longitudinal and swept grooves.

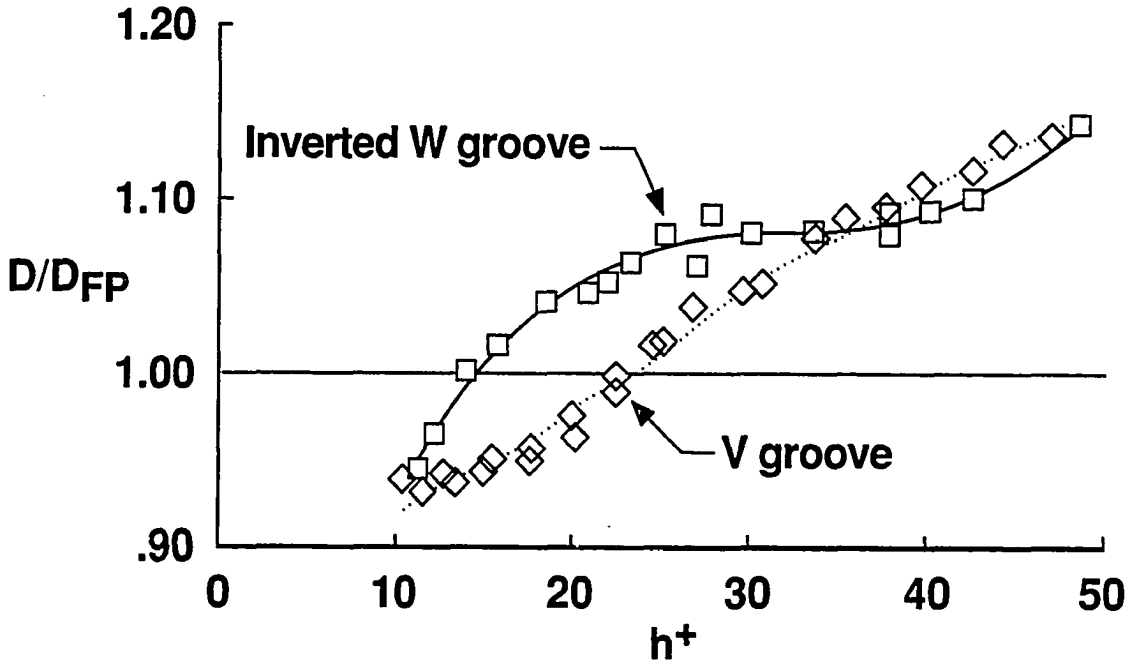

Figure 4.7 Net drag of riblet films in low-speed flow.

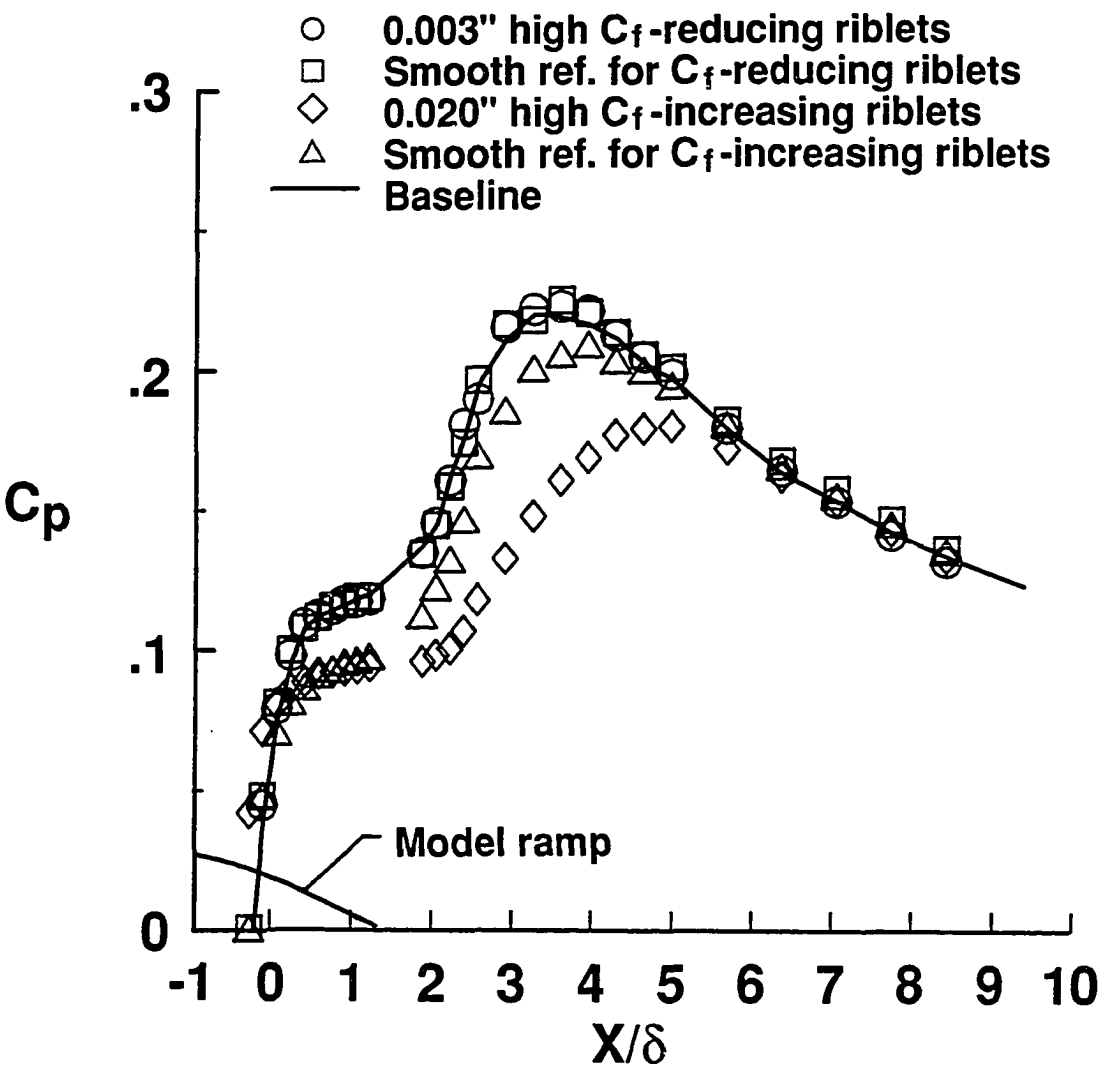

Figure 4.8 Effect of protrusion height on streamwise pressure distribution for riblets.

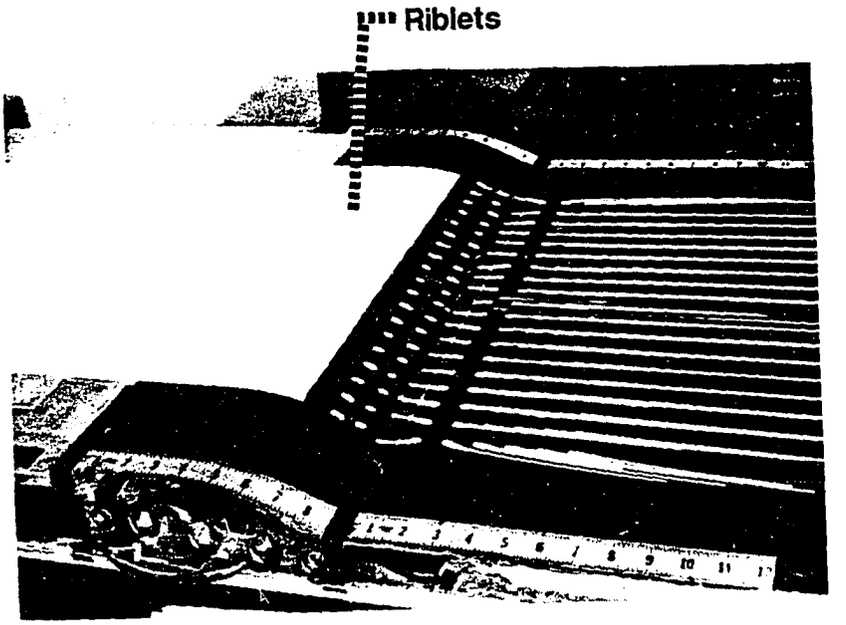

(a) 0.003-in.-high C_f-reducing riblets.

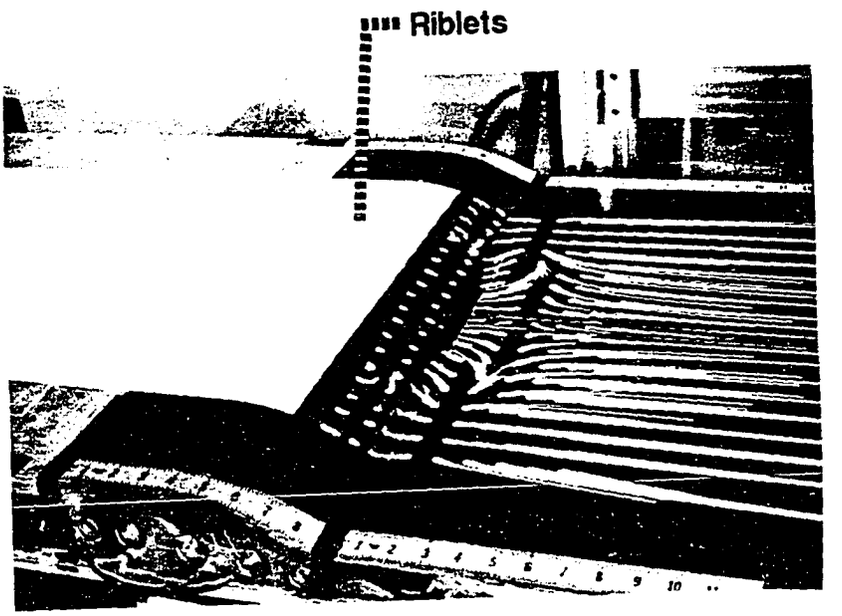

(b) 0.020-in.-high C_f-increasing riblets.

Figure 4.9 Oil-flow visualizations for riblets.

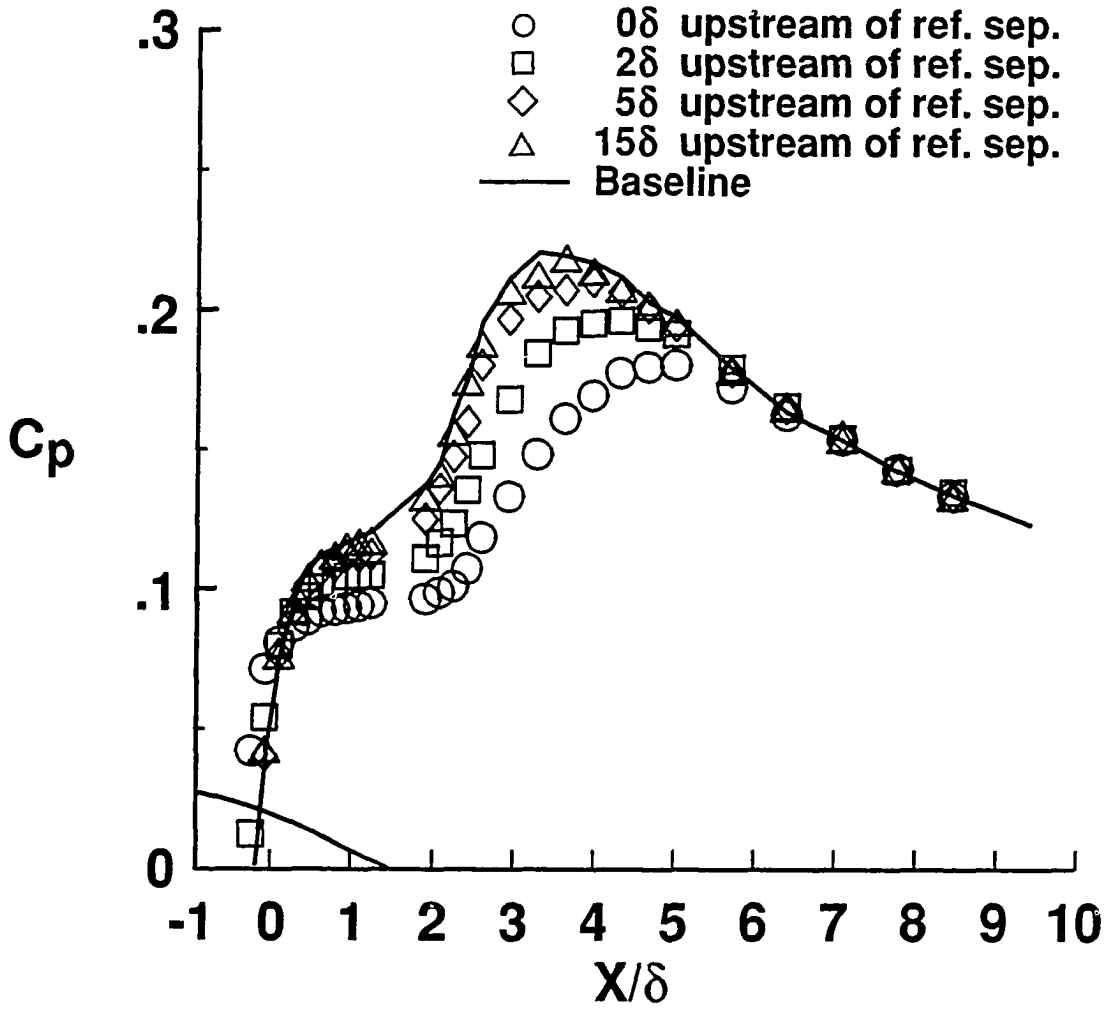

Figure 4.10 Effect of trailing-edge location on streamwise pressure distribution for 0.020-in.-high riblets.

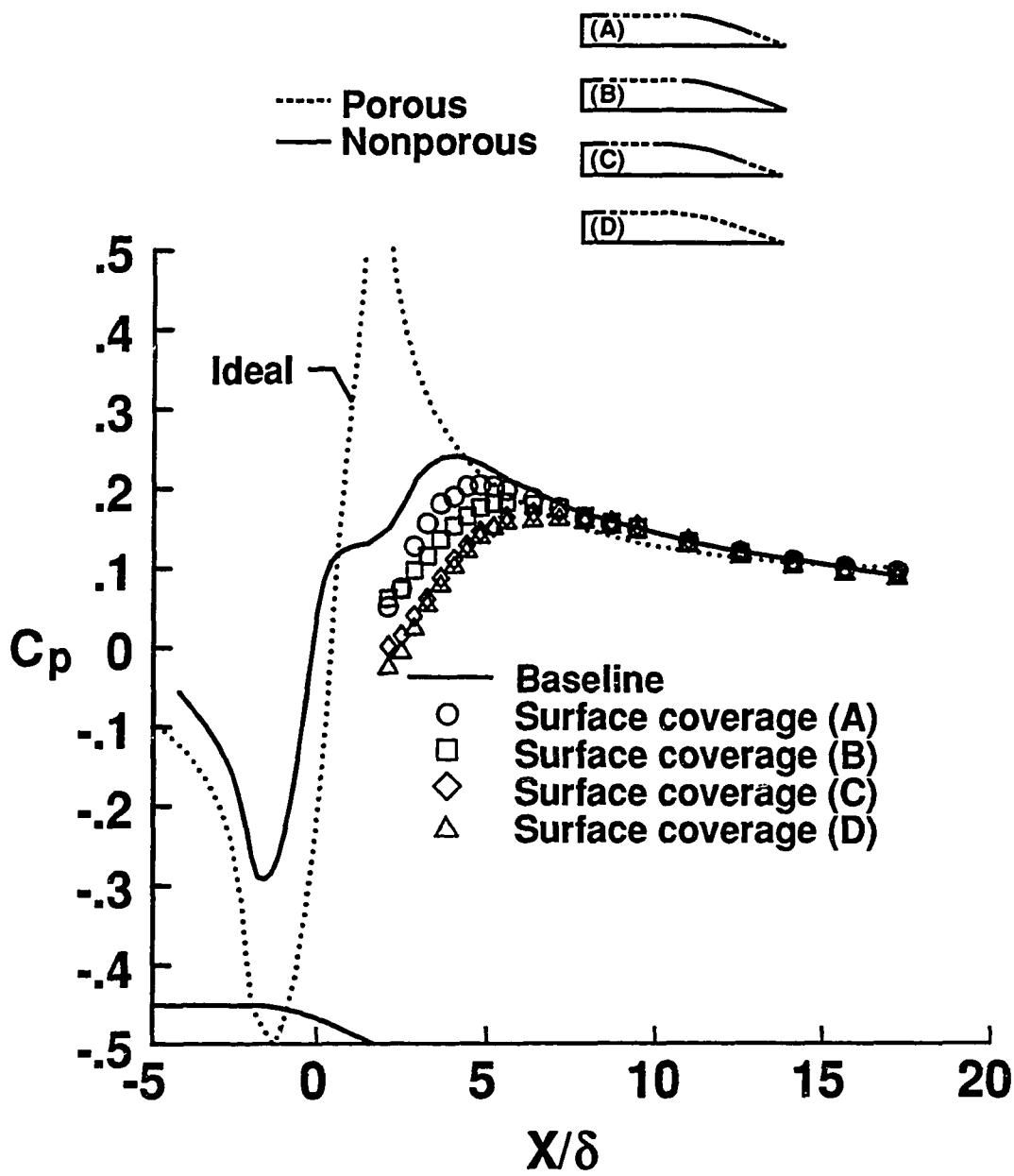

Figure 4.11 Effect of surface coverage on streamwise pressure distribution for passive porous surface No. 2.

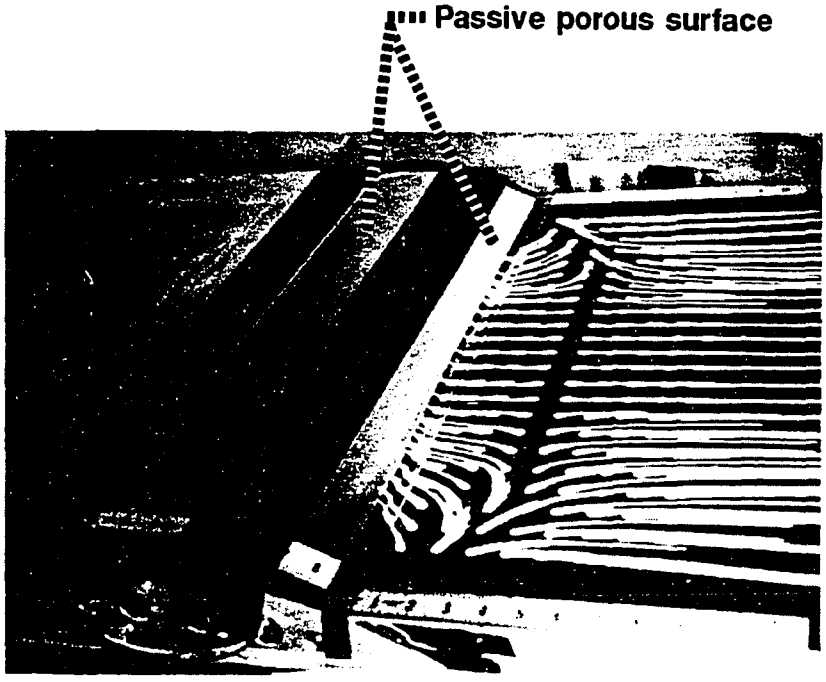

Figure 4.12 Oil-flow visualization for passive porous surface No. 2 (Case A).

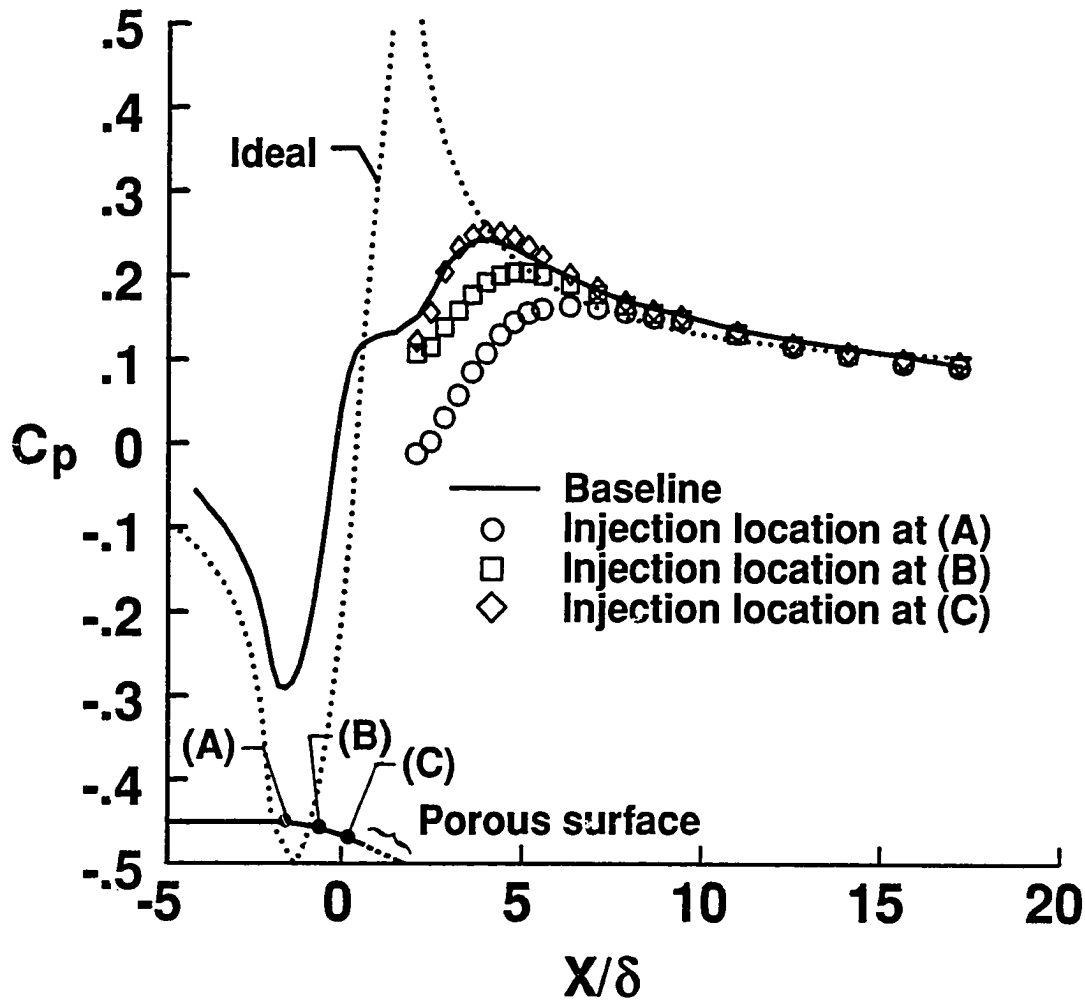

Figure 4.13 Effect of injection location on streamwise pressure distribution for passive tangential (outflow) bleeding.

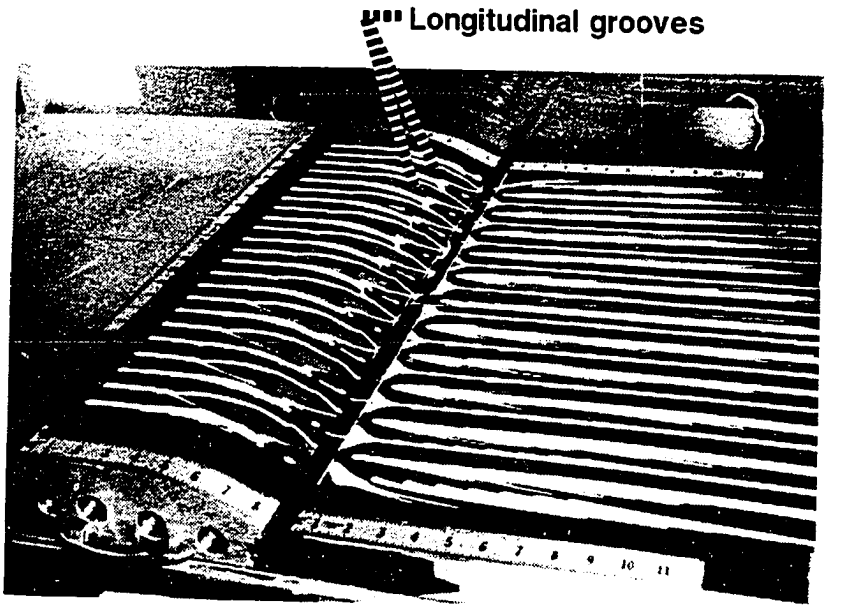

(a) Groove spacing $\sim 1.5\delta$.

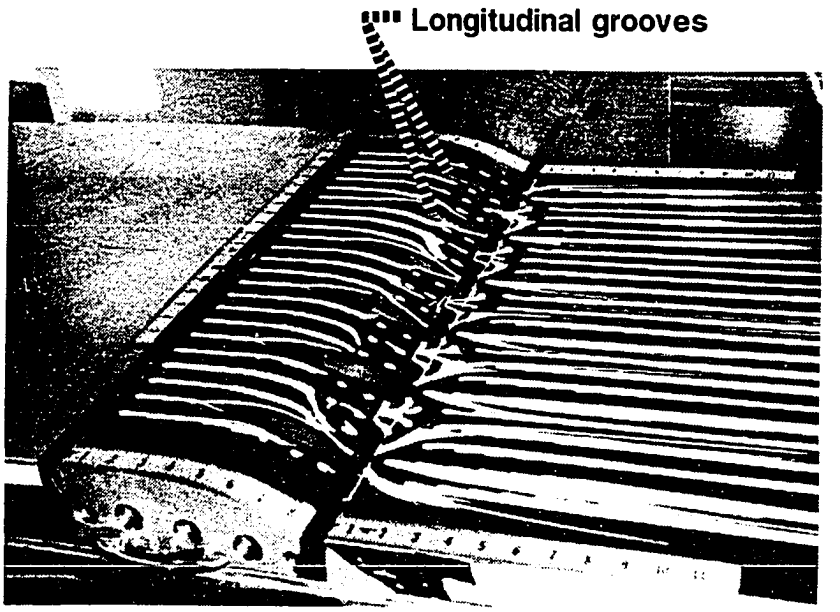

(b) Groove spacing $\sim 3\delta$.

Figure 4.14 Oil-flow visualizations showing the effect of groove spacing for 'short' longitudinal V-grooves.

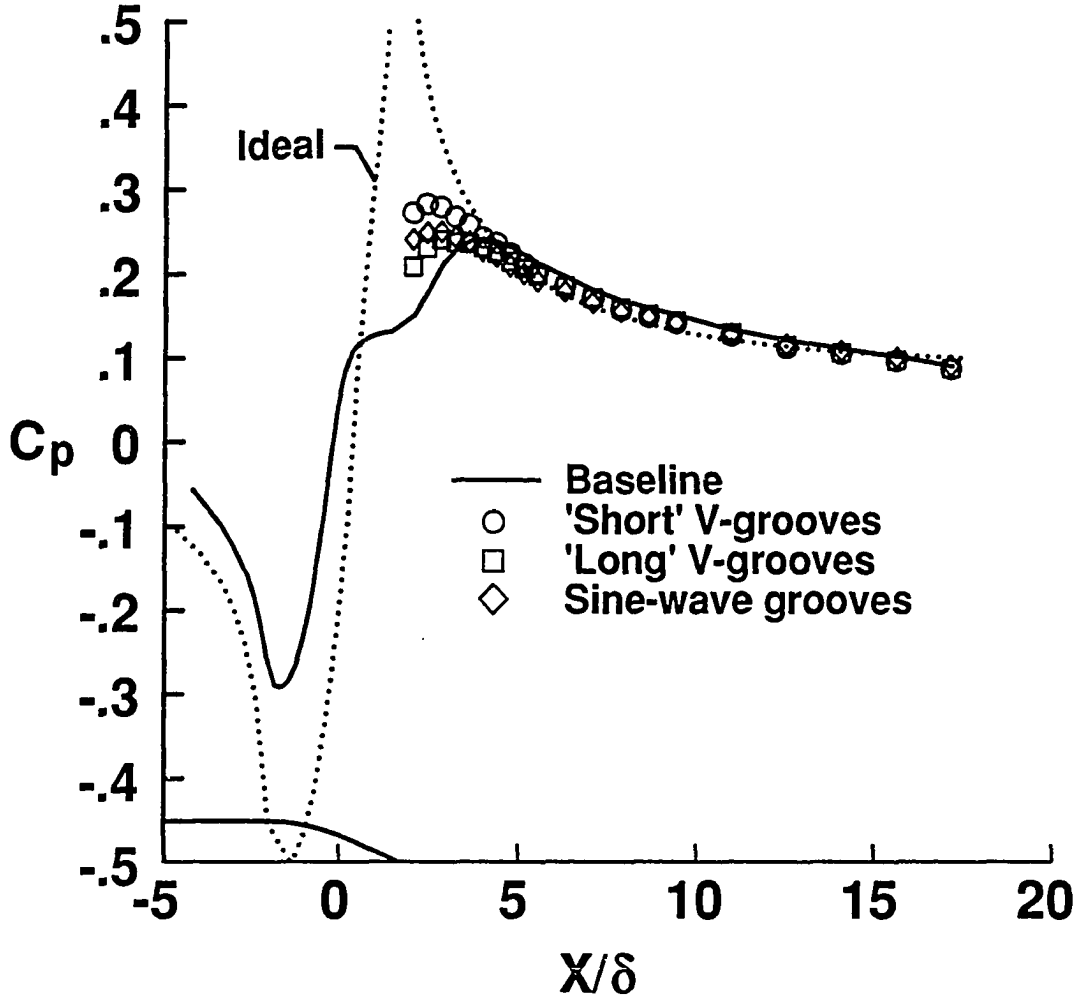

(a) Groove spacing $\sim 1.5\delta$.

Figure 4.15 Effect of groove spacing on streamwise pressure distribution for longitudinal grooves.

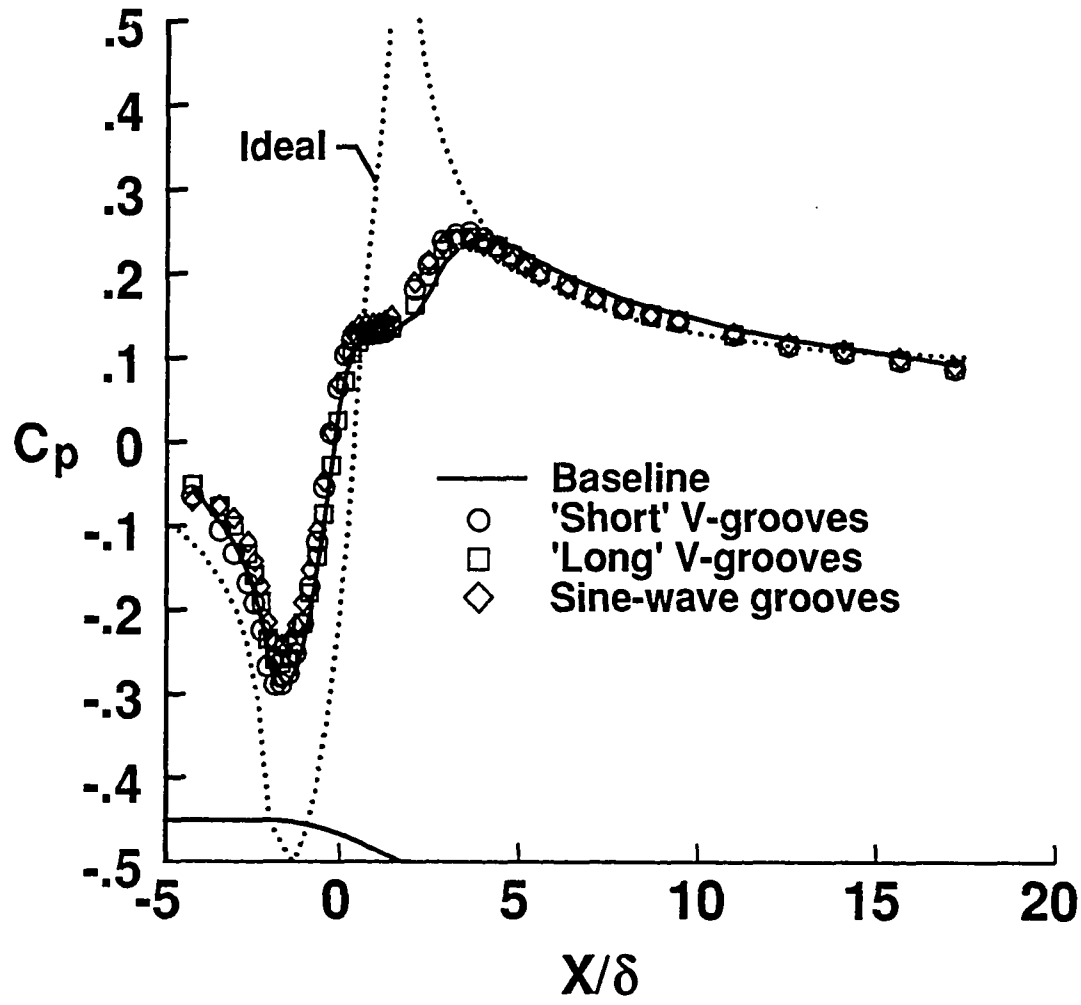

(b) Groove spacing $\sim 3\delta$.

Figure 4.15 Concluded.

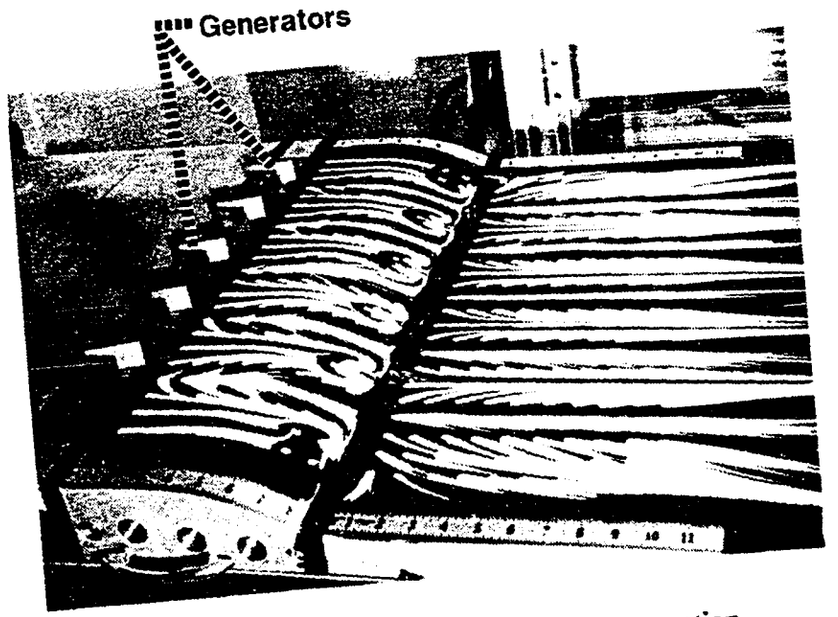

(a) Generators at 5δ upstream of baseline separation.

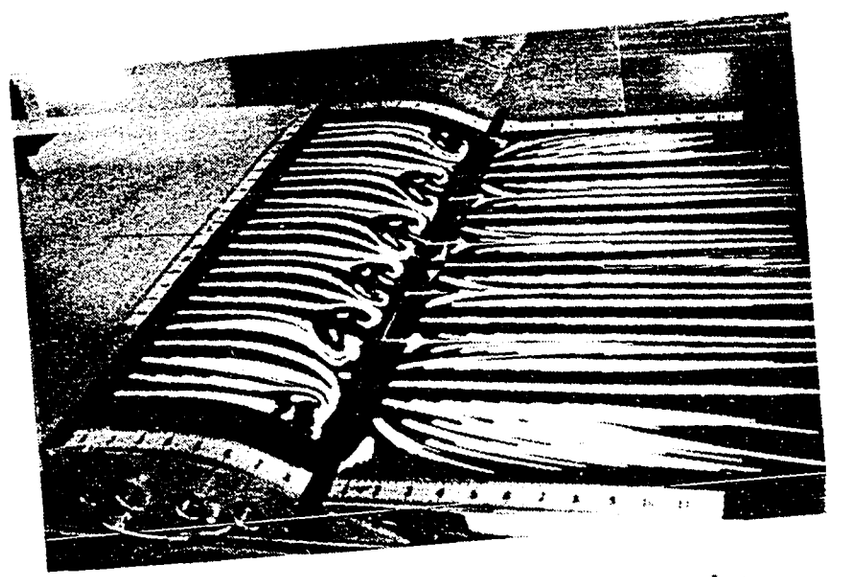

(b) Generators at 15δ upstream of baseline separation.

Figure 4.16 Oil-flow visualizations showing the effect of streamwise location for 0.8δ high counterrotating vortex generators.

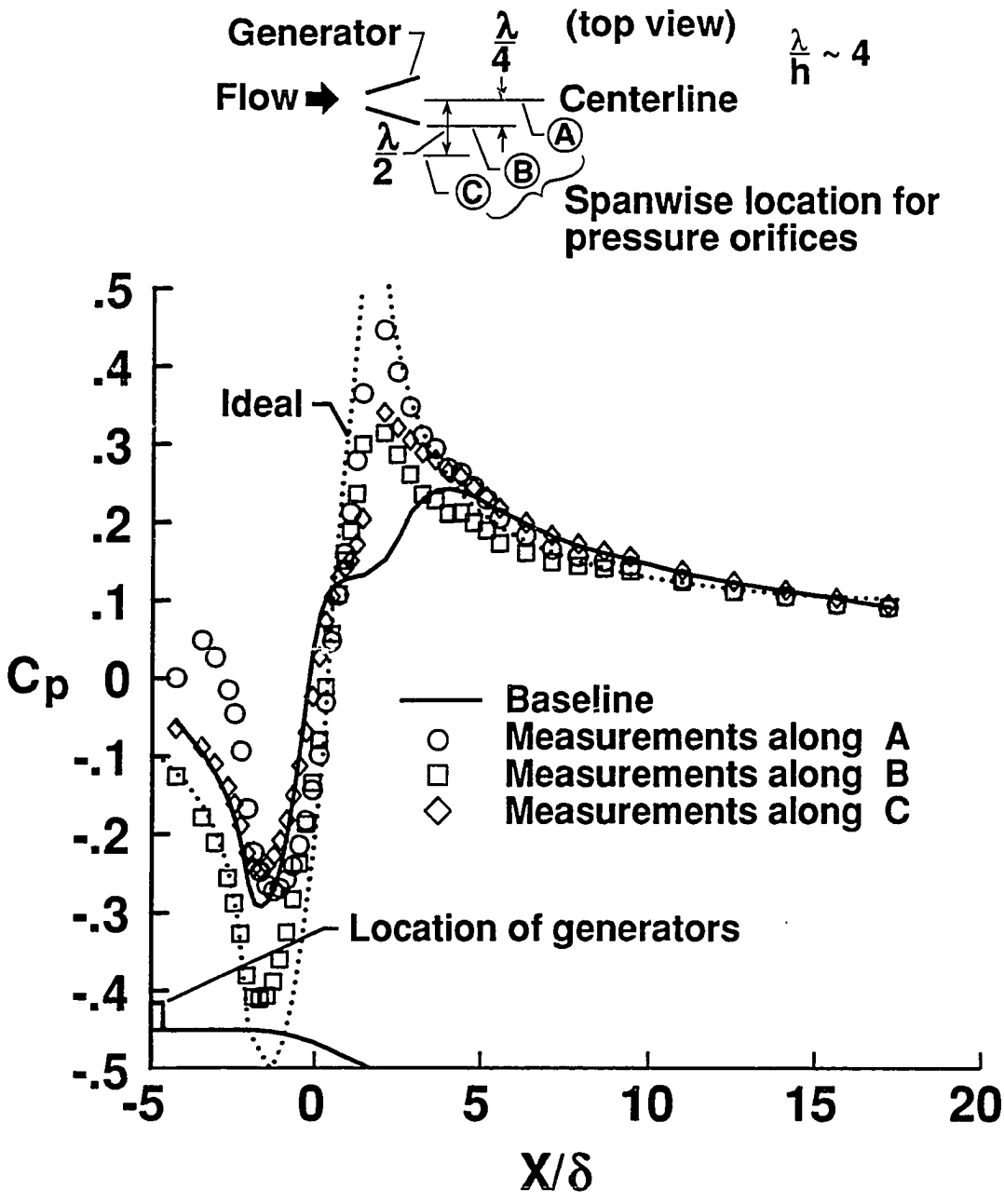

Figure 4.17 Spanwise variation of the streamwise pressure distribution for 0.8δ high counterrotating vortex generators placed at 5δ upstream of baseline separation.

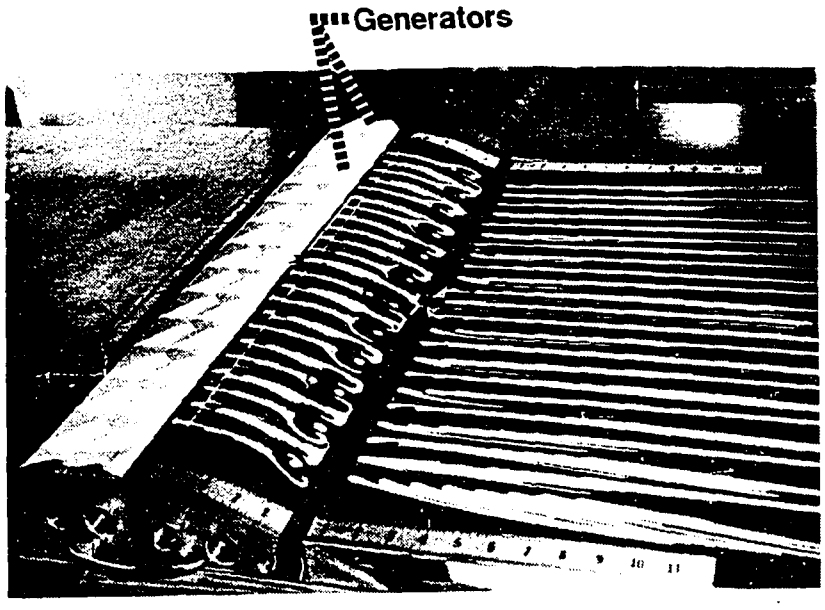

(a) 0.4δ high doublet vortex generators.

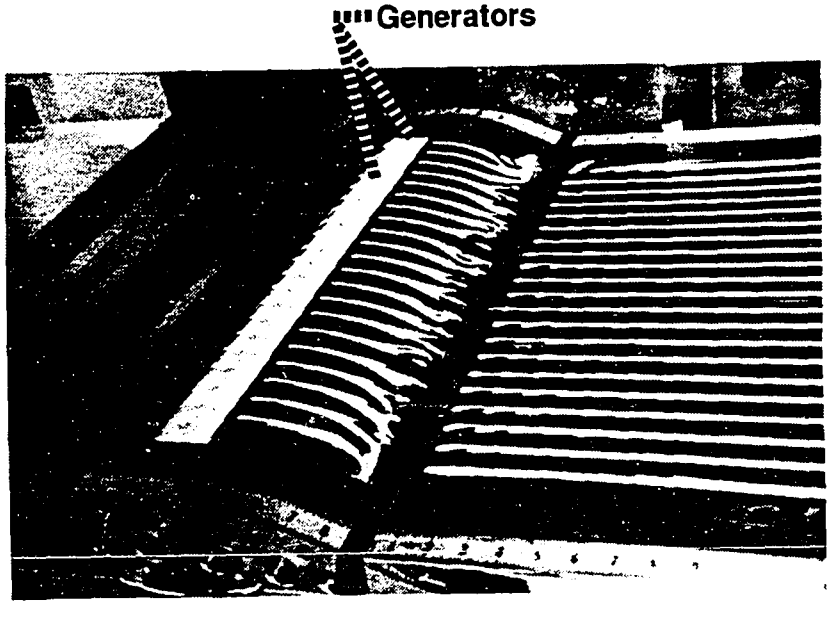

(b) 0.1δ high doublet vortex generators.

Figure 4.18 Oil-flow visualizations showing the effect of device height for doublet vortex generators at 2δ upstream of baseline separation.

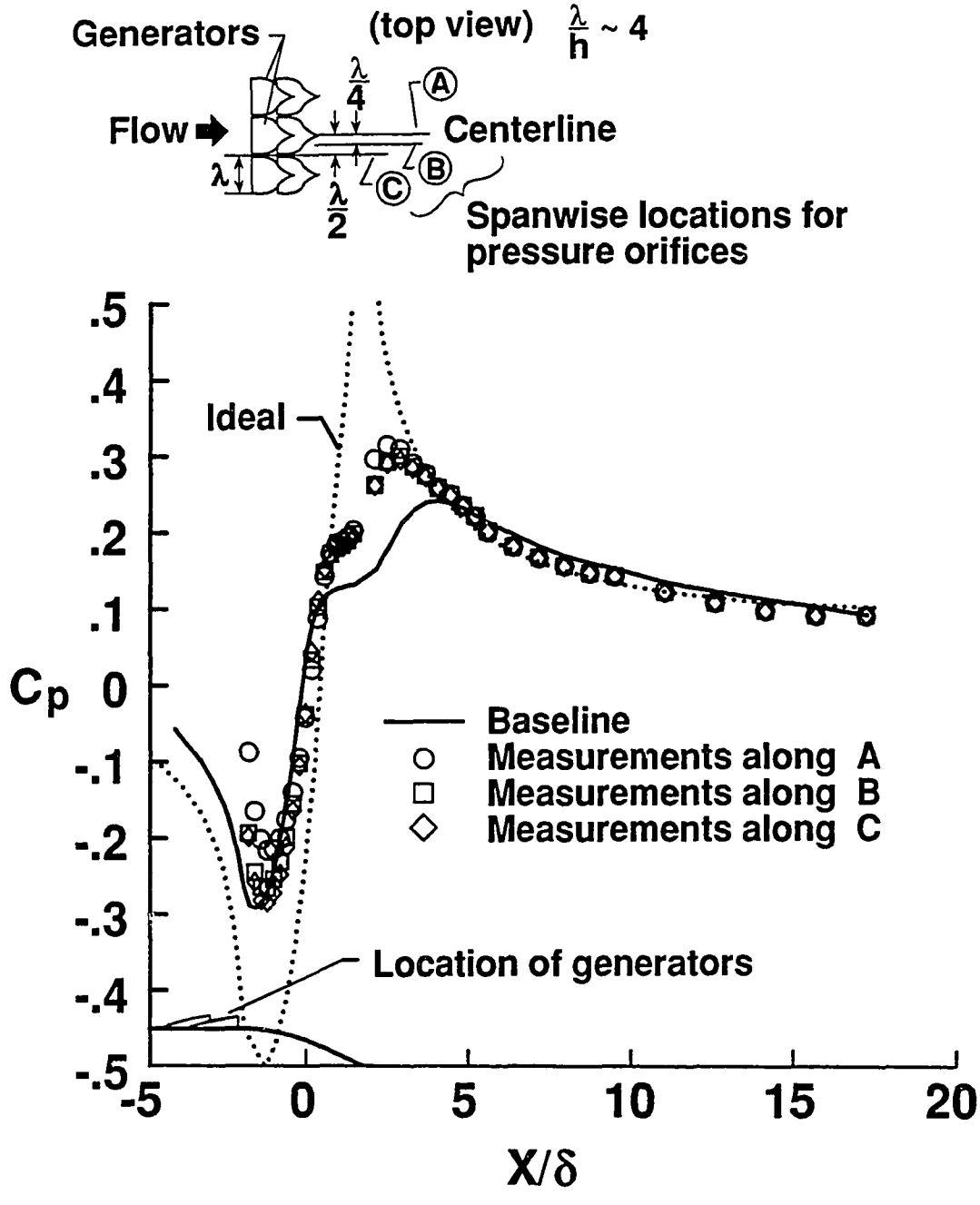

(a) 0.4δ high doublet vortex generators.

Figure 4.19 Effect of device height on streamwise pressure distribution for doublet vortex generators at 2δ upstream of baseline separation.

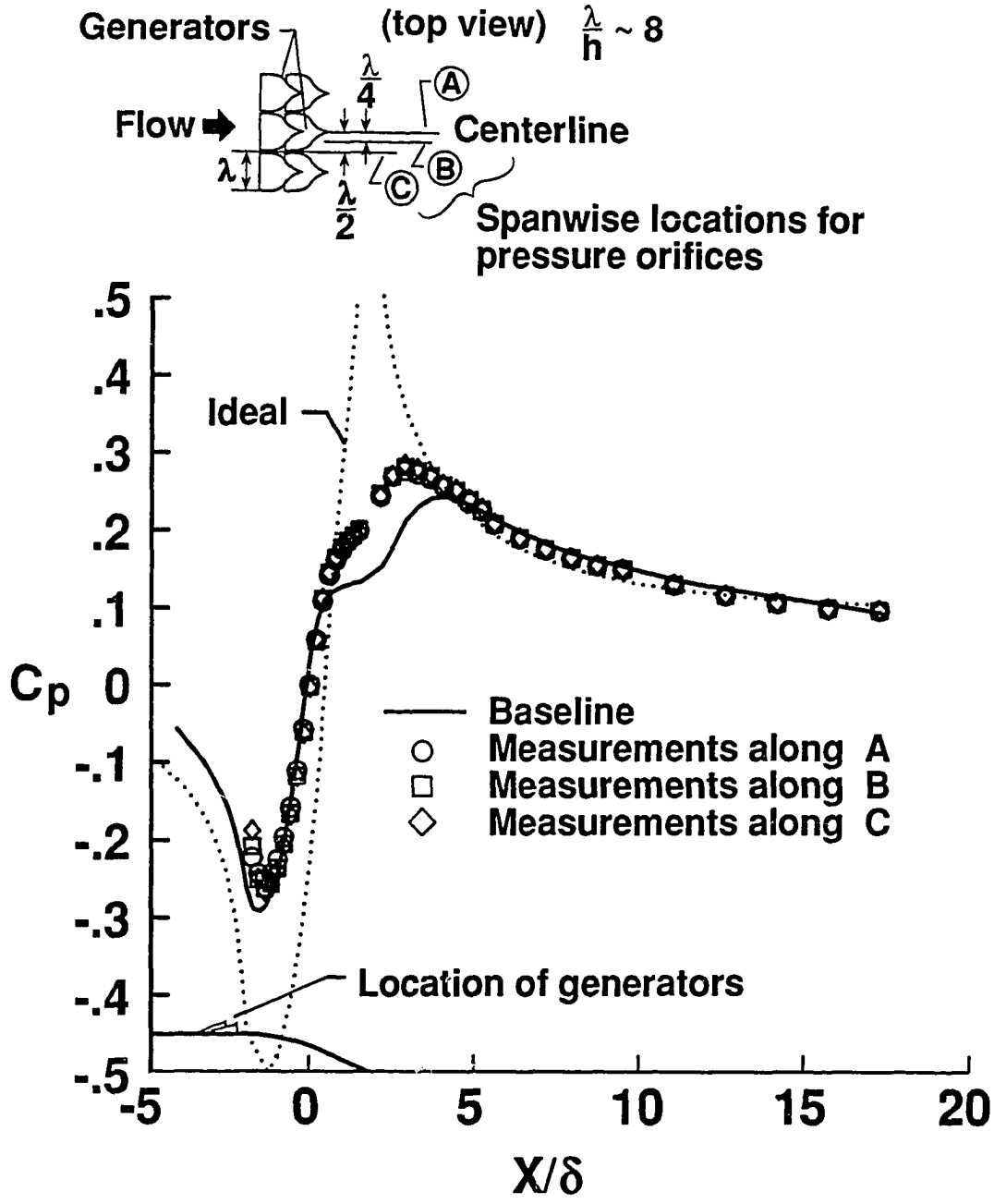

(b) 0.1δ high doublet vortex generators.

Figure 4.19 Concluded.

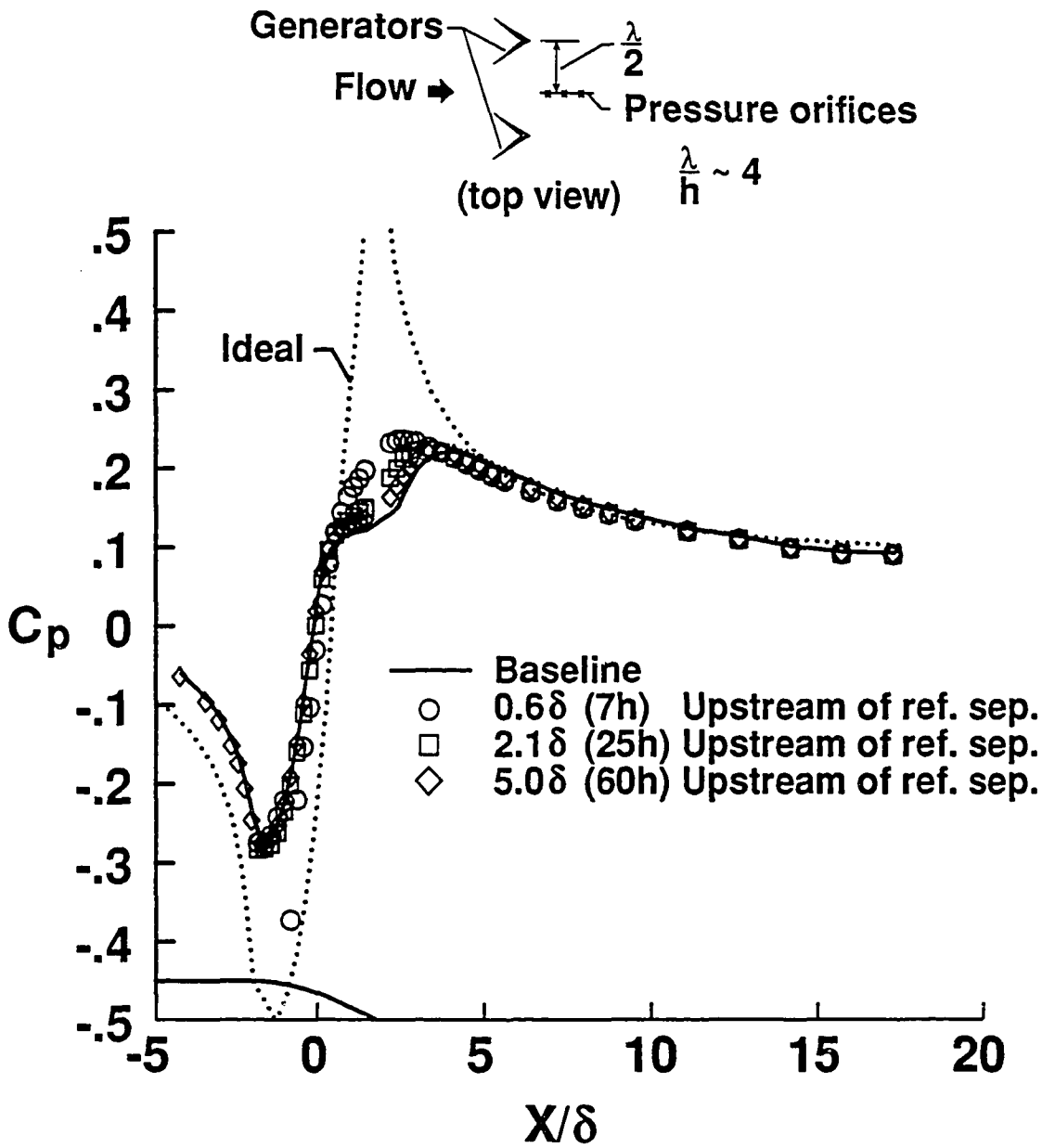

(a) Wishbone generators in forward configuration.

Figure 4.20 Effect of generator configuration on streamwise pressure distribution for 0.09δ high submerged vortex generators at various streamwise locations.

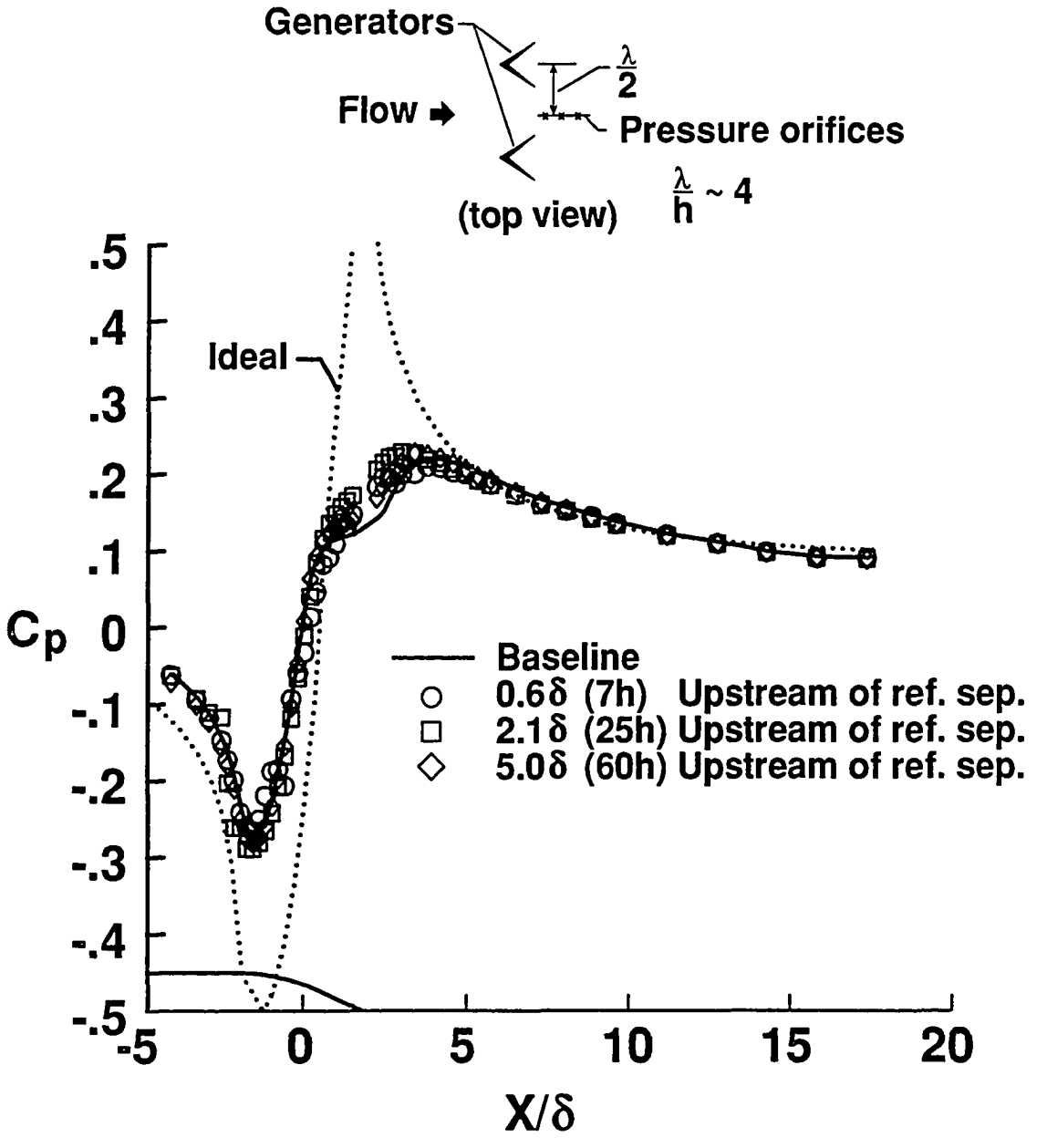

(b) Wishbone generators in reverse configuration.

Figure 4.20 Continued.

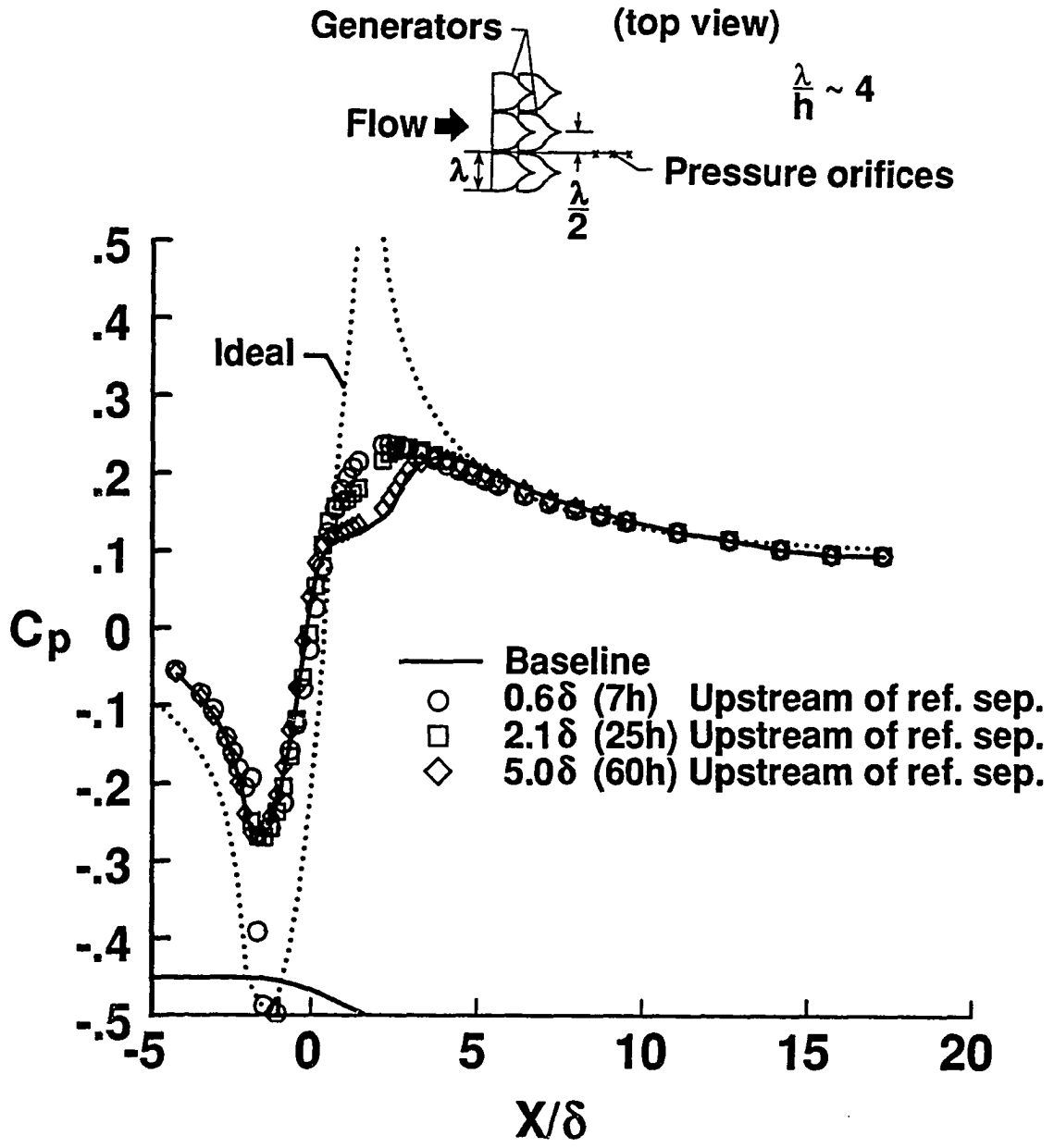

(c) Doublet vortex generators.

Figure 4.20 Concluded.

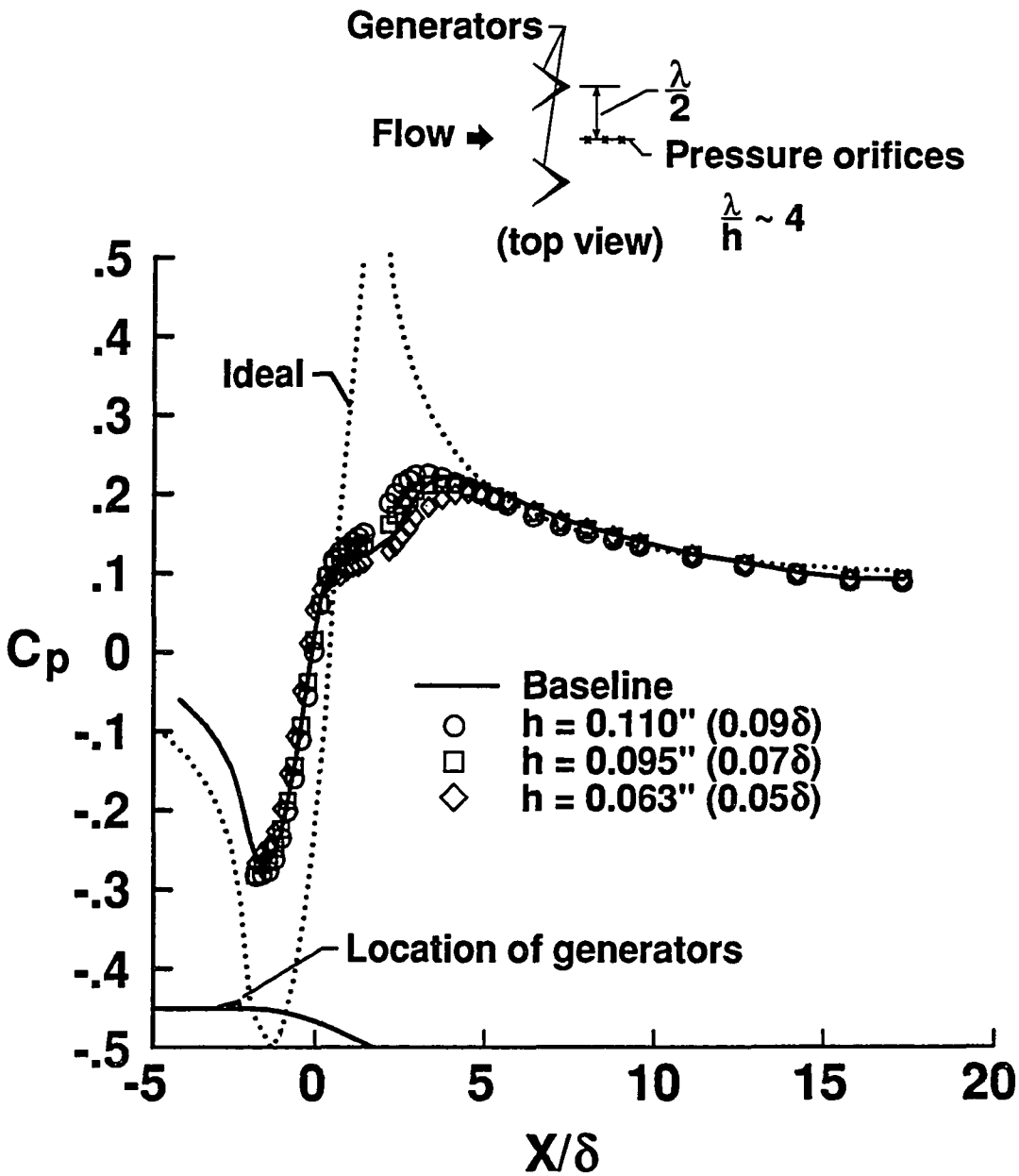

Figure 4.21 Effect of device height on streamwise pressure distribution for wishbone vortex generators at 2δ upstream of baseline separation.

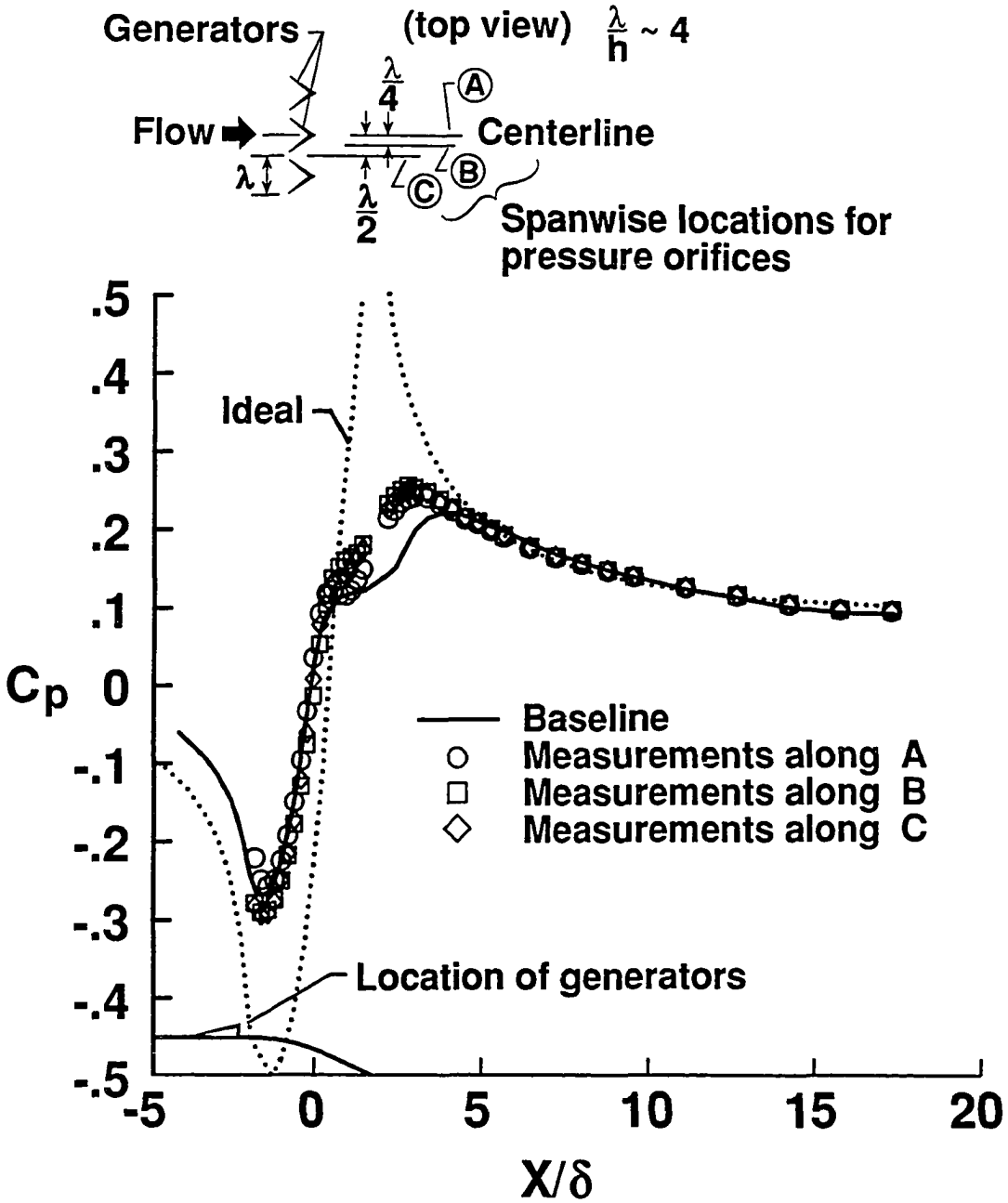

(a) Generators in forward configuration.

Figure 4.22 Effect of device orientation on steamwise pressure distribution for 0.2δ high wishbone vortex generators at 2δ upstream of baseline separation.

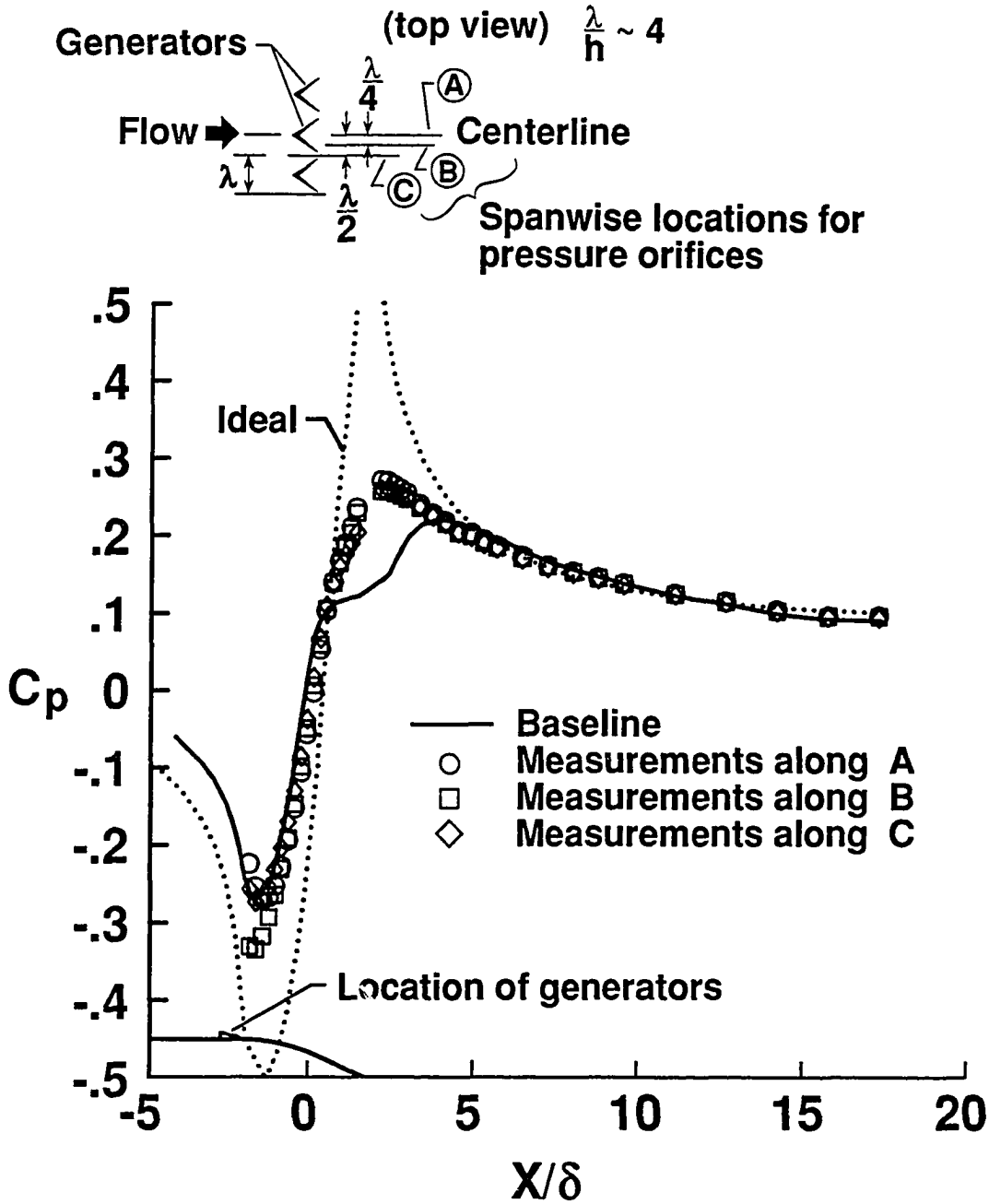

(b) Generators in reverse configuration.

Figure 4.22 Concluded.

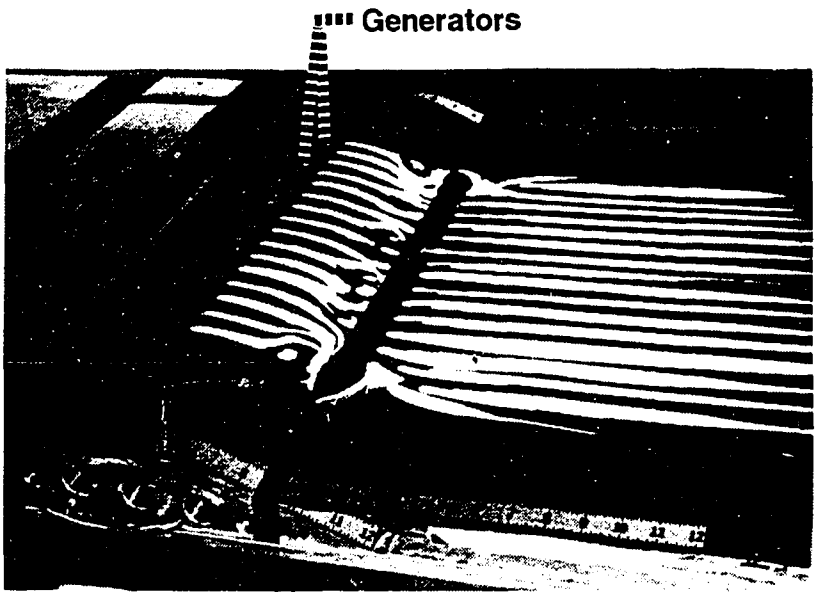

(a) Generators in forward configuration.

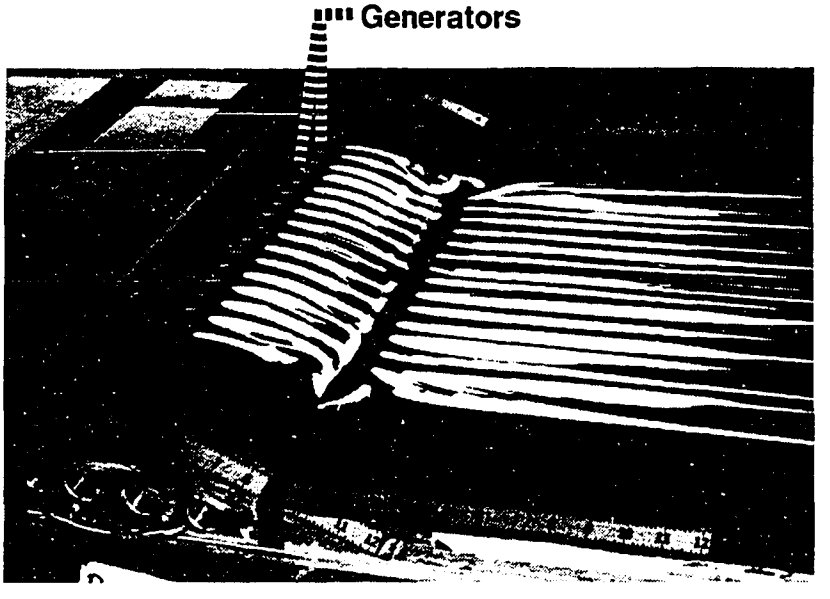

(b) Generators in reverse configuration.

Figure 4.23 Oil-flow visualizations showing the effect of device orientation for 2δ high wishbone vortex generators at 2δ upstream of baseline separation.

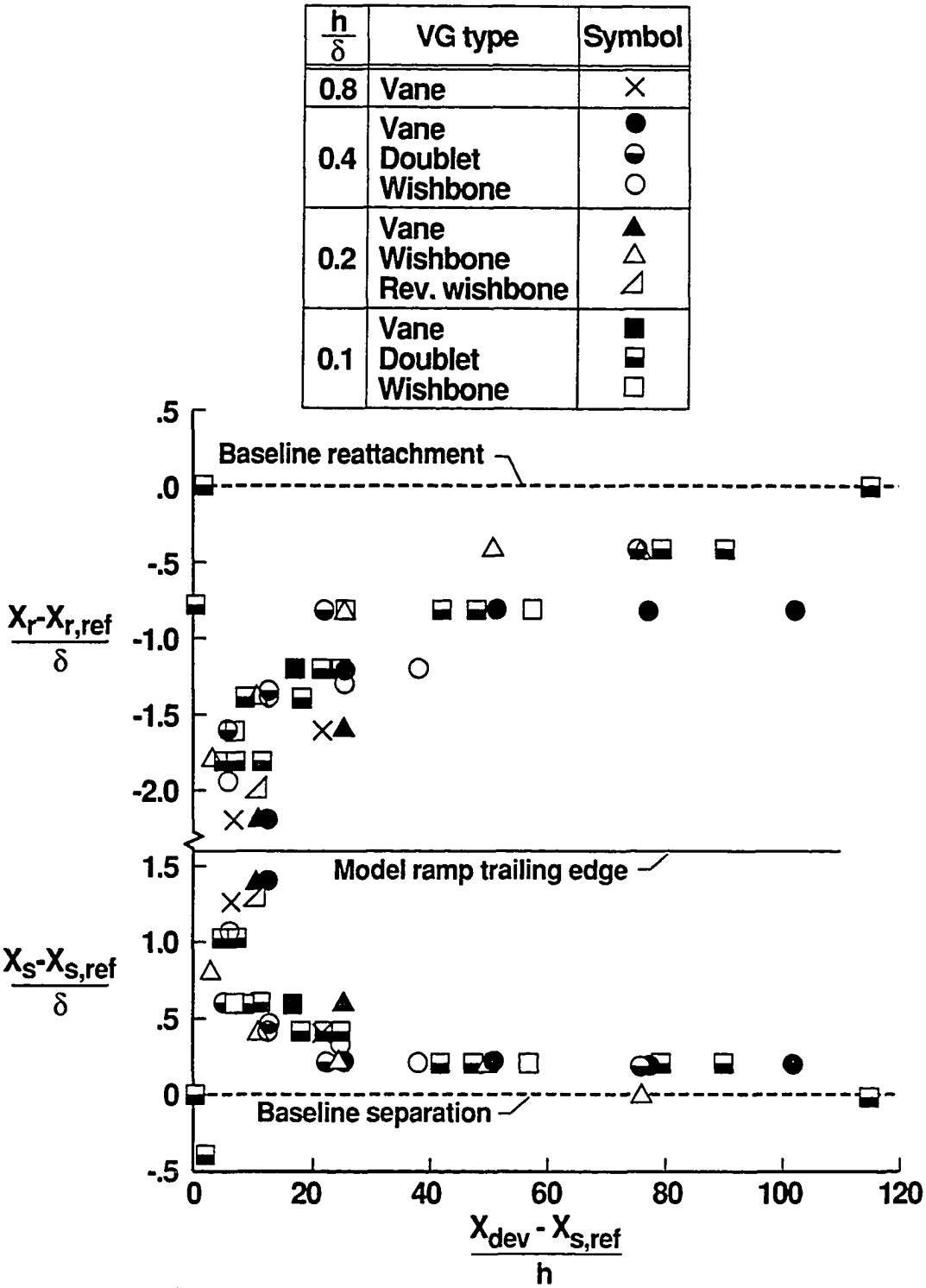

Figure 4.24 Effect of streamwise device location on separation control for all vortex generators.

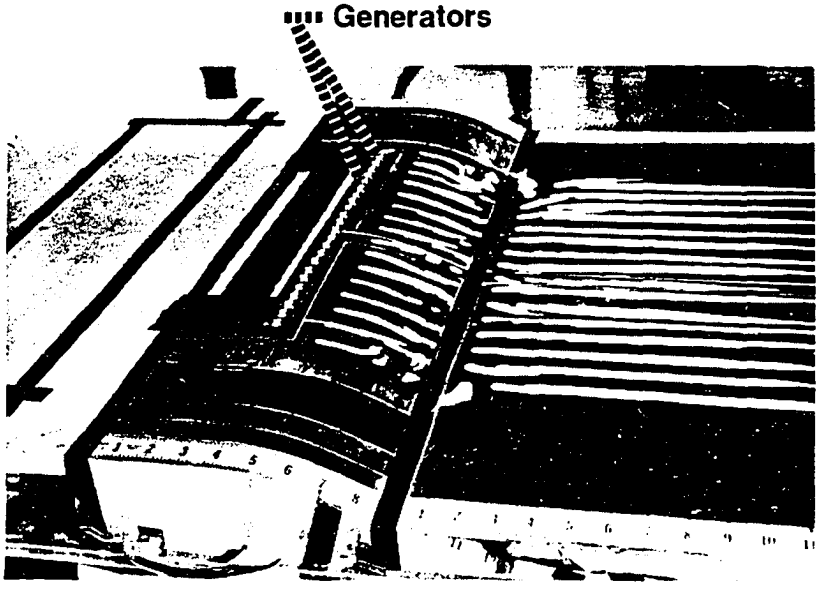

(a) 0.1δ high vane-type vortex generators.

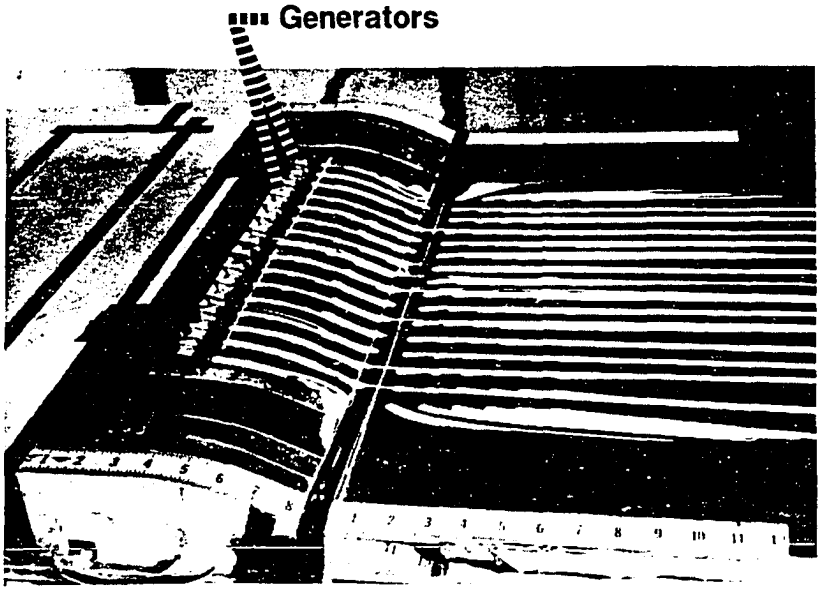

(b) 0.2δ high vane-type vortex generators.

Figure 4.25 Oil-flow visualizations showing the effect of device height for sub-δ-scale vane-type vortex generators at 2δ upstream of baseline separation.

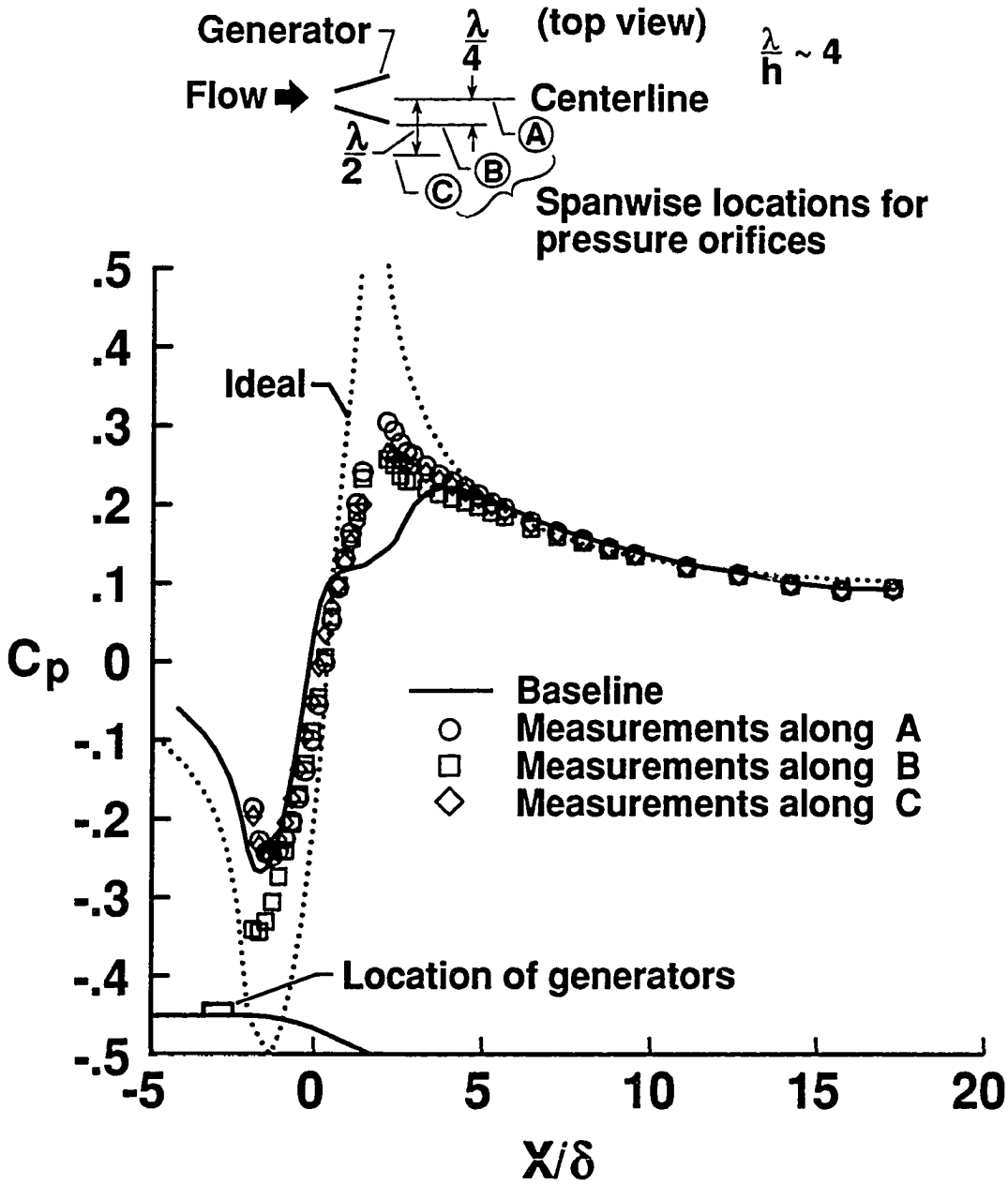

Figure 4.26 Spanwise variation of the streamwise pressure distribution for 0.2δ high counterrotating vortex generators placed at 2δ upstream of baseline separation.

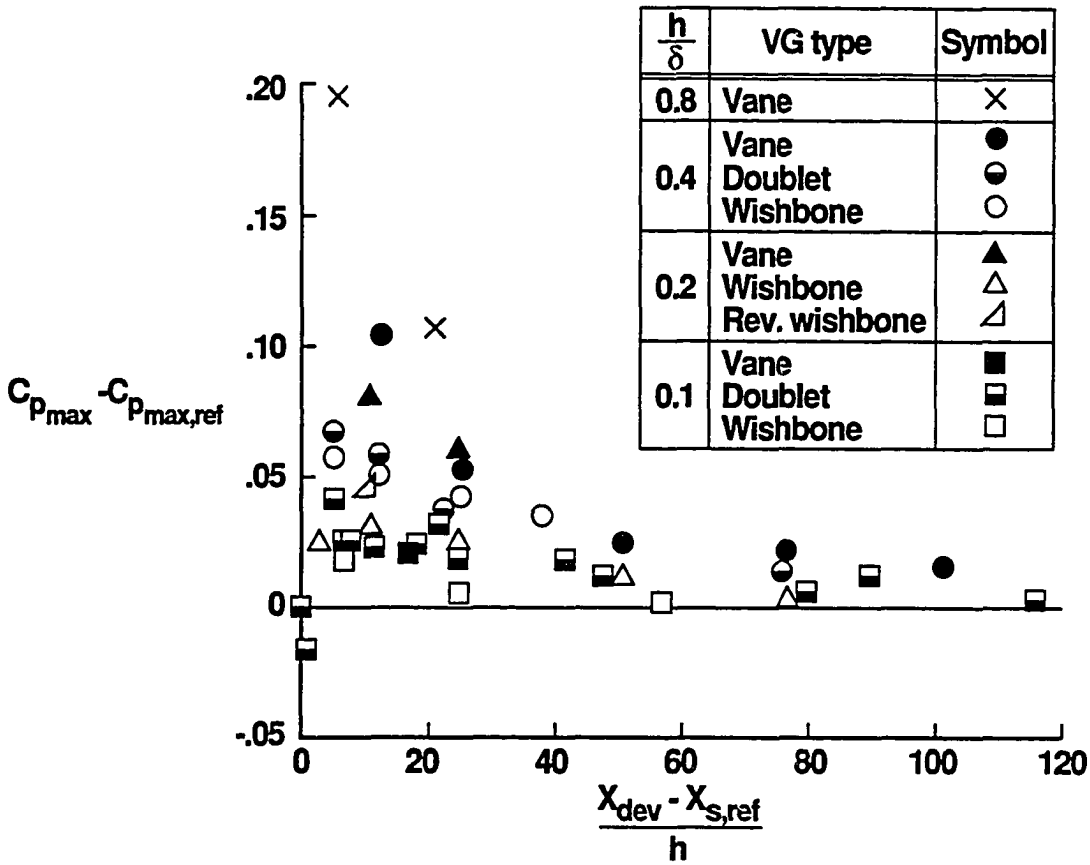

Figure 4.27 Effect of streamwise device location on maximum pressure recovery for all vortex generators.

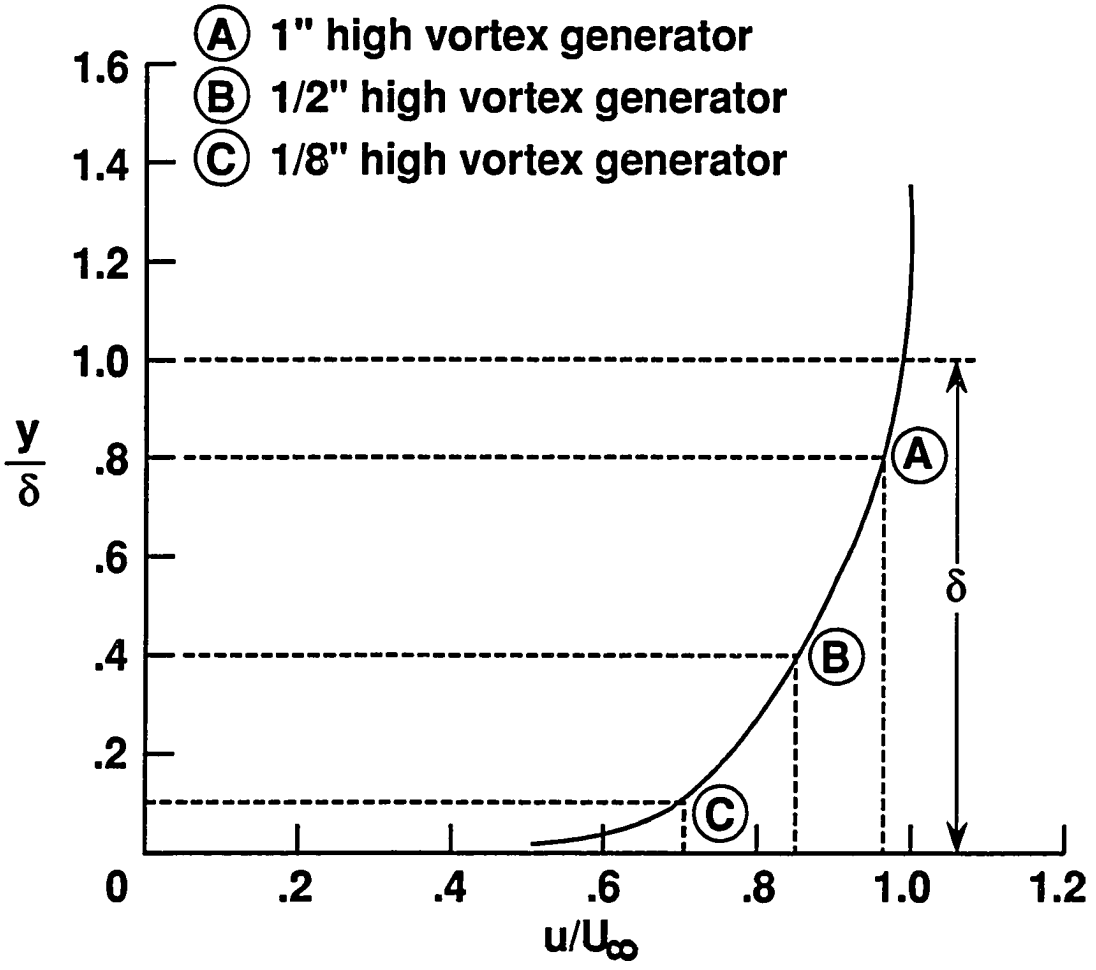

Figure 4.28 Location of vortex generator heights relative to the boundary-layer velocity profile.

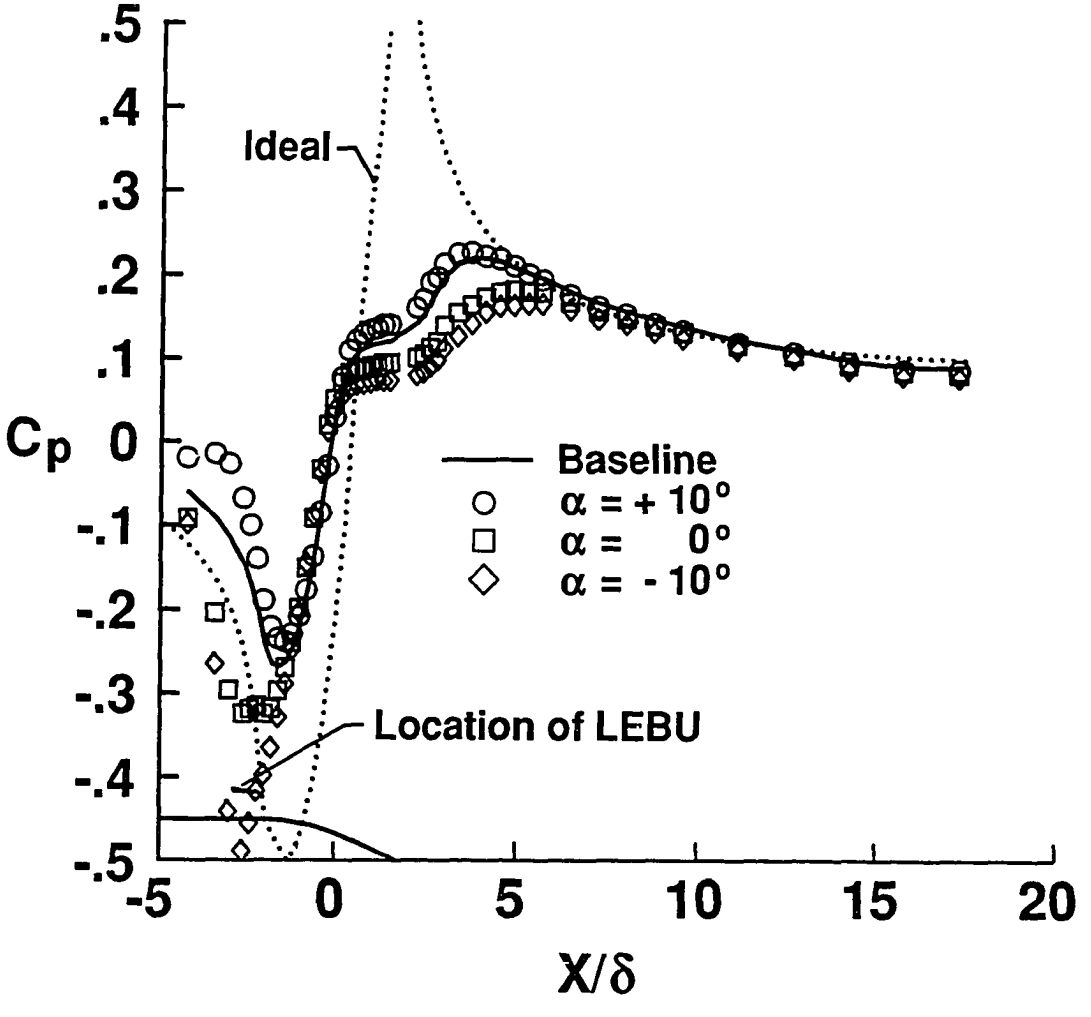

Figure 4.29 Effect of device angle of attack on streamwise pressure distribution for 1δ chord LEBU's at 2δ upstream of baseline separation and $h = 0.8\delta$.

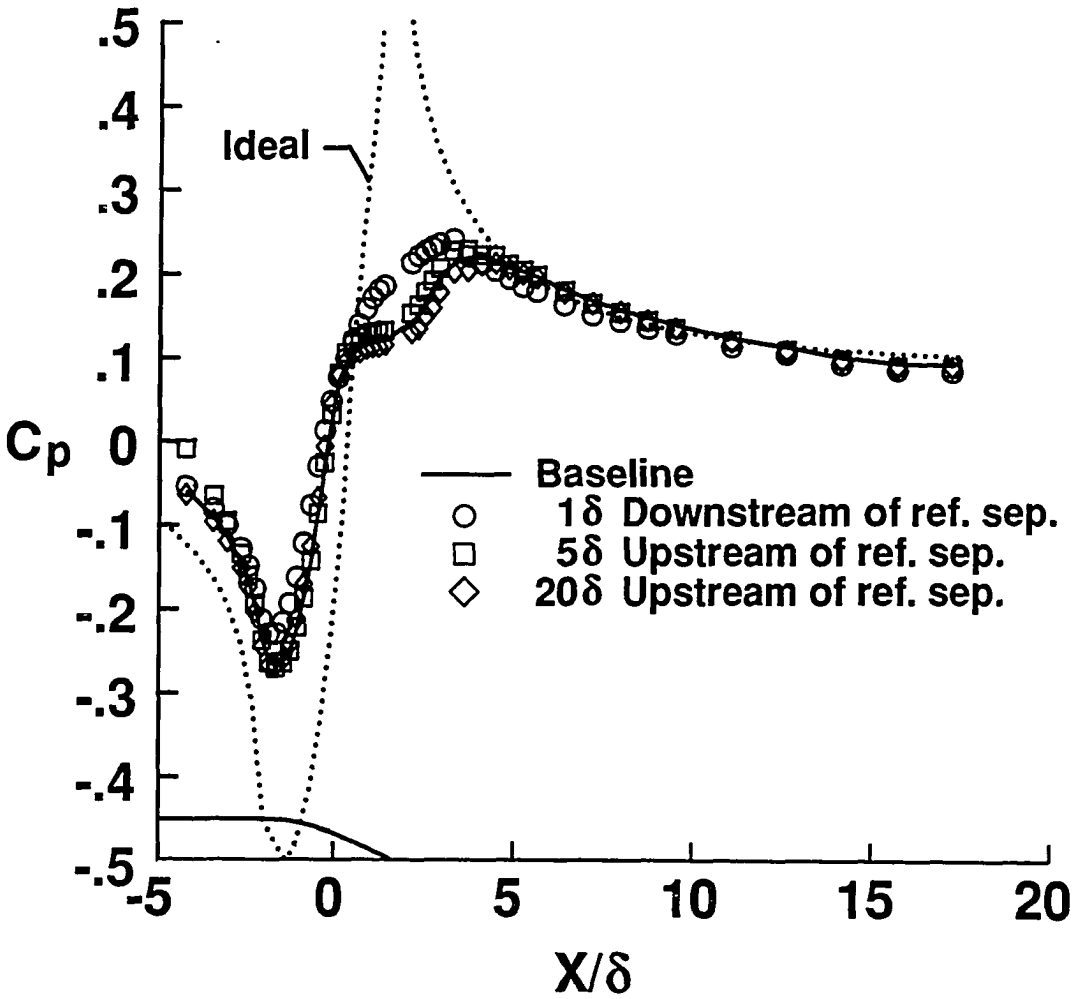

Figure 4.30 Effect of device location on streamwise pressure distribution for a 1δ chord LEBU at $h = 0.8\delta$ and $\alpha = 10°$.

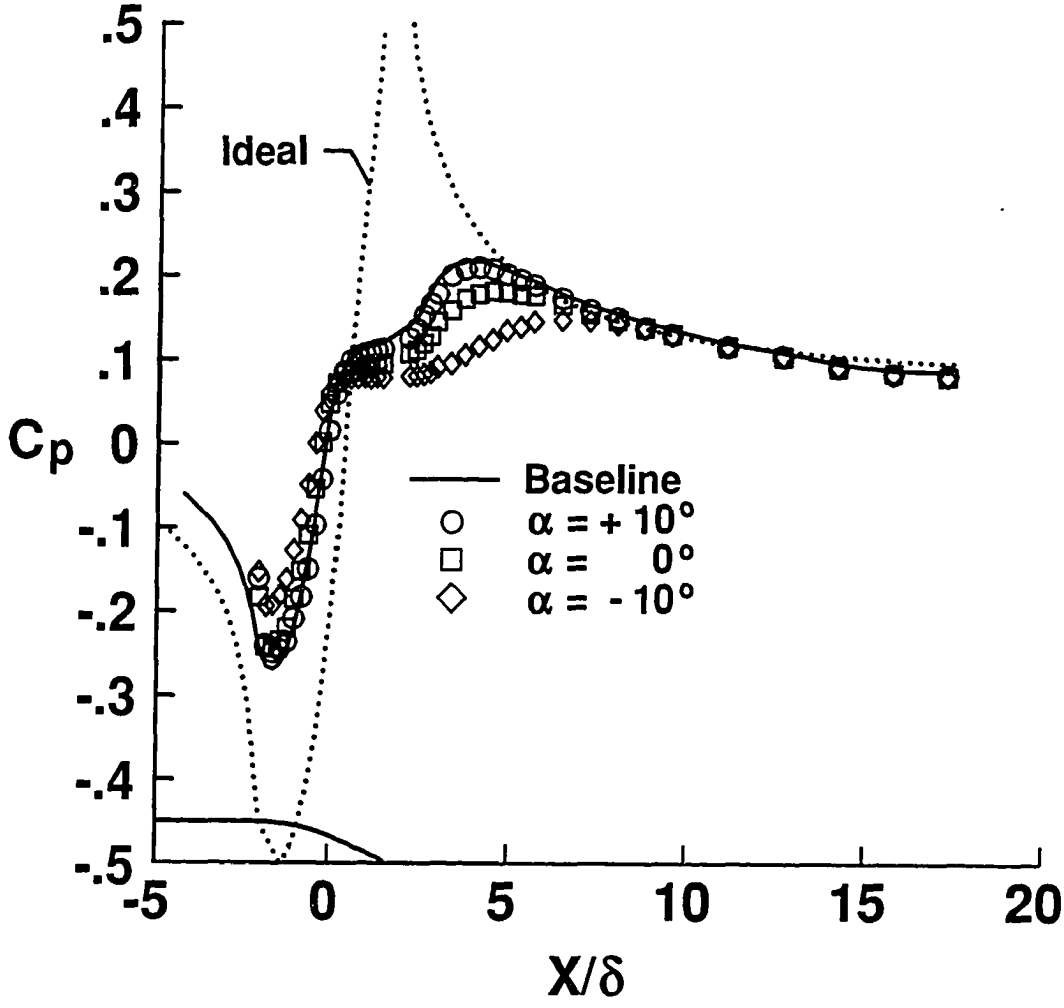

Figure 4.31 Effect of device angle of attack on streamwise pressure distribution for 1δ chord LEBU's at 5δ upstream of baseline separation and $h = 0.4\delta$.

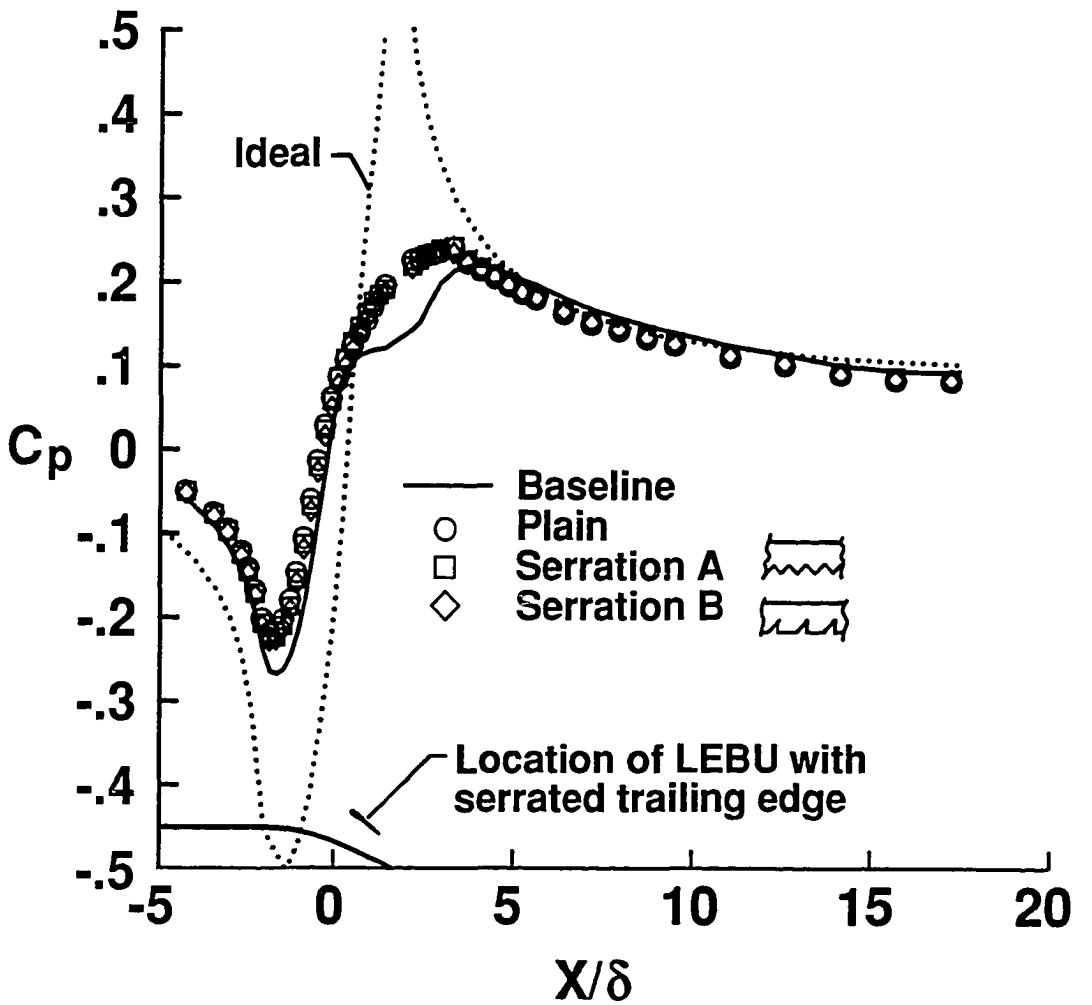

Figure 4.32 Effect of trailing-edge serrations on streamwise pressure distribution for 1δ chord LEBU's at baseline separation, $h = 0.8\delta$, and $\alpha = 10°$.

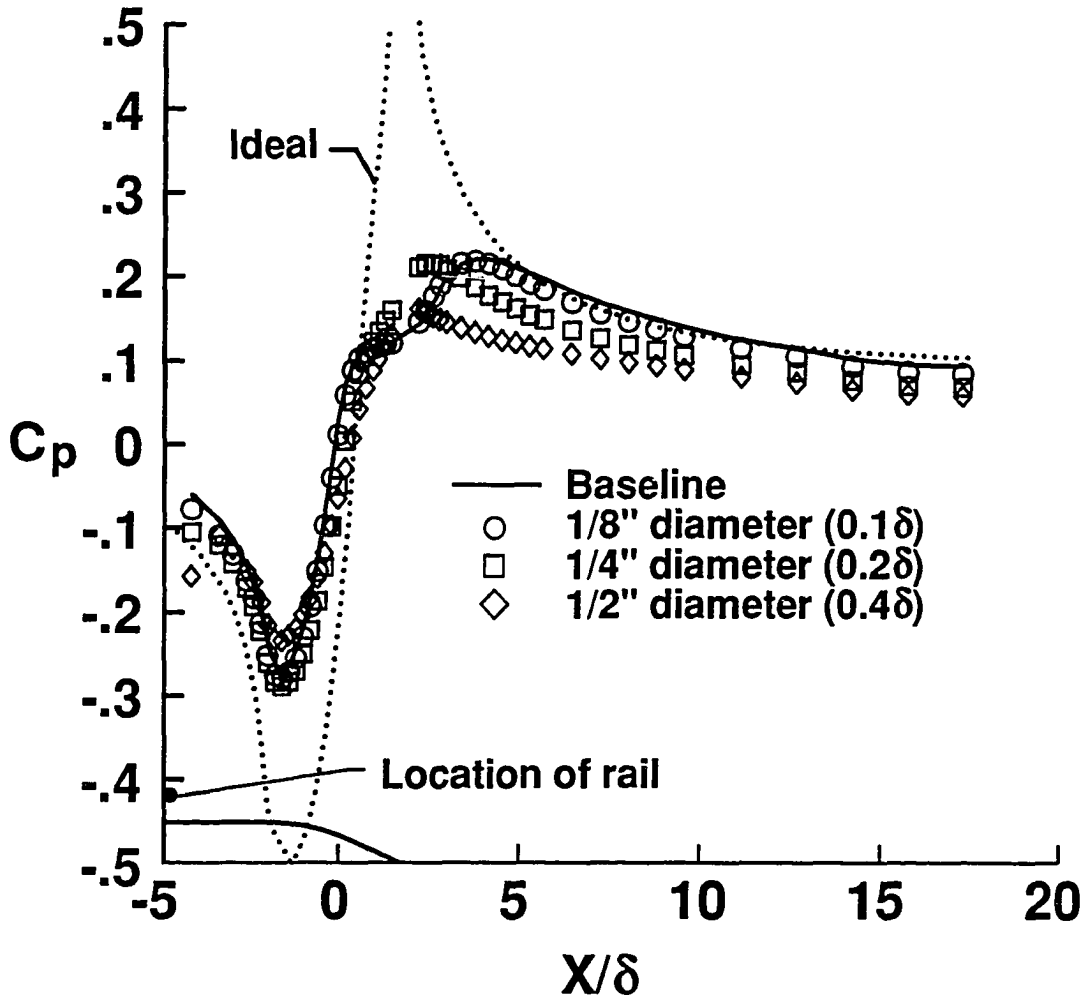

Figure 4.33 Effect of device diameter on streamwise pressure distribution for spanwise cylinders at 5δ upstream of baseline separation and $h = 0.8\delta$.

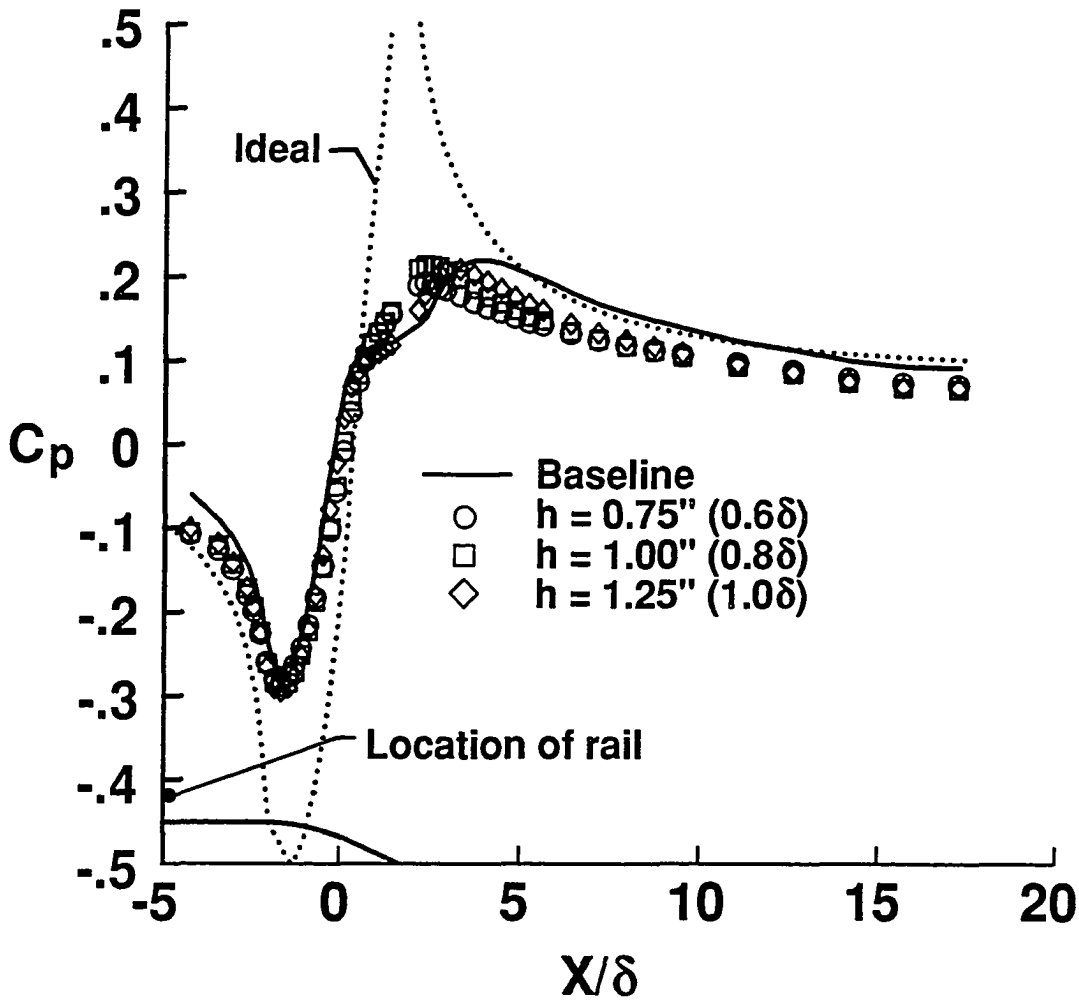

Figure 4.34 Effect of device height on streamwise pressure distribution for a spanwise cylinder at 5δ upstream of baseline separation and $\bar{d} = 0.2\delta$.

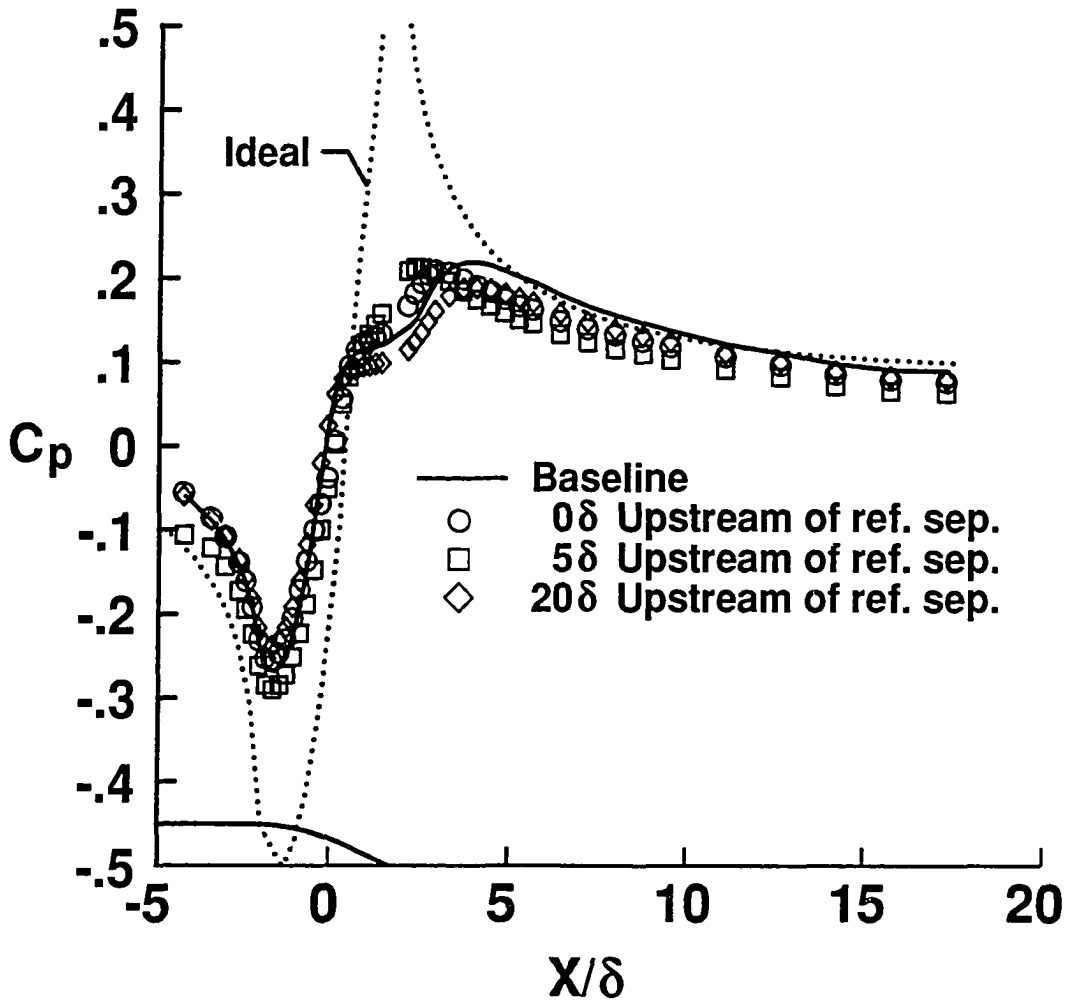

Figure 4.35 Effect of device location on streamwise pressure distribution for a spanwise cylinder at $h = 0.8\delta$ and $d = 0.2\delta$.

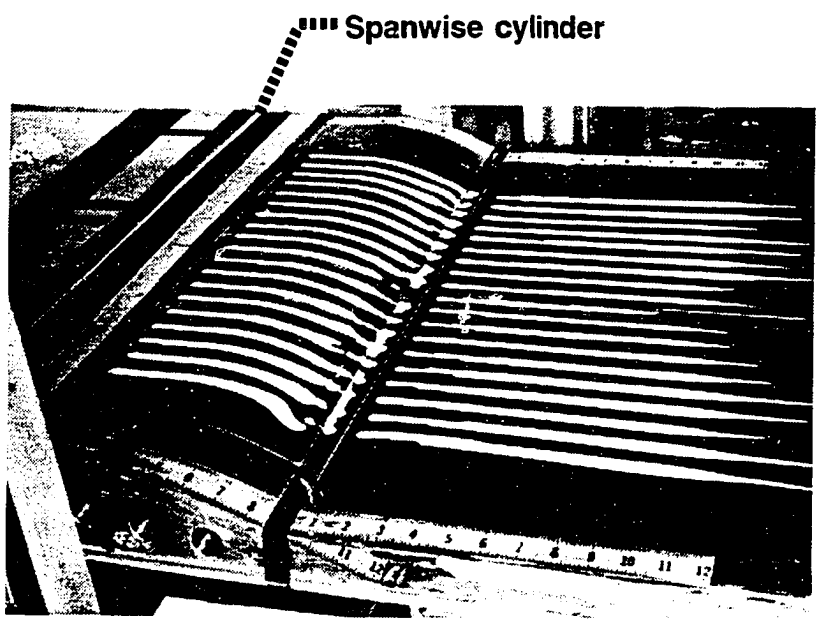

Figure 4.36 Oil-flow visualization for a spanwise cylinder at $h = 0.8\delta$, $d = 0.2\delta$, and 5δ upstream of baseline separation.

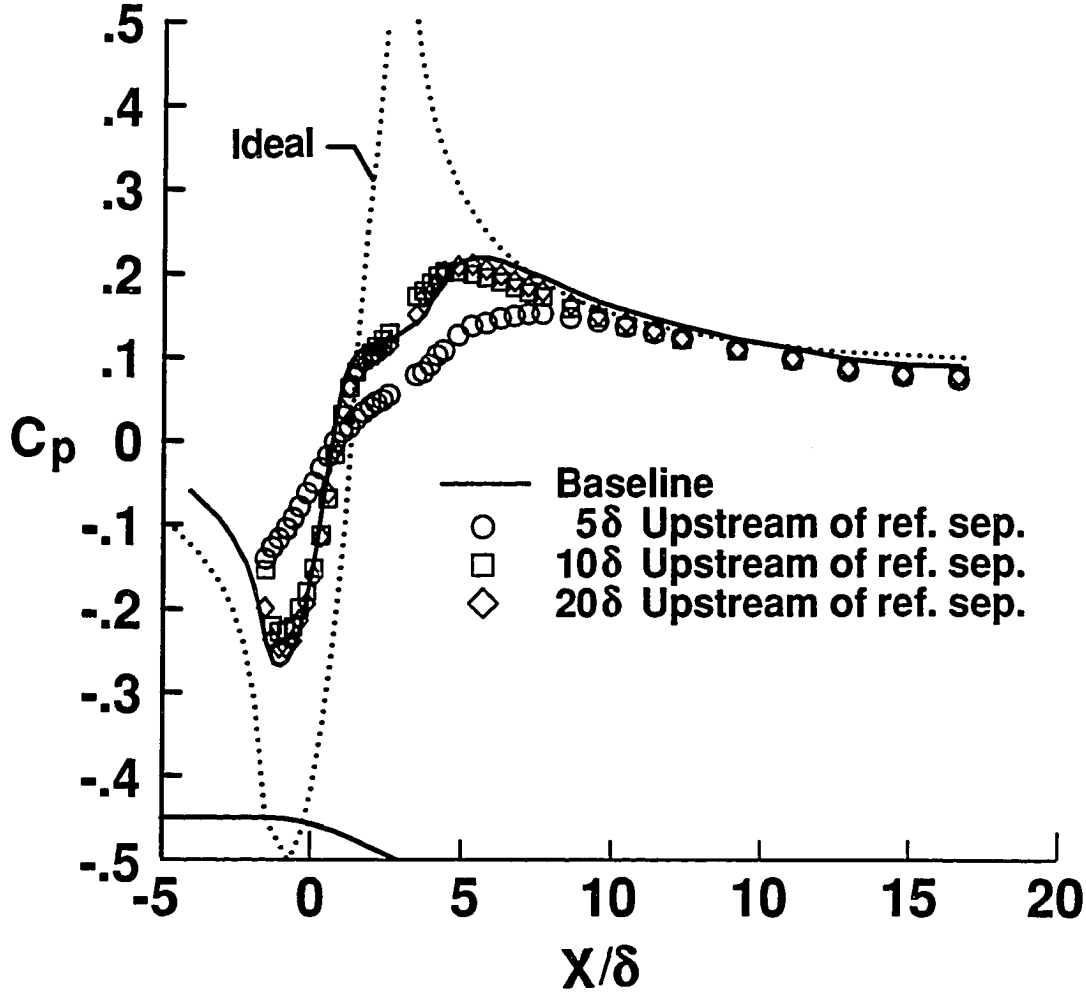

Figure 4.37 Effect of device location on streamwise pressure distribution for a spanwise cylinder with $d = 0.2\delta$ and $h = 0.1\delta$.

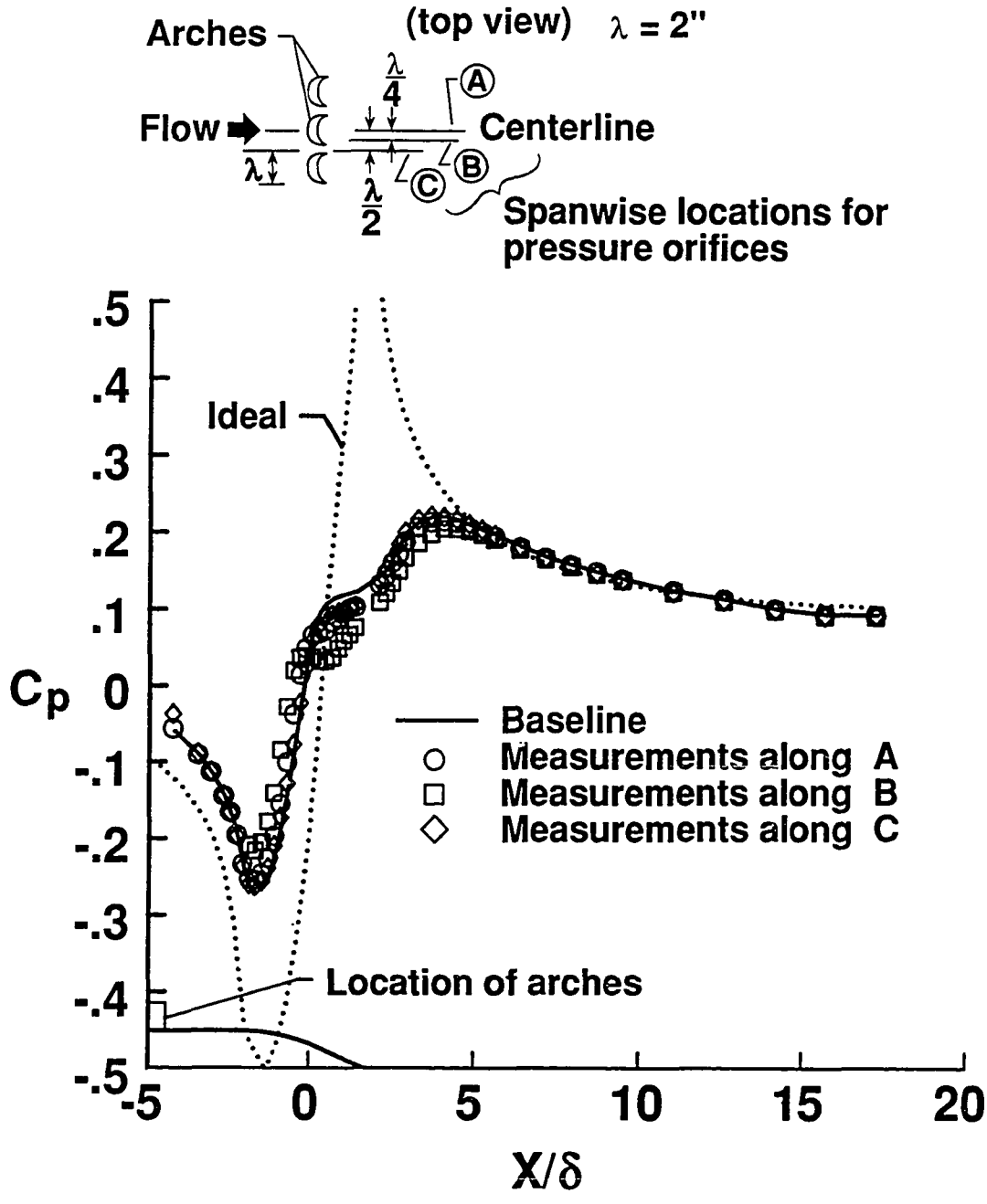

Figure 4.38 Spanwise variation of the steamwise pressure distribution for arches (model No. 2) at 5δ upstream of baseline separation.

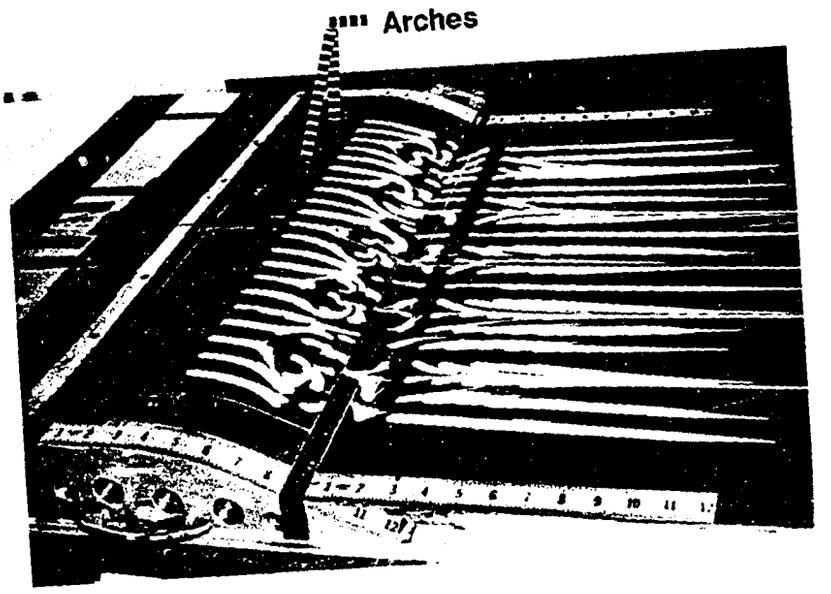

(a) Arches at 2δ upstream of baseline separation.

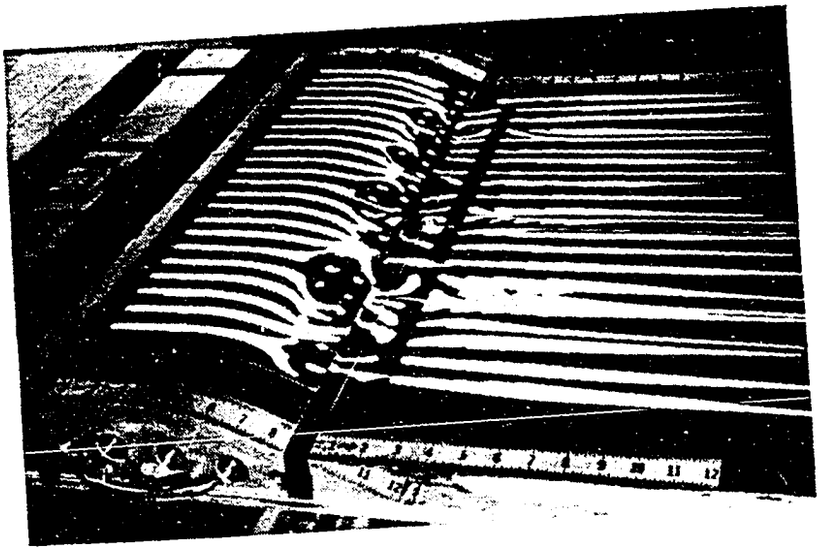

(b) Arches at 40δ upstream of baseline separation.

Figure 4.39 Oil-flow visualizations for arches (model No. 4).

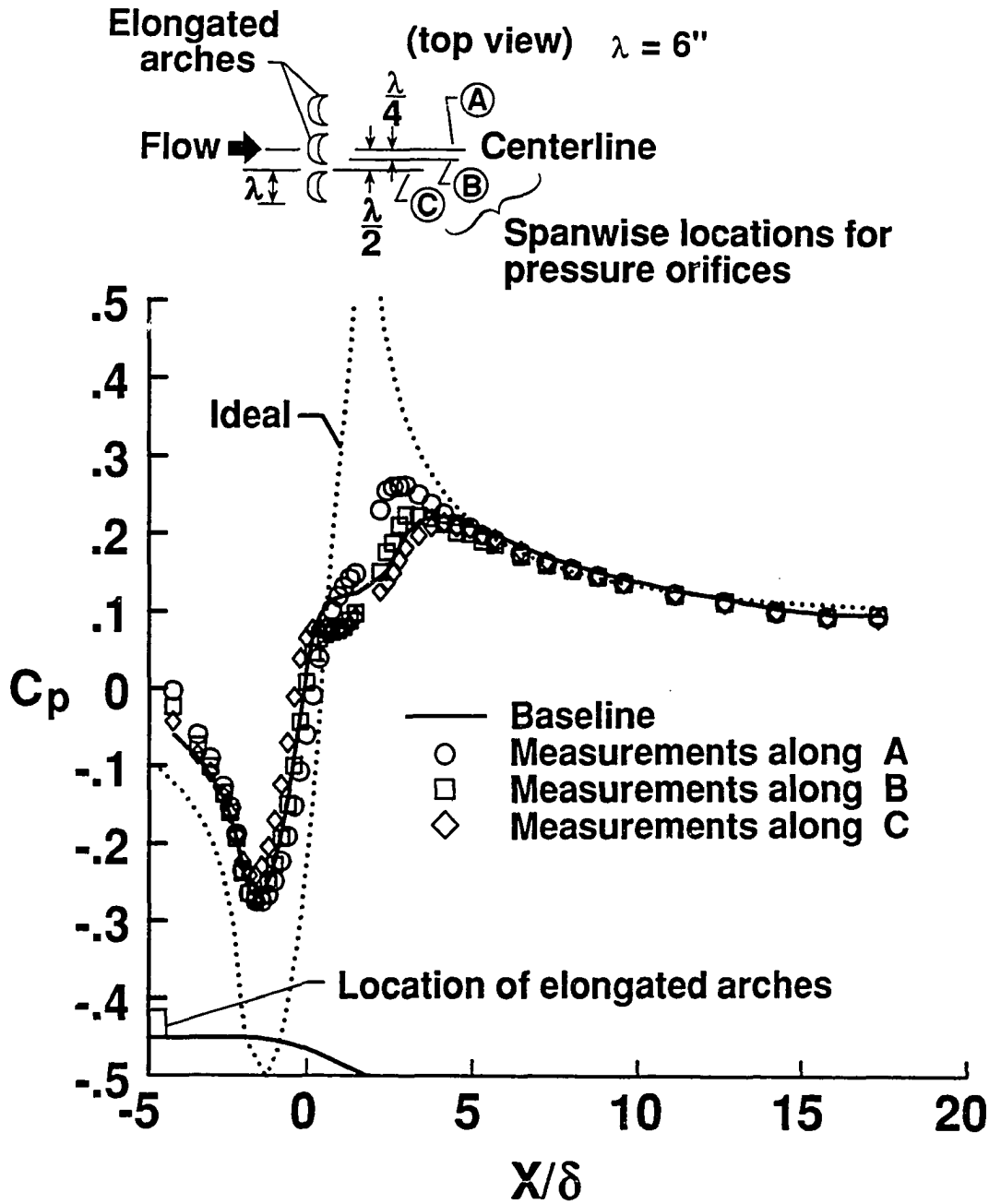

Figure 4.40 Spanwise variation of the streamwise pressure distribution for elongated arches (model No. 6) at 5δ upstream of baseline separation.

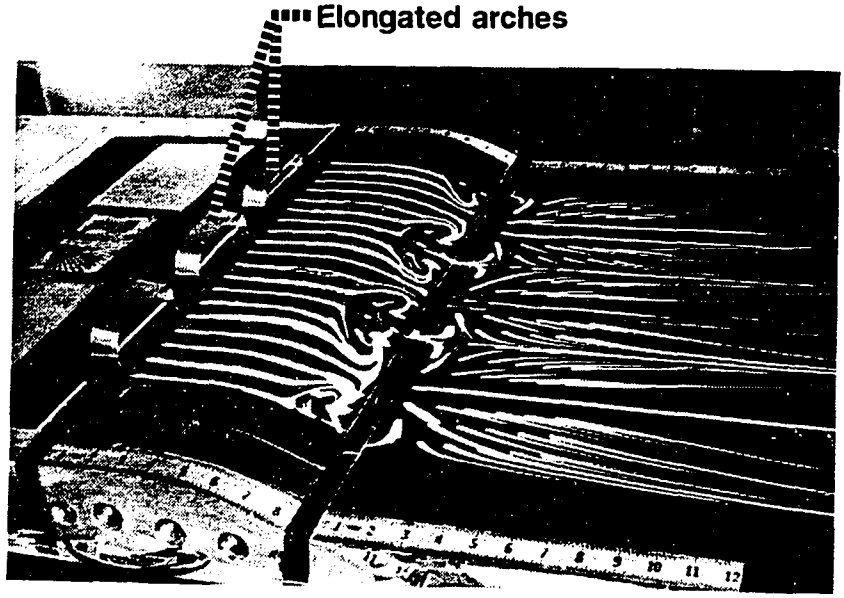

(a) Arches at 5δ upstream of baseline separation.

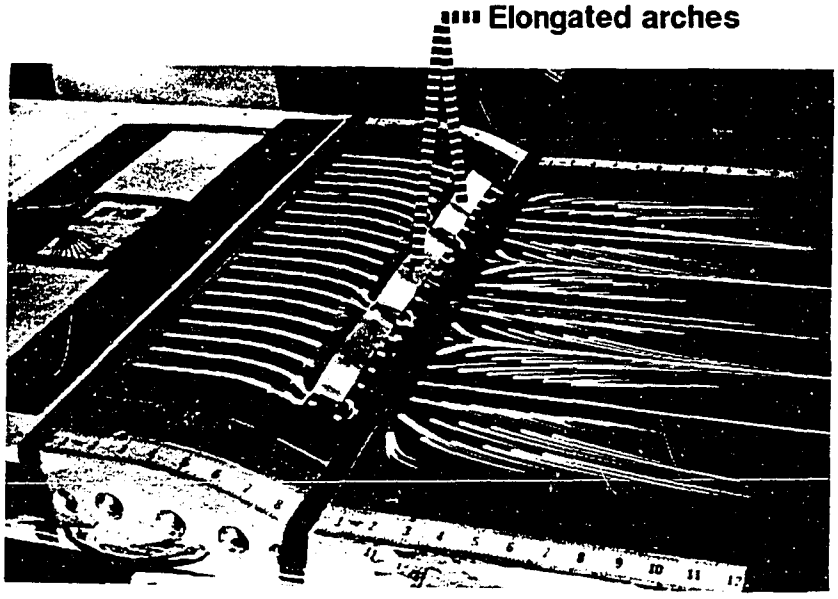

(b) Arches at 1δ downstream of baseline separation.

Figure 4.41 Oil-flow visualizations for elongated arches (model No. 6).

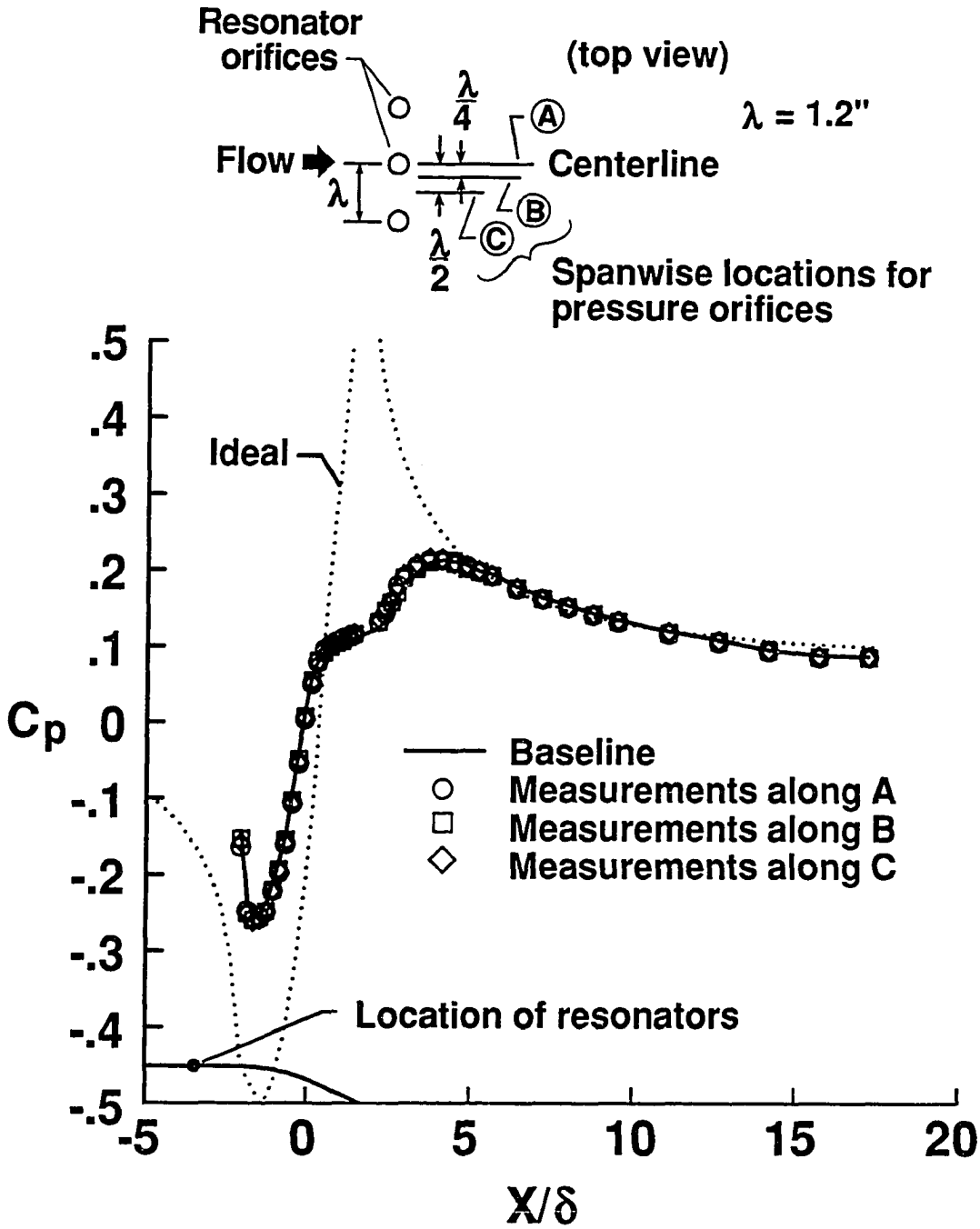

Figure 4.42 Spanwise variation of the streamwise pressure distribution for Helmholtz resonators at 3.5δ upstream of baseline separation and $D_o = 0.5$ in.

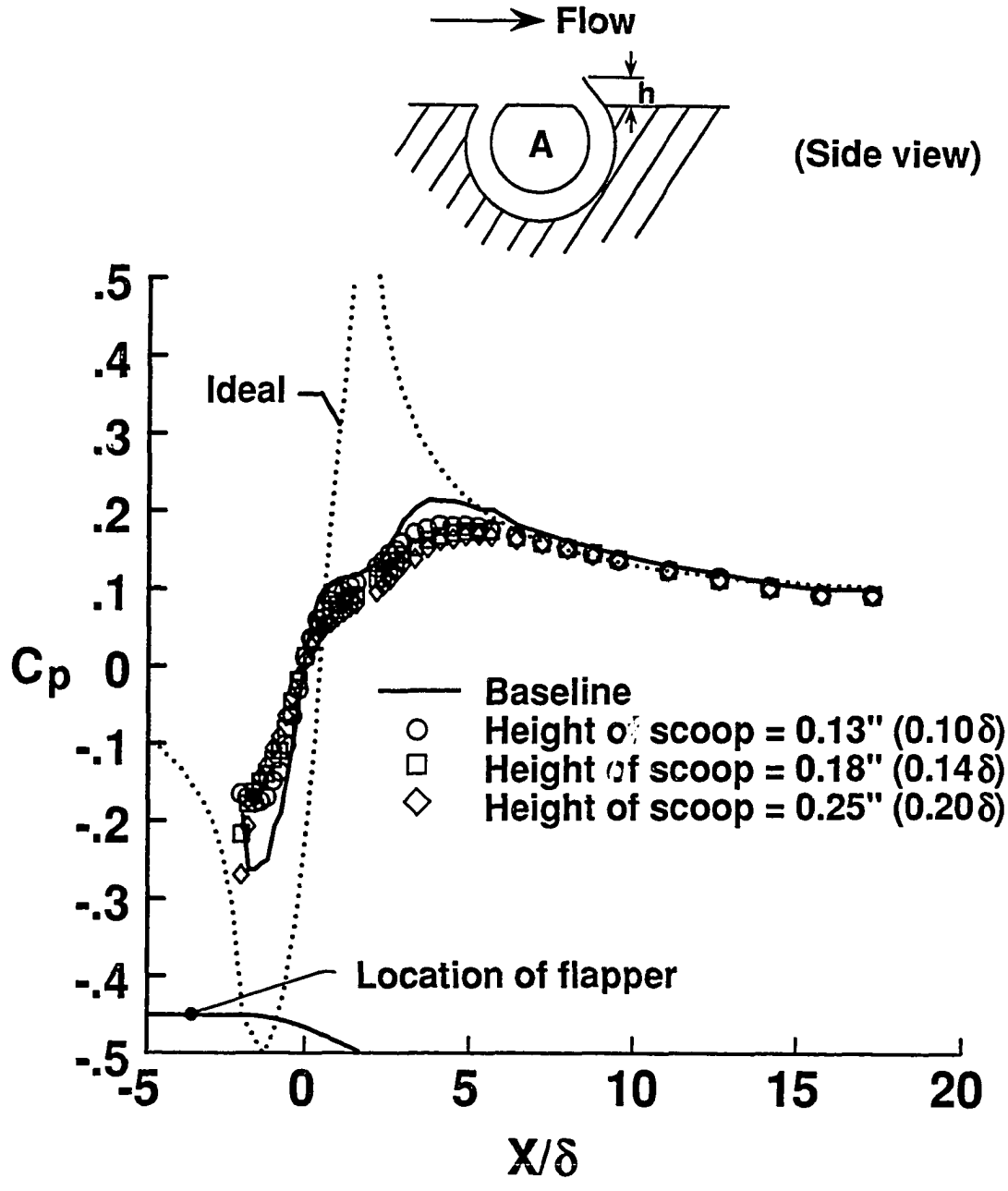

Figure 4.43 Effect of scoop height on streamwise pressure distribution for Viets' flapper model A at 3δ upstream of baseline separation.

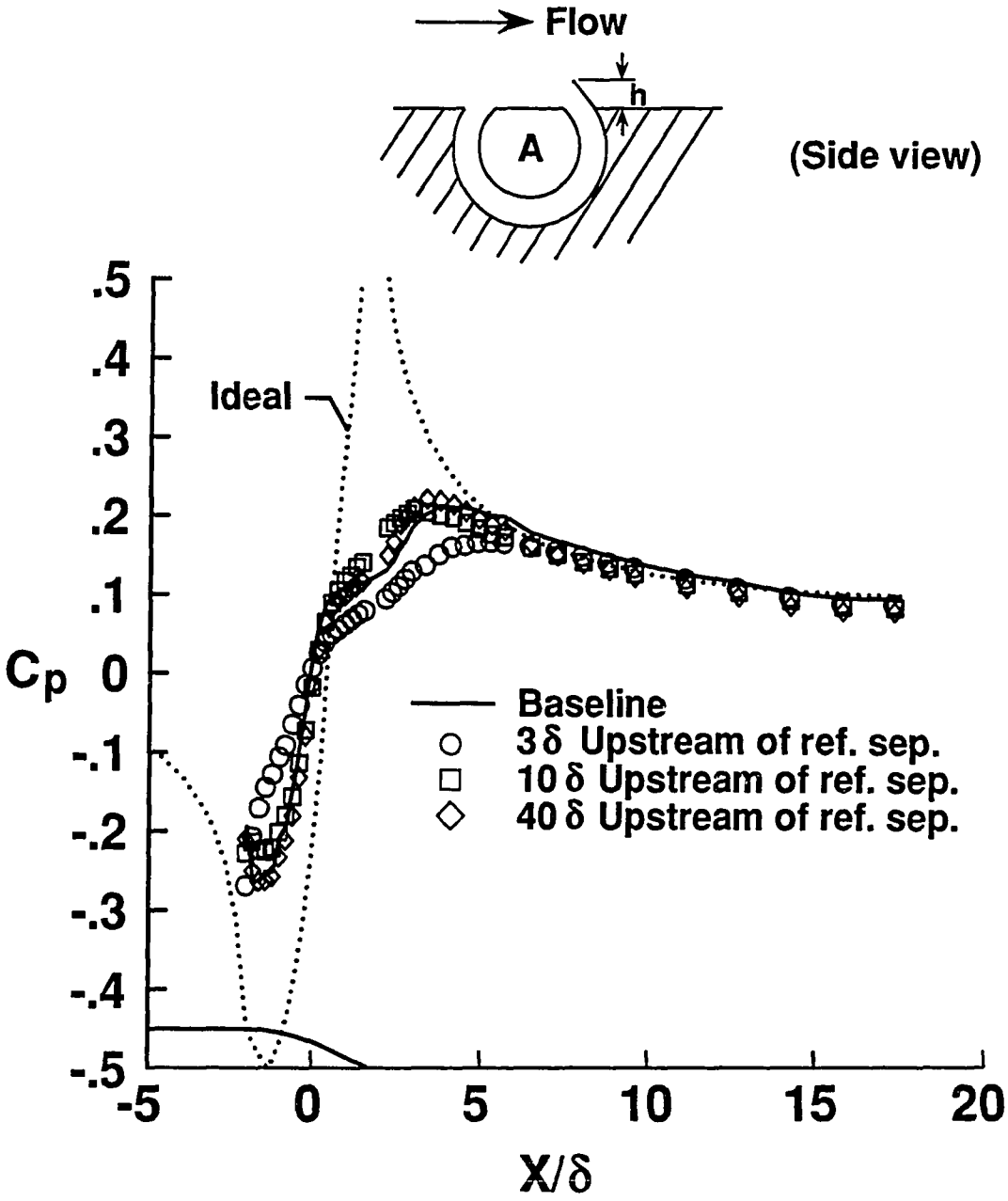

Figure 4.44 Effect of device location on streamwise pressure distribution for Viets' flapper model A with a scoop height of 0.2δ.

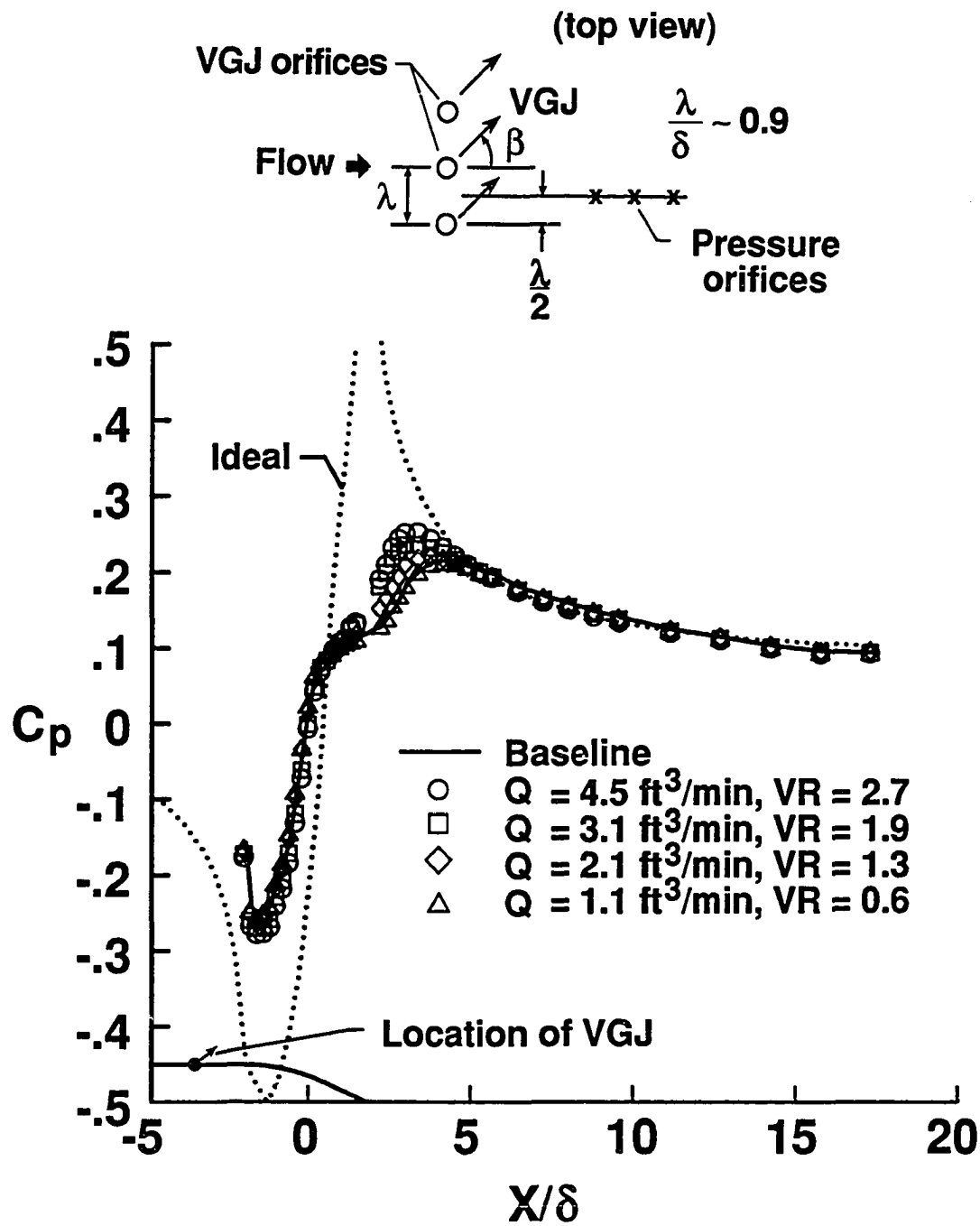

Figure 4.45 Effect of volumetric flow rate and/or velocity ratio on streamwise pressure distribution for VGJ's with $D_o = 1/16$ in., $\alpha = 45°$, and $\beta = 90°$.

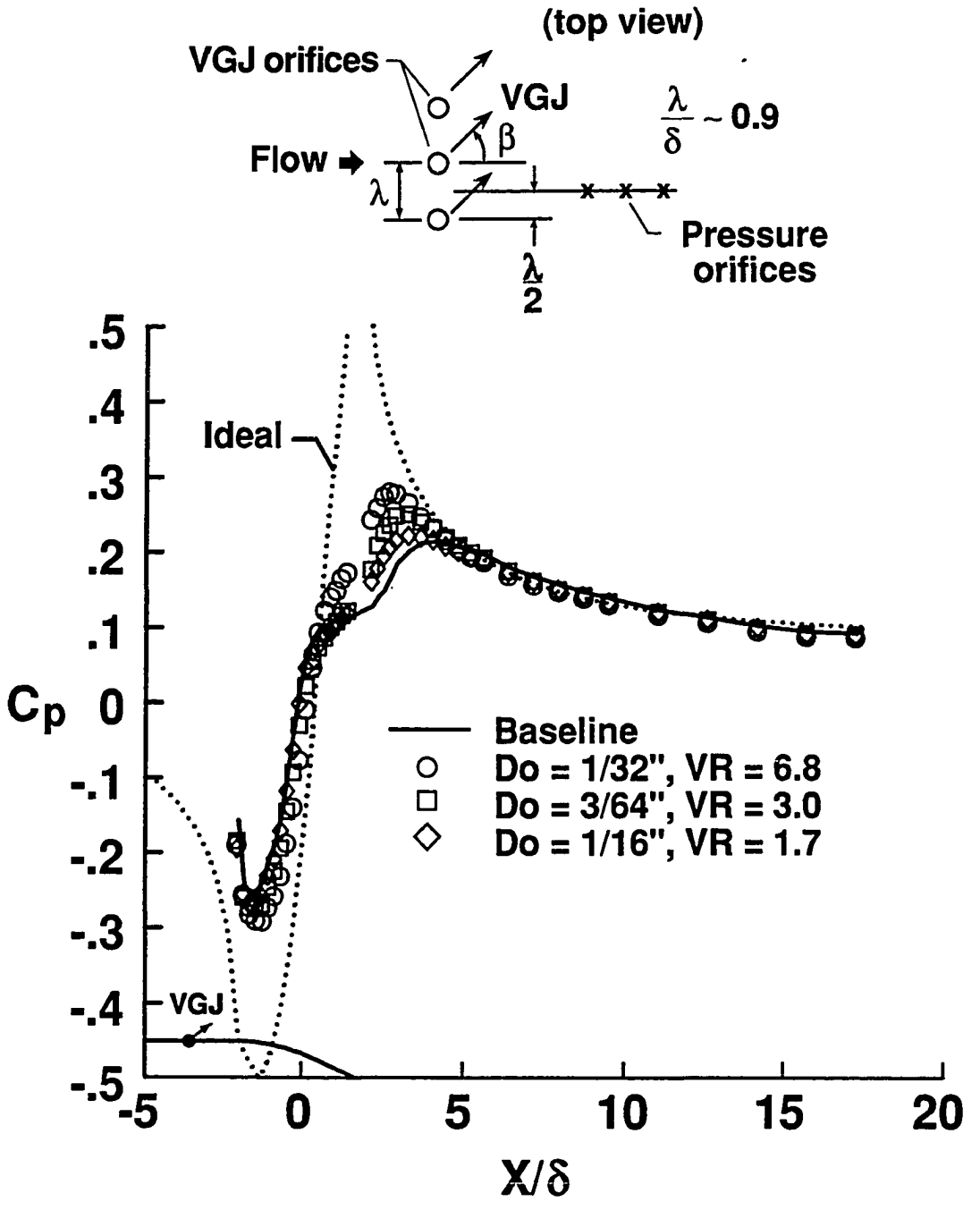

Figure 4.46 Effect of orifice diameter and/or velocity ratio on streamwise pressure distribution for VGJ's with Q = 2.9 ft^3/min., $\alpha = 45°$, and $\beta = 90°$.

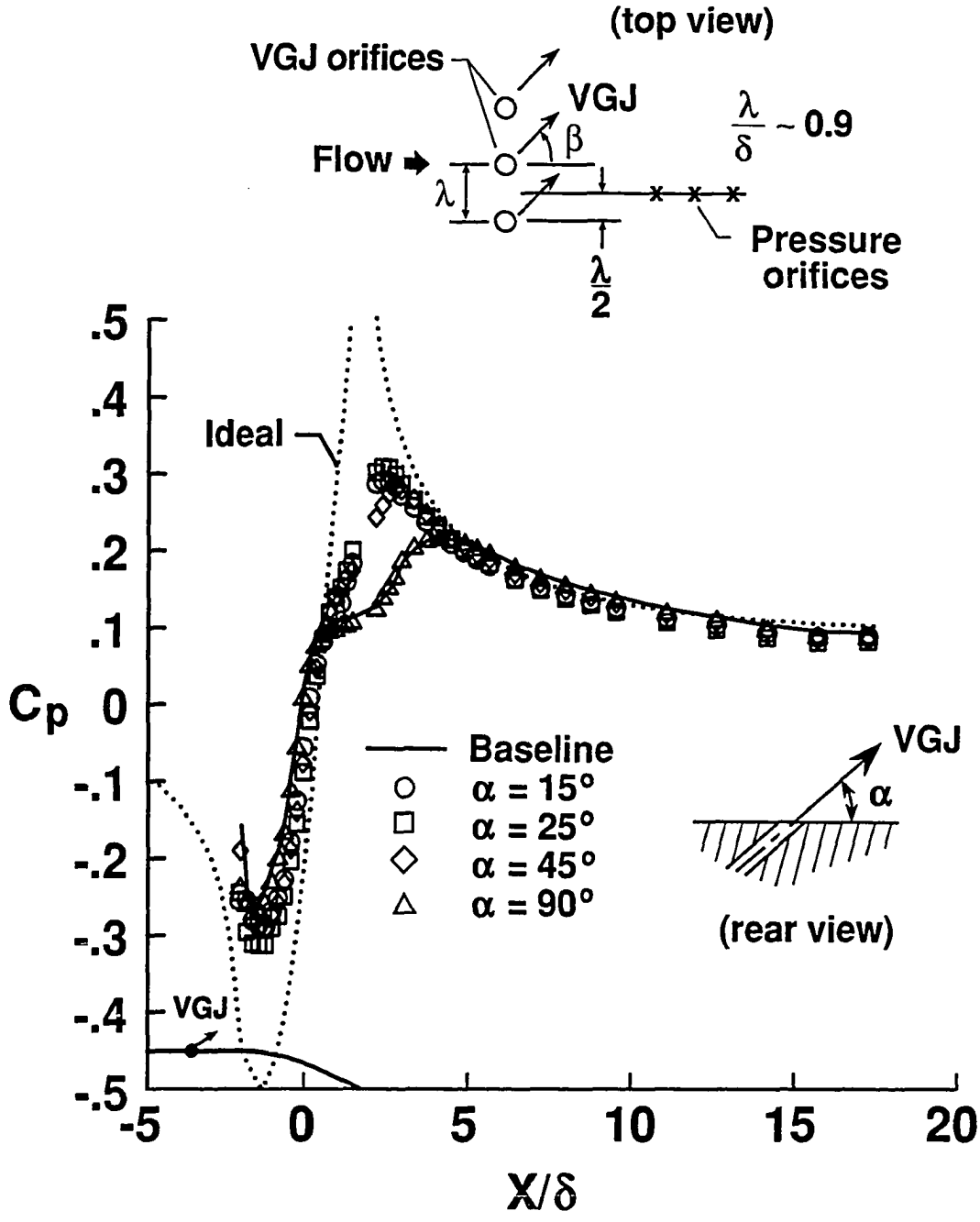

Figure 4.47 Effect of jet inclination angle on streamwise pressure distribution for VGJ's with $D_o = 1/32$ in., VR = 6.8, and $\beta = 90°$.

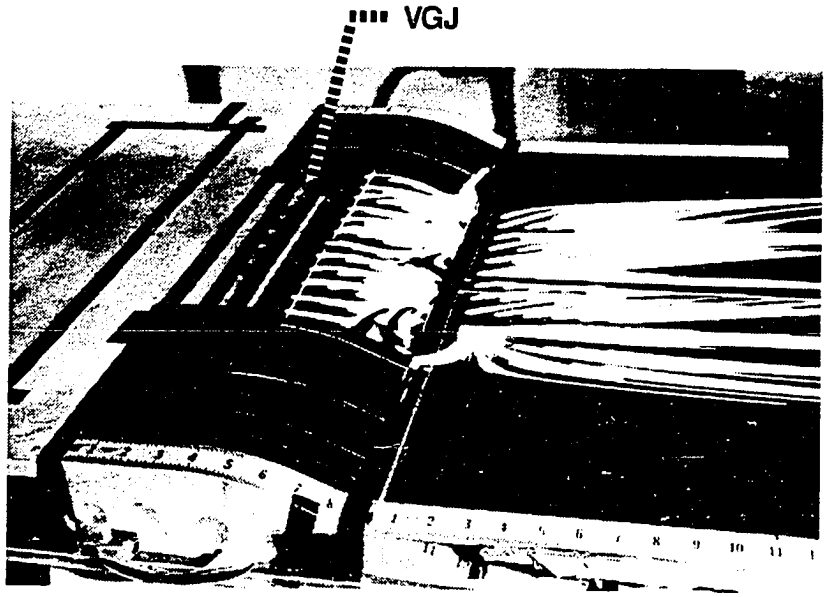

(a) $\alpha = 15°$.

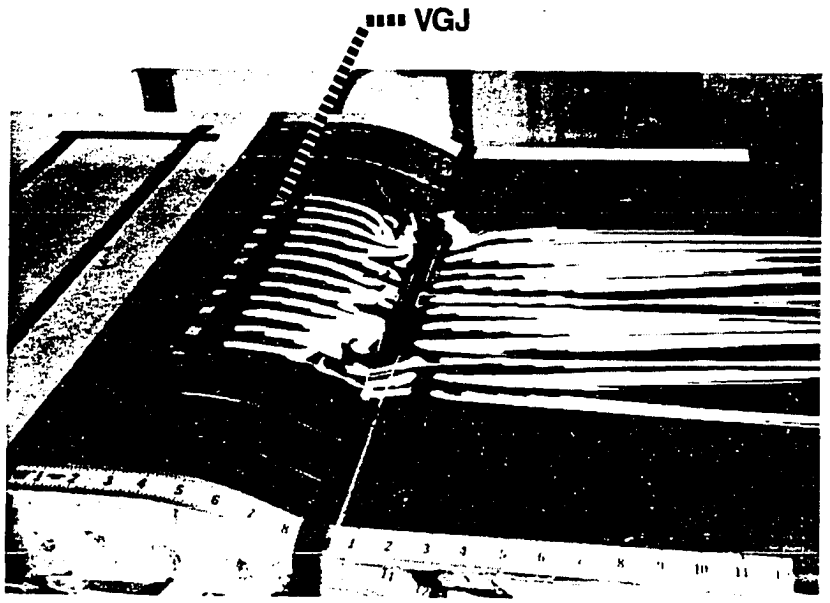

(b) $\alpha = 45°$.

Figure 4.48 Oil-flow visualizations for VGJ's with $D_o = 1/32$ in., VR = 6.8, and $\beta = 90°$.

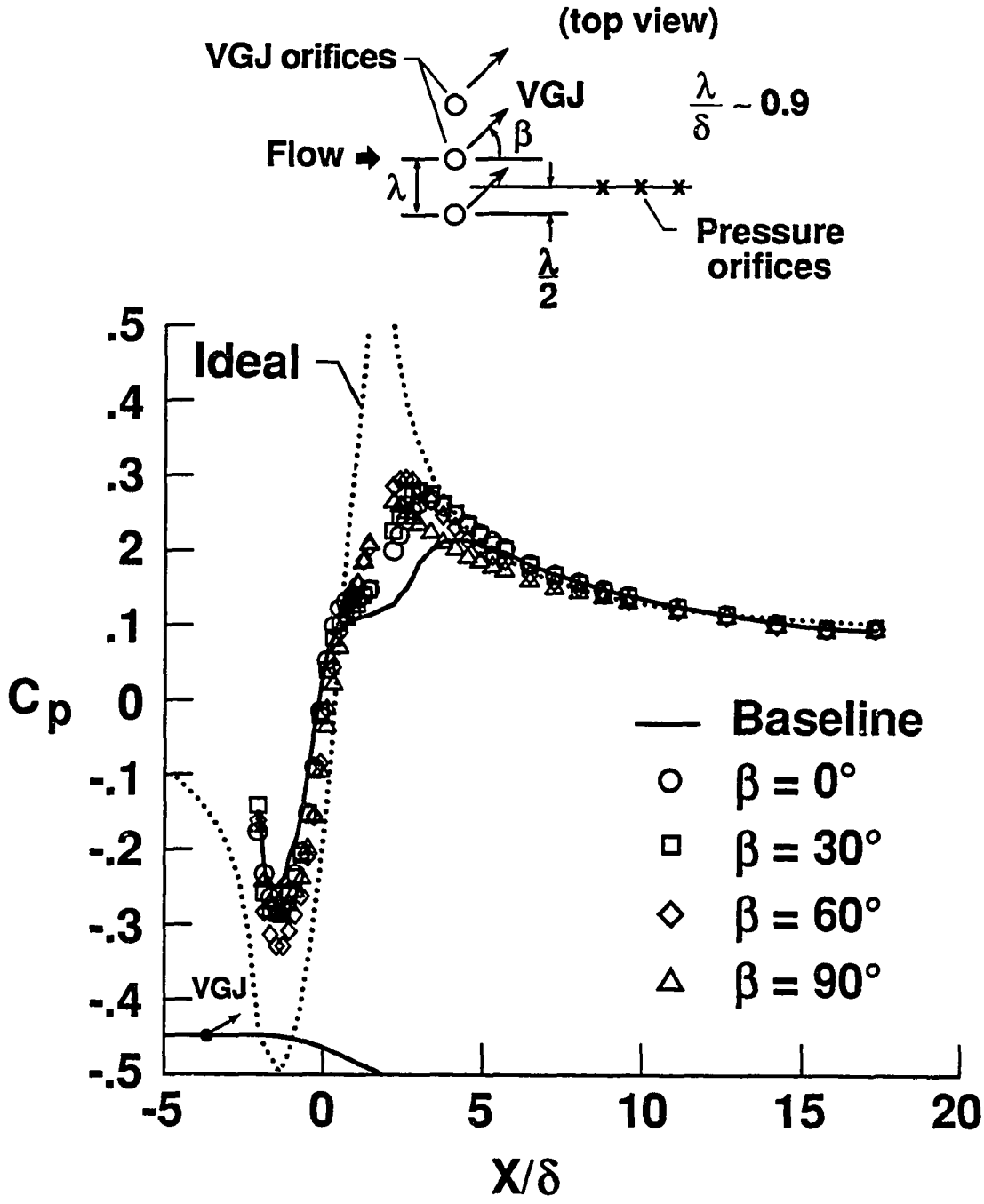

(a) $\alpha = 15°$.

Figure 4.49 Effect of jet azimuthal angle on streamwise pressure distribution for VGJ's with $D_o = 1/32$ in. and VR = 6.8.

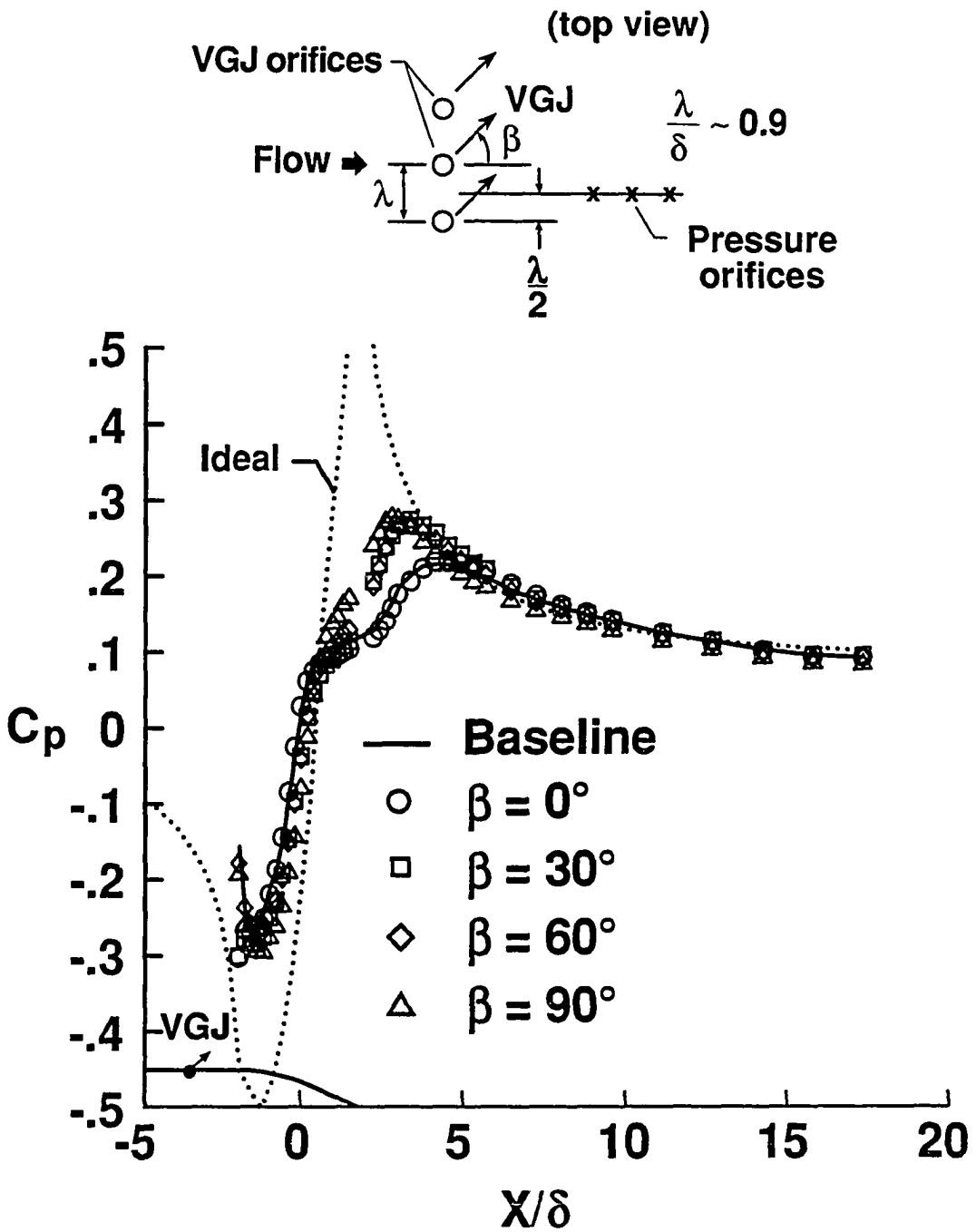

(b) $\alpha = 45°$.

Figure 4.49 Concluded.

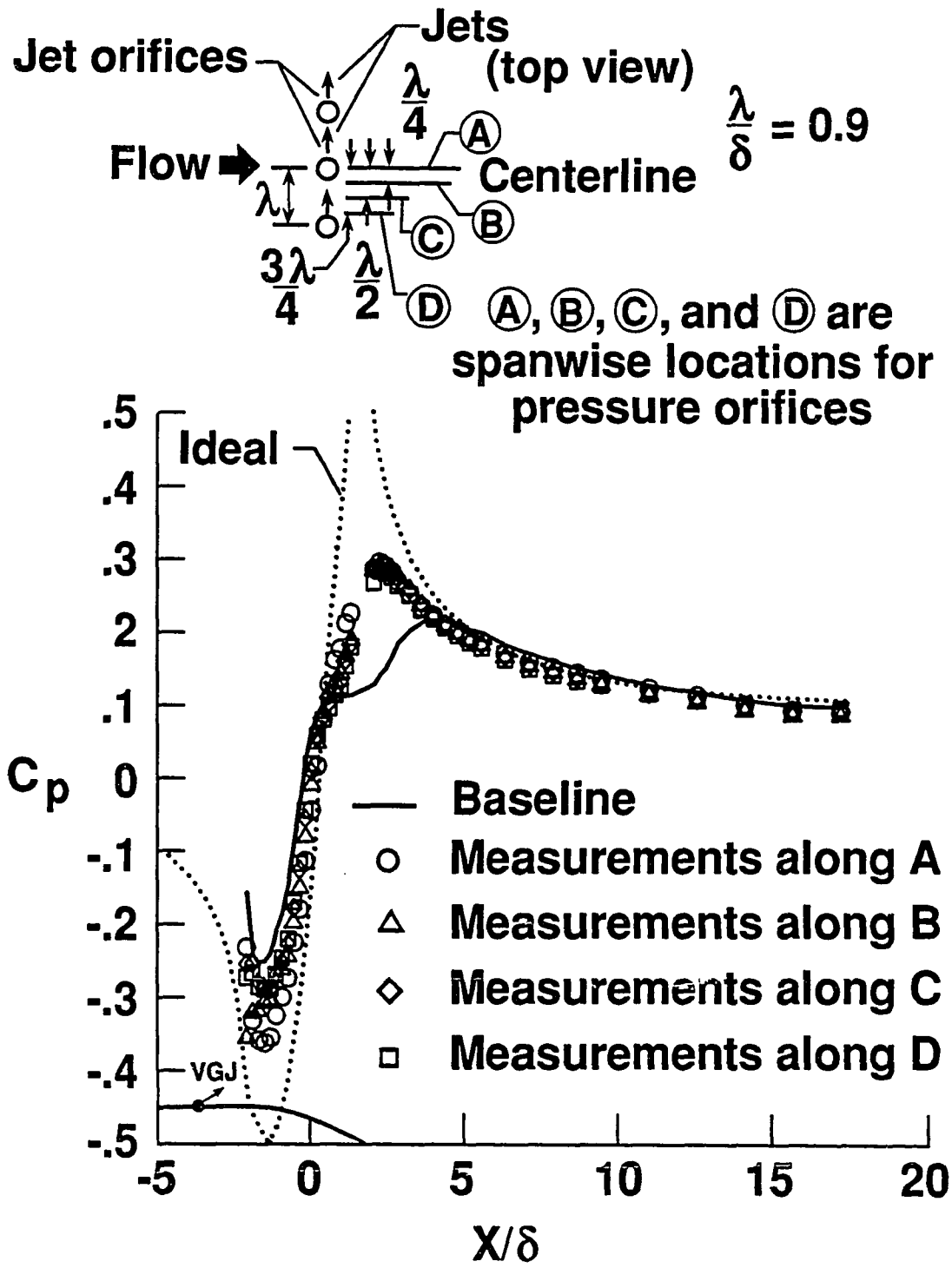

Figure 4.50 Spanwise variation of the streamwise pressure distribution for co-rotating VGJ's with $D_o = 1/32$ in., VR = 6.8, $\alpha = 15°$, and $\beta = 90°$.

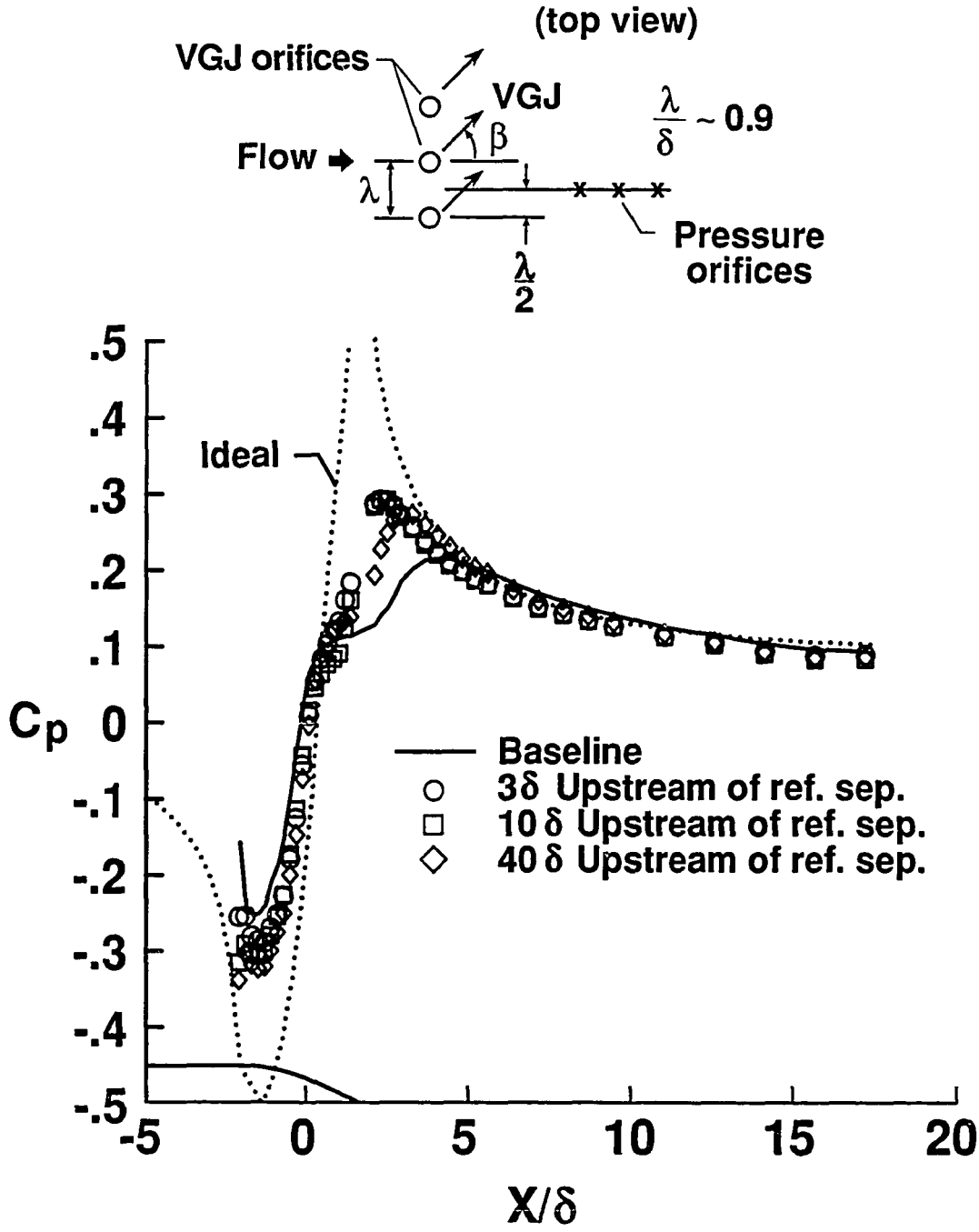

Figure 4.51 Effect of device location on streamwise pressure distribution for VGJ's with $D_o = 1/32$ in., VR = 6.8, $\alpha = 15°$, and $\beta = 90°$.

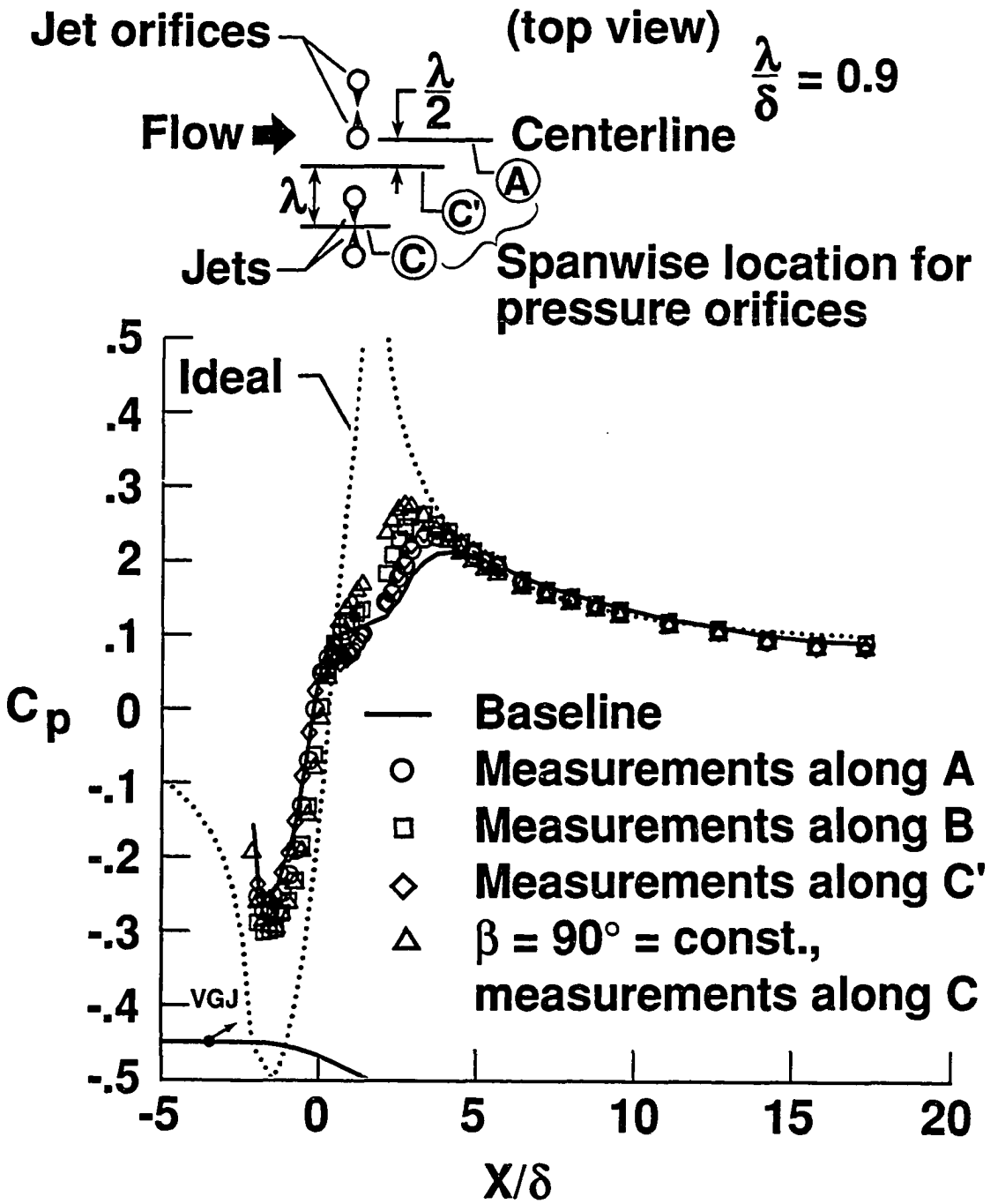

Figure 4.52 Spanwise variation of the streamwise pressure distribution for counterrotating VGJ's with $D_o = 1/32$ in., VR = 6.8, $\alpha = 45°$, and $\beta = \pm 90°$.

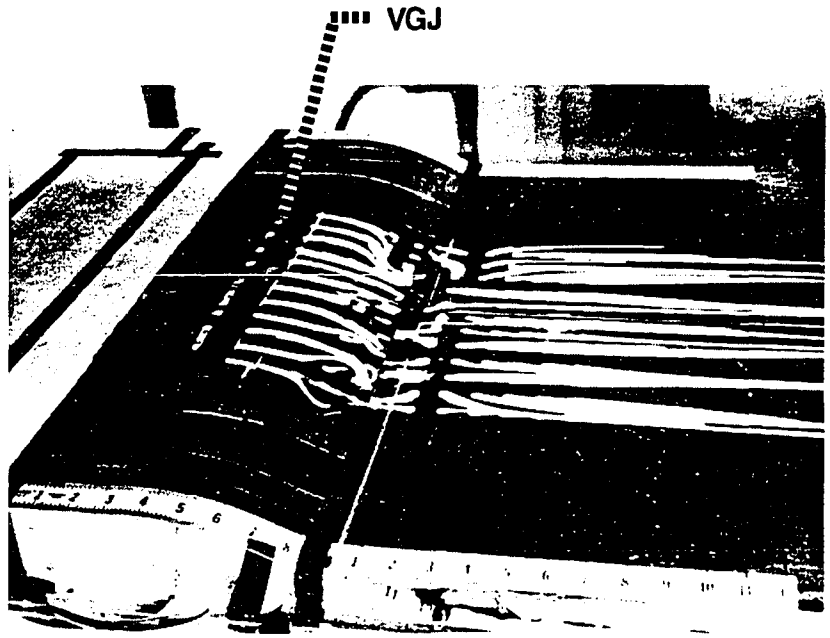

Figure 4.53 Oil-flow visualization for counterrotating VGJ's with $D_o = 1/32$ in., VR = 6.8, $\alpha = 45°$, and $\beta = \pm 90°$.

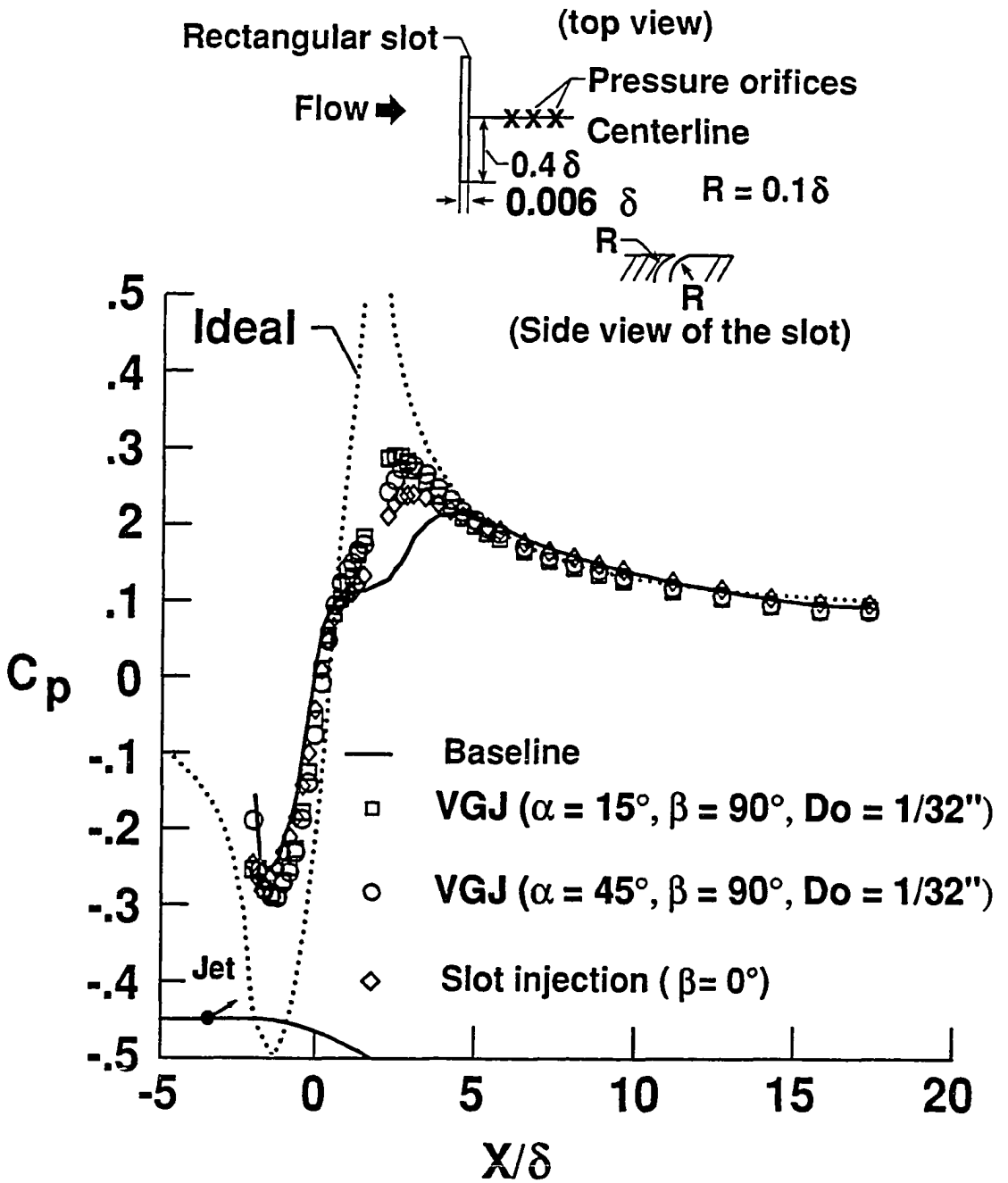

Figure 4.54 Streamwise pressure distributions for rectangular-slot injection (0.008 × 0.95 in.) and VGJ's with equal flow areas, VR = 6.8, and Q = 2.9 ft^3/min.

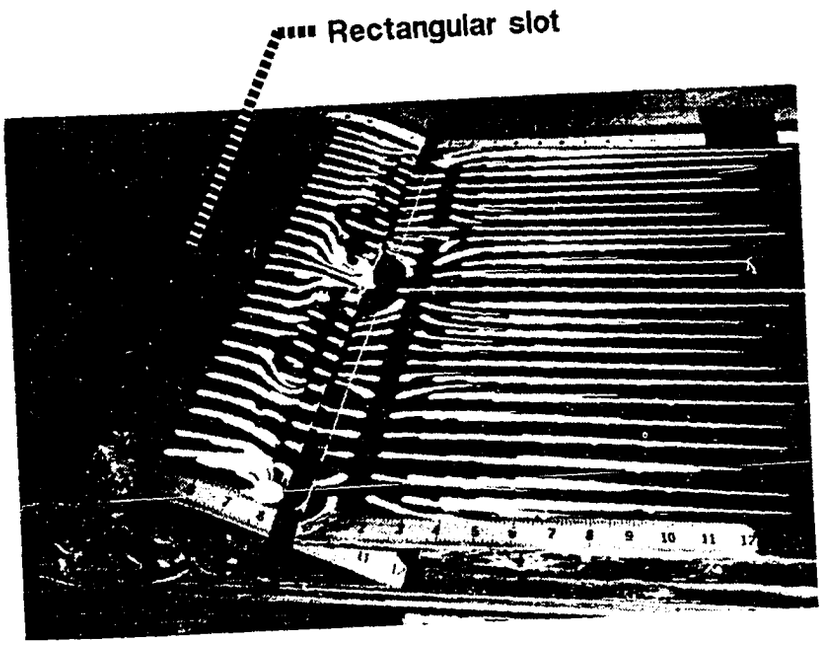

Figure 4.55 Oil-flow visualization for rectangular-slot injection (0.008 × 0.95 in.) with VR = 6.8 and Q = 2.9 ft^3/min.

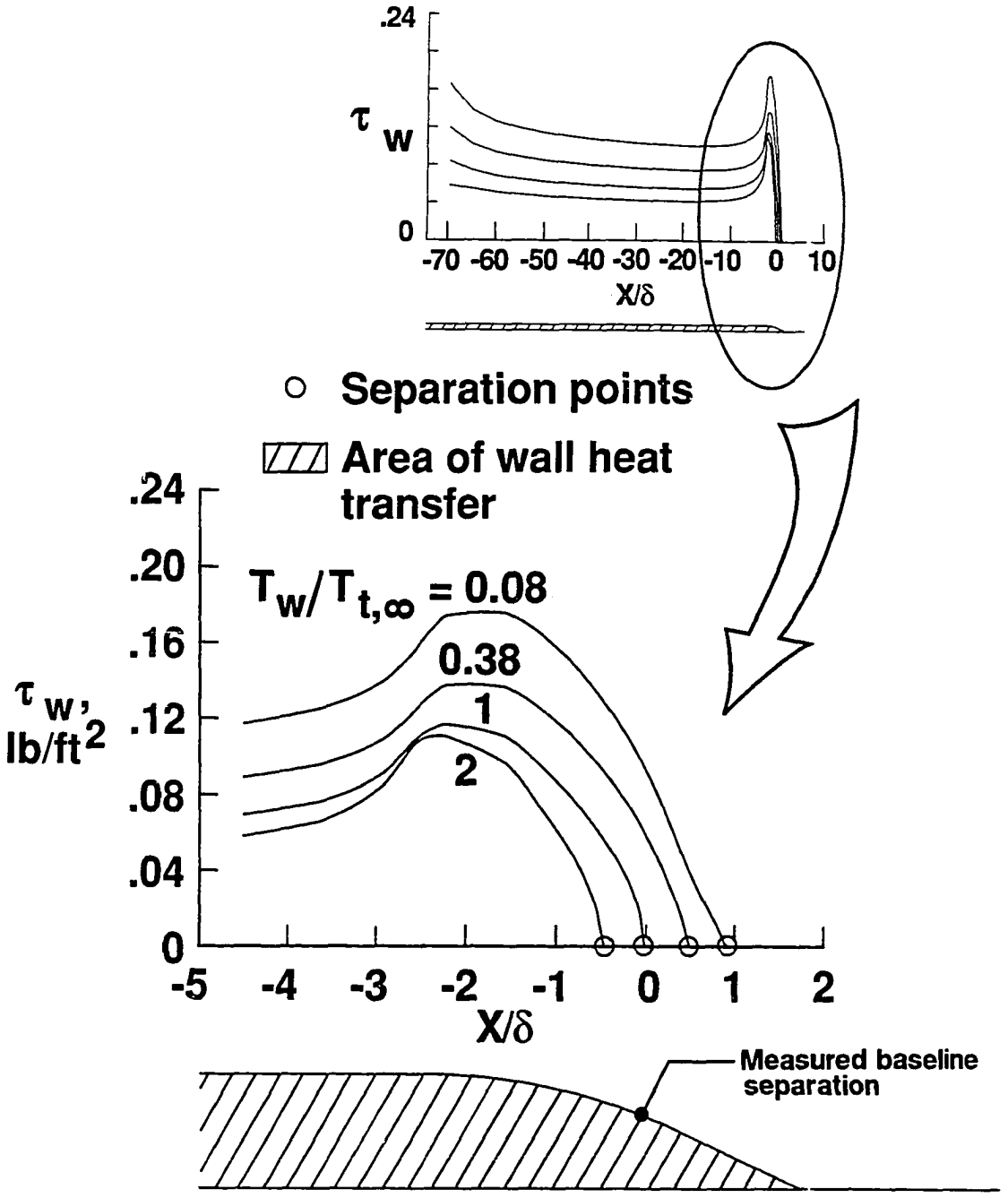

(a) Full surface coverage.

Figure 4.56 Comparison of wall shear stress distribution between full and partial thermal control for a backward-facing ramp.

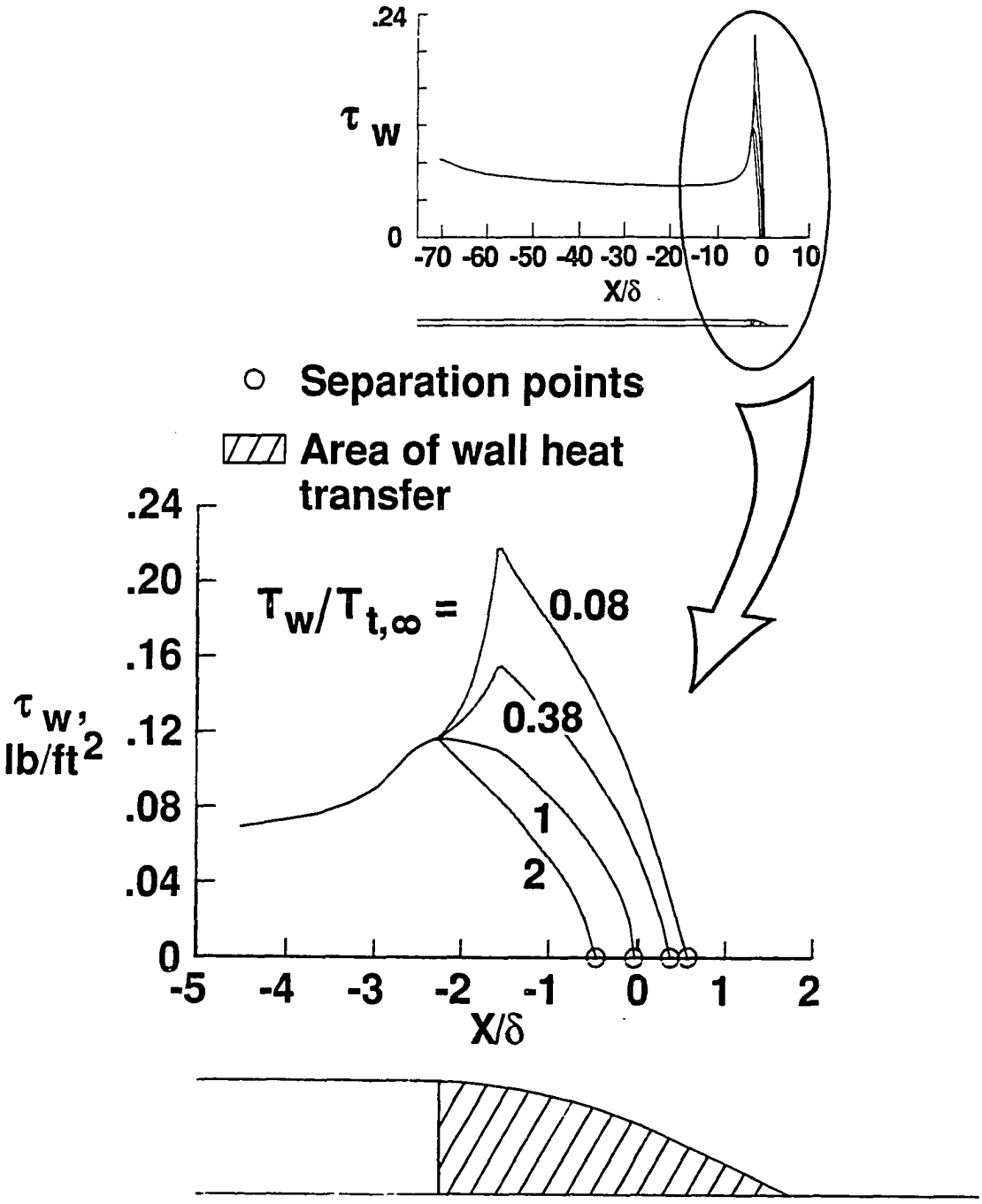

(b) Partial surface coverage from 2δ upstream of the adiabatic reference separation.

Figure 4.56 Continued.

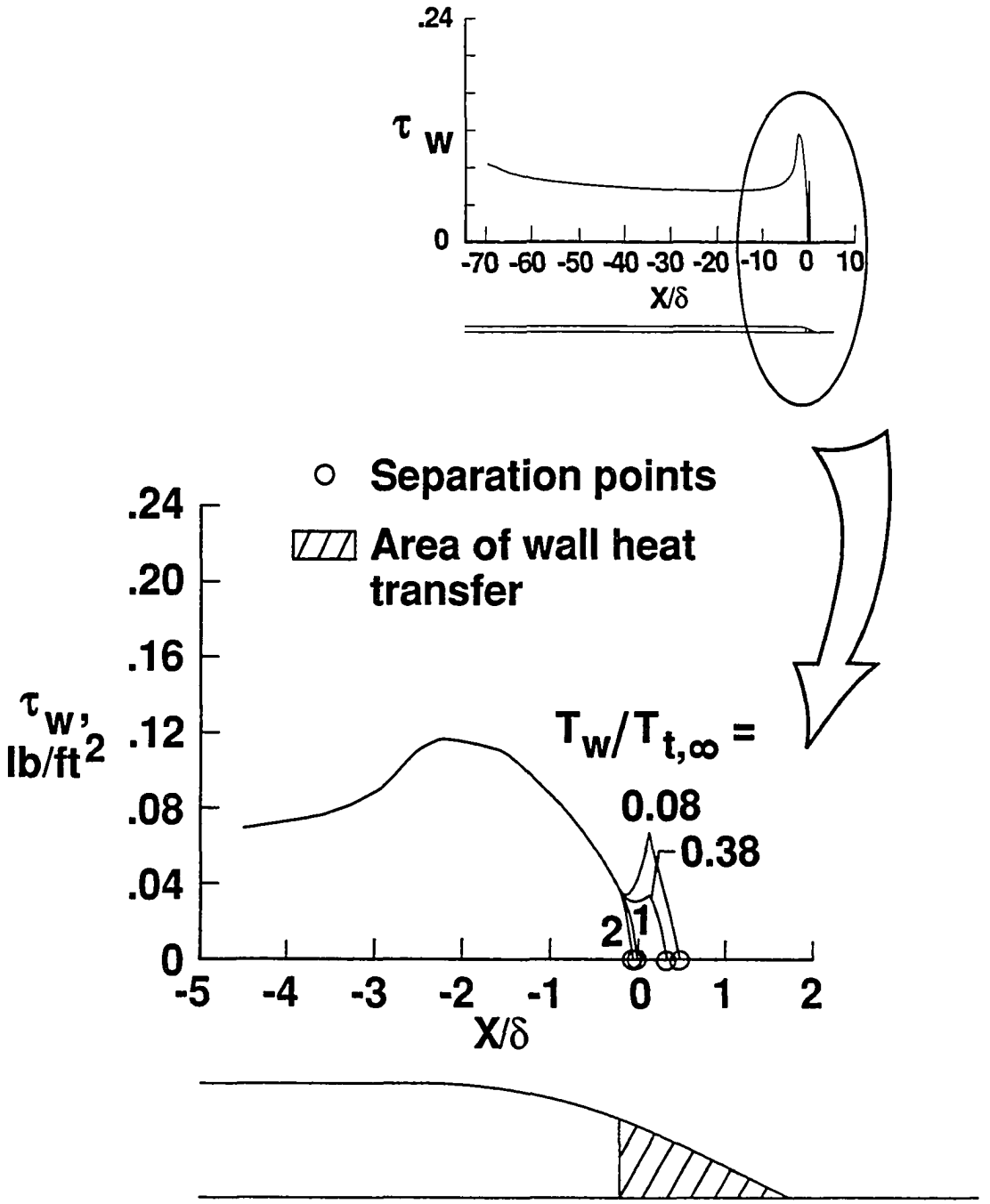

(c) Partial surface coverage from 0.2δ upstream of the adiabetic reference separation.

Figure 4.56 Continued.

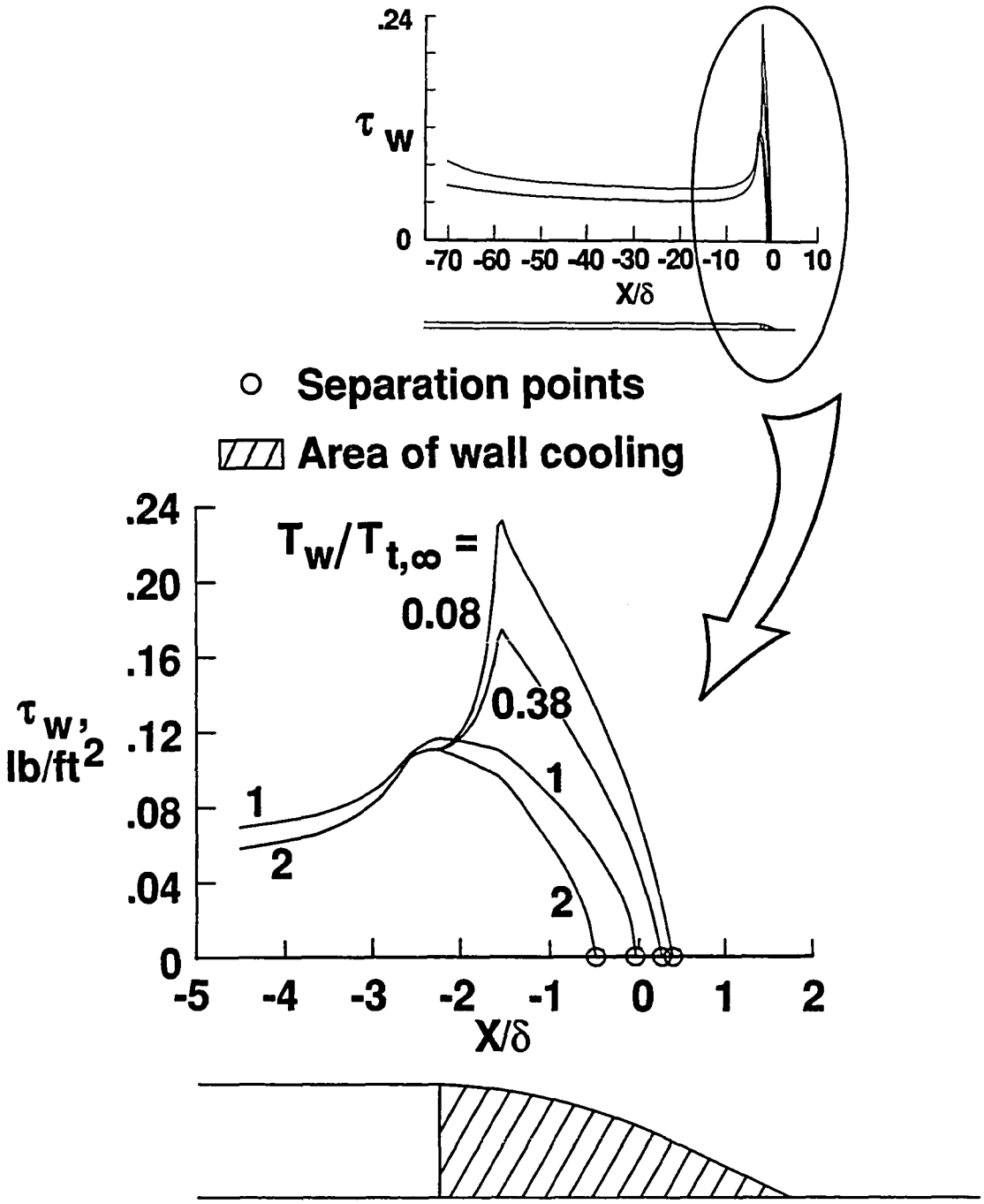

(d) Partial wall cooling on a heated wall.

Figure 4.56 Concluded.

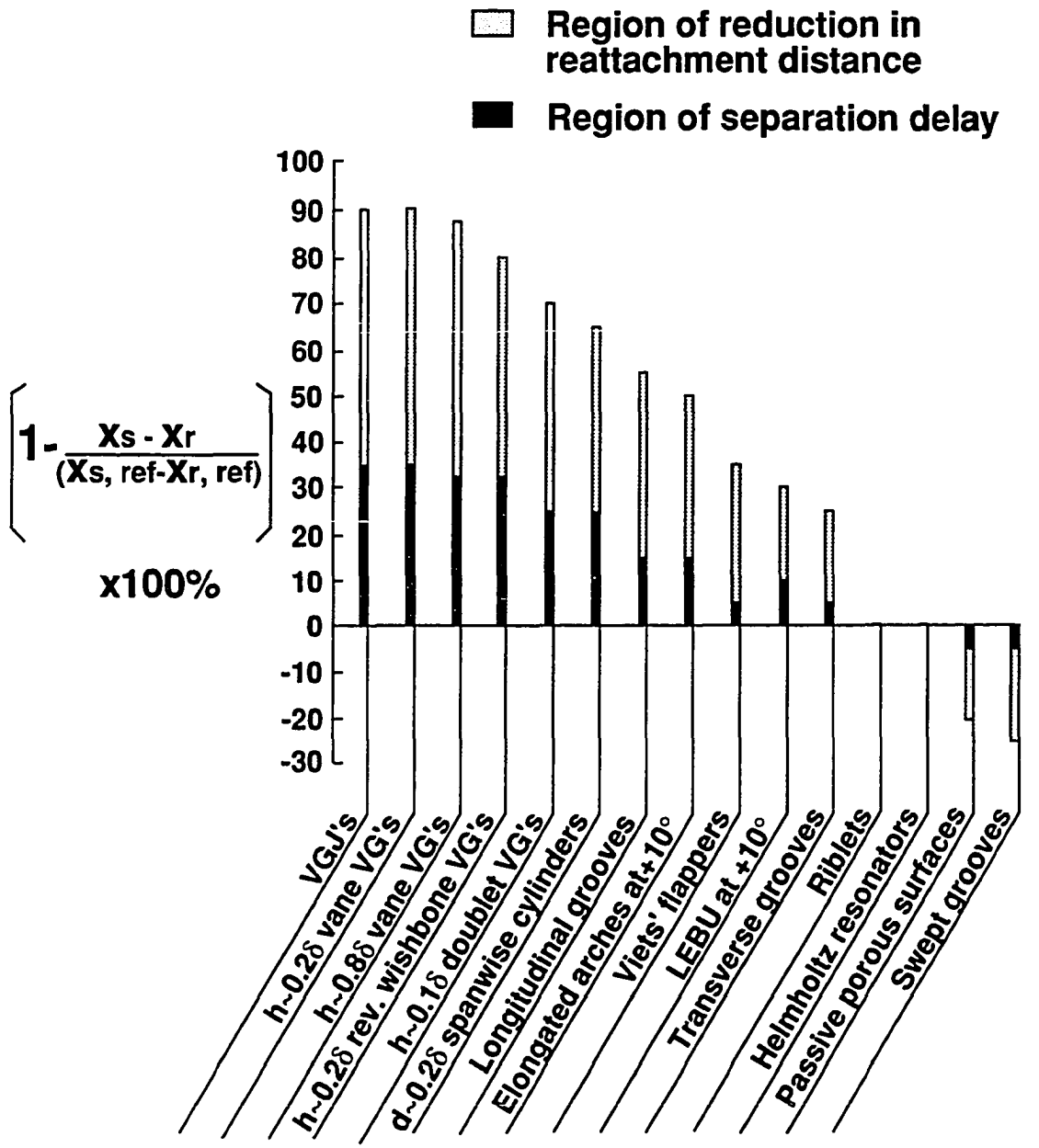

Figure 4.57 Summary: Reduction in the extent of separation due to flow control devices.

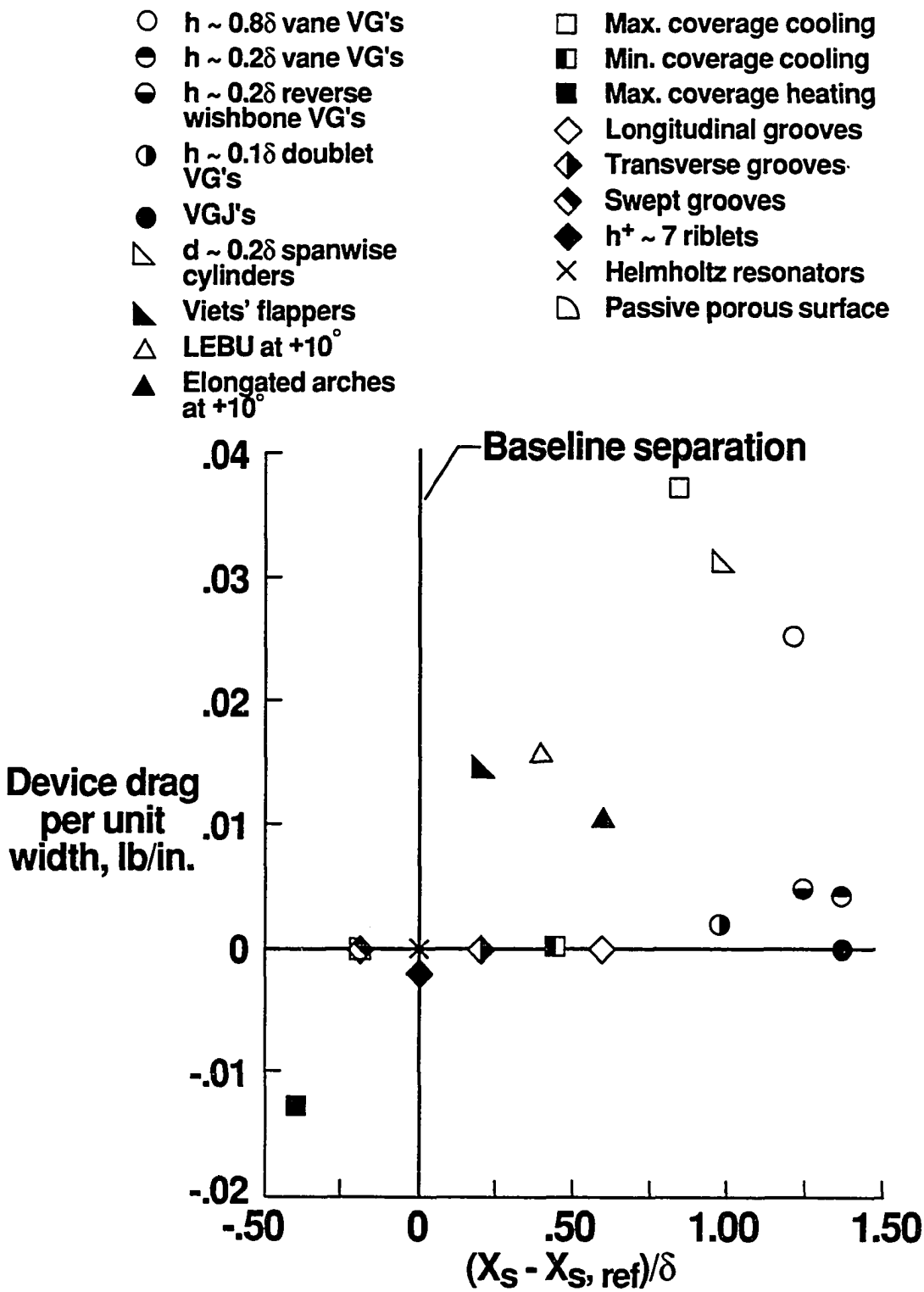

Figure 4.58 Summary of device aerodynamic drag versus separation control effectiveness.

CHAPTER 5

WATER-TUNNEL RESULTS

5.1 Submerged Vortex Generators

In the water-tunnel tests, the dye-flow visualization technique was used as a tool for qualitative study. However, several points need to be addressed concerning deficiencies of the technique: (1) in the regions where the fluid was unmarked, there is no visual data available, and vital information could be lost as a result; and (2) the embedded history of the marked fluid could be misleading because the dye tends to concentrate toward low-speed rather than high-speed regions, thereby providing an unbalanced flow picture.

Dye-flow visualization tests were conducted for both doublet and wishbone vortex generators with a device height, h, of 0.5 in. For each type of vortex generator, three devices located 2 in. ($4h$) apart in the lateral direction were studied. The laser light sheet was used to illuminate five y-z (end view) planes downstream of the generators at increments of 1 inch. The results show that doublet vortex generators in the laminar boundary layer (U_∞ = 1 in/s, R_θ = 110) shed streamwise counterrotating vortices. A sketch of the downstream flow structure is shown in Figure 5.1a. The mushroom-shaped pattern of the marked fluid remained intact for at least 8h downstream of the generators. The maximum height of the vortex pair was approximately $1.2h$ to $1.3h$. For the turbulent boundary-layer flow (U_∞ = 8.3 in/s, R_θ = 1000), the steady vortex pair was replaced by a highly-mixed wake structure with counterrotating streamwise vortices observed along its core (Figure 5.1b). The core height of the wake structure grew quickly from $2h$ to $3h$ within an inch downstream of the generator and remained nearly constant thereafter.

The wishbone vortex generators oriented with apexes pointing downstream (forward configuration) shed horseshoe vortices in a laminar boundary layer, as shown in Figure 5.2a (also see Figure 3.2 for the photograph). Each horseshoe vortex consisted of a pair of counterrotating streamwise vortices as the *legs* with a U-shaped transverse vortex as the *head.* Apparently, the *leg* vortices were shed by the sidewalls and the *head* vortex was produced by the downstream-pointing apex. The shedding frequency of the horseshoe vortices was approximately 1 Hz. The Strouhal number based on device height was approximately one. The formation of the horseshoe vortices began at approximately $6h$ downstream from the wishbone generator. Upstream of the formation site, the observed flow structure consisted of steady counterrotating longitudinal vortices with a core height of $1.5h$. Once the hairpin structure was evident, the height of the vortical structure, indicated by the dye, ranged between $1.2h$ and $2.6h$. These horseshoe vortices may have played a key role in the reduction of the size and magnitude of the laminar separation bubble over the low Reynolds number airfoil that was reported by Kehro et al. [44]. In the turbulent boundary layer, the horseshoe vortices could not be observed, but counterrotating motion was clear (Figure 5.2b). The maximum height of the observed vortex pair varied between $2h$ and $3h$ downstream of the streamwise location ($\sim$ 3 in.) where the head of the horseshoe vortex formed in the laminar flow.

When immersed in the laminar boundary layer, wishbone vortex generators with apexes pointing upstream (reverse configuration) shed counterrotating streamwise vortex pairs similar to those of the doublet vortex generators, as shown in Figure 5.3a. Nevertheless, the vortex pairs reached a maximum core height of only $1h$. Also, the longitudinal vortices were formed between, rather than downstream of each generator. It is noted that the lower vortex structure was formed between the devices where the height of protruding sidewalls was lower than that of the apex. Unlike the forward configuration, the near-wall fluid could not be gathered by the upstream-pointing apex in order to form horseshoe vortices downstream. In the turbulent boundary layer, the

steady laminar vortex pair was replaced by the highly-mixed counterrotating vortical flow (Figure 5.3b). The shape of the vortical structure was more elongated in the spanwise direction (elliptical) than was the flow structure associated with either the doublets or the wishbones (forward configuration). However, this is at least partly related to the spanwise spacing between the devices. The maximum height of the turbulent vortical wake for the reversed wishbones was between $1.7h$ and $1.9h$, which was about 60% of the value for wishbone generators in the forward configuration.

One possible explanation for the effectiveness of the 0.2δ high reversed wishbone vortex generators in the wind-tunnel tests is that the vortex cores of these generators are closer to the surface and thereby provide enhanced mixing in regions where momentum is lowest. With the 0.09δ high doublet and wishbone generators in the forward configuration, where momentum at the generator tip is much lower than the 0.2δ high case, mixing is accomplished with high-momentum fluid further away from the wall (up to $3h$) which should be more beneficial for separation control.

It should be pointed out that the horseshoe vortices generated by the wishbone vortex generators oriented in the forward configuration are very similar to those of the hairpin (or arch-type) vortices generated by flow over a hemisphere [92] or a mixing tab [93,94], as illustrated in Figures 5.4a and 5.4b, respectively. They [92–94] determined that the legs of a hairpin vortex help to pump low-speed fluid that is inboard of the legs away from the surface, and help to bring fluid which is outboard of the legs down towards the surface. The head region of the hairpin vortex entrains the low-momentum fluid pumped up by the legs and carries it farther away from the wall. Gretta [94] also showed that these hairpin vortices could combine with other hairpin-like vortices in the streamwise direction to form larger structures. A recent detailed evaluation of the direct numerical simulation of a turbulent boundary layer by Robinson [95] has revealed the presence of manifold hairpin-like vortices, most generally asymmetric in shape. He also indicated that such structures are intimately involved in the significant transport of fluid both to and

away from the surface. This suggests that if such structures are generated artifically, the potential is present for capitalizing on the dynamics of hairpin vortices for momentum transport in a turbulent boundary layer.

A number of investigators have examined the fluid mixing effect of streamwise vortices embedded in turbulent boundary layers, since they are also identified as a significant structure in boundary-layer turbulence (see Robinson [95,96], Smith and Schwartz [97], Ersoy and Walker [98]). Both single streamwise vortices and co-rotating and counterrotating pairs have been examined to determine the interaction of the vortices with the adjacent fluid, as well as the interaction between two adjacent vortices. It is established that the presence of streamwise vorticity above a surface causes the ejection of low-momentum near-wall fluid from the surface (Peridier et al. [99]), as well as inducing movement of higher-momentum outer-region fluid towards the wall.

Generally speaking, the velocity deficit within a turbulent boundary layer is most prevalent near the surface, within the inner 20% or so of the boundary layer. It is within this region where adverse external pressure gradients tend to lower the velocity and thus hasten flow separation. The sub-δ-scale vortex-generator concept, via the doublets, wishbones, or vane-types, is to increase the momentum transfer between the outer and the inner portions of the boundary layer thereby increasing the velocity gradient near the surface. This is different than the conventional δ-scale vortex generator, where the device is sized to transfer momentum from outside the boundary layer to the surface, as illustrated by a conceptual sketch in Figure 5.5.

5.2 Large-Eddy Breakup Devices at Angle of Attack

A NACA 0009 airfoil with a chord length of 1.15 in. and a span of 15 in. (covered the central 94% of the test section) was used as a LEBU in the water-tunnel investigation. The airfoil was mounted 0.8δ above the wall and was inclined at angles of attack of $\alpha = +10°$, 0°, and $-10°$. The observed downstream flow structure in the x-y plane is

depicted in Figure 5.6. At $\alpha = 0°$, unsteady streamwise vortical structures were often observed in the wake. These structures were most likely formed because of pressure fluctuations which occur in the turbulent boundary layer. The vortical structures appeared intermittently and often changed direction of rotation. The distance between the LEBU trailing edge and the formation of these unsteady structures was about 50% of the LEBU chord. Similar flow characteristics have also been noted in the flow visualization results of Govindaraju and Chambers [100] for a 0.8%-thick LEBU ribbon with Re_ℓ up to 22000.

At $\alpha = +10°$, the airfoil LEBU shed transverse vortices at both leading and trailing edges. The Re_ℓ was approximately 6000, which means that the airfoil LEBU at $\alpha = +10°$ was within its stall region. The resulting wake resembles the Karman vortex street shed from a cylinder. The transverse vortices produced from the trailing edge of the LEBU appeared to exhibit a stronger influence than those shed from the leading edge. The trailing-edge vortices shed from the lower side of the LEBU airfoil had a direction of rotation opposite to the sign of the mean vorticity in the turbulent boundary layer. Downstream of the LEBU, an upward movement of the near-wall turbulent eddies was observed. This phenomenon may be caused by the interaction of the trailing-edge vortices with the boundary-layer eddies. For the negative angle-of-attack case, the trailing-edge vortices appeared to exhibit a stronger influence than those shed from the leading edge. These trailing-edge vortices rotated in the same direction as the eddies in the turbulent boundary layer. The eddy structures near the wall appeared to experience an increase in rotational speed downstream of the device, suggesting a reinforcement of the near-wall eddies by the trailing-edge vortices.

Wind-tunnel results indicated that although a LEBU at a negative angle of attack can enhance eddy structure, it also tends to divert momentum away from the wall, which has an adverse effect on flow separation control. Apparently, diverting the momentum directly toward the wall is a more important factor in controlling flow separation than

the enhancement of large-eddy structure, as demonstrated by LEBU's at a positive angle of attack.

Based on both water-tunnel flow visualization and wind-tunnel data, Figure 5.7 illustrates a conceptual view of the effect of a LEBU at angle of attack on the downstream turbulent boundary layer. Immediately downstream of the LEBU at $\alpha = +10°$, the velocity profile probably became fuller because of the redirection of longitudinal momentum toward the wall via the *down-turning* effect of the LEBU. Further downstream of the device, vortices in the lower wake likely moved down through the boundary layer and induced a vertical uplift of fluid away from the wall. This motion then tended to reduce the velocity gradient and momentum near the wall. However, this process could not cancel the initial momentum addition to the wall region via the turning effect of the LEBU until 20δ downstream of the device as demonstrated in Figure 4.30. For the LEBU at $\alpha = -10°$, the opposite was true initially. The velocity profile became less full (or more Blasius-like) because of the redirection of longitudinal momentum away from the wall via the *up-turning* effect of the device. Further downstream of the device, the upper wake vortices grew larger in size through entrainment of the outer flow and induced circulation that brought the higher-momentum outer-region fluid towards the wall. But again, this process appeared too weak to overcome the initial momentum diversion away from the wall in order to eventually have a positive effect on flow separation control.

5.3 Spanwise Cylinders

In the water-tunnel tests, a 0.25-inch-diameter ($d/\delta \sim 0.2$) cylinder was mounted at distances of 0.063 in. ($g/\delta = 0.05$) and 0.875 in. ($g/\delta = 0.7$) from the wall. The cylinder had a span of 15 in. that covered the middle 94% of the test section. As expected, the spanwise cylinder generated a Karman vortex street when placed in the outer position ($g/\delta = 0.7$), as shown in Figure 5.8. For the near-wall case ($g/\delta = 0.05$), only vortices shed from the top side of the cylinder could be observed several diameters downstream

from the device. As a result, the downstream flow structure was dominated by transverse vortices which rotated with the same sign of vorticity as that of the mean boundary layer. These transverse vortices appeared to be larger and exhibited a higher rotational speed than those produced by the LEBU at $\alpha = 10°$. The Reynolds number based on the cylinder diameter and the Reynolds number based on the frontal projected height of the LEBU at $\alpha = -10°$ were the same—both were approximately 1000.

A conceptual view of the effect of a spanwise cylinder on the downstream turbulent boundary layer is shown in Figure 5.9. The spanwise cylinder, when placed far from the wall ($g/\delta = 0.7$), apparently generated a more vigorous and slightly stronger vortex street than the LEBU at angle of attack. The velocity profile became fuller immediately downstream of the cylinder because of the displacement effect of the device. The vortices in the lower wake reached the wall quickly at a distance of less than 5δ downstream of the device. The impingement of these vortices on the wall likely produced yet an even fuller velocity profile locally. However, this interaction process probably also induced a strong uplift of the near-wall fluid downstream and eventually, at about 20δ from the cylinder, produced a less full velocity profile that is more likely to separate, as shown in Figure 4.35. The spanwise cylinder placed near the wall ($g/\delta = 0.05$), on the other hand, initially generated a near-wall velocity deficit immediately downstream of the device. Further downstream, the vortices shed from the upper surface of the cylinder rotated in the same direction as the eddies in the turbulent boundary layer. This motion suggested a reinforcement of the near-wall eddies and a movement of higher-momentum outer-region fluid towards the wall. This momentum transport through eddy reinforcement produced a slight positive effect in separation control at a distance of about 10δ downstream from the device, as shown from the wind-tunnel results of Figure 4.37.

5.4 Vortex Generator Jets

In the water-tunnel investigation, three VGJ's with $\alpha = 15°, \lambda = 2$ in., VR = 4, and $D_o = 1/32$ in. were installed at various jet azimuthal angles, β (Figure 2.1k). The visualized dye patterns as seen from an end view located 2 in. downstream of the jet for both turbulent and laminar boundary layers are sketched in Figure 5.10. As the value of β increased from 0° to 90°, the following flow phenomena were observed: (1) the rotational speed of the turbulent vortex increased, (2) vortex core size generally increased, (3) one member of the laminar vortex pair was attenuated, while the other was amplified and moved closer to the wall, and (4) the sign of the vorticity for the laminar and turbulent jets was opposite. Figures 5.11a and 5.11b show the end (plane) view of the flow visualized using the laser-induced fluorescent-dye technique downstream of a VGJ ($\beta = 90°$) within both a laminar and a turbulent boundary layer, respectively.

Conceptual models for the formation of jet-induced vortices are shown in Figure 5.12 for both laminar and turbulent boundary-layer flows at the maximum β of 90°. For the turbulent case, the velocity gradient is concentrated near the wall, with the rest of the boundary layer being dominated by eddies. Hence, as soon as the jet left the orifice, the crossflow-induced vortex pair within the jet experienced relative motion consistent with the direction of the mean transverse vorticity in the boundary layer, and this relative motion was strengthened as β approached 90°. In addition, the member of the vortex pair with rotational direction opposite the mean transverse vorticity in the boundary layer was attenuated. Thus, downstream of the jet orifice, only a single longitudinal vortex rotating in the same sense as the turbulent eddies was observed, as shown in Figure 5.12b. Typically, at 1 in. downstream of the jet orifices, the core diameters of these vortices were on the order of 0.2δ for $\beta = 0°$ and 0.3δ for $\beta = 90°$. The streamwise growth rate of the core diameters was approximately 0.1δ per inch. Wind-tunnel results indicated that the effect of jet-induced co-rotating streamwise vortices can be strong and persistent within a turbulent boundary layer.

The exact physical mechanism responsible for vortex roll-up when jets are skewed within a turbulent boundary layer is still not fully understood. Current flow visualization results suggest that the main mechanisms are entrainment, concentration, and turning of spanwise boundary layer vorticity by the skewed jet. The jet with the largest skew angle ($\beta = 90°$) apparently captured the greatest amount of the vorticity present in the approaching turbulent boundary layer and re-oriented it into a concentrated streamwise vortex. Then, being fed continuously with vorticity contained in the approaching boundary layer, this streamwise vortex persisted in strength for a considerable downstream distance, thus increasing its effectiveness for near-wall boundary-layer energization. The physical mechanism of boundary-layer energization via embedded streamwise vortices is the same as those discussed in Section 5.1.

Generally, for the laminar flow, the velocity gradient is less concentrated near the wall, and the mean transverse vorticity is *much lower* than that of a turbulent boundary layer. Fluid approaching the jet from upstream would have a tendency to move outward ($+y$) due to the large y-component of momentum introduced into the boundary layer by the jets. This would create a large positive streamwise gradient in the y-component of velocity $\left(\frac{\partial v}{\partial x}\right)$. In addition, the wall-normal gradient of the x-component of velocity $\left(\frac{\partial u}{\partial y}\right)$ would be decreased due to the outward movement of low-speed fluid. The spanwise component of mean vorticity is

$$\omega_z = \left(\frac{\partial v}{\partial x} - \frac{\partial u}{\partial y}\right).$$

The value of ω_z is positive if $\frac{\partial v}{\partial x}$ is larger than $\frac{\partial u}{\partial y}$, which is a likely result here considering the high jet-to-freestream velocity ratio (VR = 4). A positive value of ω_z corresponds to rotation with an opposite sense (counterclockwise for freestream flow from left to right) to that normally associated with a laminar boundary layer (clockwise). Counterclockwise vorticity of this sense would result in the relative movement of the counterrotating vortex pair as indicated in the cores sketched in Figure 5.10, when β increased from 0° to 90°, as well as the attenuation of the vortex with opposite rotation. Thus, downstream of the

jet orifice, the near-wall vortex is much stronger than the one farther from the wall and has a direction of rotation (Figure 5.12a) opposite the mean transverse vorticity in the boundary layer.

5.5 Flow Physics Summary

From the water-tunnel and wind-tunnel results, one can generalize that the embedded streamwise (or longitudinal) vortices, whether generated by wall protuberances (such as sub-δ-scale vortex generators) or skewed jets, provide the most effective and efficient means of delaying or mitigating flow separation in two-dimensional turbulent boundary layers. In other words, transferring momentum from the outer region of the turbulent boundary layer via embedded streamwise vortices is evidently more efficient than such transfer via either enhanced Reynolds stresses or quasi-coherent dynamic transverse vortices.

Flow control devices that generate transverse vortices within the boundary layer tended to have a much larger device drag and associated (device-induced) mean momentum deficit than those which generated streamwise vortices. Furthermore, the three-dimensional helical (or spiral) pathlines over which the streamwise vortices travel downstream appear to be more efficient than the two-dimensional (spanwise) circular pathlines over which transverse vortices travel.

An embedded three-dimensional hairpin vortex that exhibited both streamwise (legs) and spanwise (head) vortices may also have good potential in separation control, especially if the device height is restricted to the order of 0.1δ, as shown from the wind-tunnel results of wishbone vortex generators oriented in the forward direction.

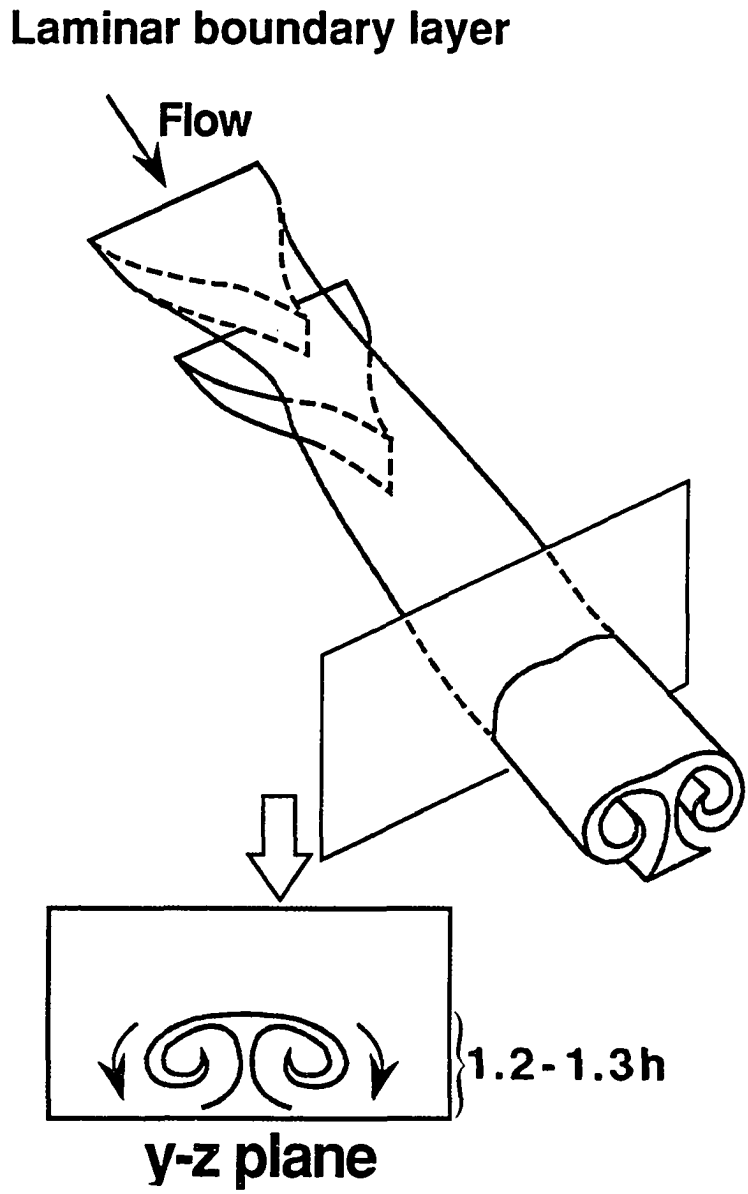

(a) Generator in laminar boundary layer.

Figure 5.1 Flow structure downstream of a doublet vortex generator.

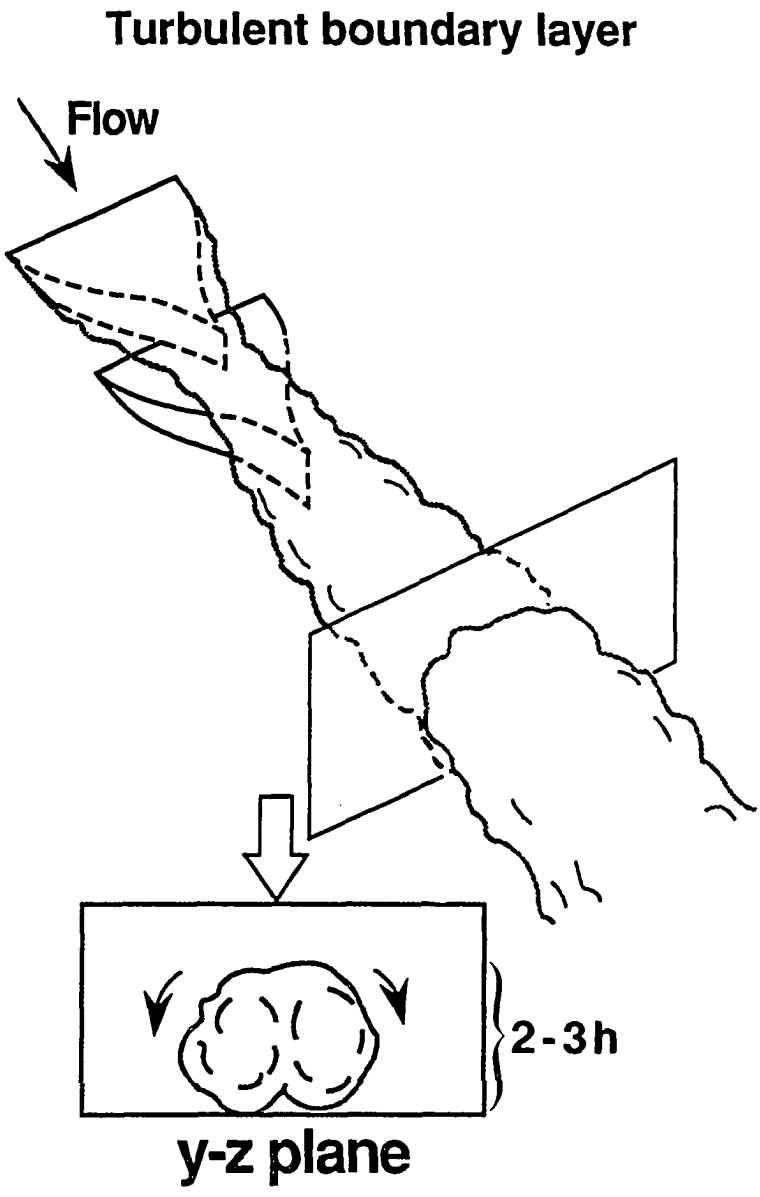

(b) Generator in turbulent boundary layer.

Figure 5.1 Concluded.

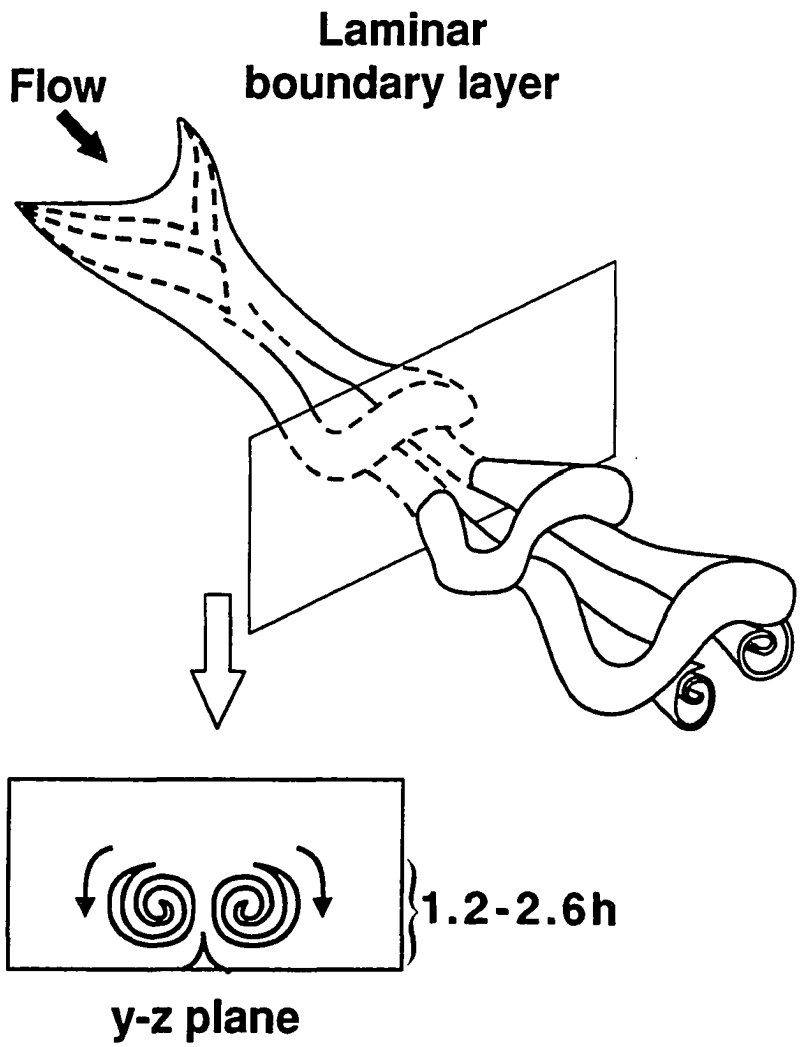

(a) Generator in laminar boundary layer.

Figure 5.2 Flow structure downstream of a wishbone vortex generator in forward configuration.

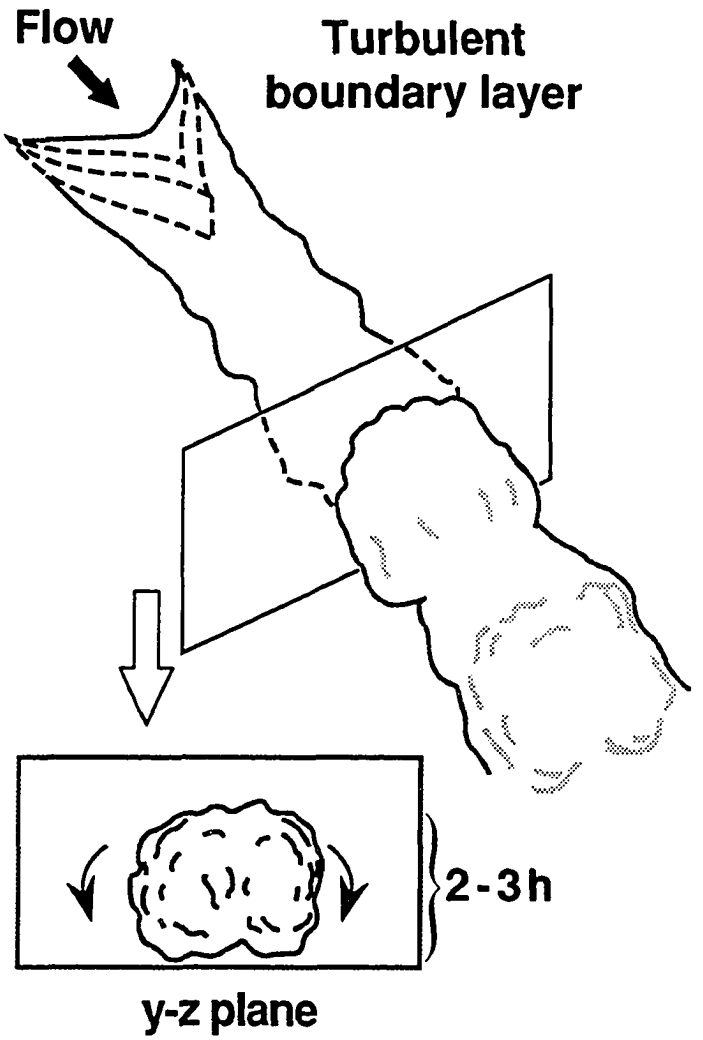

(b) Generator in turbulent boundary layer.

Figure 5.2 Concluded.

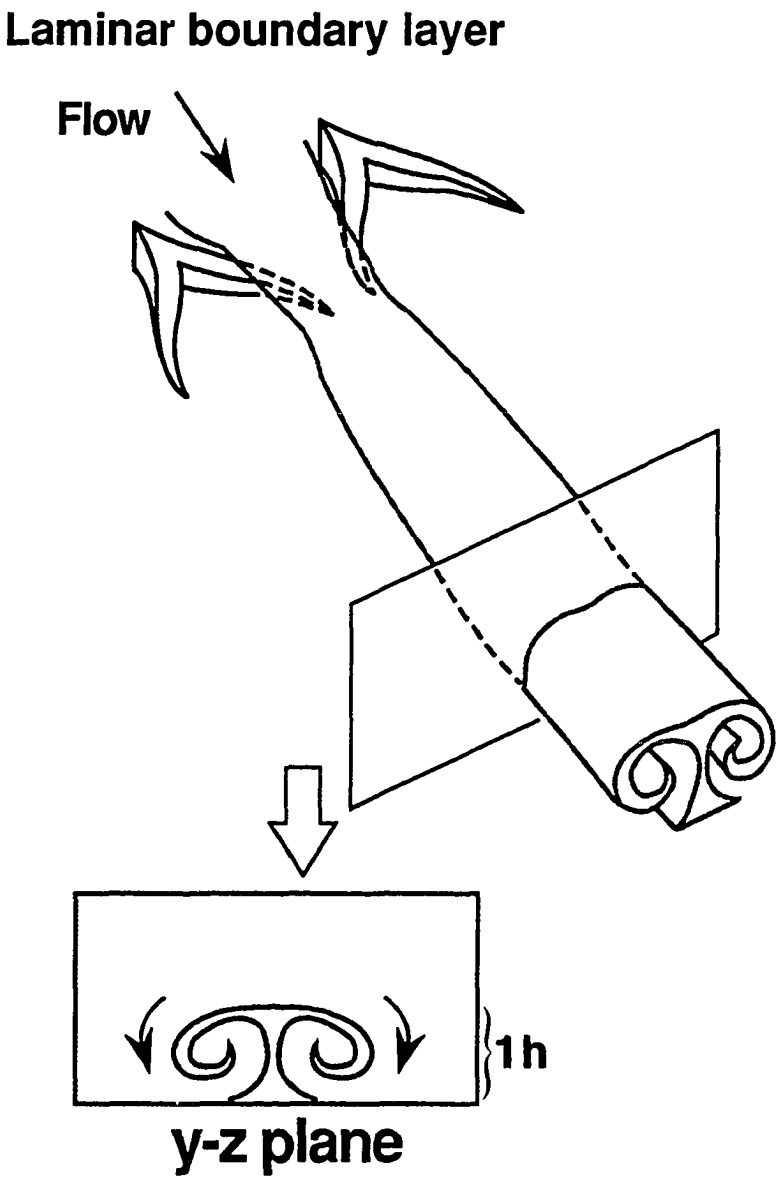

(a) Generators in laminar boundary layer.

Figure 5.3 Flow structure downstream of wishbone vortex generators in reverse configuration.

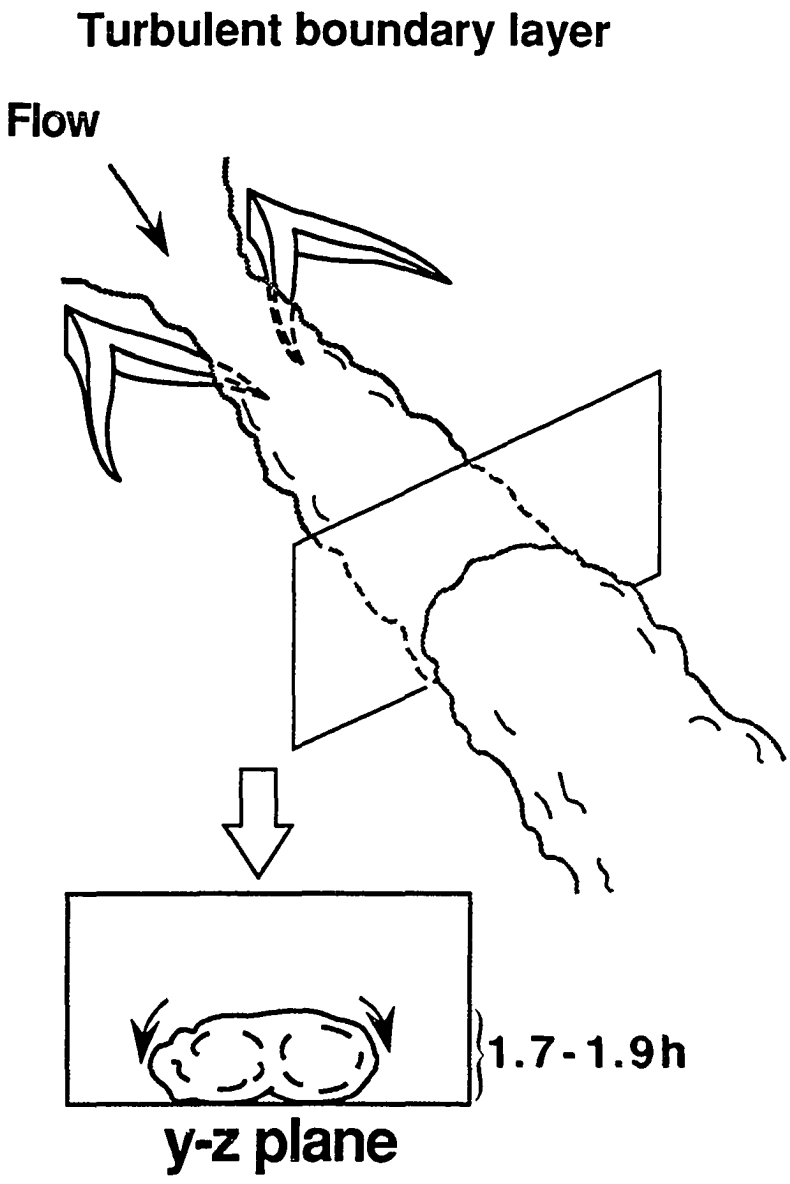

(b) Generators in turbulent boundary layer.

Figure 5.3 Concluded.

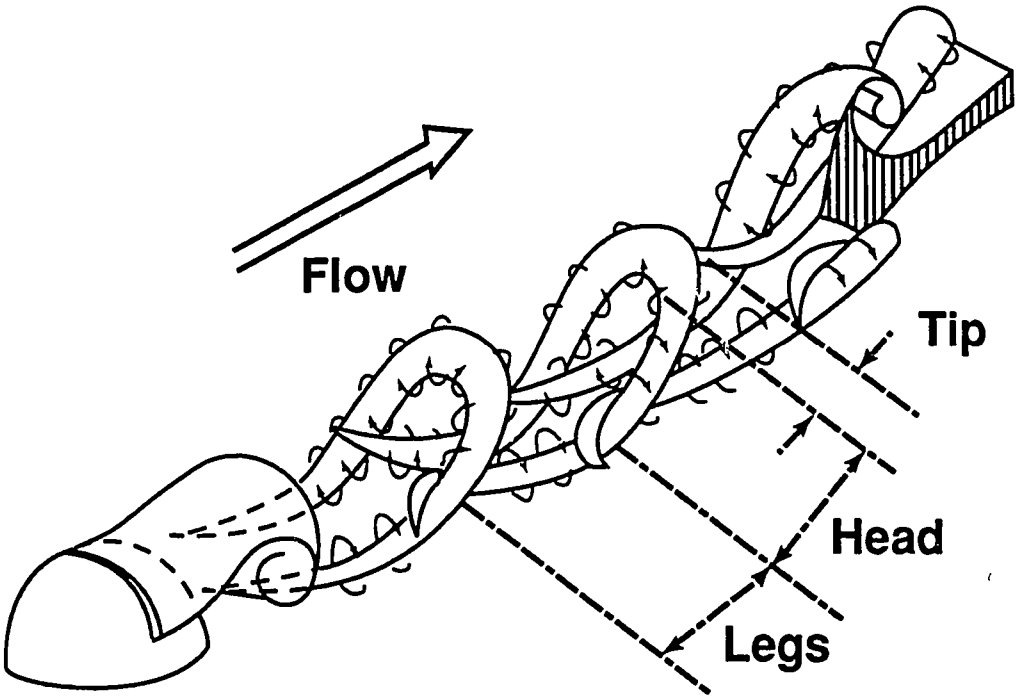

(a) By a hemisphere (Acarlar and Smith [92]).

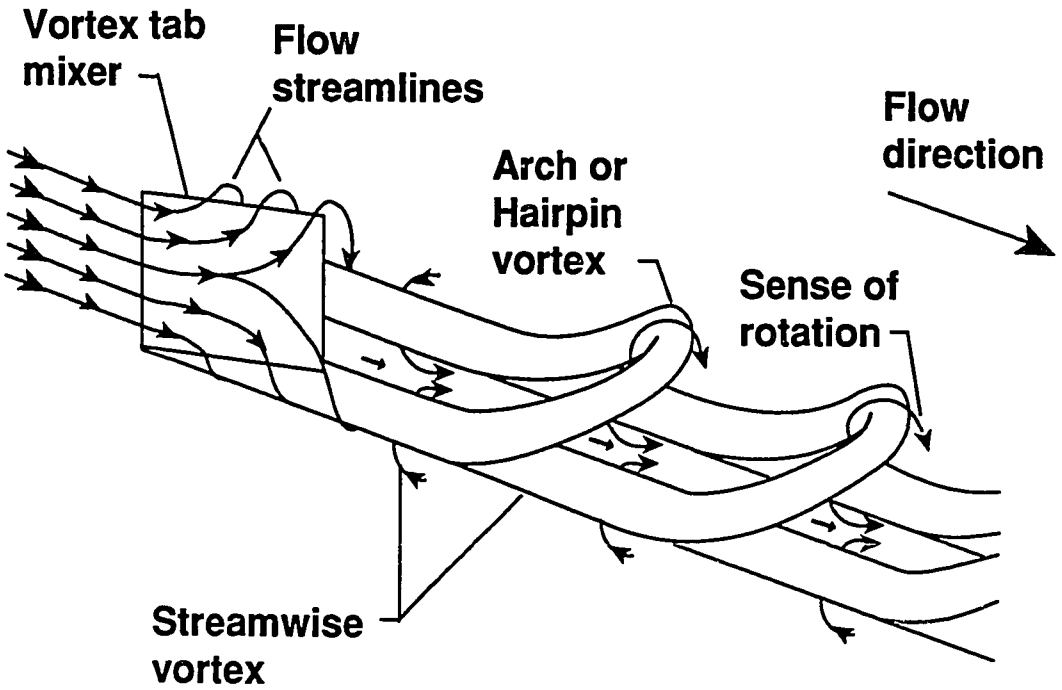

(b) By a mixing tab (Smith et al. [93]).

Figure 5.4 Illustration of the generation of hairpin vortices.

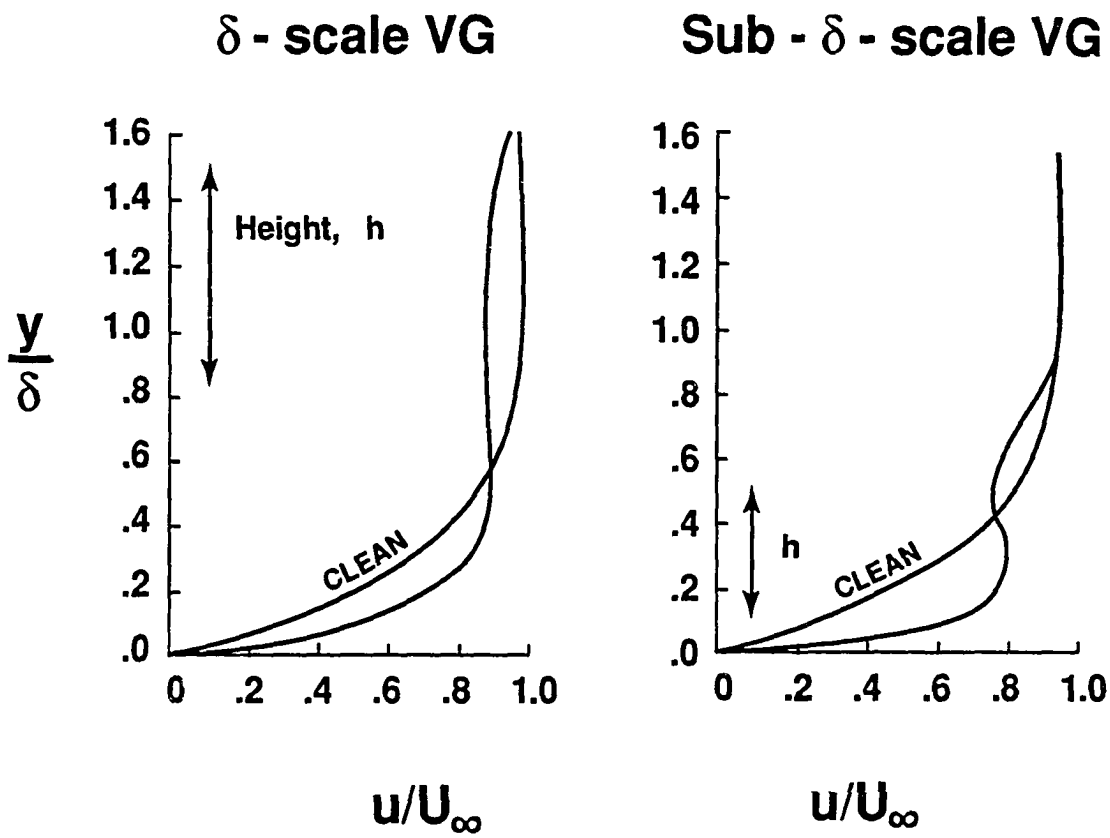

Figure 5.5 Illustration of boundary-layer energization via δ- and sub-δ-scale vortex generators.

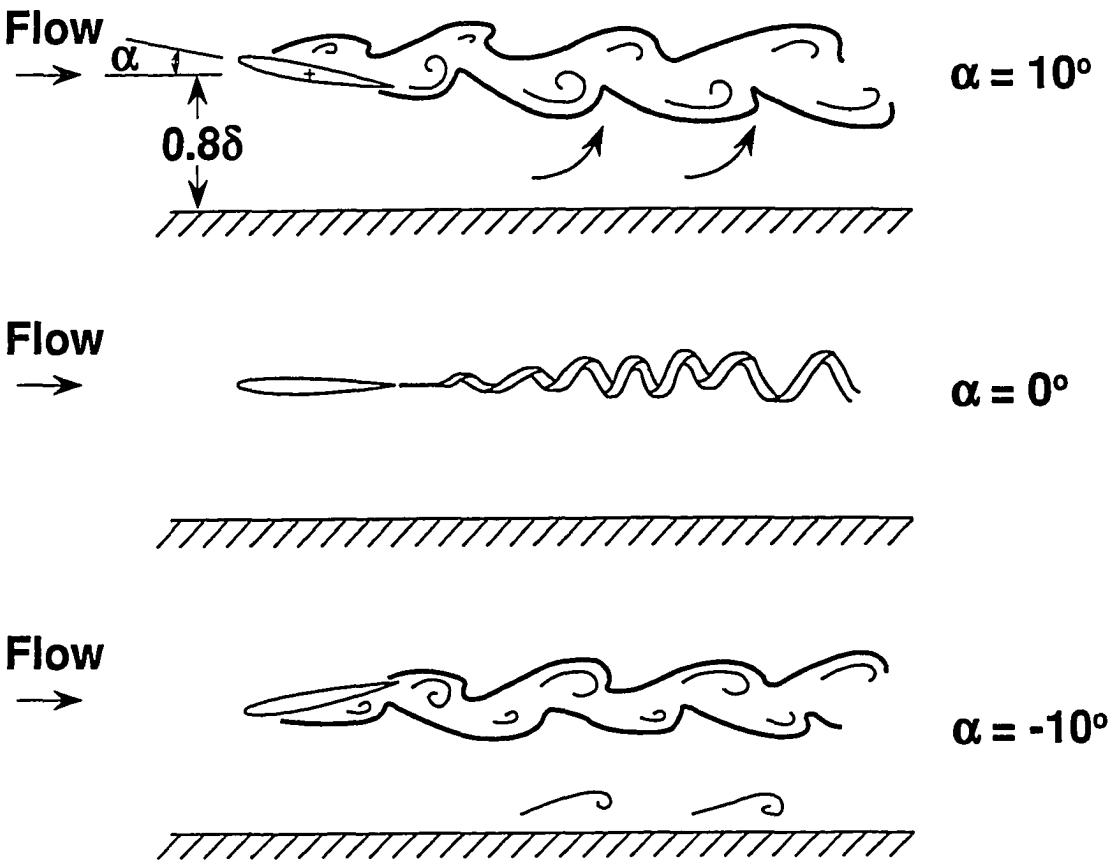

Figure 5.6 Flow structure downstream of a LEBU airfoil at angle of attack in a turbulent boundary layer.

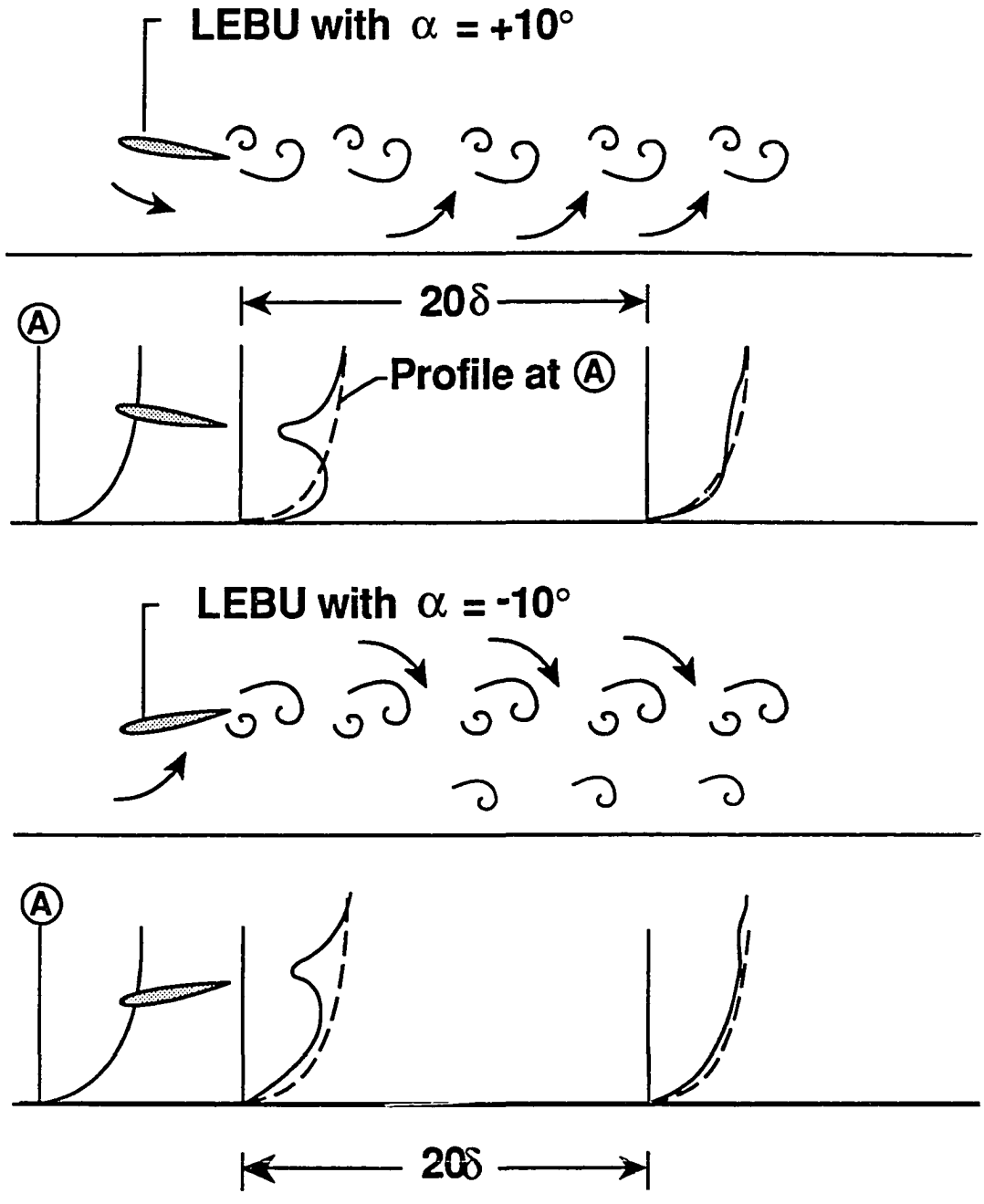

Figure 5.7 Illustration of the effect of a LEBU at angle of attack on the downstream turbulent boundary layer.

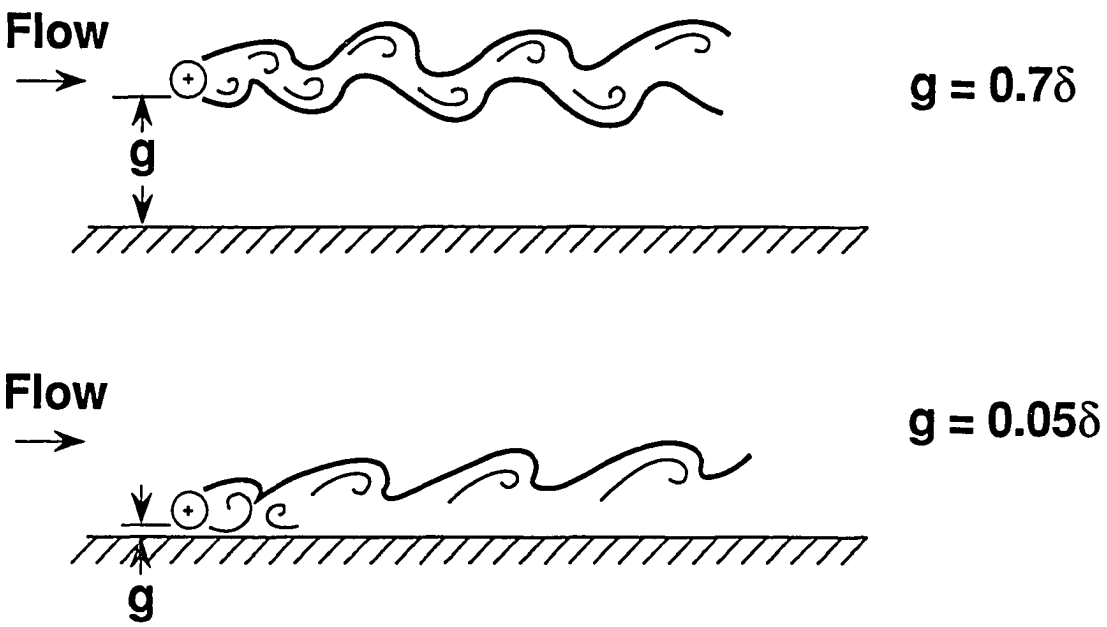

Figure 5.8 Flow structure downstream of a spanwise cylinder ($d = 0.2\delta$) in a turbulent boundary layer.

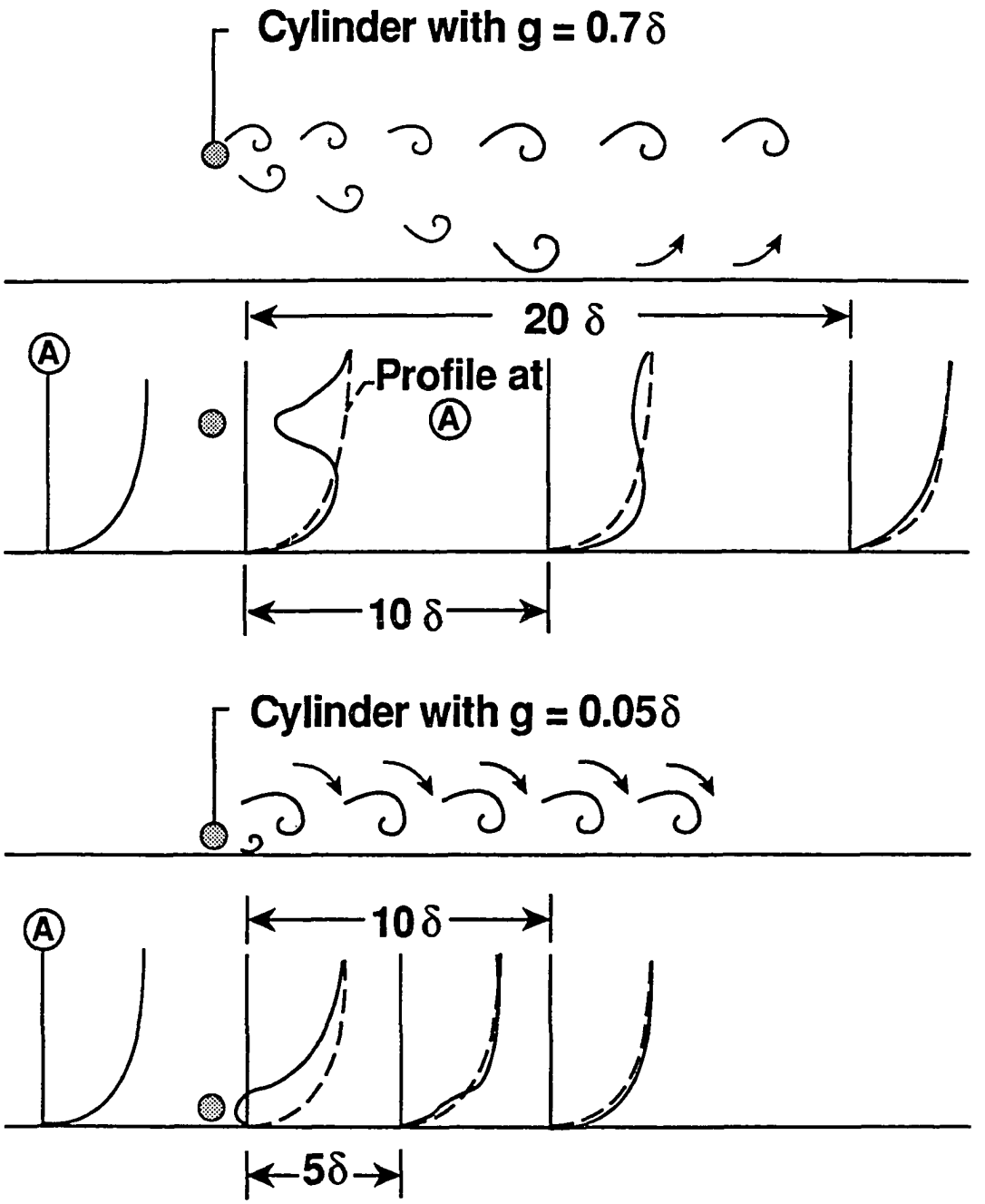

Figure 5.9 Illustration of the effect of a spanwise cylinder on the downstream turbulent boundary layer.

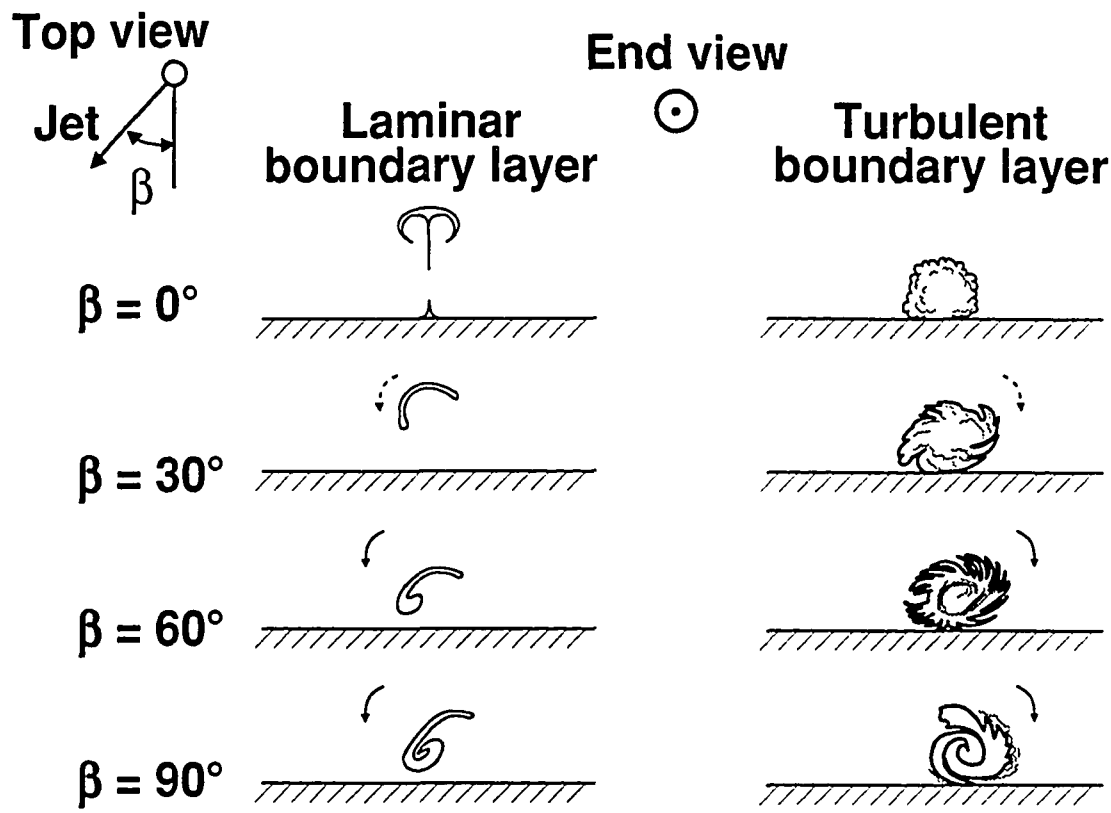

Figure 5.10 Flow structure in y-z plane 2 in. downstream of VGJ's.

(a) Laminar boundary layer.

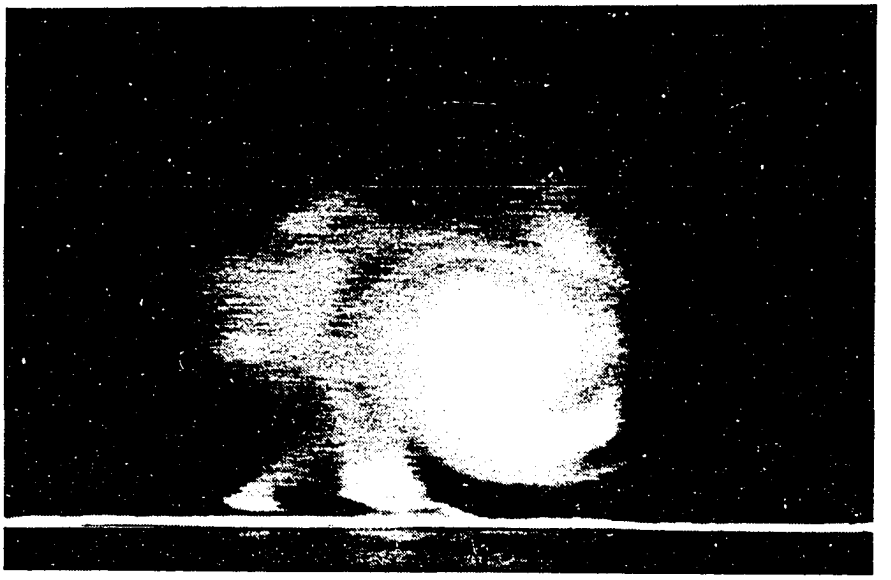

(b) Turbulent boundary layer.

Figure 5.11 End view photographs of laser-induced fluorescent-dye visualization downstream of a VGJ with $\beta = 90°$ and $\alpha = 15°$.

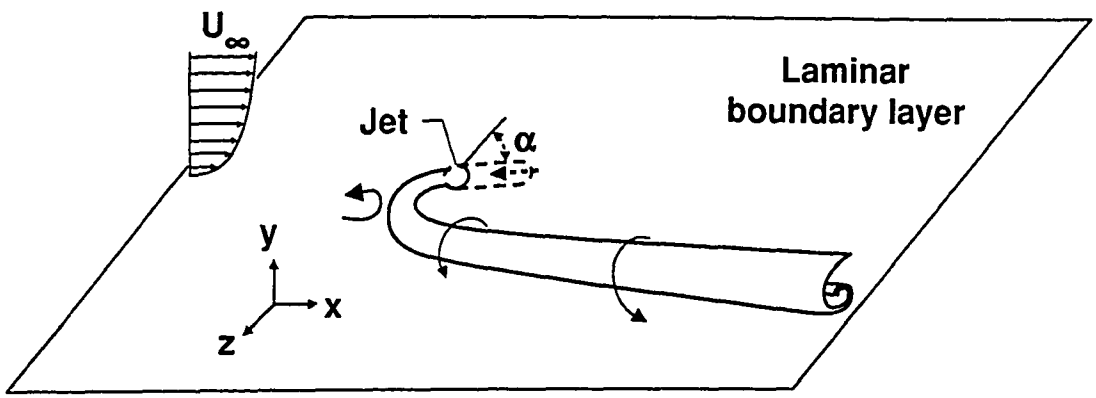

(a) VGJ in laminar boundary layer.

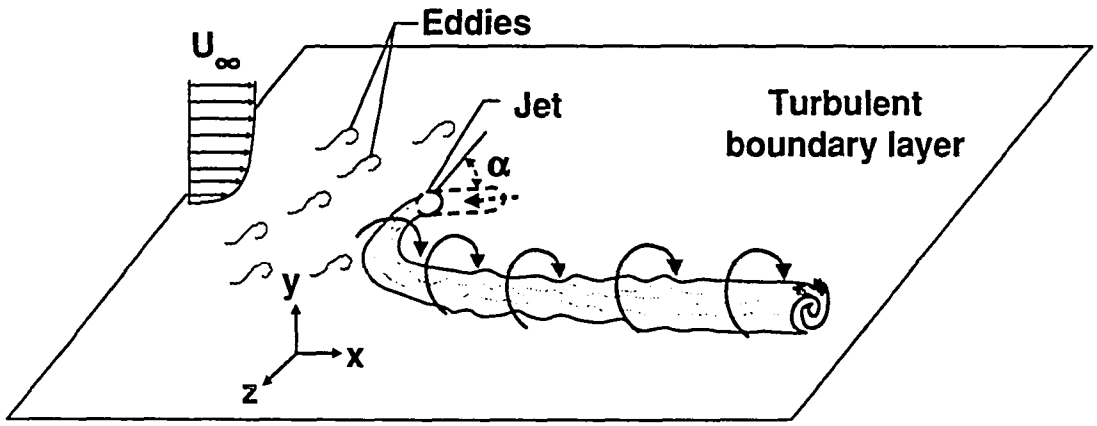

(b) VGJ in turbulent boundary layer.

Figure 5.12 Flow model for a VGJ ($\beta = 90°$, $\alpha = 15°$).

CHAPTER 6

CONCLUSIONS AND RECOMMENDATIONS

Several passive and active separation control techniques for controlling two-dimensional turbulent flow separation over a backward-facing ramp were investigated in a wind tunnel. The following conclusions are drawn from the study:

1. Transverse grooves, located in the maximum $+dP/dx$ region with a height-to-width ratio greater than 2.5, reduced the extent of separation by 25% over the baseline configuration. Unlike the transverse and longitudinal grooves of equivalent size, the 45° swept-groove configurations tested in the present study enhanced separation.
2. Riblets that decreased skin friction had virtually no effect on flow separation, while riblets that increased skin friction enhanced flow separation when placed in the immediate region of the flow separation. The separation enhancement due to the drag-increasing riblets can be eliminated by increasing the distance between the trailing edge of the riblet and the separated-flow region to at least 15δ.
3. All passive porous surface configurations tested tended to enhance separation. This was probably the result of an increased momentum deficit near the wall for the normal injection experiments and insufficient mass flow for tangential injection.
4. Closely-packed, large longitudinal grooves with $\lambda/\delta \sim 1.5$ reduced the extent of separation by up to 55%. A 'short' longitudinal V-groove configuration with a constant groove slope performed slightly better than either the 'long' longitudinal V-groove or sine-wave groove configurations, while imposing a much smaller volume-loss penalty.

5. Submerged doublet, wishbone, and vane-type vortex generators with $h/\delta \sim 0.1$ to 0.2 were effective in separation control, and optimum streamwise locations were between 5 to 10 device heights upstream of separation. Properly placed, these vortex generators can perform almost as well as conventional δ-scale vortex generators which have a device height (and device drag) an order-of-magnitude higher. Vane-type vortex generators with $h \sim 0.2\delta$ reduced the extent of separation by almost 90%. Wishbone generators with device height below 0.05δ ($y^+ \sim 150$) demonstrated an adverse effect on pressure recovery and separation control.
6. LEBU's at a small positive angle of attack of 10°, placed near baseline separation, were effective in suppressing the extent of separation by up to 30% while LEBU' s at a negative angle of attack enhanced separation. Trailing-edge serrations on LEBU's did not produce any noticeable changes in the separated flow.
7. For reducing the extent of flow separation, the most effective diameter for spanwise cylinders was 0.2δ, the most effective height was 0.8δ, and the most effective streamwise location was at 5δ upstream of baseline separation. Due to high device drag, the streamwise pressure distributions showed an adverse effect on pressure recovery for most of the cylinders tested.
8. Arch configurations with $\alpha = 0°$ (nonlifting arches) did not significantly affect flow separation. The vortical structures produced by the arches lasted a long distance (up to 40δ) downstream of the devices. Elongated arches with $\alpha = 10°$ (lifting arches) reduced the extent of separation by up to 50% when placed at the baseline separation line.
9. The Helmholtz resonators examined had little or no effect on flow separation even though they generated acoustical disturbances.

10. Viets' fluidic flappers enhanced flow separation significantly when placed close (3δ upstream) to the baseline separation line. However, when the devices were moved 10δ upstream of the separation, they reduced the extent of separation by up to 35%.
11. Most VGJ configurations examined were effective in reducing the extent of separation by up to 90%. VGJ's seemed to perform best for azimuth angles, β, of 60° to 90° and for inclination angles, α, of 15° to 25°. There was no effect on separation for VGJ's blowing vertically ($\alpha = 90°$). For constant flow rate, the smallest diameter jet tested (1/32 in.), corresponding to the highest velocity ratio, was the most effective in separation control. Furthermore, the effect of the VGJ's lasted a long distance (at least 40δ) downstream.
12. Wall heat-transfer computations indicated that wall cooling delays flow separation but also increases wall shear stress. Compared to the full-surface coverage case, partial wall cooling with minimum surface coverage from just 0.2δ upstream of the adiabatic reference separation can still maintain at least a 50% effectiveness in separation delay, while reducing the increase in skin-friction drag by two orders of magnitude.

The flow physics associated with five of the vortex generating devices were investigated in a water tunnel. The following conclusions were drawn from that study:

1. Wishbone vortex generators in the forward orientation shed horseshoe vortices at low speeds. Doublet vortex generators and wishbone vortex generators in the reverse orientation shed streamwise counterrotating vortices.
2. LEBU's at $\alpha = -10°$ produced eddies which rotated in the same direction as the mean transverse vorticity in a turbulent boundary layer. However, these LEBU's also tended to divert momentum away from the wall, which increased separation. The opposite was true for LEBU's at $\alpha = +10°$.

3. Spanwise cylinders located near the wall produced eddies which rotated in the same direction as the mean transverse vorticity in a turbulent boundary layer, but wind-tunnel results indicated that minimum distances of 10δ downstream from the device were required to allow recovery from the device-induced momentum deficit.
4. As azimuthal angle, β, of the VGJ's increased from 0° to 90°, both the downstream rotational speed and vortex core size increased for the longitudinal (co-rotating) vortices. For $\beta \gg 0°$, the signs of observed vorticity for laminar and turbulent jets were opposite each other.

Finally, it is concluded that embedded streamwise (longitudinal) vortices, whether generated by protuberances or jets, provide the most effective and efficient means of delaying or mitigating flow separation in two-dimensional turbulent boundary layers. In other words, transferring momentum from the outer region of the boundary layer by means of embedded streamwise vortices is evidently more efficient than such transfer by either enhanced Reynolds stresses or quasi-coherent dynamic transverse vortices.

Future work is recommended for successful flow-control devices such as sub-δ-scale vortex generators and VGJ's. Detailed flowfield surveys downstream of these vortex generating devices will be extremely helpful in gaining further understanding of the associated flow physics. Such understanding is very important for aiding direct numerical simulation of the device-induced complex flowfields. If possible, sub-δ-scale vortex generators and VGJ's should be examined in three-dimensional separated flows as well as in high-Reynolds-number and/or high-speed tunnels.

REFERENCES

1. Maskell, E. C., "Flow Separation in Three Dimensions," Royal Aircraft Establishment RAE Report Aero 2565, Farnborough, England, 1955.

2. Smith, A. M. O., Stokes, T. R., Jr., and Lee, R. S., "Optimum Tail Shapes for Bodies of Revolution," *Journal of Hydronautics*, Vol. 15, Nos. 1–4, 1981, pp. 67–73.

3. Bushnell, D. M., "Flow Separation Control," Invited Lecture at University of Kansas, 1986.

4. Gad-el-Hak, M., and Bushnell, D. M., "Separation Control: Review," *Journal of Fluids Engineering*, Vol. 113, 1991, pp. 5–30.

5. Migay, V. K., "Diffuser with Transverse Fins," *Energomashinostroenie*, No. 4, 1960, p. 31.

6. Migay, V. K., "Increasing the Efficiency of Diffusers by Fitting transverse Fins," *Teploenergetika*, No. 4, 1961, pp. 41–43.

7. Migay, V. K., "The Efficiency of a Cross-Ribbed Curvilinear Diffuser," *Energomashinostroenie*, No. 1, 1962, pp. 45–46.

8. Migay, V. K., "A Study of Finned Diffusers," *Teploenergetika*, No. 10, 1962, pp. 55–59.

9. Chang, P. K., *Control of Flow Separation*, Hemisphere Publishing Corporation, Washington, D.C., 1976.

10. Stull, F. D., and Velkoff, H. R., "Effects of Transverse Ribbs on Pressure Recovery in Two-Dimensional Subsonic Diffusers," AIAA Paper 72-1141, November–December 1972.

11. Stull, F. D., and Velkoff, H. R., "Flow Regimes in Two-Dimensional Ribbed Diffusers," *Journal of Fluids Engineering*, Vol. 97, No. 1, 1975, pp. 87–96.

12. Howard, F. G., Goodman, W. L., and Walsh, M. J., "Axisymmetric Bluff-Body Drag Reduction Using Circumferential Grooves," AIAA Paper 83-1788, July 1983.

13. Howard, F. G., and Goodman, W. L., "Axisymmetric Bluff-Body Drag Reduction Through Geometrical Modification," *Journal of Aircraft*, Vol. 22, 1985, pp. 516–522.

14. Walsh, M. J., "Turbulent Boundary Layer Drag Reduction Using Riblets," AIAA Paper 82–0169, January 1982.

15. Walsh, M. J., and Lindemann, A. M., "Optimization and Application of Riblets for Turbulent Drag Reduction," AIAA Paper 84-0347, January 1984.

16. Walsh, M. J., Sellers, W. L., III, and McGinley, C. B., "Riblet Drag at Flight Conditions," *Journal of Aircraft*, Vol. 26, No. 6, 1989, pp. 570–575.

17. Truong, T. V., and Pulvin, Ph., "Influence of Wall Riblets on Diffuser Flow," *Applied Scientific Research*, Vol. 46, No. 3, 1989, pp. 217–227.

18. Schlichting, H., *Boundary Layer Theory*, 7th edition, McGraw-Hill, New York, 1979.

19. King, P. I., Martens, N. W., and Franke, M. E., "Effect of Riblet on Flow Separation in a Subsonic Diffuser," Presented at the 3rd Joint ASCE/ASME Mechanics Conference, San Diego, California, July 9–12, 1989.

20. Bahi, L., Ross, J. M., and Nagamatsu, H. T., "Passive Shock Wave/Boundary Layer Control for Transonic Airfoil Drag Reduction," AIAA Paper 83-0137, January 1983.

21. Savu, G., and Trifu, O., "Porous Airfoils in Transonic Flow," *AIAA Journal*, Vol. 22, 1984, pp. 989–991.

22. Nagamatsu, H. T., Dyer, R., and Ficarra, R. V., "Supercritical Airfoil Drag Reduction by Passive Shock Wave/Boundary Layer Control in the Mach Number Range .75 to .90.," AIAA Paper 85-0207, January 1985.

23. Nagamatsu, H. T., Trilling, T. W., and Bossard, J. A., "Passive Drag Reduction on a Complete NACA 0012 Airfoil at Transonic Mach Numbers," AIAA Paper 87–1263, June 1987.

24. Barnwell, R., Bushnell, D. M., Nagamatsu, H. T., Bahi, L., and Ross, J., "Passive Drag Control of Airfoils at Transonic Speeds," U.S. Patent No. 4,522,360, 1985.

25. Raghunathan, S., McIlwain, S., and Mabey, D., "Wide Angle Diffusers with Passive Boundary-Layer Control," AIAA Paper 90-1600, June 1990.

26. Howard, F. G., Quass, B. F., Weinstein, L. M., and Bushnell, D. M., "Longitudinal Afterbody Grooves and Shoulder Radiusing for Low-Speed Bluff Body Drag Reduction," ASME Paper 81-WA/FE-5, November 1981.

27. Quass, B., Howard, F., Weinstein, L., and Bushnell, D., "Longitudinal Grooves for Bluff-Body Drag Reduction," *AIAA Journal*, Vol. 19, 1981, pp. 535–537.

28. Selby, G. V., and Miandoab, F. H., "Effect of Surface Grooves on Base Pressure for a Blunt Trailing-Edge Airfoil," *AIAA Journal*, Vol. 28, 1990, pp. 1133–1135.

29. Taylor, H. D., "The Elimination of Diffuser Separation by Vortex Generators," United Aircraft Corporation Report No. R-4012-3, 1947.

30. Taylor, H. D., "Design Criteria for and Applications of the Vortex Generator Mixing Principle," United Aircraft Corporation Report No. M-15038-1, 1948.

31. Taylor, H. D., "United Aircraft Research Department Summary Report on Vortex Generators," United Aircraft Corp. Research Dept., Report R-05280-9, 1950.

32. Schubauer, G. B., and Spangenber, W. G., "Forced Mixing in Boundary Layers," *Journal of Fluid Mechanics*, Vol. 8, Part 1, 1960, pp. 10–32.

33. Pearcey, H. H., "Shock Induced Separation and Its Prevention by Design and Boundary-Layer Control," *Boundary Layer and Flow Control its Principle and Applications*, Vol. 2, ed. G. V. Lachman, Pergamon Press, Oxford, England, 1961, pp. 1166–1344.

34. Nickerson, J. D., "A Study of Vortex Generators at Low Reynolds Numbers," AIAA Paper 86-0155, January 1986.

35. Bragg, M. B., and Gregorek, G. M., "Experimental Study of Airfoil Performance with Vortex Generators," *Journal of Aircraft*, Vol. 24, 1987, pp. 305–309.

36. Calarese, W., Crisler, W. P., and Gustafson, G. L., "Afterbody Drag Reduction by Vortex Generators," AIAA Paper 85-0354, January 1985.

37. Wortmann, A., "Alleviation of Fuselage from Drag Using Vortex Flows," Department of Energy Report No. DOE/CE/15277-T1, 1987.

38. Henry, J. R., Wood, C. C., and Wilbur, S. W., "Summary of Subsonic Diffuser Data," NACA RML-56F05, 1956.

39. Feir, J. B., "The Effects of an Arrangement of Vortex Generators Installed to Eliminate Wind Tunnel Diffuser Separation," UTIAS Technical Note No. 87, June 1965.

40. Brown, A. C., Nawrocki, H. F., and Paley, P. N., "Subsonic Diffusers Designed Integrally with Vortex Generators," *Journal of Aircraft*, Vol. 5, No. 3, 1968, pp. 221–229.

41. Kuethe, A. M., "Effect of Streamwise Vortices on Wake Properties Associated with Sound Generation," *Journal of Aircraft*, Vol. 9, No. 10, 1972, pp. 715–719.

42. Holmes, A. E., Hickey, P. K., Murphy, W. R., and Hilton, D. A., "The Application of Sub-Boundary Layer Vortex Generators to Reduce Canopy Mach Rumble Interior Noise on the Gulfstream III," AIAA Paper 87-0084, January 1987.

43. Rao, D. M., and Kariya, T. T., "Boundary-Layer Submerged Vortex Generators for Separation Control—An Exploratory Study," AIAA Paper 88-3546-CP, July 1988.

44. Kehro, M., Hutcherson, S., Lieback, R., and Blackwelder, R., "Vortex Generators Used to Control Laminar Separation Bubbles," AIAA Paper 90-0051, January 1990.

45. McCormick, D. C., "Shock-Boundary Layer Interaction Control with Low-Profile Vortex Generators and Passive Cavity," AIAA Paper 92-0064, January 1992.

46. Wheeler, G. O., "Means of Maintaining Attached Flow of a Flow Medium," U.S. Patent No. 4455045, 1984.

47. Wheeler, G. O., "Low Drag Vortex Generators," U.S. Patent No. 5058837, 1991.

48. Mossman, E. A., and Randall, L. M., "An Experimental Investigation of the Design Variables for NACA Submerged Duct Entrances," NACA RMA7130, 1948.

49. Corke, T. C., Guezennec, Y., and Nagib, H. M., "Modification in Drag of Turbulent Boundary Layers Resulting from Manipulation of Large-Scale Structures," *Viscous Flow Drag Reduction*, ed. G. R. Hough, AIAA *Prog. in Astro & Aero.*, Vol. 72, 1980, pp. 128–143.

50. Anders, J. B., "Outer-Layer Manipulators for Turbulent Drag Reduction," *Viscous Drag Reduction in Boundary Layers*, eds. D. M. Bushnell and J. N. Hefner, AIAA *Prog. in Astro & Aero.*, Vol. 123, 1990.

51. Moser, A., "Experimental Investigation of Wake/Boundary-Layer Interacting and the Flow Control Rail," McDonnell Douglas Res. Lab. Rpt. MDC Q-511, December 1973.

52. Sajben, M., Chen, C. P., and Kroutil, J. C., "A New Passive Boundary-Layer Control Device," AIAA Paper 76-700, 1976.

53. Marumo, E., Suzuki, K., and Sato, T., "A Turbulent Boundary Layer Disturbed by a Cylinder," *Journal of Fluid Mechanics*, Vol. 87, Pt. 1, 1978, pp. 121–141.

54. De, Z. M., and Savill, A. M., "Wake/Boundary Layer and Wake/Wake Interactions—Smoke Flow Visualization and Modeling," Presented at 2nd Asian Congress of Fluid Mechanics, Beijing, China, October 1983.

55. Bearman, P. W., and Zdravkovich, M. M., "Flow Around a Circular Cylinder Near a Plane Boundary," *Journal of Fluid Mechanics*, Vol. 89, Pt. 1, 1978, pp. 33–47.

56. Sakamoto, H., and Arie, M., "Vortex Shedding from a Rectangular Prism and a Circular Cylinder Placed Vertically in a Turbulent Boundary Layer," *Journal of Fluid Mechanics*, Vol. 126, 1983, pp. 147–165.

57. Sakamoto, H., and Arie, M., "Flow Around a Normal Plate of Finite Width Immersed in a Turbulent Boundary Layer," *Journal of Fluids Engineering*, Vol. 105, 1983, pp. 98-104.

58. Panton, R. L., and Miller, J. M., "Excitation of a Helmholtz Resonator by a Turbulent Boundary Layer," *Journal of Acoustical Society of America*, Vol. 58, No. 4, Oct. 1975, pp. 800–806.

59. Panton, R. L., "Excitation of Helmholtz Resonators by Turbulent Boundary Layers; the Effect of Orifice Geometry," AIAA Paper 88-0181, January 1988.

60. De Metz, F. C., and Farabee, T. M., "Laminar and Turbulent Shear Flow Induced Cavity Resonances," AIAA Paper 77-1293, October 1977.

61. Flynn, K., Panton, R., and Bogard, D., "The Effect of a Row of Helmholtz Resonators on the Turbulence of a Boundary Layer," AIAA Paper 89-0961, March 1989.

62. Viets, H., "Coherent Structures in Time Dependent Shear Flows," in *Turbulent Boundary Layers*, AGARD/NATO CPP-271, Paper No. 5, Nevilly Sur Seine, France, 1980.

63. Viets, H., Ball, M., and Bougine, D., "Performance of Forced Unsteady Diffusers," AIAA Paper 81-0154, January 1981.

64. Viets, H., Palmer, G. M., and Bethke, R. J., "Potential Applications of Forced Unsteady Flows," *Unsteady Separated Flows*, eds. M. S. Francis and M. W. Luttges, U.S. Air Force Academy, Colorado Springs, CO, 1984, pp. 21–27.

65. Wallis, R. A., "The Use of Air Jets for Boundary-Layer Control," Aerodynamics Research Laboratories, Australia, Aero Note 110, 1952.

66. Compton, D., and Johnston, J., "Streamwise Vortex Production by Pitched and Skewed Jets in a Turbulent Boundary Layer," AIAA Paper 91-0038, January 1991.

67. Pearcey, H., and Stuart, C., "Methods of Boundary-Layer Control for Postponing and Alleviating Buffeting and Other Effects of Shock-Induced Separation," SMF Paper No. FF-22, Institute of the Aeronautical Sciences, 1959.

68. Zhang, S., and Li, F., "Experiments About the Air Jet Vortex Generator," *Proceedings of 8th Institute of Aeronautics and Astronautics*, Cincinnati, Ohio, 1987, pp. 513–516.

69. Ball, W. H., "Tests of Wall Blowing Concepts for Diffuser Boundary Layer Control," AIAA Paper 84-1276, June 1984.

70. Johnston, J., and Nishi, M., "Vortex Generator Jets—Means for Flow Separation Control," *AIAA Journal*, Vol. 28, No. 6, 1990, pp. 989–994.

71. Lees, L., "The Stability of the Laminar Boundary Layer in Compressible Fluid," NACA Report 876, 1947.

72. Lee, J. D., "The Influence of Heat Transfer on the Drag of Airfoils," AFWAL-TR-81-3030, April 1981.

73. Brewer, G. D., and Miranda, L. R., "Experimental Study of Achieving Laminar Flow Control by Cryogenic Wall Cooling," Lockheed-California Co., Report LR 29012, March 1979.

74. Theisen, J. G., Brewer, G. D., and Miranda, L. R., "Laminar Flow Stabilization by Surface Cooling on Hydrogen Fueled Aircraft," AIAA Paper 79-1863, August 1979.

75. Lin, J. C., and Ash, R. L., "Wall Temperature Control of Low-Speed Body Drag," *Journal of Aircraft*, Vol. 23, No. 1, 1986, pp. 93–94.

76. Coles, D. E., "The Turbulent Boundary Layer in a Compressible Fluid," Rand Report R-403-PR, 1962.

77. White, B. R., "Low-Reynolds-Number Turbulent Boundary Layers," *Journal of Fluids Engineering*, Vol. 103, 1981, pp. 624-630.

78. "Model 1050/1050AA Constant Temperature Anemometer Instruction Manual," TSI, Inc., St. Paul, 1984.

79. Sandborn, V. A., *Resistance Temperature Transducers*, Metrology Press, Fort Collins, 1972.

80. Perry, A. E., *Hot-Wire Anemometry*, Oxford University Press, New York, 1982.

81. Buchhave, P., George, W. K., and Lumley, J. L., "The Measurement of Turbulence with the Laser Doppler Anemometer," *Annual Review of Fluid Mechanics*, Vol. 11, 1979, pp. 443–503.

82. Adrian, R. J., and Fingerson, L. M., "Laser Anemometry; Theory, Application, and Techniques," TSI, Inc., St. Paul, 1982.

83. White, F. M., *Viscous Fluid Flow*, McGraw-Hill, New York, 1974.

84. Gersten, K., Herwig, H., and Wauschkuhn, P., "Theoretical and Experimental Investigation of Two-Dimensional Flow with Separated Regions of Finite Length," AGARD-CP-291, Paper 23, 1980.

85. Komerath, N. M., Ahuja, K. K., and Chambers, F. W., "Prediction and Measurement of Flows Over Cavities—A Survey," AIAA Paper 87-0166, January 1987.

86. Neary, M. D., "Time-Dependent Self-Sustaining Oscillations of Cavity Flow," AIAA Paper 87-0142, January 1987.

87. Wilkinson, S. P., "Influence of Wall Permeability on Turbulent Boundary-Layer Properties," AIAA Paper 83-0294, January 1983.

88. Panton, R. L., and Miller, J. M., "Resonant Frequencies of Cylindrical Helmholtz Resonators," *Journal of Acoustical Society of America*, Vol. 57, pp. 1533–1535.

89. Cebeci, T., Mosinskis, G. J., and Smith, A. M. O., "Calculation of Separation Points in Incompressible Turbulent Flow," *Journal of aircraft*, Vol. 9, No. 9, 1972, pp. 618–624.

90. Keith, J. S., Ferguson, D. R., and Heck, P. H., "User Manual for Steam-tube Curvature Analysis—Analytical Method for Predicting the Pressure Distribution about a Nacelle at Transonic Speeds," NASA CR-112239, General Electric Company.

91. Harris, J. E., and Blanchard, D. K., "Computer Program for Solving Laminar, Transitional, or Turbulent Compressible Boundary-Layer Equations for Two-Dimensional and Axisymmetric Flow," NASA TM 83207, February 1982.

92. Acarlar, M. S., and Smith, C. R., "An Experimental Study of Hairpin-Like Vortices as a Potential Flow Structure of Turbulent Boundary Layers," Report FM-5, Department of Mechanical Engineering and Mechanics, Lehigh University, 1984.

93. Smith, C. R., Greco, J. J., and Hopper, P. B., "Low-Loss Conditioning Using Concepts of Passive Vortex Generation," *Proceedings of ASME Forum on Industrial Applications of Fluid Mechanics*, ed. T. Morrow, ASME Press, 1990, pp. 57–62.

94. Gretta, W. J., "An Experimental Study of the Fluid Mixing Effects and Flow Structure Due to a Surface Mounted Passive Vortex Generating Device," M.S. Thesis, Department of Mechanical Engineering and Mechanics, Lehigh University, 1990.

95. Robinson, S. K., "Coherent Motions in the Turbulent Boundary Layer," *Annual Review of Fluid Mechanics*, Volume 23, pp. 601–639, 1991.

96. Robinson, S. K., "The Kinematics of Turbulent Boundary Layer Structure," NASA TM 103859, April 1991.

97. Smith, C. R., and Schwartz, S. P., "Observation of Streamwise Vortices in the Near-Wall Region of a Turbulent Boundary Layer," *Physics of Fluids*, Vol. 26, No. 3, 1983, pp. 641–652.

98. Ersoy, S., and Walker, J.D.A., "Viscous Flow Induced by Counter-Rotating Vortices," *Physics of Fluids*, Vol. 28, No. 9, 1985, pp. 2687–2698.

99. Peridier, V. J., Smith, F. T., and Walker, J. D. A., "Vortex-Induced Boundary-Layer Separation. Part 2: Unsteady Interacting Boundary-Layer Theory," *Journal of Fluid Mechanics*, Vol. 232, 1991, pp. 133–165.

100. Govindaraju, S. P., and Chambers, F. W., "Direct Measurements of Drag of Ribbon-Type Manipulators in a Turbulent Boundary Layer," *AIAA Journal*, Vol. 25, 1987, pp. 388–394.

APPENDIX A

WIND-TUNNEL SURVEY

A.1 Boundary-Layer Parameters

To validate the flow quality upstream of the separation ramp, boundary-layer velocity profiles were measured on the (floor) test plate every 6 in. along the centerline between $x = 34$ in. ($X/\delta \sim -40$) and $x = 76$ in. ($X/\delta \sim -5$). A pitot probe/pitot-static probe arrangement was used in surveying the boundary layer (see Figure A.1). The pitot probe was mounted on a traverse mechanism that was automatically controlled by a MASSCOMP computer which positioned the probe at pre-selected y-increments.

Two thousand data samples were averaged over fifty seconds at each y-position to define the mean local boundary-layer velocity. The upper probe (pitot-static) measured freestream total minus static pressure which defined the freestream velocity, while the lower probe (pitot) measured total boundary-layer pressure. This value of the total pressure, P_t, was combined with the static pressure from the upper probe, P_∞, to define the boundary-layer velocity at a point using the expression

$$u = \left[\frac{2(P_t - P_\infty)}{\rho}\right]^{1/2} \tag{A-1}$$

Between 25 and 35 points were taken in each boundary-layer survey. A typical velocity profiles at $x = 46$ in. ($X/\delta \sim -30$) is presented in Figure A.2. It can be observed in the figure that the measured profile has the shape that is usually characteristic of turbulent boundary layers—high velocity gradients near the wall.

The boundary-layer thickness, δ, was defined as the normal distance from the wall where the local velocity reaches 99.5% of the freestream velocity. Hence the displacement thickness, δ^*, and momentum thickness, θ, were obtained through integration of the velocity profiles from pitot surveys using the relation

$$\delta^* = \int_o^\delta \left(1 - \frac{u}{U_\infty}\right) dy \tag{A-2}$$

and

$$\theta = \int_o^\delta \frac{u}{U_\infty}\left(1 - \frac{u}{U_\infty}\right) dy \tag{A-3}$$

Figure A.3 shows the streamwise variation of the boundary-layer parameters δ^*, θ, and $\delta/10$ from 40δ to 5δ upstream of the baseline separation. As expected, the value of these parameters increased as a function of increasing streamwise distance, x, from the boundary-layer trip. However, these values began to level off near the separation ramp. This was likely due to the slightly accelerated local flow (that resulted in the thinning of the boundary layer) as the flow tried to turn the *corner* on the curved ramp. Throughout the survey, δ^* and θ maintained values that were approximately 15% and 11% of the local δ, respectively.

The streamwise variation of Reynolds number based on momentum thickness, R_θ, and skin-friction coefficient, C_f, are shown in Figure A.4. R_θ was defined as

$$R_\theta = \frac{U_\infty \theta}{\nu} \tag{A-4}$$

and C_f was extrapolated from Coles data [76] as shown in Figure A.5, where C_f decreases as R_θ increases.

In order to produce results which might be extended to other work, the flow past the model ramp was required to be reasonably two dimensional such that the spanwise variation of θ was no more than 5%. For this reason, spanwise velocity profile measurements were made at $x = 76$ in. ($X/\delta \sim -5$) with spanwise measurement intervals of 0.5 in. (0.4δ). The results are presented in Figure A.6 showing θ as a function of

z/W, where W denotes width of the test section. As can be seen, over the central 77% of the test section the flow was reasonably two dimensional with maximum variation in θ of no more than 4.5%.

The velocity profiles were also plotted in wall and defect variables as shown in Figures A.7 and A.8, respectively. The selected locations for these plots were at $x = 34$, 54, and 76 in. ($X/\delta \sim -40, -20$, and -5, respectively). The semi-log plot of Figure A.7 compares the present experimental data to Coles' universal law of the wall curve [76] expressed as

$$u^+ = \frac{1}{0.41} \ln y^+ + 5.0 \tag{A-5}$$

where the wall variables,

$$u^+ = \frac{u}{u_\tau} \tag{A-6}$$

$$y^+ = \frac{y u_\tau}{\nu} \tag{A-7}$$

and

$$u_\tau = U_\infty \sqrt{\frac{C_f}{2}} \tag{A-8}$$

Figure A.7 shows that the current data for all three streamwise locations are in excellent agreement with the generally accepted empirical relation for the turbulent log (or overlap) region where $30 \lesssim y^+ \lesssim (0.1\delta^+$ to $0.2\delta^+)$. The $0.1\delta^+$ term corresponds to a y^+ value of approximately 300. It should be noted that the physical size of the pitot probe limited the boundary-layer velocity measurements to within 0.015 in. from the wall. This distance corresponds to $y^+ \sim 36$ which was outside most of the wall (sublayer and buffer) region.

Figure A.8 compares the present data to the Coles' empirical law of the wake [76,77] which was expressed as

$$\frac{(U_\infty - u)}{u_\tau} = \frac{1}{0.41} \left[-\ln\left(\frac{y}{\delta}\right) + \Pi(2 - W) \right] \tag{A-9}$$

where

$$\left.\begin{aligned} \Pi &= 0.55\left[1-\exp\left(-0.243\xi^{\frac{1}{2}}-0.298\xi\right)\right] \\ \xi &= \frac{R_\theta}{425}-1 \\ W &= 2\sin^2\left[\frac{\pi}{2}\left(\frac{y}{\delta}\right)\right] \end{aligned}\right\} \qquad \text{(A-10)}$$

The figure shows that within the turbulent wake region where $0.2 \leq \frac{y}{\delta} \leq 1$ the present data are also in excellent agreement with the empirical relation.

Based on results presented in Figures A.7 and A.8, one can conclude that the boundary layer of present interest, from near the baseline separation (where $R_\theta \sim 9100$) to 40δ upstream from it (where $R_\theta \sim 6300$), is well within the generally accepted turbulent flow regime.

A.2 Freestream Turbulence Intensity

Measurement of freestream turbulence intensity was performed in the test section using hot-wire anemometry as part of the effort to document tunnel flow quality. Two identical single-wire probes were used. The tungsten wires were 0.00015 in. in diameter with an unplated active length of 0.05 in. Each hot-wire probe was connected to a TSI Model 1050 constant-temperature hot-wire anemometer. The bridge output of the hot-wire anemometer was read and stored via the Nicolet digital oscilloscope during wind tunnel tests. The data were then read by a HP1000 computer through the IEEE-488 interface bus.

Both hot-wire probes were calibrated against a pitot-static probe at the same location where the freestream velocity fluctuation measurement was made. The measurement was made at $x = 46$ in. ($X/\delta \sim -30$) and the approximate center of the cross sectional plane of the test section. The pitot-static and hot-wire probes were all separated sufficiently (2 in.) so that the disturbance caused by one device did not interfere with the others. It was necessary to insure that the pitot-static and hot-wire probes were all sensing the same velocity. To verify this, the pitot-static probe was traversed through all three

probe locations and it was observed that there was no measurable velocity gradient in this region. The hot wires were operated at overheat ratios of 1.6 and were calibrated by recording the mean voltage, $\overline{E}$, from the anemometer bridge output as a function of freestream velocity in the range of 8 ft/s $< U_\infty <$ 152 ft/s. This gave a pair of coordinates on the calibration curve. It is accepted that such a relationship between bridge output and freestream velocity can be expressed as a fourth order polynomial [78,79]

$$U_\infty = a_0 + a_1\overline{E} + a_2\overline{E}^2 + a_3\overline{E}^3 + a_4\overline{E}^4 \qquad \text{(A-11)}$$

A computer program was written to fit the polynomial using the method of least squares and to obtain the coefficients of the polynomial (i.e., a_0, a_1, a_2, a_3, a_4). A set of data points and the fitted curves are shown in Figure A.9 for the two hot wires. The coefficients of the polynomial were used to obtain velocities from hot-wire measurements.

When measuring low-intensity turbulence such as in the freestream, it is quite often necessary to correct for electronic (instrument) noise [80]. The method employed here was to (digitally) take the square root of the product of the two hot-wire signals. Since the noise signals in each of the two independent hot-wire system would not correlate with each other nor with any fluctuating hot-wire signal, the terms associated with the noise automatically dropped out after taking the time average of the product of the two hot-wire signals, as demonstrated below.

For example, assume

$$e_1 = e_t + e_{n1}$$

$$e_2 = e_t + e_{n2}$$

where

e_1 and $e_2 \equiv$ fluctuating hot-wire signals from hot wires 1 and 2, respectively.

$e_t \equiv$ the freestream turbulence signal measured by both hot wires.

e_{n1} and $e_{n2} \equiv$ electronic noise within hot-wire systems 1 and 2, respectively.

So

$$e_1 \cdot e_2 = (e_t + e_{n1})(e_t + e_{n2})$$
$$= e_t^2 + \{e_t e_{n1} + e_t e_{n2} + e_{n1} e_{n2}\}$$

the terms inside the bracket, { }, are now uncorrelated, and hence upon taking the time average of the above equation the terms inside the bracket are zero. Then

$$\overline{e_t^2} = \overline{e_1 \cdot e_2}$$

or

$$e_t' = \sqrt{\overline{e_t^2}} = \sqrt{\overline{e_1 \cdot e_2}} \tag{A-12}$$

The streamwise fluctuating velocity u' is expressed

$$u' = \frac{1}{k} e_t' \tag{A-13}$$

$k = \frac{\Delta \overline{E}}{\Delta U_\infty}$ is the local slope of the calibration curve (Figure A.9).

The freestream turbulence intensity was defined as u'/U_∞. Variation of freestream turbulence intensity as a function of freestream velocity is shown in Figure A.10. At the freestream velocity (U_∞ = 132 ft/s) associated with the present study, the intensity was approximately in the range of 0.3 to 0.4%. For low speed tunnel applications this is considered low turbulence intensity level and was acceptable for the present study [18].

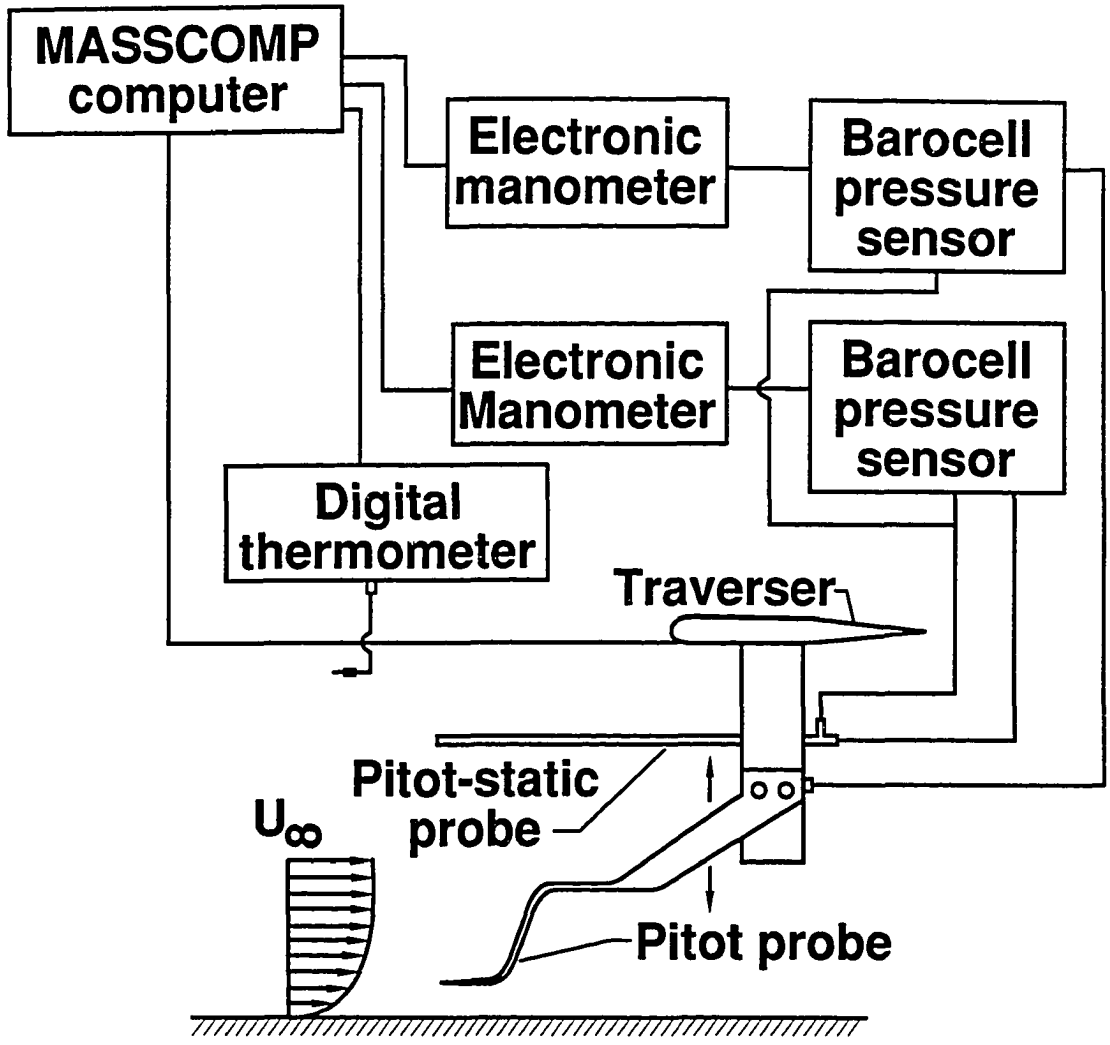

Figure A.1 Schematic representation of the pitot survey system.

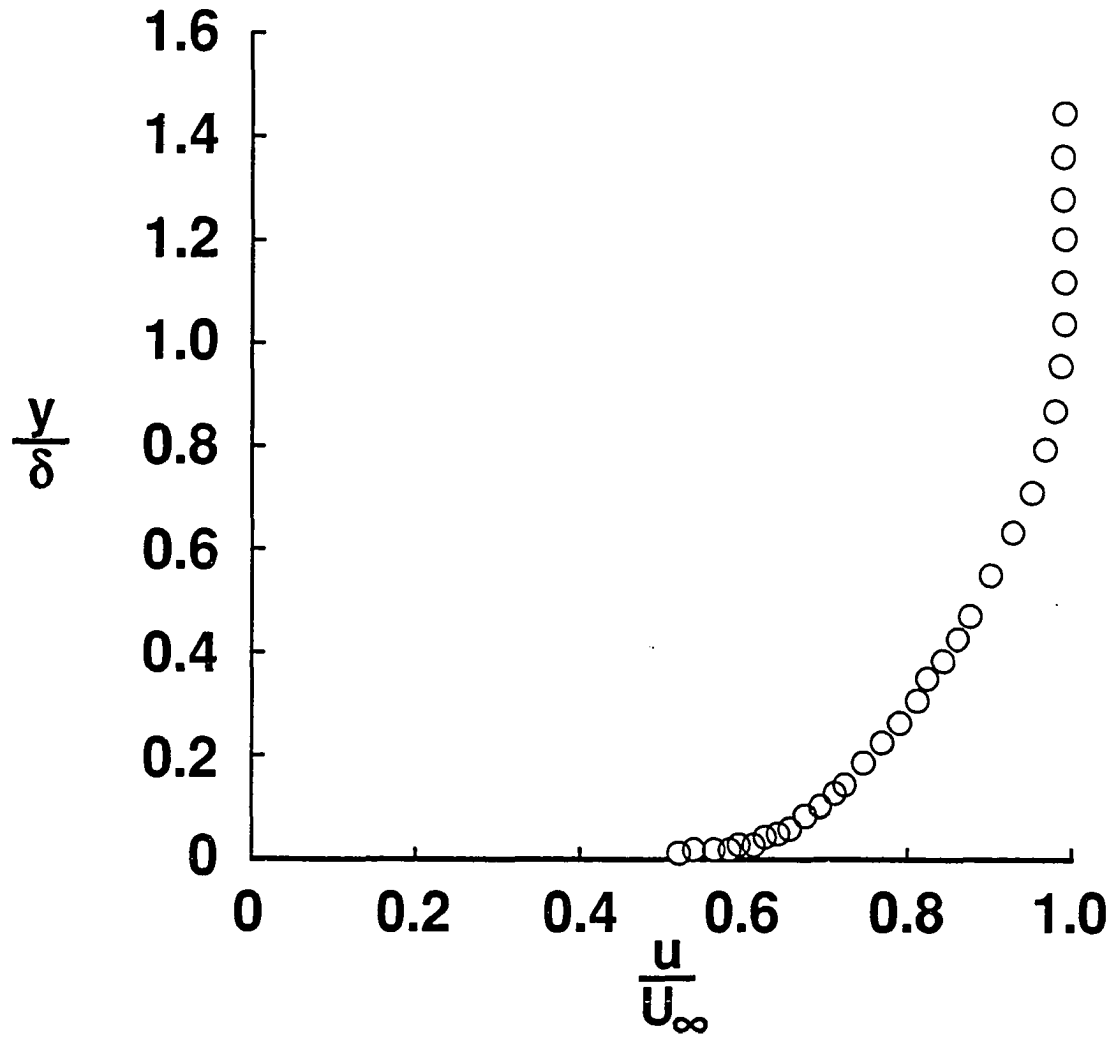

Figure A.2 Typical boundary-layer velocity profile at $x = 46$ in. and $R_\theta = 7451$.

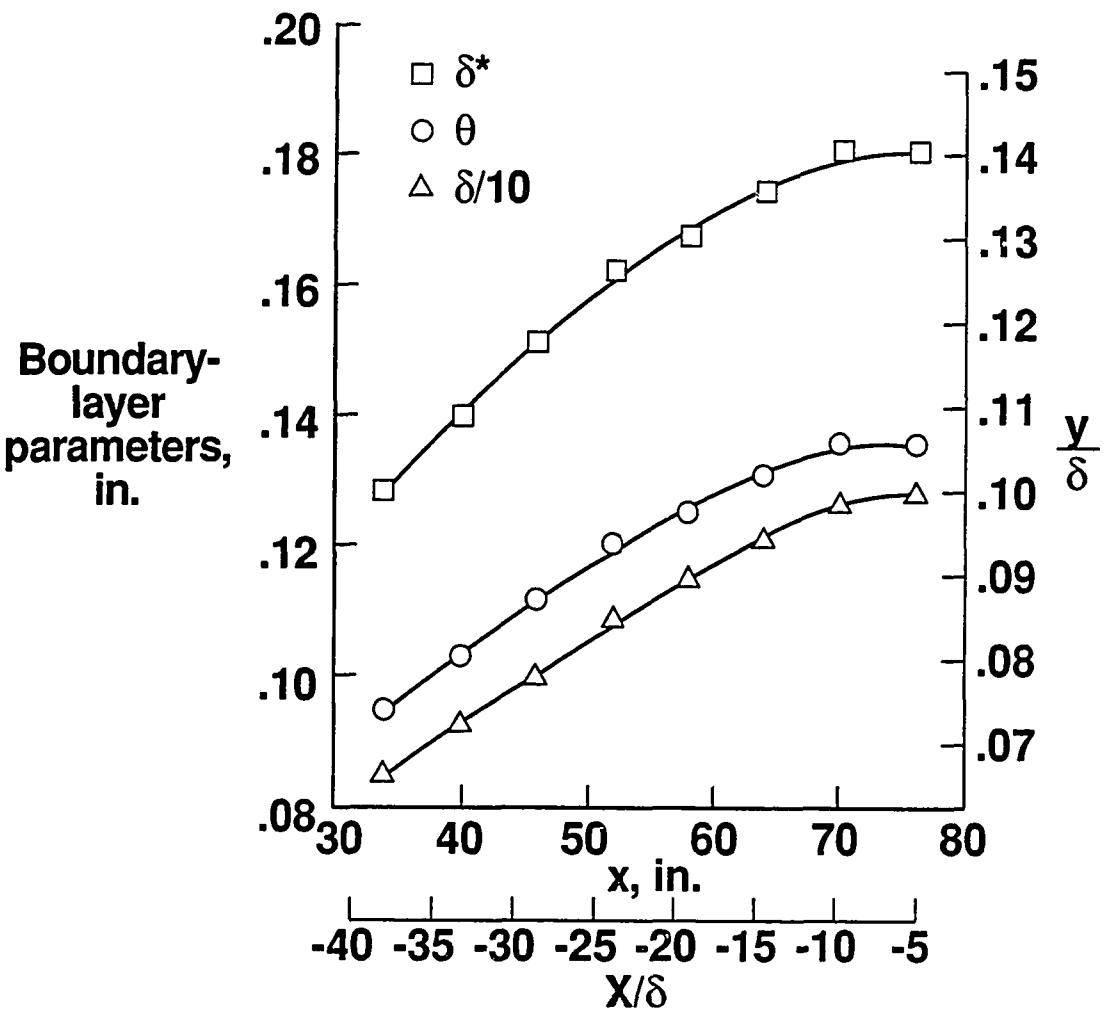

Figure A.3 Streamwise variation of δ^*, θ, and $\delta/10$ between $x = 34$ and 76 in.

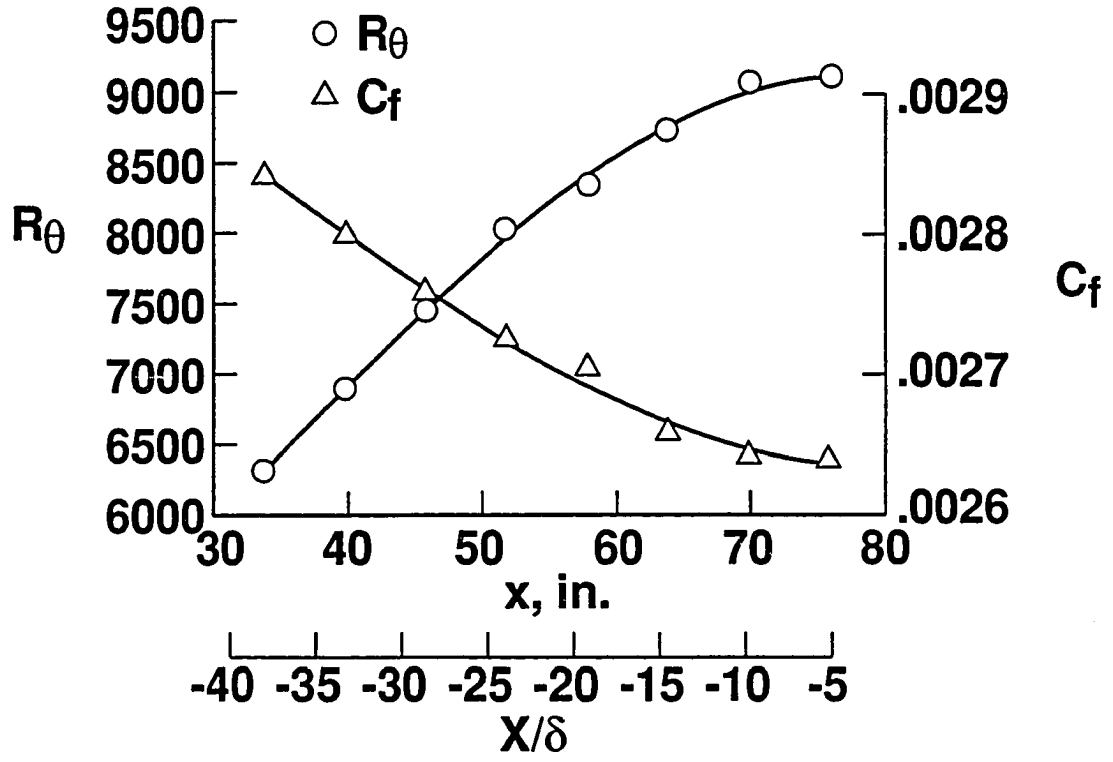

Figure A.4 Streamwise variation of R_θ and C_f between x = 34 and 76 in.

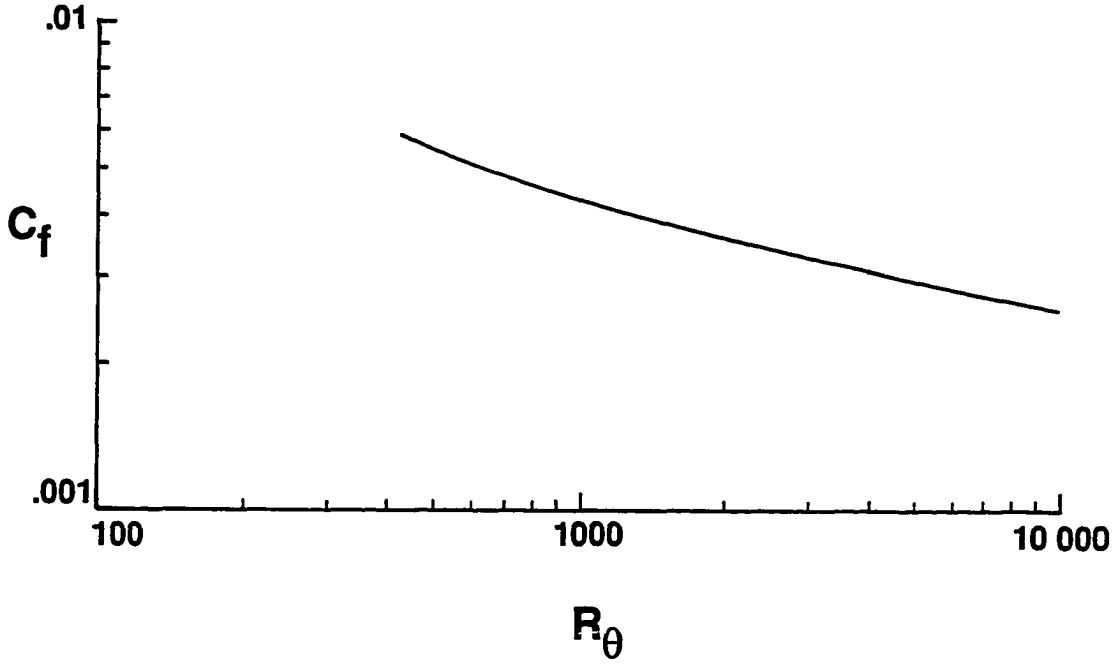

Figure A.5 C_f versus R_θ from Coles [76].

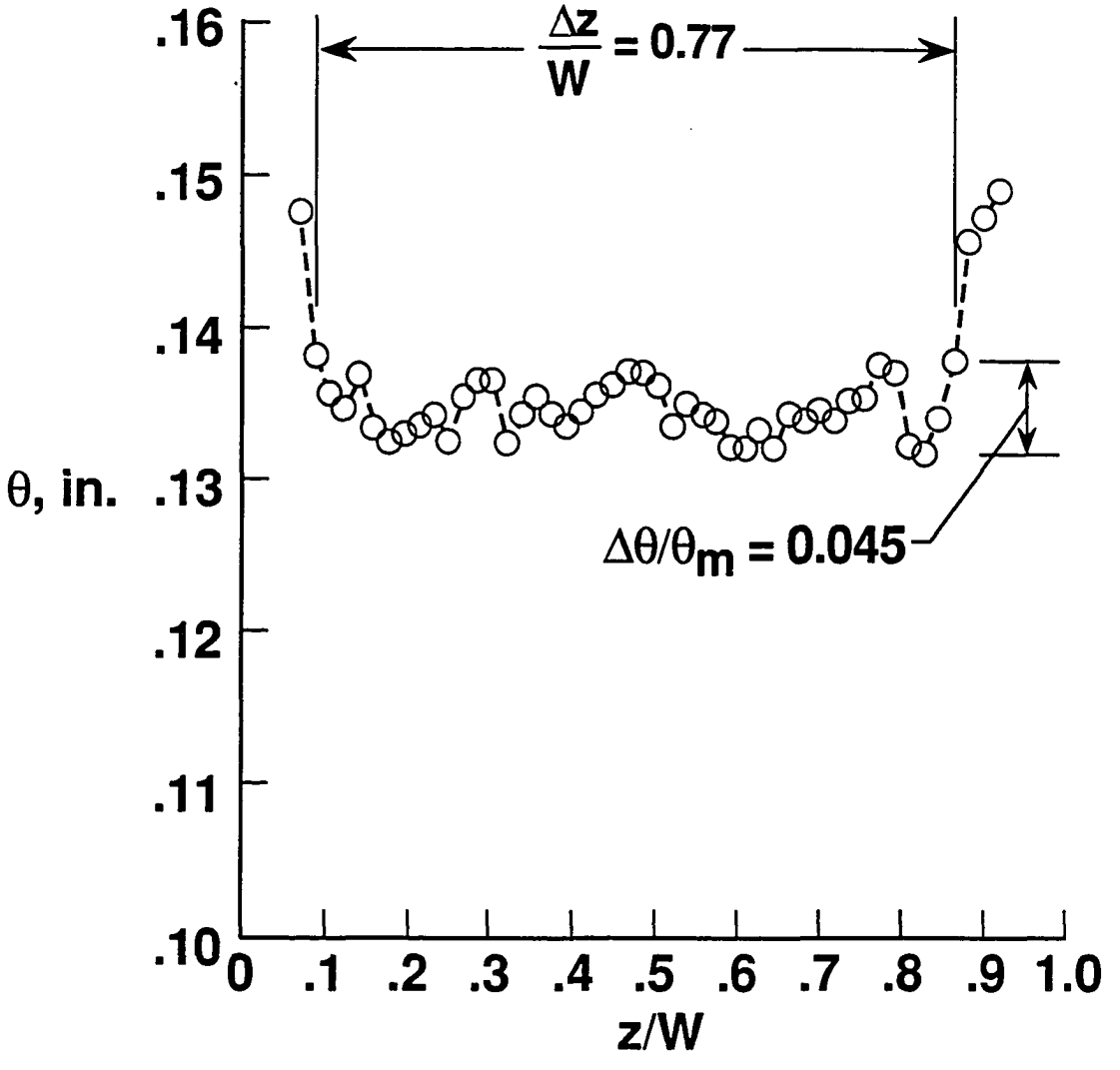

Figure A.6 Spanwise variation of θ at x = 76 in. and R_θ = 9100.

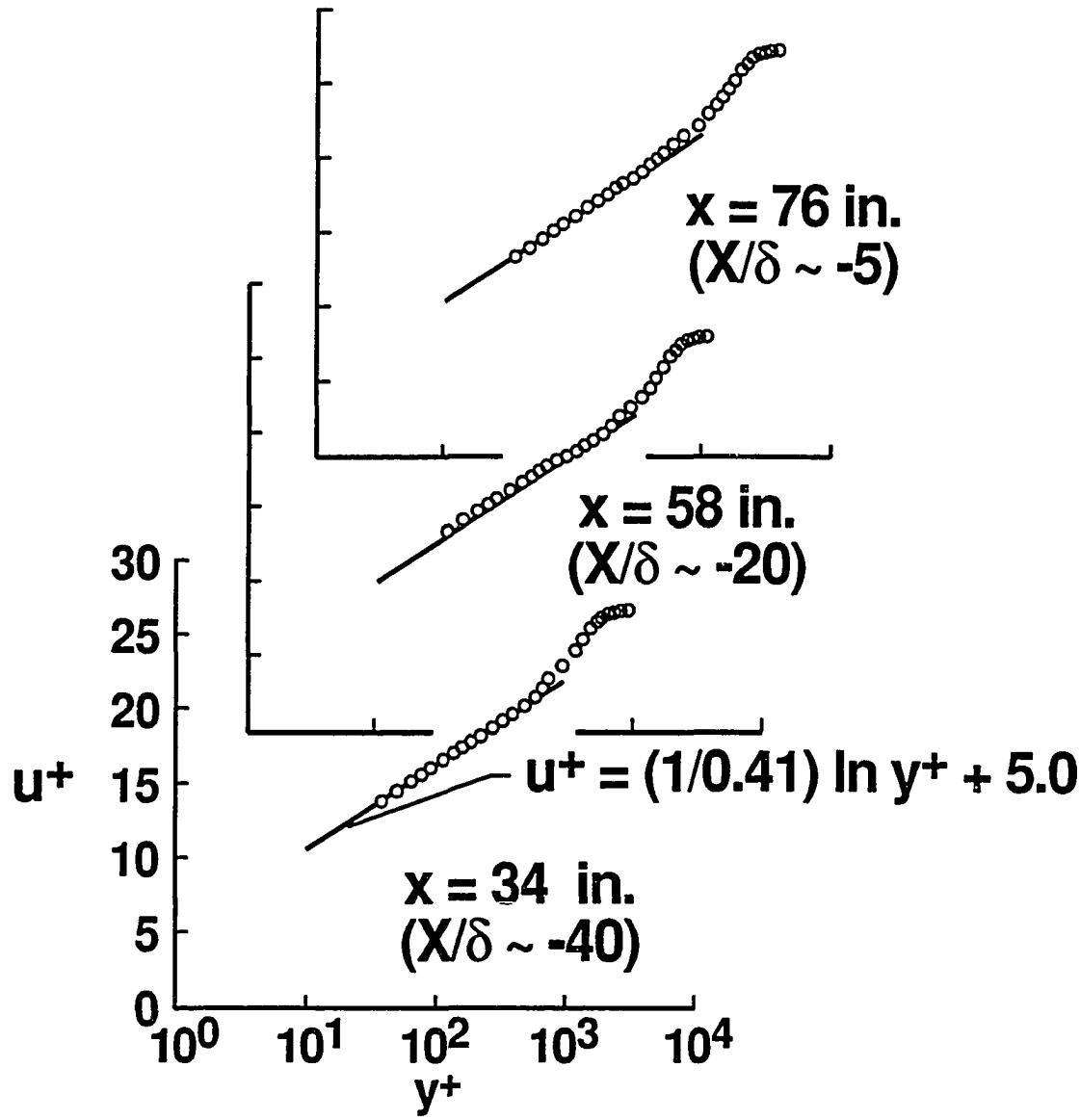

Figure A.7 Law-of-the-wall plot at $x = 34$, 58, and 76 in.

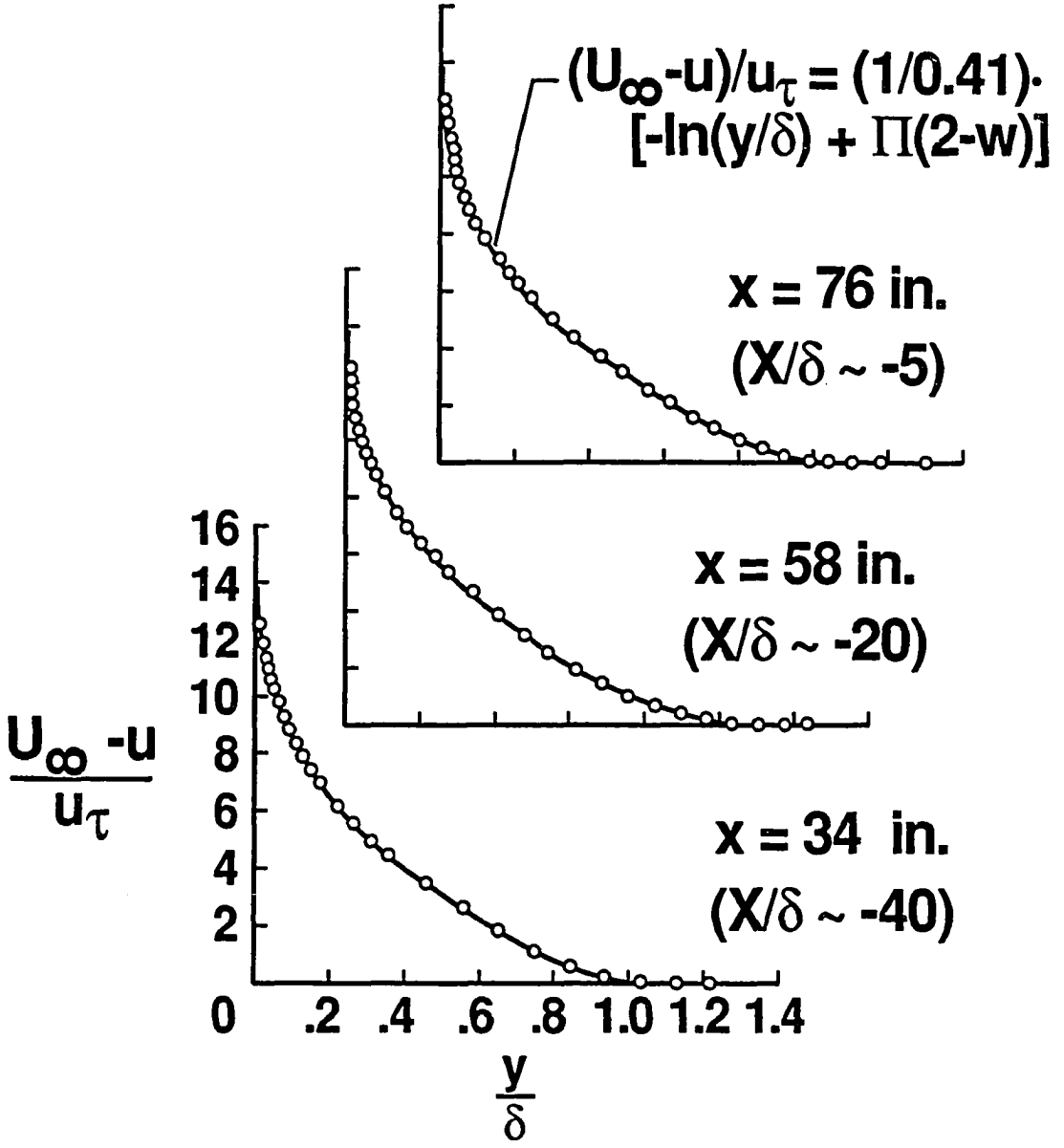

Figure A.8 Velocity defect profile at x = 34, 58, and 76 in.

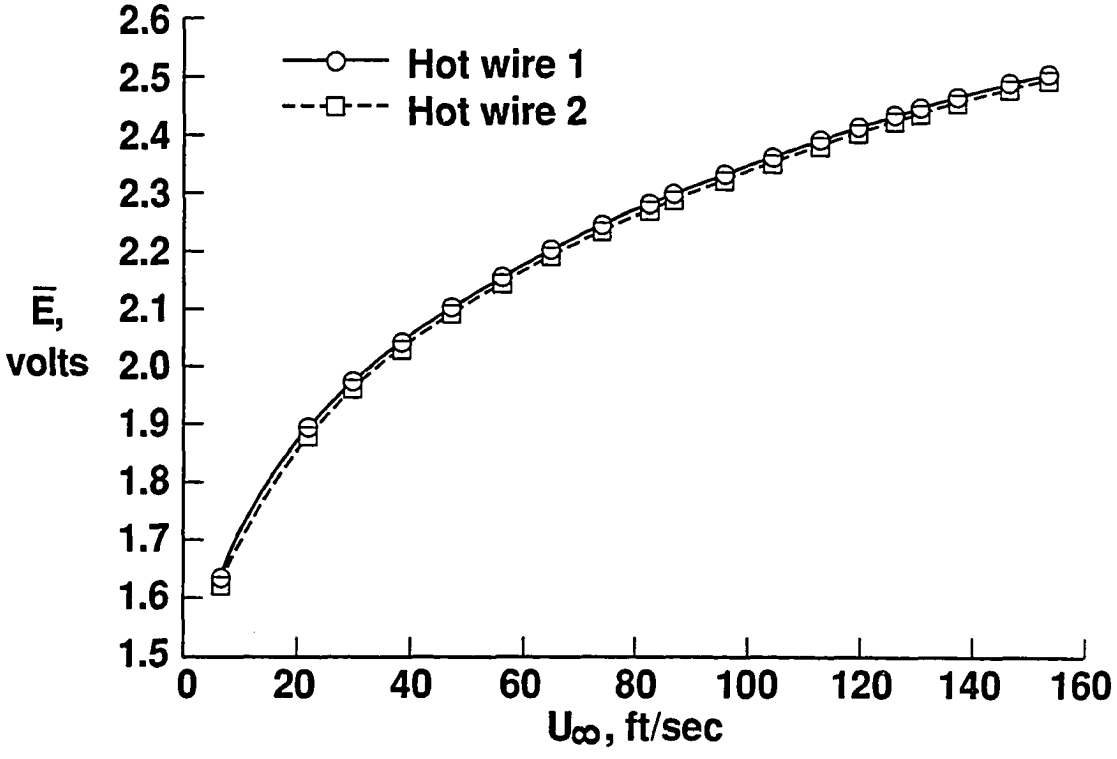

Figure A.9 Hot-wire calibration curves.

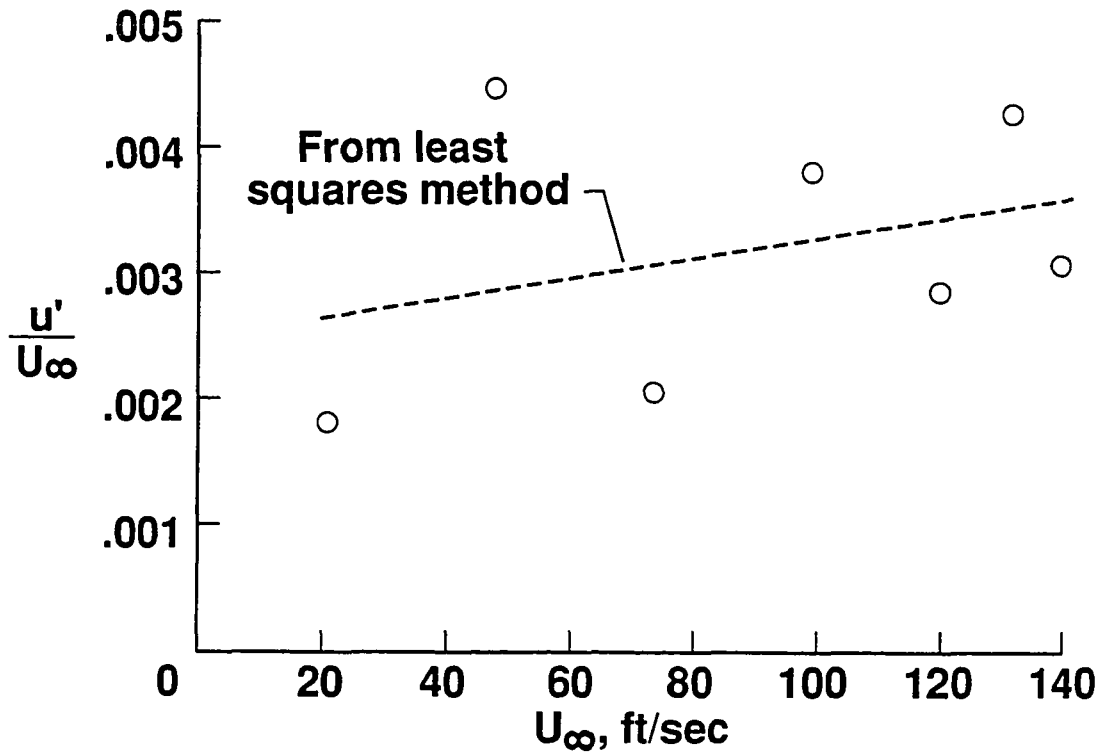

Figure A.10 Freestream turbulence intensity.

APPENDIX B

WATER-TUNNEL SURVEY

Boundary-layer velocity profile measurements were made with a fiber-optically-linked laser-Doppler velocimeter system developed by Complere Inc. In the current study, this system was designed to measure one component (u) of the instantaneous velocity vector. The laser velocimeter system is schematically shown in Figure B.1. The light source was an Argon-ion laser (Coherent Innova Model 90-6) with a maximum power of 6 watts. The laser beam output was split into two parallel, equal intensity beams within a Bragg cell, and one of the beams was frequency shifted in order to detect the orientation of the measured velocity vector. The resultant beams were each separated into three pairs of beams of different wavelength, Λ, (i.e., $\Lambda = 476.5$, 488, and 514.5 nm) by a dispersion prism. Only the $\Lambda = 467.5$ nm (violet) beams were used in the present investigation. These two resultant beams were then passed through a pair of optical fibers via a fiber optic coupler and focused by appropriate optics to define the probe volume. Interference of the two light beams of equal wavelength in the probe (measuring) volume produced a number of nearly parallel fringes (i.e., bright and dark stripes) whose spacing is expressed as

$$\delta_f = \frac{\Lambda}{2 \sin \phi} \tag{B-1}$$

where ϕ is the half-angle of the two beams defining the probe volume (see Figure B.1).

The emitting and collecting optics (forward scattering) were fitted onto a three-dimensional traverse system that moved at very accurate intervals (steps of 0.00005 in.) along each perpendicular axis. Velocity data were collected by the system when naturally occurred small rust particles (i.e., iron-oxide) within the water tunnel passed through the

probe volume. A small particle crossing the intersection volume with velocity u scattered the light of both beams, part of which was collected by a photodetector. The frequency of each collected beam was shifted from the incident light frequency by an amount proportional to the particle velocity (Doppler-Fizeau phenomenon). Optical mixing of the two collected beams on the photodetector produced a photocurrent, I, such that

$$I \sim E_{s1}^2 + E_{s2}^2 - 2E_{s1}E_{s2}\cos\left[2\pi\left(f_{s2} - f_{s1}\right)t_i\right] \tag{B-2}$$

where E_{s1} and E_{s2} are the amplitudes of the scattered beams and f_{s1} and f_{s2} are the scattered beam frequencies. The difference $f_{s2} - f_{s1}$ is equal to the *Doppler frequency*

$$f_D = \frac{2\sin\phi}{\Lambda}u \tag{B-3}$$

which was independent of the observation angle. Thus, the flow velocity component, u, perpendicular to the two-beam bisector was determined directly from the measurement of f_D, via Equations (B-2) and (B-3). The Doppler frequency was found using a frequency counter, which basically time a fixed number, N, of zero crossings. Then, from Equations (B-1) and (B-3) the particle velocity is simply

$$u = \delta_f f_D = \frac{\delta_f N}{\Delta t_i} \tag{B-4}$$

where Δt_i is the total time interval to count N zero crossings.

A great advantage of the response Equation (B-4) is that it is linear and it contains no undetermined constants, thus eliminating the need for calibration [81,82].

Both turbulent and laminar boundary-layer velocity profiles were measured on the test-section centerline at a location 34 in. downstream of the boundary-layer trip (i.e., x = 34 in. or 170 trip diameters). One thousand data samples were taken at each y-position to define the local boundary-layer velocity. The measured turbulent boundary-layer velocity profile (U_∞ = 8.3 in/s) is presented in Figure B.2 using conventional

variables and in Figure B.3 using the inner law variables where u^+, y^+, and u_τ are defined in Equations (A-6, 7, and 8), respectively.

It can be observed in Figure B.2 that the measured profile has high velocity gradients near the wall that is characteristic of turbulent boundary layers. In Figure B.3, the measured velocity profile is compared with the generally accepted Coles' empirical relation $\left(\text{i.e., } u^+ = \frac{1}{0.41}\ln y^+ + 5.0\right)$ for the turbulent log region. It can be seen that good agreement exists in the log region. However, the data stays close to Coles' empirical curve in the wake region which is an indication of a slight favorable-pressure-gradient [83], A similar effect seems to exist for the laminar boundary layer. Figure B.4 shows the measured laminar velocity profile compared with the Blasius solution. Good agreement is observed between the two profiles over $0.4 < \frac{y}{\delta} < 1$. The slightly larger velocity gradient for the measured data at $\frac{y}{\delta} < 0.4$ probably was caused by the marginally favorable pressure gradient within the test secton due to the growth of wall boundary layers. Because the magnitude of $\frac{dp}{dx}$ is relatively small, it is believed that the marginally favorable pressure gradient was acceptable for the present study since no quantitative measurements were conducted. Vortices formed by the flow control devices should be similar under both zero and slightly favorable pressure-gradient boundary layers. The boundary-layer thickness, δ, was determined to be 1.8 in. for turbulent flow and 1.2 in. for laminar flow. Also, R_θ was calculated to be 1000 for turbulent flow and 110 for laminar flow via Equations (A-3) and (A-4).

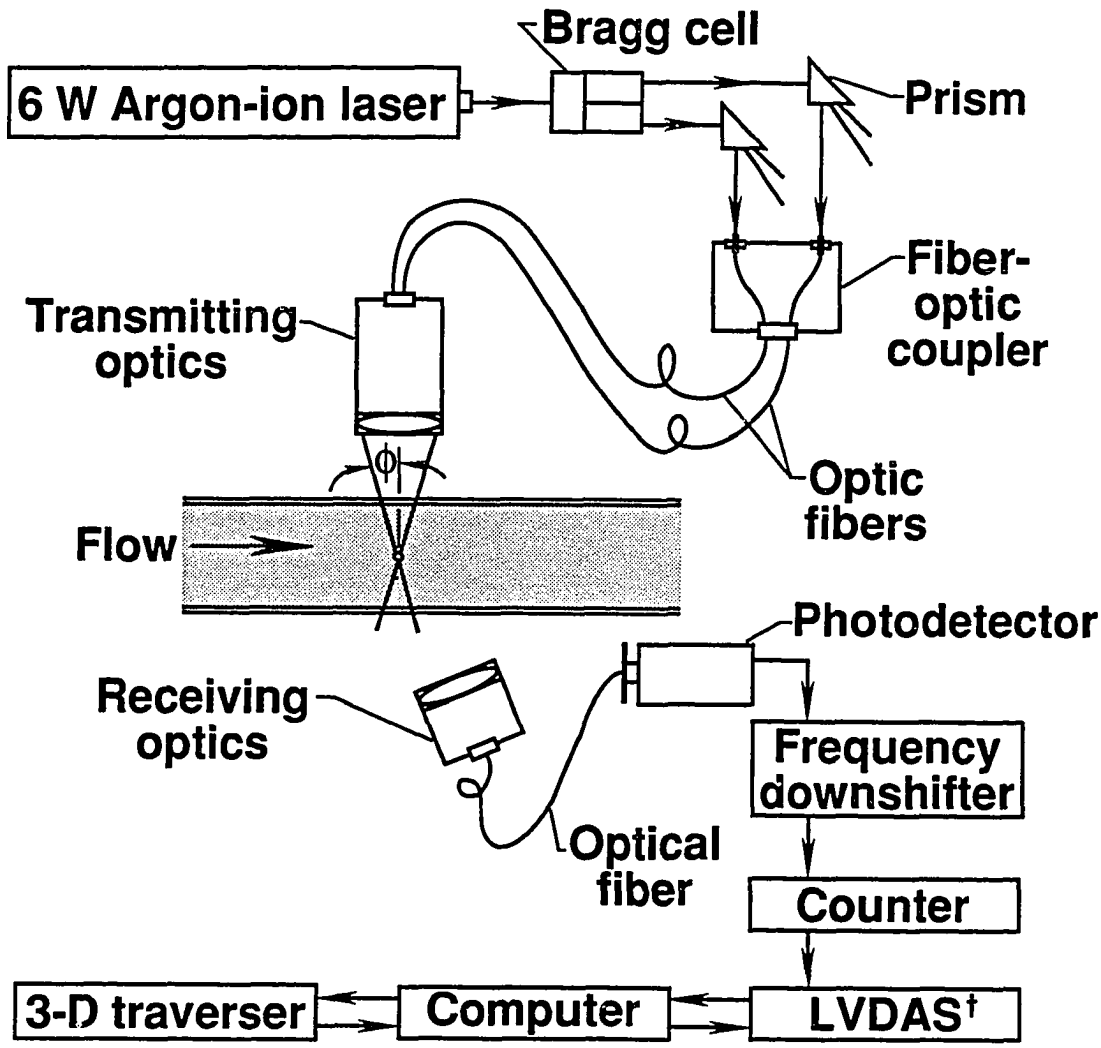

†Laser Velocimeter Data Acquisition System

Figure B.1 Schematic representation of the laser-Doppler velocimeter system.

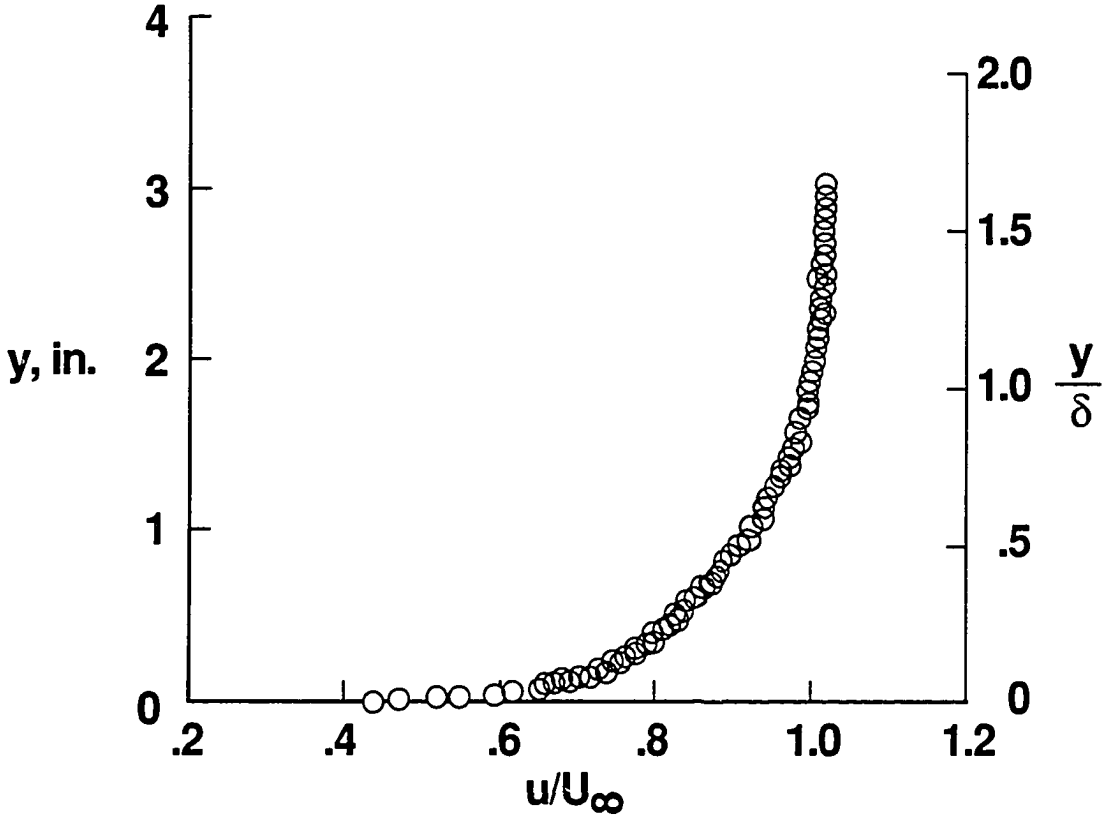

Figure B.2 Typical turbulent boundary-layer velocity profile in water tunnel ($x = 34$ in., $U_\infty = 8.3$ in/s).

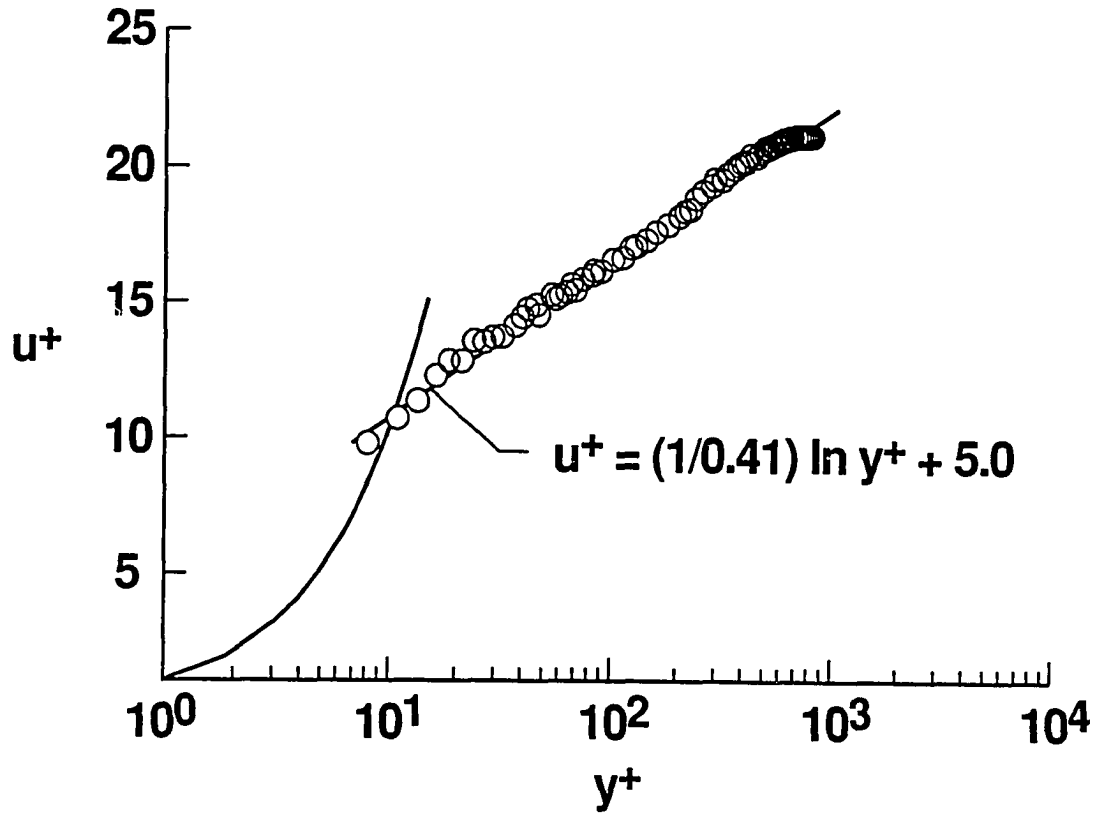

Figure B.3 Water tunnel law-of-the-wall plot ($x = 34$ in., $U_\infty = 8.3$ in/s).

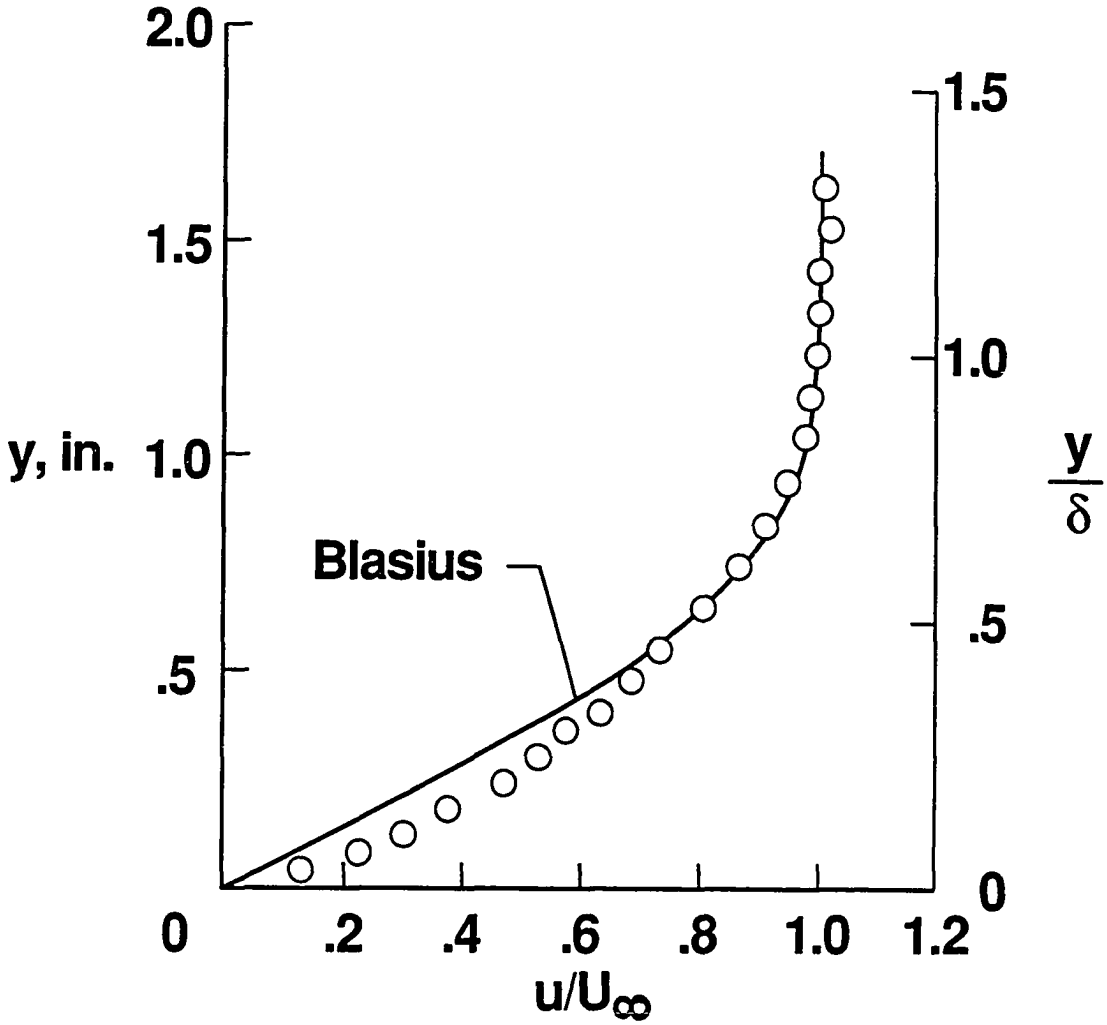

Figure B.4 Typical laminar boundary-layer velocity profile in water tunnel ($x = 34$ in., $U_\infty = 1$ in/s).